Mass spectrometric methods for measuring dynamic processes, drug-induced effects and target engagement on the cell surface glycoproteome

Dissertation

zur Erlangung des
Doktorgrades der Naturwissenschaften (Dr. rer. nat.)

der

Naturwissenschaftlichen Fakultät I – Biowissenschaften –

der Martin-Luther-Universität
Halle-Wittenberg,

vorgelegt

von Herrn Mathias Kalxdorf

geb. am 18.09.1988 in Rostock

Gutachter: Prof. Dr. Andrea Sinz
Prof. Dr. Mike Schutkowski
Prof. Dr. Michael Glocker

Tag der öffentlichen Verteidigung: 26.06.2018

Index

List of figures

List of figures

List of figures - Appendix

List of tables

Abbreviations

Abbreviation	Description
ABC	ATP-binding cassette
ABPP	Activity-based protein profiling
ACN	Acetonitrile
AQUA	Absolute quantification
ATP	Adenosine triphosphate
AUC	Area under the curve
CAA	2-chloroacetamide
CD	Cluster of differentiation
CHAPS	3-[(3-cholamidopropyl)dimethylammonio]-1-propanesulfonate
CID	Collision induced dissociation
CSTPP	Cell surface thermal proteome profiling
Ctrl	Control
DARTS	Drug affinity responsive target stability
DDM	n-dodecyl-β-D-maltopyranoside
DTT	Dithiothreitol
EC50	Half maximal effective concentration
ECM	Extracellular matrix
ELISA	Enzyme-linked immunosorbent assay
ESI	Electrospray ionization
ETD	Electron transfer dissociation
FA	Formic acid
FACS	Fluorescence-activated cell sorting
FCS	Fetal calf serum
FDA	Food and drug administration
FDR	False discovery rate
GalNAc	N-acetylgalactosamine
GlcNAc	N-acetylglucosamine
GO	Gene Onthology
GPCR	G-protein coupled receptor
HCD	Higher energy collisional dissociation
HT	Heat treatment
IAA	Iodoacetamide
IBAQ	Intensity-based absolute quantification
ICAT	Isotope-coded affinity tags
IMAC	Immobilized metal ion affinity chromatography
ITRAQ	Isobaric tags for relative and absolute quantification
Kd	Dissociation constants
m/z	Mass to charge ratio
mAb	Monoclonal antibody
MALDI	Matrix-assisted laser desorption ionization
MS	Mass spectrometry
MW	Molecular weight
NCE	Normalized collision energy
NHS	N-hydroxysuccinimide ester

Abbreviation	Description
o.n.	Overnight
PBS	Phosphate buffered saline
PEG	Polyethylene glycol
PMA	Phorbol-12-myristate-13-acetate
PNGase F	Peptide-N-Glycosidase F
ppm	Parts per million
PSM	Peptide spectra matched
PTM	Post-translational modification
qupm	Quantified unique peptides matched
qusm	Quantified unique spectra matched
RT	Room temperature, 25 °C
RTK	Receptor tyrosine kinase
SCX	Strong cation exchange
SDS	Sodium dodecyl sulfate
SILAC	Stable isotope labeling with amino acids in cell culture
SLC	Solute carrier
SPS	Synchronous precursor selection
TCEP	Tris-(2-carboxyethyl)phosphine
TEAB	Triethylammonium bicarbonate
TFA	Trifluoroacetic acid
TIC	Total ion chromatogram
TM	Transmembrane
TMT	Tandem mass tag
TOF	Time of flight
TPP	Thermal proteome profiling
Tris	Tris-(hydroxymethyl)-aminomethane
XIC	Extracted ion current

Abstract

The plasma membrane proteome plays a crucial role in inter- and intracellular signaling, cell survival and cell identity thus rendering it a prominent target for pharmacological intervention. However, the relatively low abundance of this subproteome in conjunction with challenging extractability and solubility still hampers its comprehensive analysis. In this thesis, a selective chemical glycoprotein tagging and enrichment strategy was combined with mass spectrometry to enable comprehensive analysis of the cell surface glycoproteome. Based on this methodology, a toolbox of techniques was developed allowing qualitative and quantitative characterization of cell surface proteomes, facilitating analysis of cell surface phosphoproteomes as well as studying target engagement of small molecules and biopharmaceuticals to plasma membrane proteins.

To benchmark the workflow and to provide guidance for cell line selection for functional experiments, an inventory of cell surface glycoproteomes of 15 standard laboratory human cell lines and three primary lymphocytic cell types was generated. On average about 850 plasma membrane and secreted proteins were identified per experiment including in total more than 300 transporters and ion channels. Primary cells displayed distinct expression of surface markers and transporters underpinning the importance of carefully validating model cell lines selected for the study of cell surface-mediated processes. For quantitative analysis of dynamic changes in the cell surface proteome by highly multiplexed experiments, an isobaric mass tag-based chemical labeling strategy was employed. This enabled the time-resolved analysis of plasma membrane protein presentation during differentiation of the monocytic suspension cell line THP-1 into macrophage-like adherent cells. Time-dependent changes observed in membrane protein presentation and phosphorylation reflect a functional remodeling during the phenotypic transition in three distinct phases: rapid surface presentation and secretion of proteins from intracellular pools concurrent with rapid internalization of no longer needed proteins and finally delayed presentation of newly synthesized macrophage markers. Perturbation of this process using marketed receptor tyrosine kinase inhibitors revealed the BCR-Abl inhibitor dasatinib to severely compromise macrophage differentiation due to an off-target activity. Interestingly, this effect could only be observed when the drug was present during differentiation, suggesting that dynamic processes can be highly vulnerable to drug treatment and should be monitored more rigorously to identify adverse drug effects.

The combination of cell surface labeling with the recently described thermal proteome profiling enabled selective monitoring of protein stability and surface presentation changes in the plasma membrane proteome. These effects are indicative for direct interactions between an added substance (small molecule, native ligand or antibody) and a cell surface protein or provide a readout of downstream pharmacological events. The cell surface thermal proteome profiling approach enables selective monitoring of treatment-induced effects on cell surface accessible proteins with excellent coverage of this subproteome. Interferences by intracellularly stored pools of these proteins are circumvented. The applicability of the approach was demonstrated by showing target engagement to receptor tyrosine kinases, integrins, ABC transporters and other target classes. Endogenous ligands like CXCL12, IL2 and VLDL induced target internalization instead of altered thermal stability. Furthermore, cellular treatment with the HSP90 inhibitor luminespib during heat-shock enabled the identification of HSP90 clients on the cell surface of cancer cells.

In summary, this thesis presents a methodological framework which enables the mapping of cell type specific surface protein presentation and the accurate quantification of changes in this subproteome upon differentiation or compound treatment. In addition, drug-protein interactions at the plasma membrane can be monitored via changes in protein thermal stability or cell surface presentation.

1. Introduction

1.1. The Plasma membrane proteome

The plasma membrane constitutes the physical interface between a cell and its environment, and plays a key role in a multitude of processes like intercellular interactions, intercellular communications and cell adhesion, as well as in outside-in and inside-out signal transmission. These crucial functions, necessary to sense environmental changes and to respond appropriately e.g. to autocrine, endocrine or other environmental signals, are performed by integral plasma membrane proteins as well as membrane associated proteins with extracellular domains. For instance, adhesion proteins define cell shape and motility (Neugebauer and Reichardt, 1991), transporters are involved in the influx and efflux of molecules, including nutrients, salts and bioactive compounds (Anderle et al., 2004; Wollscheid et al., 2009), and growth factor receptors as well as G-protein coupled receptors (GPCRs) transfer external stimuli into the cell (Navarro et al., 2016). Importantly, the composition of the plasma membrane proteome is not static, but cells adjust according to their developmental status, nutrient availability or external signals (Li et al., 2011).

1.1.1. Constituents of the plasma membrane

The framework of the cell membrane is a lipid bilayer. According to the fluid-mosaic membrane model, introduced by Singer and Nicholson in 1972 (Singer and Nicolson, 1972), lipids form a two-dimensional flexible liquid with embedded proteins (Nicolson, 2014). Within this fluid, lipids as well as proteins are considered to be capable of lateral motions and rotations. Lipids constitute about 50 % of the mass of most animal cell membranes (Opekarová and Tanner, 2003). These molecules are amphipathic with a hydrophilic polar head and hydrophobic nonpolar tails usually containing fatty acids. The length and the grade of saturation of these tails affect the fluidity of the membrane by defining the possible density of lipid packing. In aqueous environments the amphipathic nature of the lipid molecules causes the spontaneous formation of a bilayer. Hydrophilic heads are exposed to water molecules forming hydrogen bonds or electrostatic interactions while the hydrophobic tails are buried in the interior. Due to low van der Waals attractive forces between most of the fatty acid tails, lateral motions and rotations of lipids and embedded proteins are enabled. Lipids with long and saturated fatty acid chains can form transient microdomains or lipid rafts (Simons and van Meer, 1988) in which attractive forces are high enough to hold adjacent molecules together. These rafts are thicker than other parts of the bilayer due to the longer and straighter fatty acid chains enabling a better accommodation of certain proteins (Alberts et al., 2002, Fig. 1). Thus, lipid rafts are thought to be involved in membrane protein organization and consolidation of functional protein complexes serving as platforms for signaling, trafficking, transport and cell structure (Tan et al., 2008).
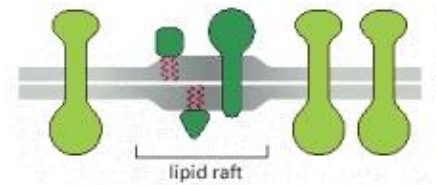
Fig. 1 Lipid rafts. Due to a different lipid composition, the lipid bilayer (grey) is thicker in the rafts enabling accommodation and aggregation of certain proteins (dark green). (From Alberts et al., 2002).

Proteins constitute up to 50 % of the mass of most animal cell membranes (Tan et al., 2008; Opekarová and Tanner, 2003). A schematic illustration of typical membrane proteins is shown in Fig. 2.
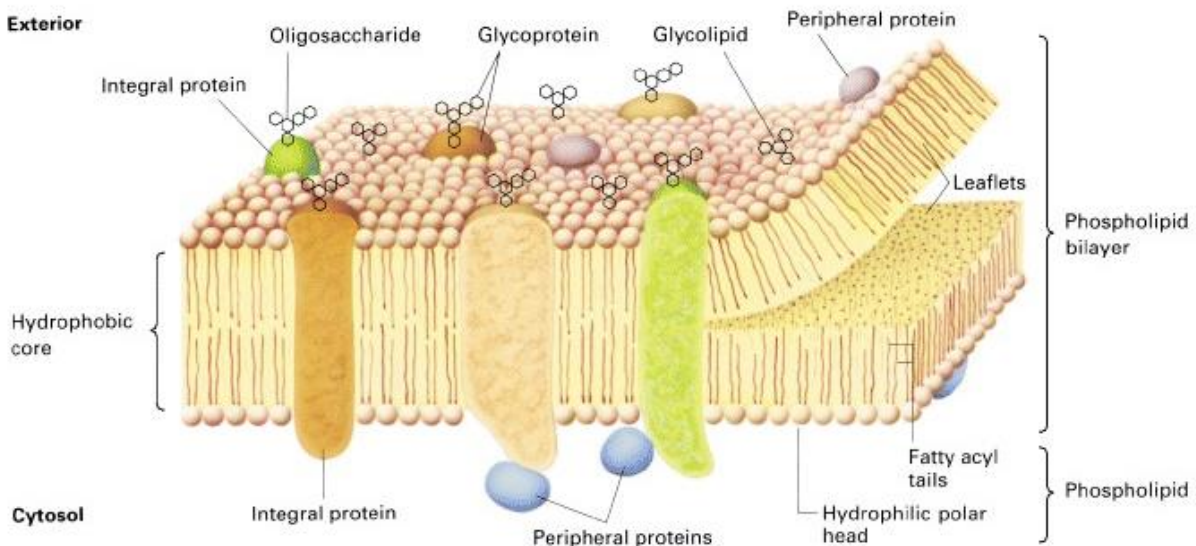
Fig. 2 Cell membrane and typical membrane proteins. Phospholipids forming a bilayer are the framework of the cell membrane. Two groups of membrane proteins can be distinguished: integral and peripheral. Integral membrane proteins span the bilayer or are tethered to the membrane by a covalently attached lipid anchor group. Peripheral membrane proteins are associated with the membrane by protein-protein interactions. Glycosylation is a common post-translational modification of plasma membrane proteins which is indicated by oligosaccharides. (Figure adapted from Alberts et al., 2002).

Proteins can be classified into integral and peripheral membrane proteins based on their interaction with the membrane. Most integral membrane proteins span the bilayer with one (single-pass transmembrane proteins) or more (multi-pass transmembrane proteins) domains buried within the membrane. These transmembrane domains are preferentially composed of hydrophobic amino acids (Hu et al., 2007), are generally 20 amino acids long (according to UniProt) and are typically forming α-helical secondary structures (Bowie, 2005). In these structures, the side chains of the hydrophobic amino acids form van der Waals interactions with the fatty acid chains of the membrane lipids. This shields the polar groups of the peptide backbone which are all hydrogen-bonded to one another (Alberts et al., 2002). Other transmembrane proteins are composed of multiple β-stranded secondary structures. These form a barrel-like transmembrane pore with hydrophobic outwards-facing and hydrophilic inwards-facing amino acid side chains. Some other integral membrane proteins are attached to the membrane by covalently linked lipid anchor groups. Peripheral membrane proteins are usually bound to the membrane by protein-protein interactions or by interactions with the polar lipid head groups. Examples of peripheral membrane proteins are cytoskeletal proteins like actin on the cytosolic face of the cell membrane and extracellular matrix proteins like collagens on the external face of the cell membrane.

Besides classification of membrane proteins based on their membrane interaction, they can be also distinguished by their function. The two main functional groups are receptors and transporters. Receptors are involved in the transmission of signals from the external space into the cells or vice versa and are used for intercellular communication as well as cell adhesion. Depending on the cellular environment, complex signaling pathways like proliferation, apoptosis or differentiation are triggered and controlled by these proteins. Malfunctions can result in uncontrolled proliferation, loss of apoptotic response or autoimmune reactions leading to pathogenesis of several diseases like cancer (Cordwell and Thingholm, 2010). Transmission of external stimuli typically involves a ligand binding event to extracellular domains of integral transmembrane receptors inducing conformational changes in their intracellular domains. Subsequent signaling cascades amplify this response at the intracellular part of the receptor,

resulting in a cellular response to the external stimulus. Based on the process of signal transmission, five classes of plasma membrane receptors can be distinguished (Cooper, 2000): (I) GPCRs, (II) receptor tyrosine kinases (RTKs), (III) Toll-like receptors, (IV) ligand-gated ion channels and (V) integrins. GPCRs form the largest family of cell surface receptors transmitting signals via guanine nucleotide-binding proteins (G-proteins, Kobilka, 2007). Receptor activation enables G protein association to cytosolic domains of the receptor resulting in the activation of these molecular switches and transmission of the signal to subsequent signaling cascades. In case of RTKs, ligand binding induces receptor dimerization and activation of the latent kinase activity by trans-autophosphorylation of tyrosine residues in the cytoplasmic domain of the receptor (Hubbard and Miller, 2007). Subsequently, adapter proteins can recognize the phosphorylated tyrosine residues, get phosphorylated and thereby link the RTK activation to intracellular signaling cascades. In the same manner, Toll-like receptor signaling involves intracellular adapter protein binding upon receptor activation and dimerization (Chattopadhyay and Sen, 2014). However, these receptors are non-catalytic and without an intrinsic kinase activity. The last two groups of receptors have different modes of action for signal transduction. In case of ligand-gated ion channels, binding of a ligand modifies the conformation of a membrane pore thereby regulating ion fluxes across the membrane. This ion translocation along an electrochemical gradient leads to a modification of membrane potentials important for signal transductions in synapses. The last class of receptors comprises the group of integrins forming functional heterodimers with an alpha and a beta subunit. These receptors are most importantly involved in cell adhesion as a large number of integrin ligands are components of the extracellular matrix, including collagens, fibronectins, fibrinogen, laminins and vitronectin (Plow et al., 2000). Integrins are pre-activated by integrin activators like talin which bind to the cytoplasmic domain of the beta subunit of the receptor (Harburger and Calderwood, 2009). This activation probably disrupts the inhibitory interactions between alpha- and beta-cytoplasmic tails and increases the affinity of the receptor for its ligands (Wegener et al., 2007). Ligand binding induces the formation of intracellular protein clusters composed of the receptor and anchor proteins triggering intracellular signaling pathways with two major functions: organization of the actin cytoskeleton and regulation of cell behavior including survival, differentiation and growth (Cabodi et al., 2010). Initial connections between the extracellular matrix (ECM) and the cytoskeleton are further reinforced by recruitment of additional cytoskeletal and signaling proteins forming multiprotein complexes and maturing cell adhesion (Giannone and Sheetz, 2006; Harburger and Calderwood, 2009).

The cell membrane forms a physical permeability barrier between the external environment and the internal compartments of a cell. This enables a controlled migration of molecules across the membrane which is regulated by transmembrane transporters. These contain multiple membrane-spanning regions that form a passage through the lipid bilayer, allowing polar or charged molecules like sugars or amino acids to cross the membrane through a protein pore (Cooper, 2000). Two classes of transporters can be distinguished: channels and carriers. Channels form pores within the membranes which can be in an opened or closed conformation (Shaikh et al., 2010). The selectivity of the channels is defined by size and polarity of the pore. This enables selected molecules to pass the cell membrane in an energetically favorable direction along a concentration and electrochemical gradient known as passive transport. Examples are the inorganic ion channels for Na^+, K^+, or Cl^-. In contrast to channels, carriers facilitate the passage of selected molecules by switching between conformational states. Upon substrate binding on one side of the membrane, conformational changes open a channel through the lipid bilayer and result in the release of the molecule on the other side. Examples for passive transport carriers are the facilitative glucose (Mueckler and Thorens, 2013) and nucleoside transporters of the solute carrier (SLC) group of membrane transporters. The

transport rate of these proteins is much lower than for channels, however, it also bears the capability of active transport of molecules in an energetically unfavorable direction using cellular energy. Two forms of active transport can be distinguished: primary and secondary active transport. Transporters using the first form are typically pumps which use metabolic energy e.g. released by ATP hydrolysis. Examples are sodium-potassium pumps and multidrug resistance transporters. For secondary active transport, used by antiporters and symporters, the released entropic energy of the transport of one substrate along its concentration gradient is used to transport a second substrate in an energetically unfavorable direction.

1.1.2. Post-translational modifications of plasma membrane proteins

Many biological processes, like signal transduction or transmembrane transport, require adjustment of protein conformational state in an appropriate time scale. In addition, correct protein function is often defined by context-dependent integration of signals. Post-translational modifications (PTM) introducing a covalent but reversible modification in an amino-acid residue (Prabakaran et al., 2012) is one way used by nature to cope with these demands. Protein phosphorylation and N-linked glycosylation are among the most frequently experimentally observed PTMs (Prabakaran et al., 2012). Especially phosphorylation is used for dynamic information encoding in molecular biology. Addition of phosphoryl groups at multiple phosphorylation sites enable complex modification patterns and gives rise to a high number of combinatorial possibilities. These allow accurate cellular responses to a wide variety of environmental stimuli and cellular mechanisms. In case of plasma membrane proteins, phosphorylation-based information encoding is used for several processes like regulation of membrane potentials by ion channels (Prabakaran et al., 2012), signal transduction by GPCRs (Prabakaran et al., 2012) and regulation of transmembrane protein trafficking (Offringa and Huang, 2013).

Glycosylation of proteins is one of the most important PTMs (Christiansen et al., 2014) with special relevance for plasma membrane proteins. Cell surface attached glycans are involved in numerous biological functions like cell adhesion, intercellular communication and signal transduction (Christiansen et al., 2014). Furthermore, they are involved in protein folding, protein trafficking to the plasma membrane via the secretory pathway (Moharir et al., 2013) and altering protein turnover (Moremen et al., 2012). Glycosylation is an enzyme-directed and site-specific process occurring in the lumen of the endoplasmic reticulum or in the Golgi complex (Xu and Ng, 2015). Approximately 700 proteins are thought to be required to generate the full diversity of mammalian glycans which are assembled from only ten monosaccharides (Moremen et al., 2012). Due to numerous possibilities for branching and anomeric linkage, glycan structures can be highly complex with a diversity greatly exceeding linear nucleic acid or polypeptide structures (Cummings, 2009). Microheterogeneity, induced by competition among multiple enzymes involved in the glycosylation process, can even increase the complexity by generating diverse glycan modifications at the same glycosylation site of otherwise identical proteins (Schachter, 1991). This diversity can enable protein functional pleiotropy in a cellular context dependent manner (Moremen et al., 2012). For cell surface proteins the two most prominent forms of this post-translational modification are N-linked and O-linked glycosylation. Typical N-linked and O-linked oligosaccharides, which in vertebrates are usually terminated by a negatively charged sialic acid residue (Varki, 2007), of transmembrane and secreted proteins are illustrated in Fig. 3.
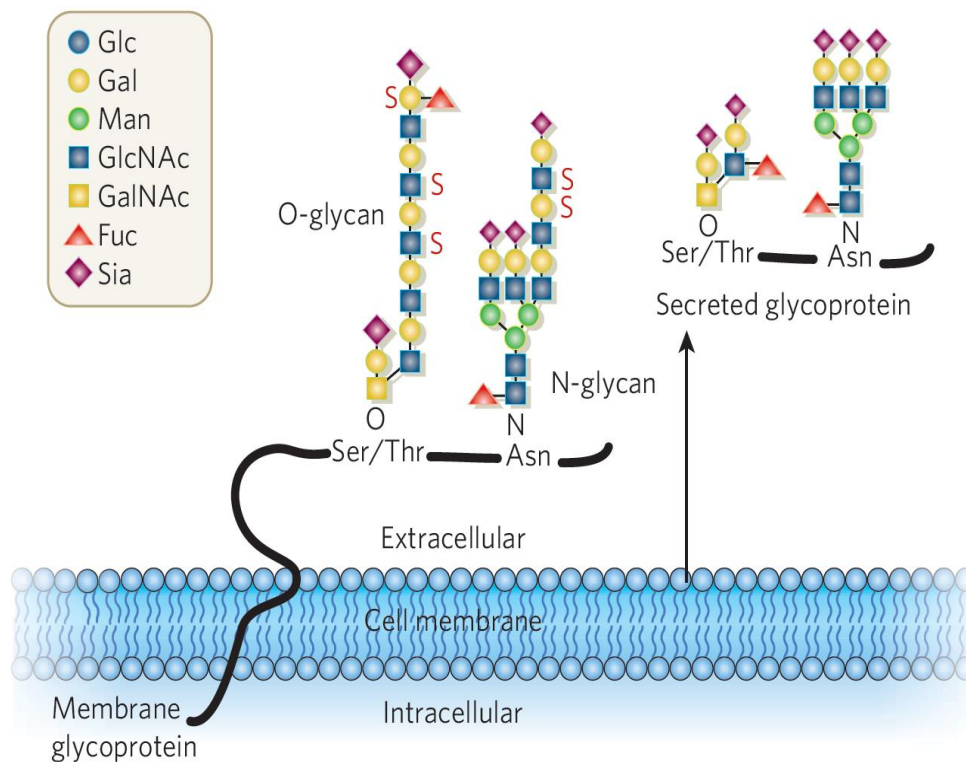
Fig. 3 Typical N- and O-linked oligosaccharides of transmembrane and secreted proteins. N-linked glycosylations are usually branched oligosaccharides linked to the amide nitrogen of an asparagine via a GlcNAc. O-linked glycosylations are linked to the hydroxyl group of a serine or threonine typically via a GalNAc**.** In vertebrates glycosylations are generally terminated by a sialic acid residue. Fuc, fucose; Gal, galactose; GalNAc, N-acetylgalactosamine; Glc, glucose; GlcNAc, N-acetylglucosamine; Man, mannose; S, sulphate ester, Sia, Sialic acid. (Figure modified from Varki, 2007).

In case of N-linked glycosylations, oligosaccharides are linked via an *N*-acetylglucosamine (GlcNAc) to the amide nitrogen of an asparagine. This reaction is catalyzed by the multimeric enzyme complex oligosaccharyltransferase transferring a preassembled lipid-linked oligosaccharide to selected asparagines within a consensus peptide sequence of N-X-S/T where X can be any amino acid except proline (Mohorko et al., 2011; Moremen et al., 2012). Other described but far less often occurring N-glycosylation sequence motifs are N-X-C, representing about 1 % of all sites in the mouse glycoproteome (Zielinska et al., 2010), N-G and N-X-V (Moremen et al., 2012). N-linked glycosylation is close to ubiquitous on proteins localized to the plasma membrane (Cordwell and Thingholm, 2010) and enriched in proteins destined for extracellular environments (Roth, 2002). In case of O-linked glycosylation, a generally shorter oligosaccharide is linked to the hydroxyl group of a serine or threonine often via N-acetylgalactosamine (GalNAc). In contrast to N-linked glycosylation, O-linked glycosylation shows no consistent sequence motif and depends on the linking carbohydrate residue (Moremen et al., 2012). However, a general preference for proline residues around glycosylated serines and threonines has been observed (Thanka Christlet and Veluraja, 2001).

1.1.3. Role of plasma membrane proteins in pharmacology

Due to the crucial roles of membrane proteins in many biological processes required for normal development and physiology, aberrant function of these proteins can lead to a range of diseases (Tan et al., 2008). For example, functional disorder of adhesion proteins can result in increased susceptibility for infections, malfunctions of transport proteins are involved in epilepsy, schizophrenia or depression and dysfunctional signal transduction proteins participate in the genesis and progression of many human cancers (Tan et al., 2008). Furthermore, during

malignant cell transformation, major changes in the plasma membrane proteome enable cancerous cells to invade tissue, trigger vascularization, evade the immune system and become independent of external survival signals (Hanahan and Weinberg, 2000). Other examples highlighting the role of cell membrane proteins in ailments are autoimmune diseases. In these, the immune system erroneously targets normal healthy body cells often via cell surface proteins (De Baets, 1994) resulting in chronic inflammatory and destructive diseases like rheumatoid arthritis and diabetes mellitus (Klabunde and Hessler, 2002; Overington et al., 2006). In line with these implications of membrane proteins in major types of diseases, approximately 60% of all FDA approved drugs target transmembrane proteins reflecting the pharmacological relevance of cell surface proteins. GPCRs (>25%) and ion channels (>10%) are the most frequently targeted protein classes (Klabunde and Hessler, 2002; Overington et al., 2006). Amongst the top10 globally selling drugs in 2014, 8 drugs were directly or indirectly targeting membrane proteins (Lindsley, 2015). For drugs with intracellular targets, the plasma membrane poses a barrier for influx and efflux. Drugs can be actively transported out of cells by ATP-binding cassette (ABC) transporters which couple ATP hydrolysis to the active efflux of small molecules. Amplified ABC transporter activity is a common mechanism towards resistance of cancer cells against chemotherapeutics (Gottesman et al., 2002). In contrast to drug efflux, the route of drug influx is controversially discussed. Besides the broadly accepted uptake by passive diffusion (Di et al., 2012) there is growing evidence for active transport mechanisms (Dobson and Kell, 2008; Kell et al., 2013) via solute carrier (SLC) transporters (Dobson and Kell, 2008; Cha et al., 2001; Kimura et al., 2005). Recently, Winter et al. demonstrated that the cell toxicity of the chemotherapeutic YM155 is dependent on protein-mediated transport via SLC35F2 thus linking expression of this transporter to efficacy of the drug (Winter et al., 2014).

1.1.4. Analysis of plasma membrane proteins

Several methods for cell surface protein analysis are available including immunostaining, transcript profiling and proteomics. Antibody-based approaches like enzyme-linked immunosorbent assay (ELISA), immunoblotting, immunohistochemistry, fluorescence microscopy and flow cytometry are frequently used techniques for the analysis of proteins of this subcellular location enabling simple and quick detection of protein expression in lysates, tissue sections and live cells. However, a limitation of most of these methods is their lack of multiplexing capabilities necessary for high-throughput proteome-wide analyses. An exception is a described flow cytometry platform for rapid analysis of more than 350 cell surface antigens (Gedye et al., 2014). However, the major limitation of all immunoaffinity methods is there reliability on antibody availability making these approaches inherently biased.

For systematic investigations of cell surface proteins "omic" approaches like transcriptomics and proteomics are preferentially utilized (Graessel et al., 2015). RNA-sequencing methods are highly sensitive enabling transcript profiling with single cell resolution (Kanter and Kalisky, 2015; Liu and Trapnell, 2016). However, transcript abundances only partially predict protein abundances (Vogel and Marcotte, 2012) since post-transcriptional, translational and protein degradation regulations influence protein levels (Vogel and Marcotte, 2012; de Sousa Abreu et al., 2009). Furthermore, information about protein subcellular localization is not available with transcriptomic approaches. Thus, comprehensive investigation of protein expression is commonly performed by mass spectrometry-based proteomics. Although less sensitive than transcriptomic approaches, proteomics enables precise protein abundance and protein copy number estimations (Wiśniewski et al., 2014) as well as distinction of protein subcellular localizations (Marx, 2015; Boisvert et al., 2010).

While early work on the plasma membrane proteome provided first insights into the protein diversity in this cellular compartment (Pshezhetsky et al., 2007), the relatively low abundance of many plasma membrane proteins and limited compatibility with generic proteomics protocols are major obstacles for the comprehensive analysis of this subproteome (Cordwell and Thingholm, 2010). Reducing sample complexity by selective enrichment and purification of cell surface proteins can increase sensitivity leading to an improved dynamic range and enabling an enhanced identification of low abundant proteins. Traditional approaches involve chemical precipitation and/or density gradient ultra-centrifugation, separating membrane proteins from soluble proteins via physical properties like hydrophobicity and organelle density. However, these methods lack the resolution to provide highly purified plasma membrane fractions (Cordwell and Thingholm, 2010). Another enrichment strategy involves selective proteolytic cleavage of surface-exposed domains of plasma membrane proteins on intact cells. This cell-surface shaving concept could provide information about cell surface topology and avoids the need for hydrophobic protein solubilization. However, instability of cells during protease treatment and subsequent cell removal by centrifugation can result in pronounced contamination with abundant cytoplasmic proteins (Cordwell and Thingholm, 2010). Other frequently used methods for plasma membrane proteome analysis are based on affinity enrichments using immuno-affinity, lectin-affinity and biotin-affinity protocols. Immuno-affinity based approaches were shown to enable highly selective enrichment of cell surface proteins (Watarai et al., 2005). However, these approaches again are reliable on antibody availability and are biased in nature. Lectin-based affinity purification exploits the fact that cell surface proteins are close to ubiquitously glycosylated (Cordwell and Thingholm, 2010) and that lectins are glycan-binding proteins with selectivity for specific carbohydrates. The use of multiple lectins can enable a high coverage of plasma membrane proteins. The last group of affinity enrichments involves selective biotinylation of surface exposed plasma membrane proteins either via accessible lysines or again via glycans. Membrane impermeable N-hydroxysuccinimide ester (NHS) biotinylation reagents allow selective biotinylation of surface accessible amine groups. However, since the biotinylation reaction per se is not selective for plasma membrane proteins, instability of cells during the biotinylation process can result in pronounced contamination with abundant cytoplasmic proteins. This problem can be circumvented by selective biotinylation of surface proteins via their glycosylations as most cytosolic proteins do not carry this post-translational modification. The glycosylation-based biotinylation process requires two individual reaction steps which additionally increases the selectivity for cell surface exposed proteins. An illustration of the method is shown in Fig. 4.
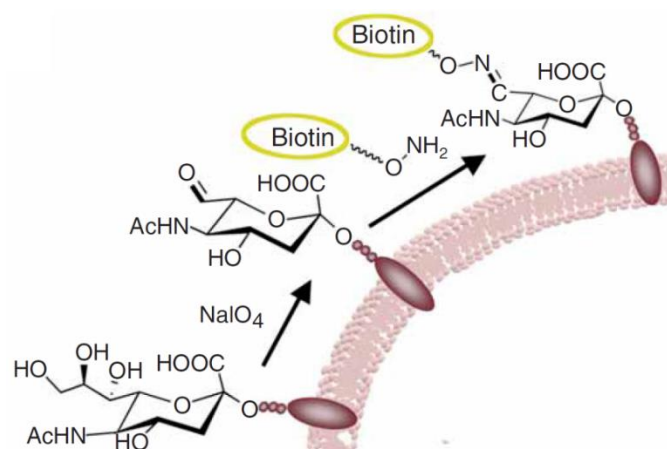
Fig. 4 Biotinylation of cell surface sialylated glycoproteins. Schematic illustration of alkoxyamine-biotin labeling of sialylated cell surface proteins after introduction of aldehydes by periodate oxidation. (Figure modified from Zeng et al., 2009).

In the first step, treatment of cells with the oxidant sodium metaperiodate induces reactive aldehydes primarily in sialylated glycans by vicinal diol cleavage. Since aldehydes are not naturally occurring in proteins, the second step enables selective biotinylation of plasma membrane proteins by oxime ligation. This reaction is biocompatible, very efficient and chemoselective (Ulrich et al., 2014). Usage of an endoglycosidase like PNGase F for elution of enriched biotinylated species constitutes an additional selection factor for cell surface proteins. To reduce sample complexity, the enrichment of labeled proteins is commonly performed after tryptic digestion enabling selective enrichment of glycosylated peptides and reducing contamination by non-specific proteins. This glycan-based plasma membrane proteome enrichment approach has been successfully applied to identify cell surface markers or to map the cell surface proteome of cell lines (Wollscheid et al., 2009; Bausch-Fluck et al., 2015). Further optimized protocols using the oxime-ligation catalyst aniline (Fig. 5) enabled increased speed and efficiency at physiological pH and low temperatures while maintaining high cell viability (Zeng et al., 2009). However, a comparison with the coverage achieved by RNA microarrays suggests that these initial studies may have offered only an initial glimpse on the true complexity of the cell surface proteome (Graessel et al., 2015).
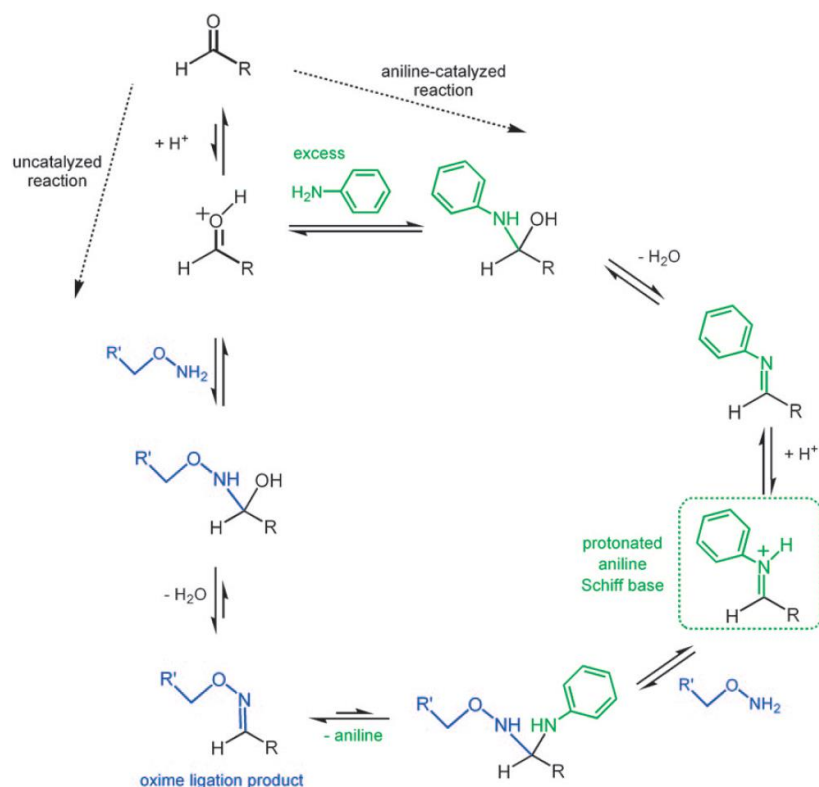
Fig. 5 Catalysis of oxime ligations by aniline. The initial step of the uncatalyzed reaction is slow since it requires protonation of the aldehyde, but not of the alkoxyamine group. Upon addition of the alkoxyamine reagent to the aldehyde, the formed carbinolamine is converted to the oxime ligation product by dehydration. Excess of aniline catalyzes the oxime ligation by forming a protonated aniline Schiff base with the aldehyde. This intermediate readily reacts with alkoxyamine reagent forming the oxime ligation product upon loss of aniline. (Figure adapted from Kohler, 2009).

The initial step of the uncatalyzed oxime ligation is slow since it requires protonation of the aldehyde, but not of the alkoxyamine group. Upon addition of the alkoxyamine reagent to the aldehyde, dehydration of the formed carbinolamine results in the oxime ligation product. Excess of aniline catalyzes the oxime ligation by forming a protonated aniline Schiff base. This intermediate readily reacts with alkoxyamine reagent forming the oxime ligation product upon loss of aniline.

1.2. Quantitative mass spectrometry based proteomics in drug discovery

Mass spectrometry (MS) based proteomics has developed into an indispensable tool for molecular, cellular and systems biology (Aebersold and Mann, 2003). The basic principle of this approach is the identification of proteins on the basis of detected unique fragment masses. It involves the generation of ions, their transfer into the gas phase and the subsequent separation according to their mass to charge ratios (*m/z*). Along with qualitative identification of proteins, ion intensities can be used for quantitative characterizations. Furthermore, detection of exact masses by MS enables determination of post-translational modifications. The aspect of unbiased identification of peptides and proteins as well as modifications by MS enables proteomics to be used in an assumption-free manner and as a powerful tool in the field of molecular cell biology. However, the broad application of proteomics in science has only become possible due to the introduction of electrospray ionization (ESI) and matrix-assisted laser desorption ionization (MALDI) in the 1980s both enabling efficient ionization and vaporization of labile molecules such as proteins (Mann, 2016). Steady improvements in methodologies and instrumentations have allowed current proteomic approaches to sequence femtomole amounts of peptides from complex mixtures (Mann, 2016), to identify more than 10,000 proteins from single cell systems (Geiger et al., 2012; Pagala et al., 2015), to map post-translational modifications (Choudhary and Mann, 2010) and to analyze protein-protein (Dengjel et al., 2010) as well as drug-protein (Savitski et al., 2014) interactions in living cells.

1.2.1. Basics of mass spectrometry-based proteomics

Currently there are two complementary strategies for mass spectrometric analysis of proteins (see Fig. 6): the top-down and the bottom-up approache (Chait, 2006).
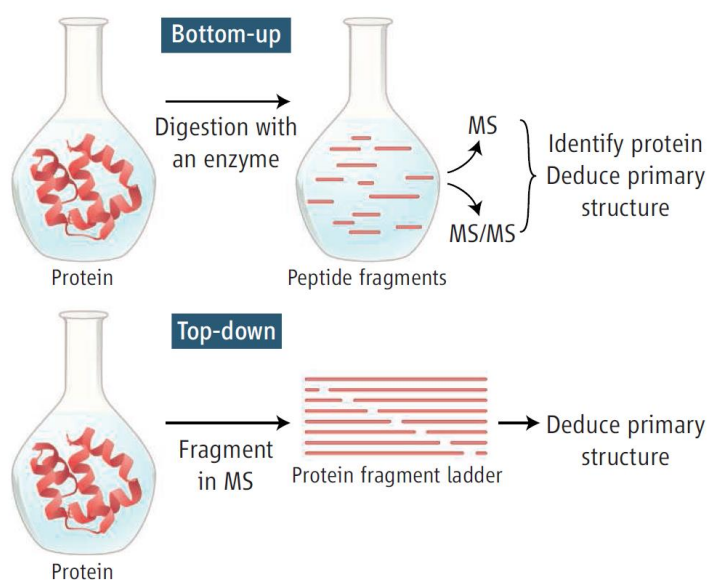
Fig. 6 Comparison of bottom-up and top-down mass spectrometry for protein identifications. In the bottom-up approach, proteins of interest are digested with a peptidase followed by mass spectrometric analysis of the resulting peptides in two steps. First, masses of intact peptides are determined (labeled "MS"). Second, peptide ions are selected and fragmented to gain information about peptide sequence, protein identity and post-translational modifications (labeled "MS/MS"). In the top-down approach, intact protein ions are directly fragmented and analyzed in the mass spectrometer. This yields information about the protein molecular mass and protein sequence. (Figure adapted from Chait, 2006)

The top-down approach aims at identifying and characterizing intact proteins by generating protein fragment ladders in the mass spectrometer. This enables discrete identification of protein isoforms as well as endogenous protein cleavages. Despite its technical challenges in protein fractionation, ionization and fragmentation, top-down proteomics can be used for large-scale proteome analysis identifying more than 1000 proteins with molecular weights of up to 100 kDa (Tran et al., 2011). However, most proteomic studies utilize the bottom-up proteomic approach which is also termed "shotgun proteomics". It involves protein digestion prior to MS analysis thereby circumventing the lack of efficient fractionation methods for intact proteins (Tran et al., 2011). Furthermore, peptides can be ionized more efficiently, produce less complex spectra and yield fragmentation spectra which are easier to interpret. A typical bottom-up proteomics workflow is illustrated in Fig. 7.
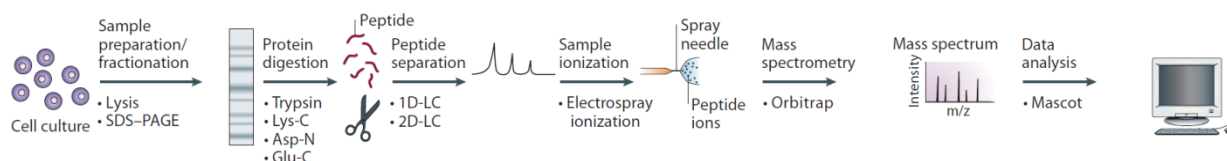
Fig. 7 Scheme of a bottom-up proteomics workflow. Proteins are extracted from a biological source like cell cultures or tissues and often purified by SDS-PAGE. Proteins are in-gel digested and the resulting peptide mixture is separated using single or multi-dimensional liquid chromatography. Peptides are ionized using electro spray ionization and analyzed by a mass spectrometer. Finally, the peptide-sequencing data are searched against protein databases. (Figure modified from Steen and Mann, 2004)

Proteins are extracted from cell culture or tissue followed by an optional protein fractionation step e.g. by gel electrophoresis. Subsequently, they are digested into peptides using a protease like trypsin. This protease is commonly used in proteomic workflows due to its high cleavage specificity and stability. Furthermore, by cleaving after unmodified lysines and arginines, this enzyme generates defined peptide fragments with an optimal average length of 14 amino acids and typically at least two defined N-terminal and C-terminal positive charges (Burkhart et al., 2012). Peptides are separated using reversed phase chromatography under acidic conditions, ionized by electrospray ionization and analyzed in the mass spectrometer. To reduce sample complexity, peptide mixtures can also be pre-fractionated prior to the MS analysis with separation mechanisms orthogonal to acidic reverse phase chromatography. During MS analysis, masses of eluting peptides (precursors) are determined by MS1 scans typically followed by fragmentation of selected precursors and detection of fragment ions in MS2 scans (MS/MS spectra). In data dependent acquisition mode, a fixed number of the most abundant precursor ions (TopN, often five or ten) is consecutively isolated and fragmented. The fragmentation is performed by an energy transfer in the gas phase and results in a characteristic breakage of the weakest bonds within the peptide which are typically the amide bonds between amino acids (Steen and Mann, 2004). Ideally, breakage occurs to a similar degree at each amide bond generating a ladder from which the amino acid sequence can be directly derived. However, typical MS/MS spectra contain only partial sequence information, necessitating statistical algorithms to determine the best match to a protein database. For that, a search engine like Mascot (Perkins et al., 1999) matches observed precursor and fragment masses with *in silico* digested and fragmented peptides derived from a protein database, and returns a probability-based ranking of matching peptide sequences.

1.2.1.1. Ionization methods

The two common ionization methods used in proteomic approaches are matrix-assisted laser desorption ionization (MALDI) and electrospray ionization (ESI). Both methods are suitable for

an efficient ionization and low fragmentation of non-volatile analyte molecules (Karas et al., 1987; Ho et al., 2003). For MALDI, analyte molecules are co-crystallized with an excess of a suitable matrix, commonly sinapinic acid, α-cyano-4-hydroxycinnamic acid or 2,5-dihydroxybenzoic acid. These matrices absorb light upon a pulsed irradiation by a laser which triggers ablation and desorption of analyte and matrix molecules. Subsequently, the analyte molecules, either ionized already in the co-crystal or during the desorption process in the gas phase, can be accelerated into the mass spectrometer by applying an electrical field. The MALDI methodology is illustrated in Fig. 8.
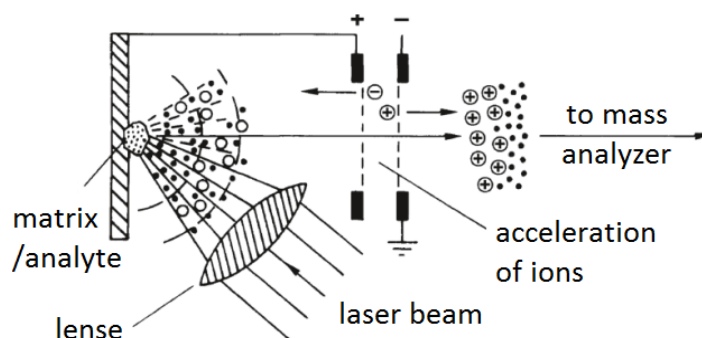
Fig. 8 Illustration of MALDI. Matrix molecules absorb light upon a pulsed irradiation by a laser which triggers ablation and desorption of analyte and matrix molecules. Ionized molecules are accelerated into the mass spectrometer by applying an electrical field. (Figure modified from Gross, 2013)

In comparison to the pulsed mode of action of MALDI, ESI generates ions continuously at atmospheric pressure thus enabling combination with online liquid chromatography to unravel complex sample mixtures. Reversed-phase chromatography is most suitable with ESI due to the use of a compatible volatile mobile phase. The principle of ESI involves formation of a fine aerosol containing analyte ions in a high voltage electrical field. Subsequent solvent evaporation, often supported by nitrogen as drying gas, results in the formation of free ions in the gas phase which are accelerated towards the mass spectrometer. For an efficient desolvation of the ions, typically water is mixed with volatile solvents like acetonitrile. Additional acidic modifiers like formic acid serve as proton donors to produce peptides with net positive charge and potentially generate ion-pairing effects allowing an improved separation of ionic and highly polar substances in reversed phase chromatography (Chakraborty and Berger, 2005). Further addition of additives like DMSO is described to improve sensitivity of protein identification in bottom-up proteomics (Hahne et al., 2013). In the ESI source, the aerosol is generated by applying a potential difference between the capillary exit and the mass spectrometer entrance. For example, a negatively charged entrance attracts cations which are eluting from the spray needle thereby leading to the formation of a Tylor cone emitting a jet of liquid droplets (Taylor, 1964). Due to electrostatic repulsion, these droplets with similar charge drift apart and generate a fine spray. Evaporation of the solvent leads to a decreasing droplet size with increasing charge density until the electrostatic repulsion exceeds the surface tension of the solvent (Rayleigh, 1882). If this Rayleigh limit is exceeded, the droplets explosively decompose, leaving a stream of charged ions. This ESI methodology is illustrated in Fig. 9.
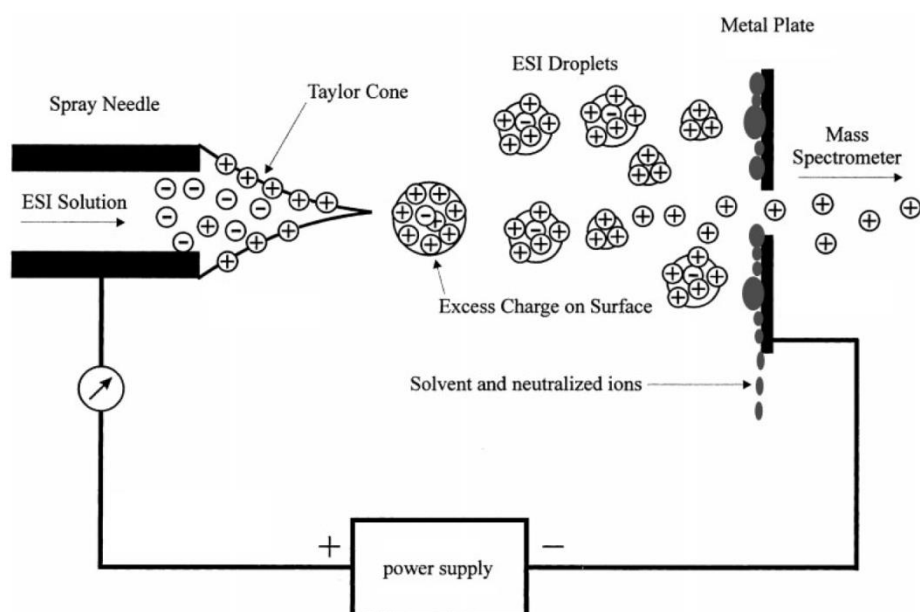
Fig. 9 Schematic illustration of the electrospray ionization process. The analyte solution is exiting a needle to which a high voltage is applied. The electric field gradient between the ESI needle and the counter electrode forms a Taylor cone with an excess of positive charges on its surface emitting a jet of liquid droplets. The solvent of the droplets evaporates, resulting in an explosive decomposition after exceeding the Rayleigh limit and leaving a stream of charged ions (Figure modified from Cech and Enke, 2001).

1.2.1.2. Mass analyzers

Several mass analyzers with different underlying physical principles are available and are often combined in hybrid instruments. This combination allows exploitation of the unique characteristics of the respective analyzer and increases the instruments application range. The performance of mass analyzers can be described on the basis of four properties: precision, accuracy, resolution and dynamic range. The mass precision of an analyzer describes the variation of detected masses between several measurements for the same mass while mass accuracy describes the proximity of experimentally observed masses to the true mass (Cox and Mann, 2009). Current instruments can achieve mass accuracy in the low parts per million (ppm) range. Resolution is a measure for the ability to distinguish two neighboring masses. This parameter is calculated by dividing the mass of an observed peak by its width. The resolution of some mass analyzers like the Orbitrap is dependent on the analyzed mass to charge ratio with lower resolving power at higher mass ranges (Makarov et al., 2009). Finally, the dynamic range of a mass analyzer describes its capability to distinguish high and low signal intensities in a spectrum and is defined as the ratio of the strongest signal to the weakest signal. The four most commonly used mass analyzers are the time of flight (TOF) analyzers, the quadrupole mass analyzers, the linear ion traps and the Orbitraps. As TOF analyzers were not used in this thesis, they will not be discussed.

The quadrupole mass analyzer is commonly used as mass filter or as pure transfer optics in hybrid mass spectrometers. It consists of four hyperbolic or cylindrical rod electrodes arranged squarely around a longitudinal axis. An electrical potential, consisting of a direct current and an alternating current component, is applied to opposing rod pairs which leads to alternating attractive and repulsive forces on ions in the x- and y-directions. Ions within a specific *m/z* range can pass the quadrupole in z-direction on stable trajectories while others collide with the rod

electrodes. Continuous or discrete changes in rod potentials enable selection of ions with defined *m/z*.

Linear ion traps combine the capabilities of mass selection, fragmentation and detection. Although their mass accuracy and mass resolution is relatively low compared to other mass analyzers like Orbitraps, linear ion traps have a high sensitivity and enable fast cycle times. Similar to the quadrupole mass analyzer, they consist of four rod electrodes arranged squarely around a longitudinal axis to confine ions radially. In addition, trapping electrodes at the ends of the quadrupole allow confining the ions axially. Modulation of the rod potentials enables selection and trapping of ions with defined *m/z* while changes in the potentials of the trapping electrodes allow mass-selective ejection of trapped ions in axial direction. Furthermore, if the linear ion trap is combined with electron multipliers, a mass-selective ejection of ions in x-direction towards these ion detectors enables record of mass spectra. Besides recording precursor ion mass spectra, ion traps are typically used for ion fragmentation. For that purpose, ions within a specific *m/z* range are trapped, excited and subsequently fragmented by collision induced dissociation (CID). However, ion trap fragmentation has an inherent critical drawback: the low mass cutoff (LMCO, Yang et al., 2009). Fragmentation can result in the generation of ions with lower *m/z* compared to the precursor ion. Ion traps fail to retain these fragment ions at the lower end of the *m/z* range. Although LMCO does not seriously hamper peptide identification, it might negatively influence peptide quantification with multiplexed isobaric tag reagents (Yang et al., 2009).

The Orbitrap mass analyzer is based on the Kingdon trap (Kingdon, 1923) and allows mass spectrometric analysis of ions with high accuracy and sensitivity. For that, ions are trapped on stable trajectories around a coaxial inner spindle-like electrode surrounded by an outer barrel-like electrode (see Fig. 10).
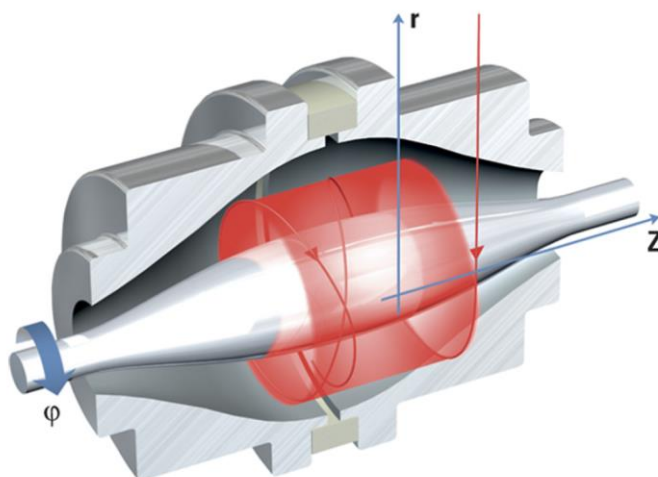
Fig. 10 Orbitrap mass analyzer. Ions are captured in a quadro-logarithmic electrostatic field. An outer electrode enclosing a central spindle electrode consists of two halves separated by a dielectric material. The image current of ions moving as concentric rings along the central electrode (oscillations in axial direction denoted as z in the drawing) is picked up by the outer electrode sections (Figure adapted from Scigelova et al., 2011)

The outer electrode is split into two halves enabling detection of image currents induced by axially oscillating ions. Prior to the transmission into the Orbitrap, ions are accumulated in the C-trap. This RF-only c-shaped quadrupole enables injection of short and highly condensed ion packages into the Orbitrap. Transmission of the packages into the Orbitrap off its plane of symmetry (red arrow in Fig. 10) automatically initiates harmonic axial oscillations of the ions. In addition, the ions orbit in a circular trajectory around the central electrode. Both movements

result in a stable spiral-like trajectory around the central electrode (red shaded area in Fig. 10). While oscillation in radial direction (r) is dependent on the initial energy of the ions, axial (z) oscillation is independent of all initial parameters and depends only on the mass to charge ratio of the ions. Finally, the frequency readout of axial oscillations of all ions can be converted into a mass spectrum by Fourier transform mathematical operations. Since the Orbitrap can only be used as mass detector but not as mass filter or for ion fragmentation, it is normally combined with a linear ion trap, or a quadrupole and a dedicated collision cell. Such hybrid devices with an Orbitrap mass analyzer are marketed exclusively by Thermo Fisher Scientific. The following three hybrid devices were used in this thesis: LTQ Orbitrap XL, Q Exactive (Plus, HF) and Orbitrap Fusion Lumos. Schematic illustrations of the three devices are shown in Fig. 11.
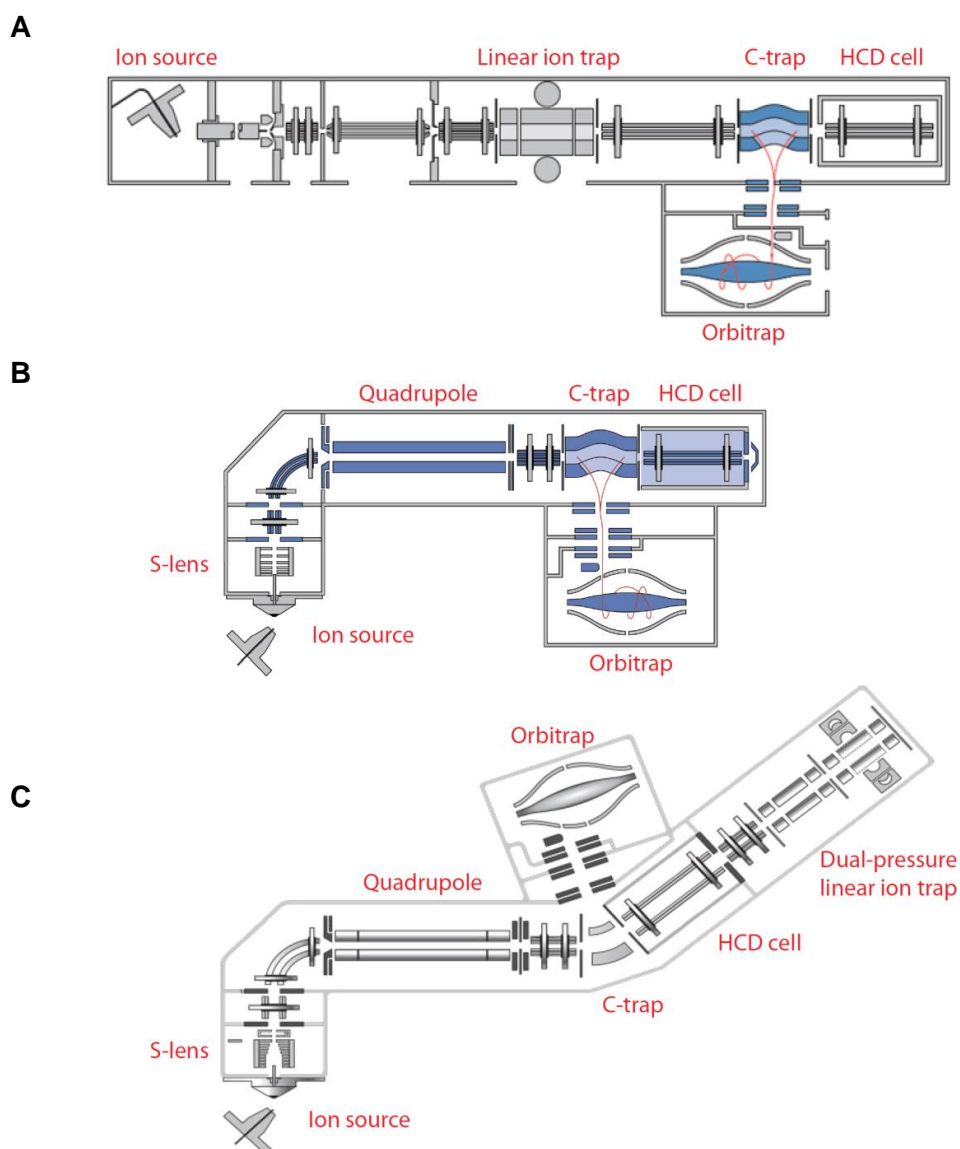
Fig. 11 Schematic illustrations of hybrid mass spectrometers.(**A**) The LTQ Orbitrap XL is an upgraded version of the LTQ Orbitrap which was the first hybrid instrument containing an Orbitrap cell. (**B**) The benchtop instrument Q Exactive combines a quadrupole mass filter and an Orbitrap mass analyzer. (**C**) The Orbitrap Fusion Lumos is the newest addition to the Orbitrap hybrid device family combining a quadrupole mass filter, a dual-pressure linear ion trap and an Orbitrap mass analyzer. (Figures modified from planetorbitrap.com)

The LTQ Orbitrap XL combines high accuracy and high precision of the Orbitrap mass analyzer with high sensitivity and fast cycle times of the linear ion trap (Olsen et al., 2007). In this setup, the Orbitrap is usually used for measuring precursor ion masses at high resolution concomitant

with rapid precursor ion isolation, fragmentation and acquisition of fragment spectra in the linear ion trap. To circumvent the limitation of LMCO in case of linear ion trap fragmentation, an additional HCD cell was implemented in the LTQ Orbitrap XL (Olsen et al., 2007). For HCD fragmentation, the precursor ions are selected by the linear ion trap and transmitted to the HCD cell. Following HCD, fragment ions are accumulated in the C-trap and fragment spectra can be acquired in the Orbitrap. A drawback of HCD fragmentation and fragment spectra acquisition in the Orbitrap is the slower cycle time as all mass measurements are performed successively in the Orbitrap cell. Furthermore, inefficient ion transfers lead to a lower sensitivity. To address the latter drawback, improvements in design and electronics, enabling a more sensitive ion transfer, were incorporated in the next generations of LTQ Orbitraps like the LTQ Orbitrap Velos (Olsen et al., 2009) and the LTQ Orbitrap Elite (Michalski et al., 2012). This development has made HCD fragmentation suitable for standard proteomic experiments.

Compared to the LTQ Orbitrap XL and the Orbitrap Fusion Lumos, the Q Exactive is a benchtop-sized mass spectrometer. This hybrid device combines a quadrupole mass filter with the Orbitrap mass analyzer (Michalski et al., 2011). The quadrupole can be used for rapid precursor ion selection followed by HCD fragmentation and high resolution spectra acquisition with the Orbitrap mass analyzer. Shorter ion paths, the lack of a linear ion trap and further improvements on electronics improved the sensitivity and increased the sequencing speed of this hybrid device.

The Orbitrap Fusion Lumos is the newest addition to the Orbitrap hybrid device family combining a quadrupole mass filter, a dual-pressure linear ion trap and an Orbitrap mass analyzer. The dual-pressure linear ion trap consists of two linear ion traps operated at a higher and a lower pressure. The higher pressure is beneficial for efficient trapping, isolation and fragmentation of ions while the lower pressure enables faster mass spectra acquisition (Olsen et al., 2009). The setup of the Orbitrap Fusion Lumos allows parallelization of MS and MS^n analyses with high acquisition rates in the Orbitrap and linear ion trap. Furthermore, multiple fragmentation techniques like CID, HCD and ETD are available at any stage of MS^n. These capabilities are for example utilized for the synchronous precursor selection (SPS) method enabling more accurate multiplexed quantification via isobaric mass tags which suffers from reporter ion ratio distortion in the MS^2 spectra caused by co-fragmentation of co-isolated interfering species (Savitski et al., 2013). SPS enables selective co-isolation and co-fragmentation of multiple MS^2 fragment ions for accurate reporter ion quantification in the MS^3 spectra (McAlister et al., 2014).

1.2.1.3. Fragmentation methods

Peptide ion fragmentation ideally generates a fragment ladder, from which the amino acid sequence can be directly inferred. Commonly used fragmentation techniques are electron transfer dissociation (ETD), collision induced dissociation (CID) and higher-energy collisional dissociation (HCD). In case of the latter two fragmentation methods, ions are excited and collided with an inert gas like helium or nitrogen. CID is commonly used for fragmentation in linear ion traps. After isolation and excitation of precursor ions in the ion trap, the inert gas is supplied. Subsequently, random collisions between the excited ions and the gas molecules lead to the conversion of the ions´ kinetic energy to vibrational internal energy (Pejchinovski et al., 2015) resulting in characteristic breakage of the weakest bonds within the peptide ion. For CID and HCD fragmentation, these are typically the amide bonds between amino acids (Steen and Mann, 2004). If the charge is retained on the N-terminus, b-ions are generated. If the charge is retained on the C-terminus, y-ions are generated (see Fig. 12). Other possible bond breakages result in the formation of a- and c-ions or x- and z-ions.
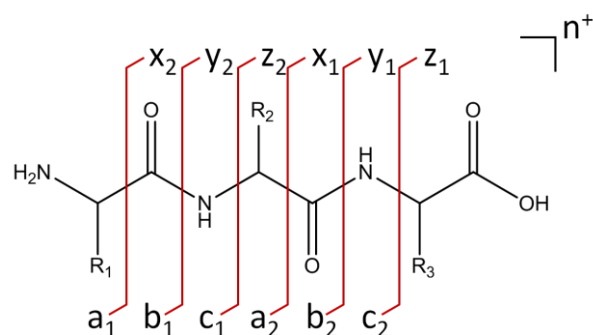
Fig. 12 Peptide fragmentation notation using the scheme of Roepstorff and Fohlman. (Figure adopted from Roepstorff and Fohlman, 1984)

The generated fragment ions can be analyzed either directly in the linear ion trap or, in case of hybrid devices, with another mass analyzer. For HCD, a fragmentation method specific for Orbitrap mass spectrometers, precursor ions are accumulated in a multipole collision cell. After higher-energy excitation of ions, collisions with inert gas molecules lead to fragmentation of peptide ions by preferential breakage of amide bonds. Depending on the mass spectrometer, generated fragment ions can be analyzed either in the Orbitrap or another mass analyzer. The third fragmentation technique, ETD, results in the preferential formation of c- and z-ions by transferring electrons to peptide cations. In a first step, radical anions are formed in a dedicated reaction chamber commonly by chemical ionization of fluoranthene. Subsequently, these radical anions are mixed, typically in an ion trap, with isolated precursor ions. Upon electron transfer to the positively charged ions, these ions are cleaved resulting in fragment ion formation.

Each of the three described fragmentation methods has been shown to have advantages and disadvantages for peptide fragmentation and identification. CID is fast but suffers from LMCO in ion traps. In turn, HCD fragmentation circumvents this limitation, however, this method is less sensitive compared to CID (Jedrychowski et al., 2011) and higher levels of dissociation energy could lead to further fragment ion breakage (Pejchinovski et al., 2015). ETD fragmentation has been shown to be especially suited for identification of PTMs, however, it is the least effective fragmentation method (Pejchinovski et al., 2015).

1.2.2. Quantitative proteomics

Besides generating qualitative lists of identified proteins e.g. in a cell system, quantitative proteomics adds additional information on protein abundances. Two principle types of quantification can be distinguished: Absolute quantification and relative quantification. Absolute quantification enables determination of concentrations or copy numbers per cell while relative quantification measures the difference in abundance between samples. However, peptide and protein abundances cannot be simply inferred from MS signal intensities since other factors like peptide structure and the surrounding matrix unpredictably influence the readout (Brönstrup, 2004). By comparing MS intensities of ions with the same physicochemical properties, these unpredictable influences can be circumvented. This can be either achieved by comparing intensities between the same peptides in separate MS analysis runs, also termed label-free quantification, or by comparing intensities of isotopologue peptides in one MS analysis run after labeling samples with stable isotopes (Fig. 13).
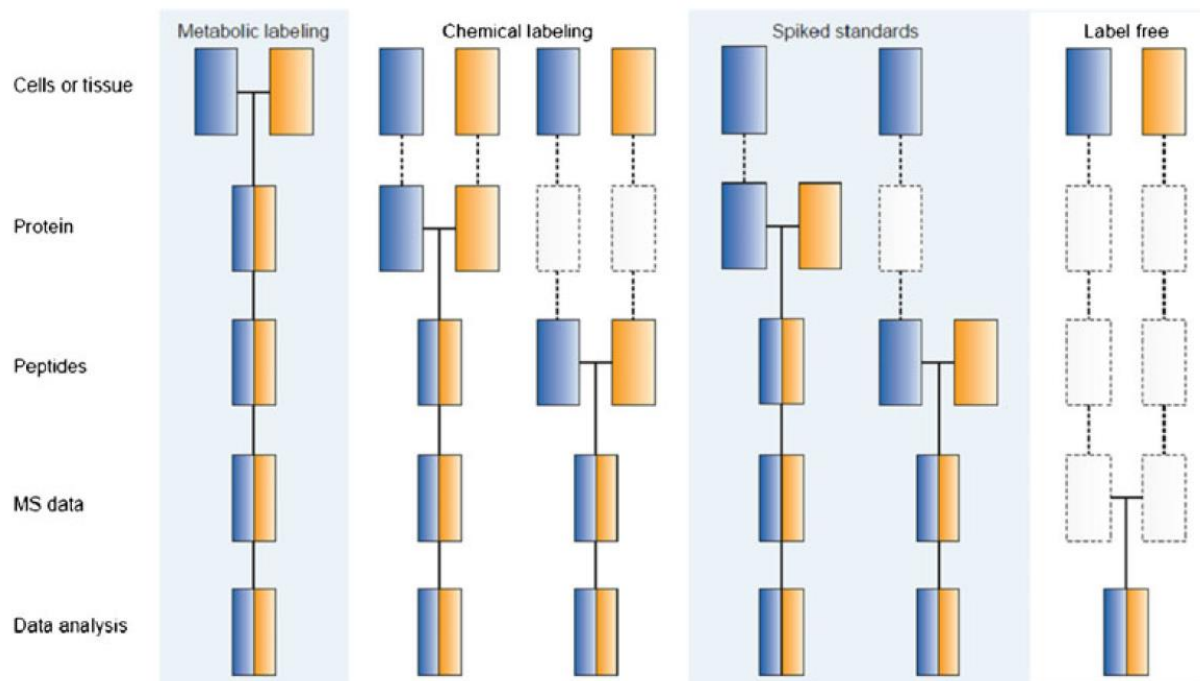
Fig. 13 Common quantitative proteomic workflows and their impact on quantitative accuracy. Blue and yellow boxes represent two experimental conditions. Horizontal lines indicate sample pooling. Dashed lines indicate the points at which experimental variations and thus quantification errors can occur. The earlier the samples are pooled, the less variability is introduced during the sample workflow (Figure modified from Bantscheff et al., 2012)

Every additional processing step that is conducted separately on the samples during a quantitative proteomics workflow can introduce variability which reduces the precision of quantification. The precision can be affected even more by separate MS analyses, as necessary in label-free approaches. In general, the later samples are combined, the less accurate is the quantification and the more replicates are necessary to detect small effects. Stable isotope labeling enables sample pooling at different stages during the workflow thereby reducing the susceptibility to accumulate variability. In principle, metabolic labeling enables most accurate quantification due to early sample pooling already on cellular level. However, it might not be applicable for all sample types like primary tissues or primary cells.

1.2.2.1. Relative quantification

For relative quantification, label-free, metabolic labeling, chemical labeling and spiked standards approaches are available. The latter three are based on stable isotope labeling. While label-free quantification does not require an extra step for stable isotope incorporation and enable higher proteome coverage compared to chemical labeling (Megger et al., 2014), these approaches have to cope with higher quantification variability and result in higher MS resource consumption due to separate analysis of each individual sample. Common approaches are based on total peptide ion counts, spectral counts or ion intensities. Spectral counting is the simplest approach. However, high variability especially for low abundant proteins with few sequenced peptides as well as saturation of spectral counts at high protein abundance levels makes this approach unreliable when working with a small number of replicates (Lundgren et al., 2010). Better accuracy and linearity can be obtained with intensity-based quantification approaches integrating precursor-ion intensities or fragment-ion intensities (Krey et al., 2014; Silva et al., 2006).

Introduction

Stable isotope labeling with amino acids in cell culture (SILAC, Ong et al., 2002) belongs to the category of metabolic labeling approaches. It utilizes cellular protein synthesis to incorporate stable isotope-containing amino acids into whole proteomes. For that purpose, essential amino acids are replaced with their heavy counterparts in the growth medium (Ong and Mann, 2006). Typically arginine and lysine are exchanged ensuring that every tryptic peptide (except the C-terminal peptide of the protein) contains at least one labeled amino acid. This labeling introduces a confined mass difference to unlabeled amino acids enabling relative quantification between up to three cell populations (Ong and Mann, 2006) in MS1 spectra. Furthermore, samples can be pooled already on cellular level reducing variability of quantification. In case of spiked standards, known amounts of isotope-labeled synthetic peptides or proteins are added during the workflow enabling relative and absolute quantification.

In contrast to metabolic labeling, chemical labeling approaches utilize reactive reagents to introduce stable isotopes into proteins or their peptides. This avoids the necessity to culture cells for several passages until complete incorporation of stable isotope-containing amino acids thus making isotope labeling also applicable for sample types like primary tissues or primary cells. With the exception of isobaric mass tags, these approaches are introducing, comparable to metabolic labeling, small mass differences to identical peptides from two or more samples enabling distinction in the MS1 spectrum. Examples are isotope-coded affinity tags (ICAT, Gygi et al., 1999) or dimethyl labeling (Boersema et al., 2009). The advantage of these methods is their high quantification accuracy, however, MS1 spectra complexity is increased by a factor of two or more depending on the level of sample multiplexing. Quantification by Isobaric mass tags like iTRAQ (isobaric tags for relative and absolute quantification, Ross et al., 2004) and TMT (tandem mass tags, Thompson et al., 2003) is based on a different concept. The labeling reagents consist of three functional elements: an amine reactive group for covalent linkage to peptides, a mass balancer comprising a peptide bond for fragmentation induced cleavage, and a mass reporter. Heavy and light isotopes are distributed within the latter two functional elements but they add up to the same mass for all isotopic variants of the isobaric mass tag. TMT11plex reagents are shown as an example in Fig. 14.
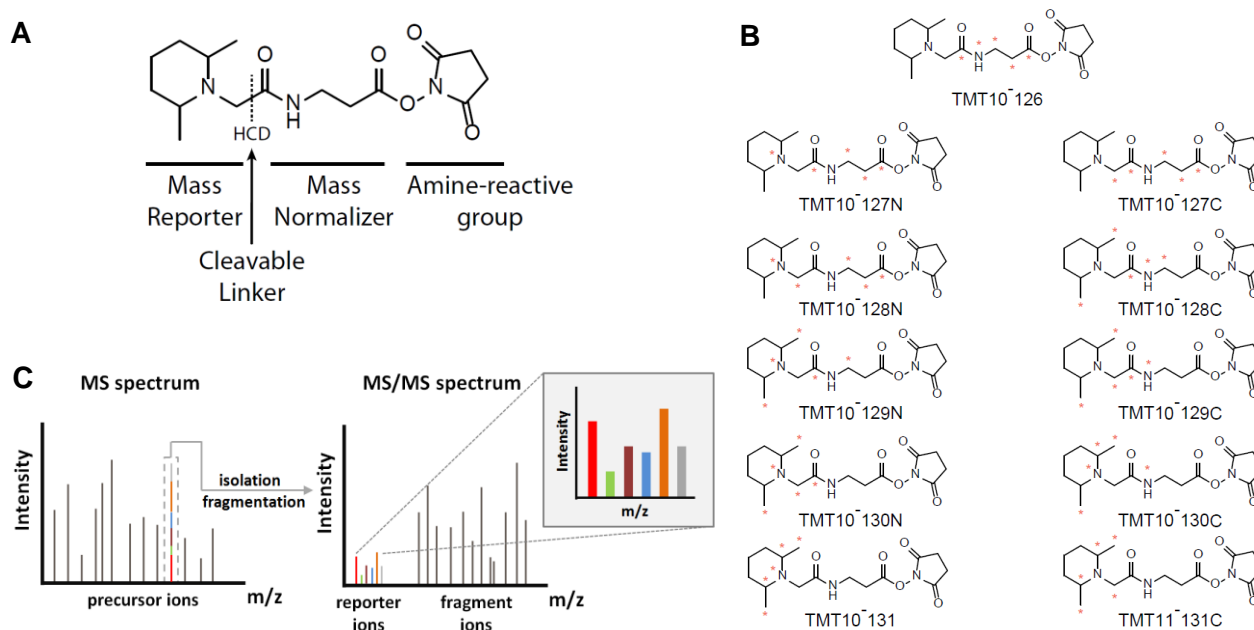
Fig. 14 Structure of isobaric TMT11plex label reagents. (**A**) Functional elements of the TMT label reagent including MS/MS fragmentation site by higher-energy collision dissociation (HCD). (**B**) TMT11plex label reagents with highlighted (red asterisks) isotope positions. (**C**) Schematic illustration of isobaric mass tag based relative quantification.

Each sample is labeled with a different isotopic variant of the isobaric mass tag. After pooling, peptides from different samples show identical liquid chromatography retention time and same mass to charge ratio in MS1 scan. However, upon precursor ion fragmentation, reporter ions, originating from the different isotopic variants of the isobaric mass tag, are released. Due to different compositions of heavy and light isotopes, these reporter ions can be distinguished based on their mass to charge ratio. Comparison of their signal intensities enables relative quantification. Currently, up to eleven samples can be multiplexed without concomitant increase in MS1 spectra complexity. However, MS2 level quantification has several disadvantages. Among others, CID-based fragmentation in ion traps cannot be used due to their LMCO limitation. Furthermore, accurate quantification of complex proteomic samples can be impaired by co-fragmentation of co-eluting peptides resulting in systematic underestimation of quantitative ratios (Savitski et al., 2013).

1.2.2.2. Absolute quantification

For absolute quantification (often referred to as AQUA, Gerber et al., 2003) , known amounts of isotope-labeled reference peptides can be spiked into the sample (Brönstrup, 2004) enabling accurate determination of concentrations or copy numbers per cell. To reduce variability between the sample and the standard, also heavy protein fragments or full length proteins can be spiked in before digestion (Hanke et al., 2008; Zeiler et al., 2012). However, this approach is biased and only enables quantification of a limited number of proteins depending on spiked-in peptides or proteins.

Although peptide abundances cannot be directly inferred from MS signal intensities, also label-free approaches were developed that can estimate absolute amounts without using isotope labeled spike in standards. Commonly used approaches are iBAQ (intensity-based absolute quantification, Schwanhäusser et al., 2011) and TOP3 (Silva et al., 2006). The iBAQ approach is based on the correlation of protein abundance with summed peptide intensities of a protein divided by the number of theoretically observable peptides. In turn, TOP3 is based on the correlation of protein abundance with the average peptide intensity for the three most intense tryptic peptides. Both approaches provide accurate proxies for protein abundances and spiking in a non-labeled standard of accurately quantified proteins enables estimation of absolute quantities of all identified proteins by linear regression (Schwanhäusser et al., 2011; Silva et al., 2006).

1.2.3. Chemoproteomics for drug discovery

Proteomics has made major contributions to pharmacology by applying to many phases in the drug discovery process (Walgren, 2004; Burbaum and Tobal, 2002). In this process, target deconvolution is a crucial step. It is required for understanding molecular mechanisms underlying the therapeutic effects of bioactive small molecule compounds or biologics like natural and endogenous molecules. Key questions are thereby which proteins are targeted by the bioactive molecules as well as what is their impact on protein expression and post-translational modification (Bantscheff, 2012). Importantly, assays designed to answer these questions should be as close as possible to native conditions to avoid discrepancies between assay results and the actual pharmacological efficacy (Bantscheff and Drewes, 2012). Chemoproteomics aims at addressing these points on proteome-wide level. This research area at the interface of chemistry, biochemistry, and cell biology (Bantscheff, 2012) comprises assays that include native proteins in live cells or cell-extracts thus trying to preserve native protein environments, protein-protein interactions and protein folding. Two major categories of chemical proteomics approaches can be distinguished: targeted profiling and global profiling

(Bantscheff, 2012). Targeted approaches employ enrichment of the protein(s) of interest while global profiling aims at cell-wide characterization of cellular response to drug treatment.

Most frequently applied techniques for target deconvolution are targeted approaches based on affinity enrichment with chemical probes. Two strategies are available: drug-centric profiling and target class-focused profiling. For a drug-centric approach, the probe is immobilized to a solid support via a linker. Proteins, bound after incubation with cell extract, are identified using mass spectrometry. This approach was for example used for the assessment of the selectivity profile of the anti-inflammatory drug SB203580 (Godl et al., 2003), for the histone deacetylase inhibitor trapoxin (Taunton et al., 1996) as well as for the immunosuppressant FK506 (Harding et al., 1989). In case of a target class-focused approach, several probes are immobilized to a solid support enabling a broad coverage of target proteins like kinases (Bantscheff et al., 2007) or histone deacetylases (Bantscheff et al., 2011). Captured proteins of the cell extract can be eluted from the affinity matrix by competition with excess of a probe of interest. In addition to the affinity-based approaches, activity-based protein profiling (ABPP) uses active-site directed probes covalently labelling conserved amino acids close to the catalytic center of enzymes (Cravatt et al., 2008). Probe-attached reporter tags allow selective enrichment and mass spectrometric identification of targeted proteins enabling proteome-wide analysis of enzyme functional states. A major limitation of the targeted approaches is the necessity to synthesize modified probes. It requires extensive structure-activity relationship studies in order to determine suitable sites for linker attachment retaining bioactivity and target affinity of the probes. However, an example for successful application of a targeted approach is the kinobeads competition assay. Seven broad-specificity kinase inhibitors are immobilized to sepharose beads enabling capturing of a major fraction of the expressed human kinome and other purine-binding proteins (Bantscheff et al., 2007; Médard et al., 2015). The affinity enrichment makes the generally low expressed kinases accessible for drug interaction analyses. By competition with increasing concentrations of an unmodified kinase inhibitor, compound selectivity as well as affinity binding constants can be determined. The free inhibitor reduces binding of the target protein to the kinobeads matrix. Analysis of concentration-dependent reduction in abundance of the captured protein, enables fitting of dose response curves and determination of IC_{50} values (Bantscheff et al., 2007; Werner et al., 2012). Finally, incorporation of the Cheng-Prusoff relationship (Cheng and Prusoff, 1973) allows inference of dissociation constants (K_d) from the determined affinity binding constants (Sharma et al., 2009).

Global profiling strategies involve drug treatment of cells or animals followed by whole-cell or organ-wide proteome analysis of drug-induced effects. Due to their unbiased nature and their conceptual simplicity, global profiling strategies are highly attractive (Bantscheff and Drewes, 2012). Furthermore, apart from cell permeability, there are no specific requirements for the compound under investigation. A limitation of these approaches is the detection of low abundant proteins. The large dynamic range and the complexity of cellular proteomes result in oversampling of abundant proteins and undersampling of low abundant proteins (Fonslow et al., 2011). Subcellular fractionation can address this limitation by reducing sample complexity. An additional limitation is the limited capability of most global profiling strategies to identify direct protein targets. Proteins displaying altered expression levels are not necessarily directly interacting with the compound but are often involved in stress response and/or housekeeping functions (Bantscheff and Drewes, 2012). Thus, studies focused on the mechanism of bioactive compounds frequently rely on biased affinity-based enrichment strategies to identify prospective binding partners (Savitski et al., 2014).

The recently published thermal proteome profiling approach avoids this necessity for biased strategies and furthermore allows the use of native unmodified small molecules (Martinez

Molina et al., 2013; Savitski et al., 2014; Reinhard et al., 2015). It is based on the principle of ligand-binding induced changes in protein thermal stability, a principle frequently employed for monitoring ligand binding to purified proteins by isothermal titration calorimetry, differential scanning calorimetry or differential scanning fluorimetry (Ward and Holdgate, 2001; Weber and Salemme, 2003; Niesen et al., 2007). Ligand-binding triggers binding energy-dependent changes in intramolecular and intermolecular interactions. This leads to a thermal stabilization or destabilization of the native protein conformation which can be accessed by monitoring heat-induced unfolding of a protein. Since denatured proteins tend to form protein aggregates (Savitski et al., 2014), these can be removed by filtration or centrifugation. Thus, protein thermal stability can be directly inferred from temperature-dependent changes in the soluble fraction of a protein usually following a sigmoidal curve (Martinez Molina and Nordlund, 2016). Finally, monitoring thermal stability changes on a proteome-wide level upon compound treatment enables unbiased identification of drug-target interactions in live cells or cell extracts. A typical thermal proteome profiling experiment is illustrated in Fig. 15.
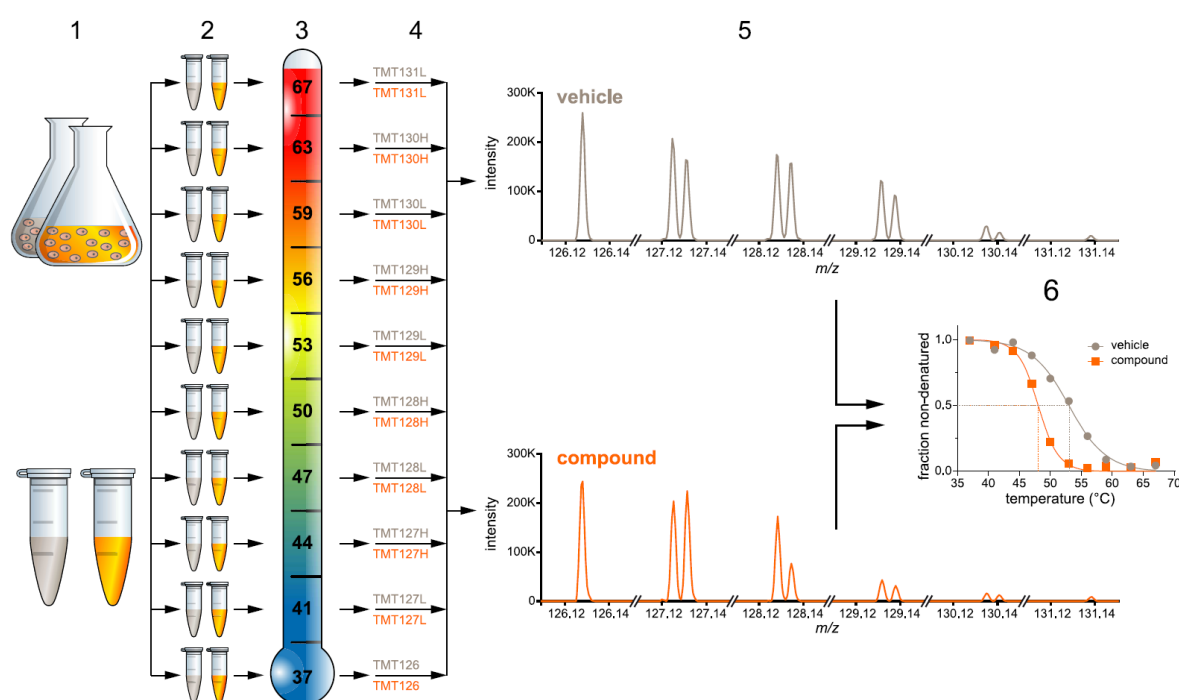
Fig. 15 Schematic illustration of a thermal proteome profiling experiment. (1) Cells or cell extracts are treated with drug or vehicle. (2) The samples are divided into 10 aliquots. (3) Samples are subjected to heating at the indicated temperatures. (4) After extraction of the soluble fractions of each condition, proteins are digested with trypsin and resulting peptide mixtures are labeled with an individual TMT reagent. (5) Pooled samples are subjected to quantitative LC MS/MS analysis. (6) The obtained reporter ion intensities are used to fit melting curves which reflect the unfolding of the proteins with increasing temperature and which allow calculation of melting points. Comparing melting points to the vehicle treated sample enables identification of drug-target interactions. (Figure adapted from Savitski et al., 2014)

Live cells or lysates are treated with vehicle or compound. Subsequently, samples are divided into ten aliquots and heated to a range of temperatures. Temperature-dependent protein aggregates are removed and soluble fractions are digested with trypsin. Resulting peptide mixtures are labeled with individual TMT reagents and pooled to a single sample followed by quantitative mass spectrometric analysis. The obtained reporter ion intensities are used to fit melting curves allowing calculation of melting points. Comparison of these between the vehicle- and the drug-treated samples enables identification of drug-target interactions as a result of changes in the thermal stability of the proteins.

Another approach for global investigation of protein-ligand interactions is drug affinity responsive target stability (DARTS, Lomenick et al., 2009; Pai et al., 2015). This approach employs the detection of changed proteolytic resistance during limited proteolysis upon small molecule binding due to either global or local thermodynamic stabilization and/or masking of cleavage site(s) from the protease. However, besides identification of targeted proteins, it also enables determination of structural changes at domain resolution (Feng et al., 2014). Under limiting conditions, proteolytic cleavage of native, non-denatured proteins is mainly determined by their tertiary structures as cleavage sites buried in the protein core or in a regular secondary structure are inaccessible to the protease. Typically surface exposed and highly flexible interdomain sequences are easily accessible and cleaved, resulting in partial digestion of proteins. Masking of these cleavage sites upon ligand binding by structural changes or by the ligand itself can result in changed limited proteolysis patterns which enables identification of drug-target interactions and which can pinpoint the binding pocket (Feng et al., 2014).

2. Objectives

The plasma membrane proteome is highly dynamic and has crucial roles in many biological processes rendering this subproteome a prominent target for pharmaceutical intervention. Furthermore, there is growing evidence for active drug in- and efflux mechanisms by membrane-bound transporters. Expression of these proteins affects drug-target engagement and can lead to drug resistance. A detailed understanding of the plasma membrane proteome composition and its dynamics can thus have a great impact on drug discovery. However, the analysis of this subproteome is challenging due to its biochemical properties and the low abundance of many membrane proteins. Accordingly, the analysis of interactions to the cell surface proteome is demanding as well. Most approaches are performed in lysates or from purified proteins and as such require extraction of proteins from their native cellular environment often resulting in denaturation and inactivation of membrane proteins. Furthermore, these conditions are highly artificial and results might not be indicative for the *in vivo* situation.

The aim of this thesis was to address these gaps by first developing sensitive and quantitative methods to characterize the surface proteome of cell lines and primary cells as well as to study dynamic processes occurring in this subproteome in live cells. For that purpose, a chemical cell surface labeling and enrichment approach should be established and combined with quantitative proteomics using tandem mass tags. These methods then should be used to generate a compendium of cell surface proteome maps for cell systems commonly used in biochemical assays as well as to study the time-dependent cell surface proteome remodeling during monocyte to macrophage differentiation. In addition, perturbation of this dynamic process with small molecules is supposed to enable novel insights in side effects of pharmaceuticals. In a second step, the established cell surface labeling and enrichment approach should be combined with the recently described thermal proteome profiling (TPP) to enable selective and unbiased monitoring of target engagement to plasma membrane proteins in live cells. For that purpose, methods should be optimized and established, requiring to develop a new robust data analysis procedure. The new methodology should be validated based on known interactions of small molecules and native ligands with cell surface proteins. These results also enable an estimation of the false discovery rate of this approach.

3. Materials and Methods

3.1. Materials

3.1.1. Solutions and Chemicals

Solutions and chemicals	Company
10-plex TMT reagents	Thermo Fisher Scientific
Acetic acid	Merck
Acetonitrile, HPLC grade	Merck
Ammonia solution, 25%	Merck
Aniline	Sigma-Aldrich
anti-CD11b (ab52478)	Abcam
anti-CD19 (3574)	Cell Signaling Technologies
anti-CD28 (555725) for CSTPP	BD Biosciences
anti-CD3 (ab5690)	Abcam
anti-CD3 (ab86883) for CSTPP	Abcam
anti-CD4 (AF-379-NA)	R&D Systems
anti-CD56 (3606)	Cell Signaling Technologies
anti-IL2RA (SAB4700360) for CSTPP	Sigma-Aldrich
anti-ITGAV (4711)	Cell Signaling Technologies
anti-ITGAV (I3783) for CSTPP	Sigma-Aldrich
anti-mouse IgG (M8642)	Sigma-Aldrich
anti-MRC2 (ab70132)	Abcam
anti-Tubulin (T9026)	Sigma-Aldrich
BCA Protein Assay Kit	Pierce
Blocking buffer for Immunoblot analysis	Li-Cor
Bradford 5x reagent	Bio-RAD
BSA HPLC standard	Bischoff Analysetechnik GmbH
Calcitriol	Cayman Chemicals
Capillaries for column packing	Polymicro
CHAPS	Sigma-Aldrich
Coomassie staining solution	Bio-Rad
Copper sulfate	Sigma-Aldrich
CXCL12	R&D Systems
cyclo-RGDfK	Bachem
CytoSelect 96-well phagocytosis assay	Cell Biolabs
Dasatinib	Santa Cruz
DDM	Anatrace
Digitonin	Sigma-Aldrich
Digitoxin	Sigma-Aldrich
Dimethylsulfoxide (DMSO)	Sigma-Aldrich
Dipyridamole	Sigma-Aldrich
Dithiothreitol	Sigma-Aldrich
DMEM	Thermo Fisher Scientific
DPBS ± Ca^{2+} Mg^{2+}	Thermo Fisher Scientific
Elacridar	Sigma-Aldrich
Empore SPE Disks C18	Sigma-Aldrich
Empore SPE Disks Cation Exchange-SR	Sigma-Aldrich
Ethanol	Merck
EZ-Link™ Alkoxyamine-PEG4-Biotin	Thermo Fisher Scientific
EZ-Link™ Sulfo-NHS-LC-LC-Biotin	Thermo Fisher Scientific
Fetal calf serum	Thermo Fisher Scientific
Folic acid	Sigma-Aldrich
Formic acid	Merck
Furosemide	Sigma-Aldrich
Glucose	Sigma-Aldrich
HEPES solution	Sigma-Aldrich
High capacity neutravidin agarose beads	Thermo Fisher Scientific
High capacity streptavidin agarose beads	Thermo Fisher Scientific
human IL2	PeproTech
human IL6	PeproTech
human VLDL	Abcam
IGEPAL CA-630	Sigma-Aldrich
IGF1	Sigma-Aldrich

Solutions and chemicals	Company
Ilomastat	Santa Cruz
Imatinib	Novartis
INS	SAFC Biosciences
Iodoacetamide	Sigma-Aldrich
IT1t	Tocris
LTQ Velos ESI Positive Ion Calibration Solution	Thermo Fisher Scientific
Luminespib	Santa Cruz
LysC	Wako
MEM	Thermo Fisher Scientific
Methanol	Sigma-Aldrich
Methotrexate	AlfaAesar
NaCl, 5 M solution	Sigma-Aldrich
Nilotinib	ChemScene
Non-essential amino acids	Thermo Fisher Scientific
NuPAGE 4x sample buffer	Invitrogen, Life technologies
NuPAGE MOPS SDS Running buffer (20x)	Life technologies
Odyssey Protein Molecular Weight Marker	Li-Cor
Ouabain	Selleckchem
Phorbol 12-myristate 13-acetate (PMA)	Orpegen
PHOS-select iron affinity beads	Sigma-Aldrich
PNGase F	Sigma-Aldrich
Probenecid	Sigma-Aldrich
Quickstart BSA standard	Bio-RAD
ReproSil-Pur 3µm (separation-column)	Dr. Maisch GmbH
RPMI medium	Thermo Fisher Scientific
SB273005	Selleckchem
SB431542	Sigma-Aldrich
Secondary antibodies: IRDye 800CW/680RD	Li-Cor
Sodium chloride	Merck
Sodium dodecyl sulfate solution	Bio-RAD
Sodium metaperiodate	Thermo Fisher Scientific
Sodium pyruvate	Thermo Fisher Scientific
Staurosporine	Santa Cruz
Streptavidin-Dylight800	Thermo Fisher Scientific
Sunitinib	Santa Cruz
Triethylammonium bicarbonate	Sigma-Aldrich
Trifluoroacetic acid	Sigma-Aldrich
Tris(hydroxymethyl)aminomethane	Sigma-Aldrich
Trypsin	Promega
Tween 20	Sigma Aldrich
Urea	Sigma-Aldrich
Water, HPLC grade	Merck
WZ811	Sigma-Aldrich
XBridge C18 (high-pH C18)	Waters

3.1.2. Equipment

Equipment	Company
Bandelin Sonopuls HD 2200	Bandelin
Biorad gel chamber	Bio-Rad
Envision 2103 Multilabel Reader	Perkin Elmer
Eppendorf Centrifuge 5415 R	Eppendorf
Eppendorf Thermomixer	Eppendorf
HERA cell 240	Heraeus
HERA safe	Heraeus
Heraeus Multifuge 3S-R	Heraeus
IKA KS 260 basic	IKA
Liquidator[96]	Steinbrenner Laborsysteme GmbH
MODEL P-2000	Sutter Instrument Co.
Multidrop Combi	Thermo Fisher Scientific
MultiScreen HTS vacuum manifold	Millipore
Novex Mini cell X cell Surelock	Life technologies
Odyssey Infrared Imaging System	Li-Cor
Orbitrap Fusion Lumos	Thermo Fisher Scientific
Orbitrap XL	Thermo Fisher Scientific
PC8500-MAG	Next Advance, Inc.

Equipment	Company
PlateLoc	Agilent Technologies
Power PAC 200	Bio-RAD
Q Exactive (Plus)	Thermo Fisher Scientific
RoboSeal	HJ-Bioanalytik GmbH
Roto-Shake Genie	Scientific Industries Inc.
SureCycler 8800	Agilent Technologies
Trans-Blot Turbo Mini-size LF PVDF Membrane	Bio-RAD
Trans-Blot Turbo Mini-size Transfer Stack	Bio-RAD
Trans-Blot Turbo Transfer Buffer	Bio-RAD
Trans-Blot Turbo Transfer System	Bio-RAD
UltiMate 3000 Nano-HPLC-System	Thermo Fisher Scientific
Univapo	UniEquip GmbH
Vacuumbrand PC2001	Vacuubrand
Zeis LSM 780	Zeis

3.1.3. Miscellaneous

Material	Company
CytoSelect 96-well phagocytosis assay	Cell Biolabs
EasySep Enrichment kits	StemCell Technologies Inc.
Histopaque LSM1077	Sigma-Aldrich
HPLC pre-columns	Thermo Fisher Scientific
HPLC separation-column capillaries	Polymicro Technologies
Mico SpinColumn	Harvard Apparatus
Microplate 96-well PP V-Bottom	Greiner Bio-One
MultiScreen 0.45 µm 96-well filter plate	Millipore
MX3000P 96-well PCR plates	Agilent Technologies
Protease inhibitor cocktail	Roche Diagnostics

3.2. Methods

3.2.1. Cell culturing

Ramos, PC-3, YT, THP-1, U937 and K562 were cultured in RPMI1640 medium containing 10% fetal calf serum (FCS). Jurkat E6.1 cells were cultured in RPMI1640 medium supplemented with 4.5 g/l glucose, 10 mM HEPES, 1 mM sodium pyruvate and 10% FCS. Panc 08.13 were cultured in RPMI1640 medium containing 15% FCS and 10 µg/L Insulin. A549 and HEK293 were cultured in DMEM containing 10% FCS. CaCo-2 were cultured in MEM supplemented with 10% FCS. HeLa and HepG2 were cultured in DMEM supplemented with 20% FCS, 1 mM sodium pyruvate and 1% non-essential amino acids. MCF-7 were cultured in MEM containing 10% FCS, 1 mM sodium pyruvate, 1% non-essential amino acids and 10 µg/L Insulin. Saos2 were cultured in McCoy's 5a medium containing 15 % FCS. U87MG were cultured in RPMI1640 medium containing 10 % FCS, 1 % glutamax and 1 % pyruvate. All cell lines were cultured at 37 °C and 5 % CO_2 except for A549 which were cultured at 37 °C and 10% CO2. All cell lines were split twice per week and one day prior to experiments with fresh culturing medium.

3.2.2. Isolation of primary lymphocytes from human blood

Human primary B-cells, T-cells and NK-cells were extracted from buffy coats of human blood (DRK Mannheim) by Histopaque density gradient centrifugation and the EasySep Enrichment kits according to manufacturer´s instructions. In brief, in the first step PBMCs were isolated from human blood. Blood was transferred to 50 mL falcon tubes and filled up to 35 mL with plain RPMI1640 medium. Subsequently, 17 mL were carefully layered on top of 17 mL density gradient separation medium LSM1077 (Histopaque). Tubes were centrifuged at 872 g for 30 min at RT. The ring of cells containing the PBMCs was carefully collected and transferred into a fresh 50 mL falcon tube and filled up to 50 mL with washing buffer (PBS containing 2 % FBS and 1 mM EDTA). Cells were centrifuged at 500 g for 5 min at RT and washed again with 10 mL washing buffer. After centrifugation at 500 g for 5 min at RT, cells were resuspended in washing buffer to a concentration of 5 x 10^7 cells/mL. Subsequently, cells were incubated for 10 min at RT after mixing with 50 µL of the respective EasySep enrichment cocktail mix (for enrichment of B-, T- or NK-cells) per 1 mL of cells followed by addition and incubation for 5 min at RT with EasySep magnetic beads at 75 µL/mL, 50 µL/mL or 100 µL/mL for enrichment of B-cells, T-cells or NK-cells, respectively. Enriched B-, T- or NK-cells were transferred to fresh falcon tubes after removal of magnetic beads over 5 min at RT.

3.2.3. Kinobeads competition assay and in-gel digestion

Kinobeads profiling was performed essentially as described (Bantscheff et al., 2007). Briefly, cells were homogenized in lysis buffer (50 mM Tris-HCl pH 7.5, 5% glycerol, 1.5 mM $MgCl_2$, 150 mM NaCl, 20 mM NaF, 1 mM Na_3VO_4, 1 mM DTT, 5mM calyculin A, 0.8% Igepal-CA630 and protease inhibitor cocktail) using a Dounce homogenizer on ice. Lysates were cleared by ultracentrifugation and adjusted to 5 mg/ml protein concentration using the Bradford assay. Compounds were dissolved in dimethyl sulfoxide and various concentrations were added to 5 ml of lysates followed by 50 µl kinobeads suspension. Samples were agitated for 30 min at 4 °C. Subsequently, the beads were washed, collected by centrifugation and bound material was eluted with SDS sample buffer. 25 µg sample was fractionated by short (20 min at 80V) SDS gel electrophoresis on 4–12% NuPAGE gels and stained with colloidal Coomassie. Samples were in gel digested by destaining the gel cut into three slices and tryptic digestion for

4 h at 37 °C with 150 ng trypsin per gel slice. After extraction twice with 2.5 % FA, once with 60 % ACN in 1 % FA and once with 100 % ACN, peptides were TMT labeled and analyzed by mass spectrometry, as described in detail below.

3.2.4. Phagocytosis assay

The phagocytosis assay was conducted based on the CytoSelect 96-well phagocytosis assay. After 48h of differentiation in presence or absence of kinase inhibitor (as described in detail below), adherent cells were detached with trypsin and 5×10^4 cells in 100 µL fresh RPMI1640 medium supplemented with 10% FCS, 100 nM PMA and 1 µM kinase inhibitor or DMSO were seeded per well in a 96-well microtiter plate. After 24 h of incubation at 37 °C and 5% CO_2, 2 µM Cytochalasin D was added to respective phagocytosis inhibition wells and plate was incubated for an additional 1 h. Nonopsonized zymosan particles (10 µL/sample) were added and cells were incubated for 1 h. The amount of engulfed zymosan particles was determined by measuring the absorbance at 405 nm with a 96-well microtiter plate reader (EnVision Plate Reader, PerkinElmer) and the relative phagocytotic activity was referenced to normally differentiated THP-1 cells.

3.2.5. Static and dynamic cell surface proteome mapping

3.2.5.1. THP-1 differentiation and drug treatment

THP-1 cells were diluted to 0.5×10^6 cells/mL into fresh culture media one day prior to differentiation experiments. For each experimental condition, 1×10^7 cells were seeded in RPMI1640 medium supplemented with 10% FCS and 100 nM PMA or 100 nM Vitamin D3 (Calcitriol) on a 15 cm petri dish and incubated at 37 °C and 5% CO_2. THP-1 cells were also treated with 1 µM kinase inhibitor (dasatinib, sunitinib, imatinib) over 1 h at 37 °C in RPMI1640 medium supplemented with 10% FCS prior to the addition of 100 nM PMA followed by 48 h of incubation. PMA-differentiation was verified by immunoblotting for up-regulation of CD11b or down-regulation of MRC2.

3.2.5.2. Biotinylation of the cell surface glycoproteome and enrichment of labeled proteins

1×10^7 suspension cells or a 15 cm petri dish of adherent cells at 70-80% confluency were washed twice with PBS followed by oxidation of carbohydrates with 1 mM Na-metaperiodate in pH 6.5 adjusted PBS at 4 °C for 10 min in the dark. Cells were washed twice with PBS followed by biotinylation with 1 mM Alkoxyamine-PEG$_4$-Biotin in presence of 10 mM Aniline for 10 min at 4 °C in the dark. Cells were washed three times with PBS. Suspension cells were pelleted at 340 g, adherent cells were detached by scraping and pelleted at 340 g. Cell pellets were frozen in liquid nitrogen and stored at -80 °C. Cell pellets were lysed by boiling for 10 min at 95 °C in 200 µl SDS lysis buffer (4 % SDS, 60 mM Tris pH 7.6, 50 mM DTT). Samples were cooled and sonicated on ice once (Bandelin Sonopuls HD 2200) at 50 % power output with 1 burst of 10 seconds. Enrichment of biotinylated proteins was performed in 96 deep well filter plates. For each enrichment, 15 µL High Capacity Streptavidin Agarose resin were prepared by washing twice with Wash-Buffer 1 (WB1: 0.4 % SDS, 20 mM Tris pH 7.5, 400 mM NaCl). Resin was incubated with lysate for 60 min at 25 °C while overhead shaking, followed by three times washing with WB1, eight times washing with Wash-Buffer 2 (WB2: 20 mM Tris pH 7.5 and 400 mM NaCl) and 8 times washing with Wash-Buffer 3 (WB3: 50 mM Triethylammonium bicarbonate (TEAB), 2 M Urea). Subsequently, resin was incubated for 45 min with 45 mM DTT in 50 mM TEAB at 25 °C followed by 30 min incubation at 25 °C with 100 mM IAA in 50 mM

TEAB. Resin was washed five times with WB3 and digested for 16 h at 25 °C in 60 µl 50 mM TEAB, 1.33 M Urea supplemented with 0.4 µg trypsin. On the following day, additional 0.4 µg trypsin in 50 mM TEAB was added and resin was incubated for an additional 4 h at 25 °C. Peptides were eluted by centrifugation. For additional PNGase F elution, resin was washed five times with Wash-Buffer 4 (WB4: 50 mM HEPES pH 7.5) followed by incubation with 0.5 units PNGase F in WB4 for 3 h at 37 °C. Peptides were eluted by centrifugation, dried in vacuo and stored at -80 °C.

3.2.5.3. Sample preparation for MS

For TMT-quantification experiments, peptide samples were resuspended in 100 µL of 200 mM TEAB 10% ACN and labeled with 10-plex TMT reagents. The labeling reaction was performed by adding 50 µl of 25 mM TMT-label reagent dissolved in ACN, incubation for 90 min at 25 °C and quenching with 2.5 % hydroxylamine in 100 mM TEAB for 15 min at 25 °C. Finally, labeled peptides were pooled. Label-free and TMT-quantification experiment samples were desalted using C18 STAGE tips (Rappsilber et al., 2007). Four plugs of C18 material (Octadecyl C18 47 mm Extraction Disks) were punched into a 200 µL pipette tip and the material was washed once with 100 µL MeOH and twice with 200 µL C18-Wash buffer (2 % ACN in 0.1 % TFA) by centrifugation for 3 min at 3000 g. Dried peptide samples were dissolved in 100 µL C18-Wash buffer and applied to the prepared C18 STAGE tips followed by centrifugation for 3 min at 3000 g. Bound peptides were washed twice with 200 µL C18-Wash buffer by centrifugation for 3 min at 3000 g, eluted twice with 50 µL of C18-Elution buffer (80 % ACN in 0.1 % TFA) by centrifugation for 2 min at 1000 g, dried in vacuo and stored at -80 °C. Samples from the THP-1 differentiation time course experiment were fractionated into 9 fractions as previously described (Kruse et al., 2011). In short, peptides were separated within 100 min by using reversed-phase chromatography at pH12 (1 mm Xbridge column) at a flow rate of 30 µL/min, fractions containing early and late eluting peptides were pooled and dried in vacuo and stored at -80 °C.

3.2.5.4. Monitoring THP-1 differentiation by cell surface phosphoproteomics

THP-1 cells were diluted to $0.5x10^6$ cells/mL into fresh culture media one day prior to differentiation experiments. On the next day, in two biological replicates $5x10^7$ cells were seeded in 50 mL RPMI1640 supplemented with 10% FCS and 100 nM PMA and incubated for 15, 30 and 60 min at 37 °C in the incubator. Two replicates of undifferentiated cells were used as controls. After biotinylation, enrichment, TMT-labeling and C18 STAGE-tip based sample cleanup as described in 3.2.5.2 and 3.2.5.3, 10 % of the sample was used for monitoring cell surface proteome abundance changes while 90 % of the sample was subjected to IMAC-based phosphopeptide enrichment. For that purpose, 60 µL bead slurry of IMAC resin (PHOS-Select™ Iron Affinity Gel) were washed 4x with wash solution (250 mM acetic acid in 30 % ACN) within 30 min while orbital shaking at 1000 rpm by removal of the liquid supernatant after centrifugation at 1000 g. Washed beads were resuspended in 150 µL wash solution, transferred to the dried peptide mixture sample and incubated for 2 h at 25 °C with 1250 rpm orbital shaking. Subsequently, a spin column was washed twice with 100 µL wash solution and beads were transferred to the spin column. Beads were washed 4 times with 150 µL wash solution by slowly pressing the liquid through the spin column and avoiding dry beads. Bound phosphopeptides were eluted twice by incubating beads for 2 min with 50 µL elution solution (400 mM NH_4OH in 30 % ACN) and letting the liquid run through the spin column. The eluted sample was acidified to pH 4 by addition of 50 µL 10 % FA and the peptide mixture was dried in vacuo.

3.2.6. Cell surface selective thermal proteome profiling

3.2.6.1. Treatment of cells with endogenous ligands

Cells were starved for 16 h in plain RPMI1640 in the incubator at 37 °C and 5% CO_2 prior to the treatment with IGF-1, INS or VLDL. In case of the treatment of cells with folate or methotrexate, cells were starved for 16 h in plain RPMI1640 without folic acid in the incubator at 37 °C and 5% CO_2. For experiments with IL2, IL6 or CXCL12, cells were treated without prior starvation. Cells were treated for 30 min (10 nM IL2, 20 nM IL6, 20 nM CXCL12, 100 nM IGF1, 100 nM INS) or 60 min (100 µg VLDL, 20 µM folate) with the respective endogenous ligand in the incubator at 37 °C and 5% CO_2.

3.2.6.2. Treatment of cells with small molecule chemicals or antibodies

Cells were treated for 60 min with 1 µM (SB273005, ouabain, dipyridamole, probenecid, elacridar, ilomastat, WZ811, IT1t, dasatinib, digitoxin, nilotinib, staurosporine, luminespib), 10 µM (SB431542), 20 µM (copper sulfate, methotrexate) or 100 µM (furosemide) in the incubator at 37 °C and 5 % CO_2. For stimulation of cells with antibodies, cells were treated with 2 µg/mL of the respective antibody for the indicated time in the incubator at 37 °C and 5 % CO_2. In case of CD3/CD28 stimulation, an anti-mouse antibody was added at 5 µg/mL for CD3/CD28 antibody crosslinking.

3.2.6.3. Heat treatment and biotinylation

Treated cells and controls were pelleted at 340 g and 4 °C for 2 min, washed by resuspending in 5 ml of ice cold PBS, and pelleted again at 340 g and 4 °C for 2 min. The supernatant was removed and cells were resuspended in 1200 µL ice cold PBS. 100 µL aliquots of this cell suspension containing a defined number of cells (K562: $5x10^6$, Jurkat: $8x10^6$, THP1: $8x10^6$, YT: $5x10^6$) were transferred into a 96 well PCR plate and centrifuged at 325 g and 4 °C for 2 min. For all following liquid handling steps, a Liquidator96 was used. 80 µL of the supernatant was removed and the plate was subjected to a defined temperature gradient (37 °C was set as reference temperature) for 3 min followed by a 3 min incubation at room temperature. Cells were resuspended by adding 100 µL Oxidation buffer (PBS adjusted to pH 6.5 containing 1.2 mM Na-metaperiodate, RT) and incubated for 10 min at RT in the dark. Cells were pelleted by centrifugation at 325 g and 4 °C for 2 min. 100 µL of the supernatant was removed and cells were resuspended by adding 100 µL ice cold Biotinylation buffer (PBS containing 1.2 mM alkoxyamine-PEG_4-biotin and 12 mM aniline) and incubated for 10 min at 4 °C in the dark. Cells were washed twice by pelleting at 325 g and 4 °C for 2 min, removing 100 µL of the supernatant and resuspending in 100 µL ice cold PBS. Cells were lysed on ice by adding 10 µL of 3x lysis buffer to the remaining 20 µL cell suspension followed by additional 40 µL of 1x lysis buffer. Insoluble cellular fragments and aggregated proteins were removed by filtration. Lysates were transferred to a 0.45 µm 96-well filter plate (pre-wetted with 1x lysis buffer) and filtered by centrifugation for 5 min at 1500 g and 4 °C. The flow-through was collected, frozen in liquid nitrogen and stored at -80 °C.

3.2.6.4. Isothermal dose response experiments

Cells were treated for 60 min with decreasing concentrations of dasatinib (serial dilution starting from 2 mM with a dilution factor of 5). This resulted in cellular treatment with nine compound concentrations and one vehicle control. Treated cells were processed as described in 3.2.6.3 with the difference that cells were heat treated only at a single temperature.

3.2.6.5. Enrichment of labeled proteins

High Capacity Neutravidin Agarose resin was washed twice with Wash-Buffer 0 (WB0, 1 % DDM or 0.8 % NP40 in PBS) and a slurry of 133.3 µL resin per mL of WB0 was prepared. Subsequently, for each enrichment 4 µL washed bead resin (30 µL slurry) was transferred onto a 96-well plate and lysate containing 150 µg protein (determined by BCA assay) was added. Resin was incubated with lysate for 120 min at RT while overhead shaking, transferred onto a 0.45 µm 96-well filter plate followed by eight times washing with Wash-Buffer 1 (WB1, 0.4 % SDS, 20 mM Tris pH 7.5, 400 mM NaCl), eight times washing with Wash-Buffer 2 (WB2: 20 mM Tris pH 7.5 and 400 mM NaCl), eight times washing with Wash-Buffer 3 (WB3: 50 mM TEAB, 2 M Urea) and four times washing with Wash-Buffer 4 (WB4, 50 mM HEPES) by using a reagent dispenser (Multidrop Combi) and vacuum manifold (MultiScreen Vacuum manifold). Residual liquid was removed by centrifugation at 325 g for 2 min. Bound proteins were eluted and peptides alkylated for 4 h with horizontal shaking at RT by on-bead digestion with 50 ng Trypsin and 50 ng LysC in 25 mM HEPES pH 8.5 containing 2.5 mM Tris(2-carboxyethyl)phosphine (TCEP) and 7.5 mM 2-chloroacetamide (CAA). Peptides were collected in a 96 well plate by centrifugation at 325 g for 2 min followed by an additional washing of the filter plate with 50 µL 50 mM HEPES followed by centrifugation at 325 g for 2 min. Peptide mixtures were dried in vacuo and stored at -80 °C

3.2.6.6. Sample preparation for MS

In case of melting curve-based data analysis, treatments and controls were labeled in separate TMT10 experiments with increasing reporter ion masses and increasing temperatures. In case of ratio-based analysis, treatments were analyzed together with controls at five temperatures in a single TMT10 experiment requiring two TMT10 experiments to cover nine temperature points with one reference temperature in both TMT10 experiments. Controls and treatments were alternatingly labeled with TMT-labeling reagents. In both cases, peptide samples were resuspended in 10 µL of 50 mM HEPES 10% ACN and labeled with 10-plex TMT reagents. The labeling reaction was performed by adding 10 µl of 25 mM TMT-label reagent dissolved in acetonitrile, incubation for 90 min at 25 °C and quenching with 2.5 % hydroxylamine in 50 mM HEPES for 15 min at 25 °C. Finally, labeled peptides were pooled and cleaned using C18-SCX STAGE tips. Three plugs of C18 material (Octadecyl C18 47 mm Extraction Disks) and three plugs of SCX material (Cation 47 mm Extraction Disks) were punched into a 200 µL pipette tip and the material was washed once with 100 µL MeOH and twice with 200 µL C18SCX-Wash buffer (2 % ACN in 0.5 % TFA) by centrifugation for 2 min at 2000 g. Dried peptide samples were dissolved in 100 µL C18SCX-Wash buffer and applied to the prepared C18-SCX STAGE tips followed by centrifugation for 2 min at 2000 g. Bound peptides were washed twice with 200 µL C18SCX-Wash buffer by centrifugation for 2 min at 2000 g. Desalted peptides bound to the C18 material were eluted to the SCX material by washing three times with 200 µL C18-Elution Buffer (60 % ACN in 0.5 % TFA) and centrifugation at 1000 g for 4 min. Finally, cleaned peptides were eluted twice with 25 µL SCX-Elution buffer (80 % ACN, 5 % NH3) by centrifugation at 2000 g for 1 min, dried in vacuo and stored at -80 °C.

3.2.7. LC-MS/MS analysis

Samples were resuspended in 0.05 % TFA in water and a defined fraction (label-free cell surface mapping: 30 %, THP1 differentiation: 10 %, Thermal proteome profiling: 25 %) was injected into an Ultimate3000 nanoRLSC coupled to a Q Exactive (Plus) or Orbitrap Fusion Lumos. Peptides were separated on custom-made 50 cm × 100 µm (inner diameter) C18 reversed-phase (Reprosil) columns at 40 °C. Gradient elution was performed from 3.5 % ACN

to 35 % ACN in 0.1 % formic acid over 2 or 4 h. Samples were online injected into mass spectrometers operating with a data-dependent top10 method. MS spectra were acquired by using 70.000 resolution and an ion target of 3E6 for MS1 scans. Higher energy collisional dissociation (HCD) scans were performed with 25 % (label-free) or 35 % (TMT-quantification) normalized collision energy (NCE) at 35.000 resolution and an ion target of 2E5.

3.2.8. Peptide and protein identification

Raw data was processed using an in-house pipeline (Franken et al., 2015). Mascot 2.4 (Matrix Science) was used for protein identification by using a 10 ppm mass tolerance for peptide precursors and 20 mDa mass tolerance for fragment ions. Enzyme specificity was set to trypsin with up to three missed cleavages. For label-free experiments, carbamidomethylation of cysteine residues was set as fixed modification and methionine oxidation and N-terminal acetylation of proteins were set as variable modifications. For TMT-quantification experiments, carbamidomethylation of cysteine residues and TMT modification of lysine residues were set as fixed modifications while methionine oxidation, N-terminal acetylation of proteins and TMT modification of peptide N-termini were set as variable modifications. Deamidation of asparagines was set as additional variable modification for PNGase F samples. The search database consisted of a customized version of the International Protein Index protein sequence database (numbers of entries: 108790, year: 2009) combined with a decoy version of this database created by using a script supplied by Matrix Science. IPI accession numbers of all identified proteins were mapped to the UniProt database (December 14th 2016) by matching the corresponding protein sequences. Unless stated otherwise, protein identifications were accepted as follows: (i) For single-spectrum to sequence assignments, this assignment was required to be the best match with a minimum Mascot score of 31 and with a 10× difference of this assignment over the next best assignment. Based on these criteria, the decoy search results indicated <1 % false discovery rate (FDR). (ii) For multiple spectrum to sequence assignments and using the same parameters, the decoy search results indicate <0.1 % FDR. All identified proteins were quantified; FDR for quantified proteins was below 1 %.

For *in-silico* digestion of UniProt-annotated plasma membrane proteins, the alternative proteases chymotrypsin, LysC, AspN, GluC, ArgC (Giansanti et al., 2016) were compared to trypsin. Typically, MS identifiable peptides have a length between 7 and 35 amino acids, with the lower limit being determined by sequence uniqueness and the upper limit being determined by the instrument's resolving power (Swaney et al., 2010; Meyer et al., 2014). Thus, peptides generated by *in-silico* digestion (R, cleaver, Bioconductor, Gibb, 2015) were filtered for lengths between 7 and 35 amino acids.

3.2.9. Peptide and protein quantification

In case of label-free quantification, the Top3 method (Silva et al., 2006) was applied in a slightly modified form (Becher et al., 2013). In brief: for each protein the maximum intensity of the extracted ion current (XIC) of the three most abundant peptide sequences was log10 transformed and averaged. The derived value is denoted as MS1 abundance and is a good proxy for protein abundance in the sample.

For TMT-quantification experiments, reporter ion intensities were read from raw data and multiplied with ion accumulation times to yield a measure proportional to the number of ions; this measure is referred to as "ion area" (Savitski et al., 2011). Spectra matching to peptides were filtered according to the following criteria: Mascot ion score >15, signal-to-background of the precursor ion >4, and signal-to-interference >0.5 (Savitski et al., 2010). Fold-changes were

corrected for isotope purity as described and adjusted for interference caused by co-eluting nearly isobaric peaks as estimated by the signal-to-interference measure (Savitski et al., 2013). Protein quantification was derived from individual spectra matching to distinct peptides by using a sum-based bootstrap algorithm.

3.2.10. Data analysis

Annotations of proteins were based on the UniProt database (December 14th 2016). Data analysis and visualization was performed in TIBCO Spotfire 6.0.2 or R (www.r-project.org). Gene ontology enrichment was obtained from DAVID Bioinformatics Resources 6.7 (Huang et al., 2009) or in R (topGO, Bioconductor, Alexa and Rahnenfuhrer, 2015). Principal component analyses were performed in Perseus 1.5.1.6 (www.perseus-framework.org) or R. Common bead background proteins were annotated based on CRAPome (Mellacheruvu et al., 2013) data (filters used for CRAPOME: streptavidin agarose beads, proteins with spectral counts ≥ 5, intracellular proteins). General data interpretation was supported by a self-developed program written in C# called "2D Protein Domain Visualizer". This application enables visualization of protein annotations (topology, domains, secondary structures, post-translational modifications, subcellular localization) from UniProt (www.uniprot.org) with additional transmembrane topology prediction by Phobius (http://phobius.sbc.su.se), protein-protein interaction information from STRING (www.string-db.org), additional information about post-translational modifications from PhosphoSitePlus (www.phosphosite.org), drug and drug target information from DrugBank (www.drugbank.ca) and ChEMBL (www.ebi.ac.uk/chembl), PubMed information hyperlinked over proteins from iHOP (Hoffmann and Valencia, 2004, www.ihop-net.org) as well as the compendium of cell surface proteome mappings generated in this thesis. This tool will be described in section 4.3.

3.2.10.1. Static and dynamic cell surface proteome mapping

Identified proteins in trypsin digest samples of cell surface proteome mappings were filtered for MS1 abundance > 0 and total number of peptide to spectrum matches ≥ 2. Identified proteins in PNGase F digest samples of cell surface proteome mappings were filtered for MS1 abundance > 0 and Mascot score ≥ 20. Relative abundance estimations for trypsin and PNGase F samples were normalized to the average density maximum of all samples.

For identification of proteins differentially expressed between cell lines and cognate primary cells, p-values were calculated by t-test based on imputed data (estimated protein abundance values of 0 replaced by normal distributed data simulating signals of low abundant proteins, normal distribution standard deviation 0.3, normal distribution mean downshifted by 1.8 to lower end of the distribution of measured values, separate for each column, Deeb et al., 2012). Significant proteins were filtered for Benjamini-Hochberg corrected p-values < 0.05. For GO-Term enrichment analysis, the enriched GO-Terms were filtered for Benjamini-Hochberg corrected p-values < 0.01. In TMT-quantification samples of differentiation experiments proteins were filtered for 3 or more quantified spectra (qusm) and 2 or more unique peptides (qupm). The 0 h time point of the differentiation experiment was set as reference. For identification of proteins significantly regulated during differentiation of THP-1 cells, a modified t-test (Smyth, 2004) was applied and data was filtered for $\log_2$ relative abundances ≥ 2 or ≤ -2 at least once between 24 h and 72 h of the time course with Benjamini-Hochberg corrected p-values < 0.01 at the respective time point. For identification of proteins significantly altered in abundance comparing cells differentiated in presence or absence of kinase inhibitors, the data was filtered

for $\log_2$ relative abundance ≥ 1 or ≤ -1 between these differentiation outcomes applicable for both replicates and p-values < 0.05.

3.2.10.2. Cell surface selective thermal proteome profiling

Samples were analyzed in two different ways.

Melting curve-based data analysis was conducted as described (Reinhard et al., 2015; Franken et al., 2015). At least two biological replicates of treatments and controls were prepared. Treatments and controls were analyzed in separate TMT10 experiments corresponding to ten different constantly increasing temperature points. Melting curves were calculated based on fold-changes relative to the lowest temperature according to the following equation derived from chemical denaturation theory (Schellman, 1994):

$$f(T) = \frac{1 - plateau}{1 + e^{-(\frac{a}{T} - b)}} + plateau$$

T represent the temperature and a, b, and $plateau$ are constants. Since fold changes are calculated relative to the reference temperature, the value of $f(T)$ at the lowest temperature was set to 1. Based on this melting curve, the melting point of a protein is defined as the temperature T_m at which the abundance of the protein represents half of the abundance observed at the reference temperature. Data of treatments and controls were normalized based on the calculated melting curves for proteins quantified in both experiments and fulfilling the following criteria: the fold-changes at the seventh highest temperature point compared with the lowest temperature point were between 0.4 and 0.6, and at the 9th and 10th highest temperature points compared to the lowest temperature point were below 0.3 and 0.2 respectively. Based on this subset of proteins, the median fold-change values for each of the 10 fold-changes were calculated and a melting curve was fitted for each experiment individually. The curve with the best R^2 was used to calculate normalization factors for all experiments by calculating for each experiment individually a fold-change between each median fold-change and the best-fitting curve at the respective temperature. These normalization factors were then applied to all protein fold-changes in the respective experiments and normalized melting curves were calculated. With these normalized melting curves for each protein, melting point differences between treatments and controls were calculated and proteins fulfilling the following criteria were regarded as significantly shifted: (I) ≥ 2 qusm, (II) ≥ 2 qupm, (III) R^2 ≥ 0.6, (IV) annotated cell surface localization according to UniProt, (V) significance of melting point difference calculated

$$if\,(\Delta T_m > s)\{-\log_{10}(\text{p - value}) > \frac{1}{(\Delta T_m - s)} + P\}$$

by t-test fulfills the criteria:

$$if\,(\Delta T_m < -s)\{-\log_{10}(\text{p - value}) > \frac{1}{(s - \Delta T_m)} + P\}$$

were ΔT_m is the average melting point difference, s the standard deviation of the data set defined as 2x median standard deviation for all proteins between replicates and P the minimal accepted $\log_{10}$ transformed p-value for a protein set to p = 0.05, (VI) $|\Delta T_m|$ ≥ s.

For ratio-based data analysis, treatments and controls were analyzed along with each other at nine different temperatures in two TMT10 experiments with one reference temperature in both TMT10 experiments. At least two biological replicates of treatments were prepared. Low and high temperature points could be mixed between both TMT10 experiments to allow a comparable overall protein concentration in both samples (e.g. TMT10 experiment #1 contains

the temperatures 1, 2, 3, 8, 9 and TMT10 experiment #2 contains the temperatures 1, 4, 5, 6, 7). Data was normalized in two steps. In the first step, at each individual temperature controls were normalized between replicates based on cell surface annotated proteins quantified with qusm ≥ 3 and qupm ≥ 2 in the individual replicate and a fold-change at the respective temperature point ≥ 0.2 relative to the reference temperature. For each temperature and each replicate, normalization factors were calculated relative to the average of maxima of the density distributions of relative fold changes at the respective temperature. These normalization factors were then applied to all protein sumionareas and fold-changes of controls in the respective experiments. In the second step, at each individual temperature the treatments were normalized to their controls based on proteins quantified with qusm ≥ 3 and qupm ≥ 2 in the individual replicate and a fold-change at the respective temperature point ≥ 0.2 relative to the reference temperature. For each treatment at each temperature and each replicate, normalization factors were calculated relative to the maxima of the density distributions of relative fold changes at the respective temperature in controls. These normalization factors were then applied to all protein sumionareas and fold-changes of treatments in the respective experiment and at the respective temperature. For data analysis, the normalized data sets of both TMT10 experiments covering all temperature points were combined. Subsequently, based on relative fold changes for each protein at each individual temperature point the abundance ratio between treatment and control as well as the average over replicates were calculated and $\log_2$ transformed if the relative fold change of this protein at the respective temperature was ≥ 0.15 in either the treatments or the controls. In addition, for each protein at each individual temperature point the significance of a difference in the protein abundance between treatments and controls was determined by left- and right-tailed t-tests based on $\log_2$ transformed relative fold changes relative to the reference temperature if the relative fold change of this protein at the respective temperature was higher than 0.15 in either the treatments or the controls. If a protein showed no or only once a significant (p-value < 0.05) difference in protein abundance between treatments and controls, the average $\log_2$ transformed abundance ratio between treatments and controls as well as the p-value were reported for the temperature with the lowest p-value. If a protein showed a significant (p-value < 0.05) difference in protein abundance between treatments and controls at more than one temperature, the average $\log_2$ transformed abundance ratios between treatments and controls were summed (collated $\log_2$ratio) for all temperatures in a row which showed a significant (p-value < 0.05) difference in protein abundance between treatments and controls. For these temperatures the respective dependent test statistics were combined (collated p-value) using Brown´s method (Brown, 1975). Melting curves and melting points were calculated based on fold-changes relative to the lowest temperature as previously described and t-test based significances of differences in the melting points between treatments and controls were calculated. Proteins fulfilling the following criteria were regarded as significantly affected by the treatment: (I) ≥ 3 qusm and ≥ 2 qupm in at least two replicates (either in first or second gradient part), (II) localized to cell surface according to UniProt, (III) cumulative significance of protein abundance between treatments and controls fulfills the criteria:

$$if\ (\Sigma r_{TvsC} > s)\{-\log_{10}(\text{p - value}) > \frac{1}{(\Sigma r_{TvsC} - s)} + P\}$$

$$if\ (\Sigma r_{TvsC} < -s)\{-\log_{10}(\text{p - value}) > \frac{1}{(s - \Sigma r_{TvsC})} + P\}$$

where Σr_{TvsC} is the cumulative $\log_2$ ratio between treatments and controls (or $\log_2$ ratio at most significant temperature), s the standard deviation of the data set defined as 2x median standard deviation of ratios for all proteins between replicates and P the minimal accepted $\log_{10}$

transformed p-value set to p = 0.05 and (IV) absolute cumulative $\log_2$ ratio between treatments and controls (Σr_{TvsC}) ≥ s. To reduce overestimations of significances of protein abundance differences at high temperatures, proteins, for which the data accumulation started at $T > T_m + d$ were T_m is the calculated melting point and d the temperature window between experimentally selected temperatures, were excluded. Furthermore, significantly affected proteins, for which data points were accumulated with high standard deviations (standard deviation > median standard deviation + standard deviation of standard deviations at respective temperature), were excluded.

For significantly affected proteins, two treatment-dependent effects could be distinguished: cell surface abundance changes and thermal stability changes. Proteins with a significant (p-value < 0.01) and an absolute relative fold change ≥ 10 % at 37 °C in treatments compared to controls were regarded as significantly internalized/surface presented. Proteins with a significant (p-value < 0.05) and an absolute thermal shift ≥ 0.5 °C in treatments compared to controls were regarded as significantly thermally shifted.

For isothermal dose response experiments, data analysis was performed as described (Savitski et al., 2014; Franken et al., 2015). In brief, for good quantified proteins (qusm > 3) with an abundance change of at least 50 % between vehicle and highest drug concentration, dose response curves were fitted. Data is normalized by dividing the protein fold changes in each condition (compound concentration or vehicle) by the median fold change of all proteins in that condition. Fold changes are transformed to a range between 0 and 1, and sigmoidal curves are fitted according to the formula:

$$y = \frac{1}{1 + 10^{(\log EC_{50} - x)\,slope}}$$

For proteins with a coefficient of determination $R^2 > 0.8$, the half-maximal effective concentration was determined and negative $\log_{10}$ transformed (pEC_{50}).

4. Results

4.1. Optimization of cell surface proteome profiling

Cell surface proteins are generally low abundant compared to many cytosolic proteins (Bausch-Fluck et al., 2015). To enable comprehensive analysis of proteins of this subcellular compartment by mass spectrometry-based proteomics, cell surface selective enrichment techniques are usually applied. Two commonly used approaches were evaluated in this thesis. The first technique is based on the restricted biotinylation of cell surface accessible amine groups with the membrane-impermeable biotinylation reagent sulfo-NHS-LC-LC-biotin (Fig. 16A). The second technique is based on selective biotinylation of glycosylated cell surface proteins. Due to the prevalence of protein glycosylation for proteins destined for extracellular environments (Roth, 2002), this two-step approach is

Fig. 16 Biotinylation reagents. (**A**) Sulfo-NHS-LC-LC-biotin. (**B**) Alkoxyamine-PEG$_4$-biotin.

intrinsically selective for cell surface proteins. First, reactive aldehydes are introduced in the carbohydrate chains by cleavage of vicinal diols primarily in sialic acids. In a second step, these aldehydes are reacted with an aldehyde-reactive biotinylation reagent, e.g. alkoxyamine-PEG$_4$-biotin (Fig. 16B). Although Hörmann et al. recently showed that the amine-directed strategy was superior in their hands (Hörmann et al., 2016), they mixed sodium metaperiodate with aniline and the alkoxyamine-biotin which results in quenching of the biotinylation reagent. Thus, a new comparison using optimized protocols was performed in this thesis. For that purpose, YT cells were biotinylated at various incubation conditions and results were compared by staining blotted proteins with Streptavidin DyLight800 (Fig. 17). A Coomassie-stained gel was used to check equal amounts of loaded proteins. The amine-directed biotinylation showed an intense smear of labeled proteins while less intense but sharper signals were detected in case of the glycosylation-directed biotinylation. A reduction of the incubation temperature to 4 °C as well as a prolonged incubation for 30 or 60 minutes did not show an influence on biotinylation signals. Reduced concentrations of sulfo-NHS-LC-LC-biotin from 1 mM to 0.1 mM and 0.01 mM showed decreased signal intensities but did not result in more defined bands. In case of alkoxyamine-PEG$_4$-biotin, a prolonged incubation for 30 or 60 minutes slightly increased signal intensities but a reduction of the reagent concentration led to a marked decrease in labeled proteins. To investigate the selectivity of this biotinylation strategy for periodate-induced aldehydes, signal intensities of biotinylated proteins were also compared in untreated, periodate-treated or alkoxyamine-PEG$_4$-biotin treated control samples. Only low intensities of endogenously biotinylated proteins were detected for all three controls indicating the selectivity and necessity for periodate-induced aldehydes in carbohydrate chains for alkoxyamine-PEG$_4$-biotin based cell surface biotinylation.
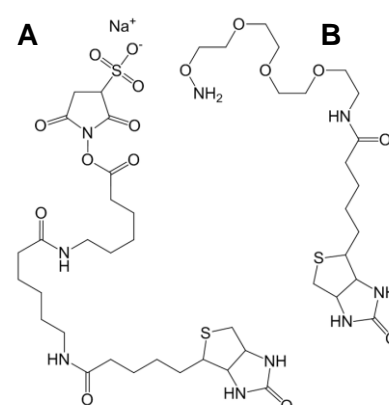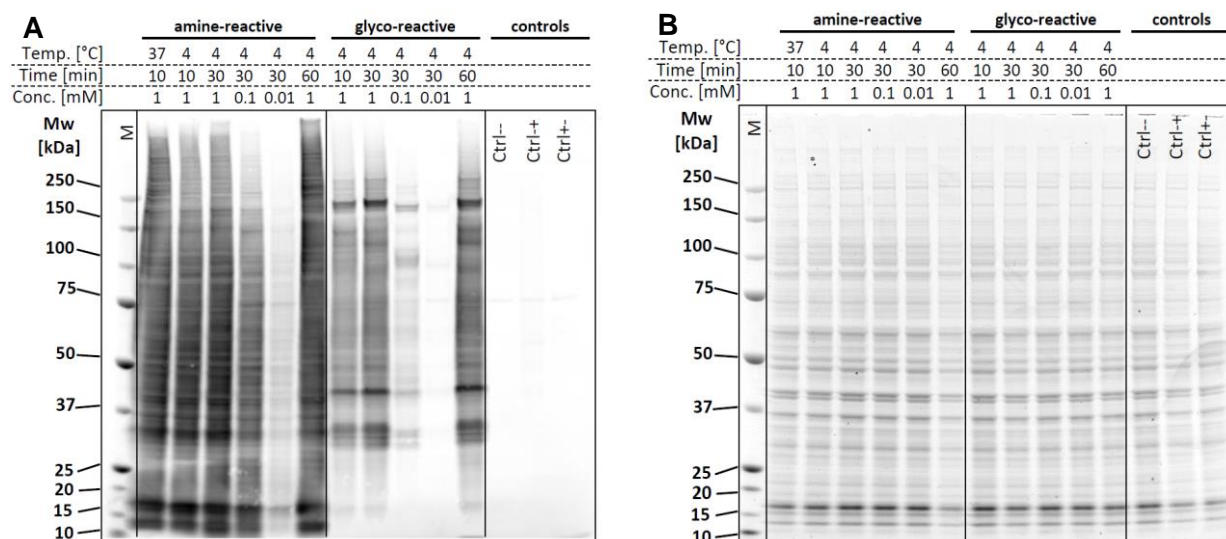
Fig. 17 Comparison of amine-reactive and glycosylation-directed protein biotinylation. For each condition 0.5x10^6 YT cells were biotinylated either with sulfo-NHS-LC-LC-biotin (amine-reactive) or after oxidation with 1 mM Na-metaperiodate over 10 min at 4 °C with alkoxyamine-PEG$_4$-biotin (glyco-reactive). Various concentrations, incubation times and temperatures were compared and 20 % of the samples were loaded on 4-12 % SDS polyacrylamide gels after lysis in 4 % SDS. Untreated (Ctrl--), without oxidation but with 1 mM alkoxyamine-PEG$_4$-biotin treated (Ctrl-+) and 1 mM Na-metaperiodate treated (Ctrl+-) cells were used as controls. (**A**) Blotted biotinylated proteins were stained with Streptavidin DyLight800. (**B**) Coomassie-stained gel as loading control.

Following protein labeling, subsequent capturing and enrichment of these proteins with streptavidin-coated beads was tested. YT cells were either biotinylated with 1 mM sulfo-NHS-LC-LC-biotin or with 1 mM alkoxyamine-PEG$_4$-biotin for 10 min. Subsequently, lysates were incubated for 60 min at RT with 15 µL of streptavidin-coated beads on an overhead shaker. The non-bound fraction was collected and proteins unspecifically bound to the affinity resin were eluted by washing beads four times with 0.4 % SDS and 400 mM NaCl, eight times with 400 mM NaCl and eight times with 2 M urea. Bound biotinylated proteins were eluted by incubating beads in 4 % SDS containing 10 mM biotin and 50 mM DTT for 15 min at 95 °C while shaking. Beads were removed and equal volumes of lysate, non-bound fraction and eluate corresponding to 1 % of the total lysate were analyzed by blotting and staining of biotinylated proteins (Fig. 18). A Coomassie-stained gel was used as loading control indicating equal amounts of loaded proteins in inputs and non-bound fractions. Untreated cells were used as controls.
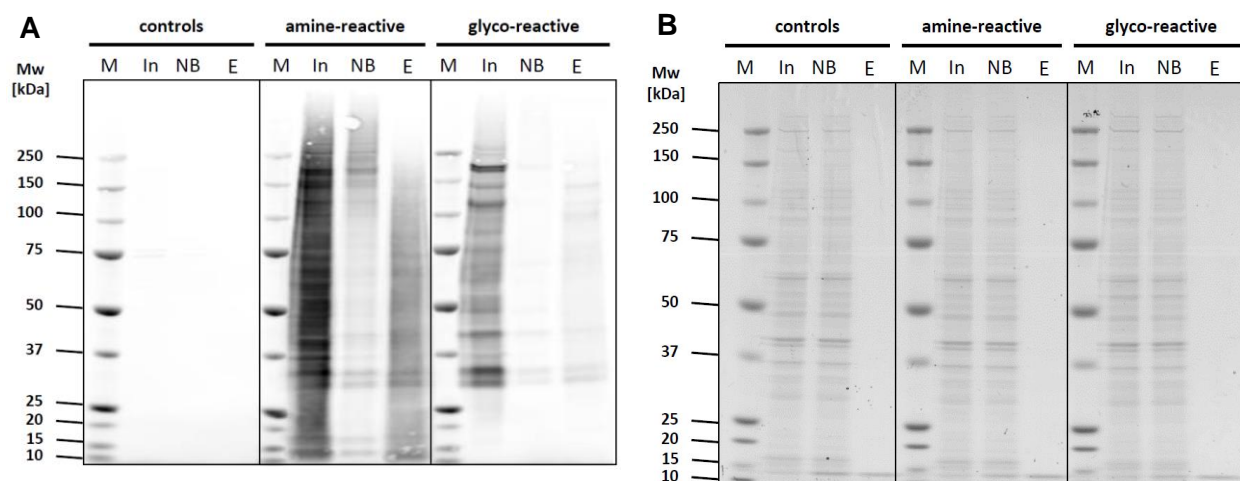
Fig. 18 Elution of biotinylated proteins from streptavidin-coated beads by boiling. For each condition 1x10^7 YT cells were biotinylated either with 1 mM sulfo-NHS-LC-LC-biotin (amine-reactive) or with 1 mM alkoxyamine-PEG$_4$-biotin (glyco-reactive) after oxidation with 1 mM Na-metaperiodate. Cells were lysed in 4 % SDS and 95 % of the lysate were incubated with 15 µL streptavidin-coated beads for 60 min at RT. After washing, bound proteins were eluted by incubating (RT) and boiling (95 °C) the beads each for 15 min in 4 % SDS containing 10 mM biotin and 50 mM DTT. Equal volumes corresponding to 1 % of the total lysate were loaded on 4-12 % SDS polyacrylamide gels. Lysate input (In), non-bound-fraction (NB) and eluate-fraction (E) after streptavidin-enrichment. Untreated cells were used as controls. (**A**) Blotted biotinylated proteins were stained with Streptavidin DyLight800. (**B**) Coomassie-stained gel as loading control.

For both strategies incubation of the lysates with streptavidin-coated beads resulted in selective and quantitative capturing of labeled proteins. Low biotin signal intensities (< 10 % of inputs) in the eluates of both approaches showed inefficient elution of captured proteins. For further comparison, 25 % of the elution fractions of both labeling strategies as well as of the control were processed by in-gel digestion and 50 % of the resulting peptide mixtures were analyzed by LC-MS/MS on a LTQ Orbitrap XL mass spectrometer using a 120 min gradient (Fig. 19). Total ion chromatograms (TIC) of all three samples showed comparable but low signal intensities suggesting low amounts of peptide species. This observation was in line with the low numbers of identified proteins in all three samples filtered for identification with at least two total peptide spectra matched (PSM). Comparable numbers of identified plasma membrane annotated proteins according to UniProt were identified in the amine-directed and glycosylation-directed biotinylation samples. However, the amine-directed sample showed higher contamination with proteins of intracellular localization as indicated by absolute numbers and fractional abundances. In this sample, less than 40 % of the total protein abundance (ms1intensity-based estimation) was associated to cell surface proteins. Furthermore, less than 20 % of this fraction was related to proteins with annotated transmembrane domains suggesting inefficient enrichment of cell surface accessible proteins. A more selective enrichment of cell surface proteins was observed for the glycosylation-directed biotinylation experiment as nearly 60 % of the total protein abundance was associated to proteins of this subcellular localization. Furthermore, this fraction was composed to more than 50 % of transmembrane proteins resulting in the highest number of identified plasma membrane receptors and transporters as well as the best overall coverage and highest number of uniquely identified cell surface transmembrane proteins.
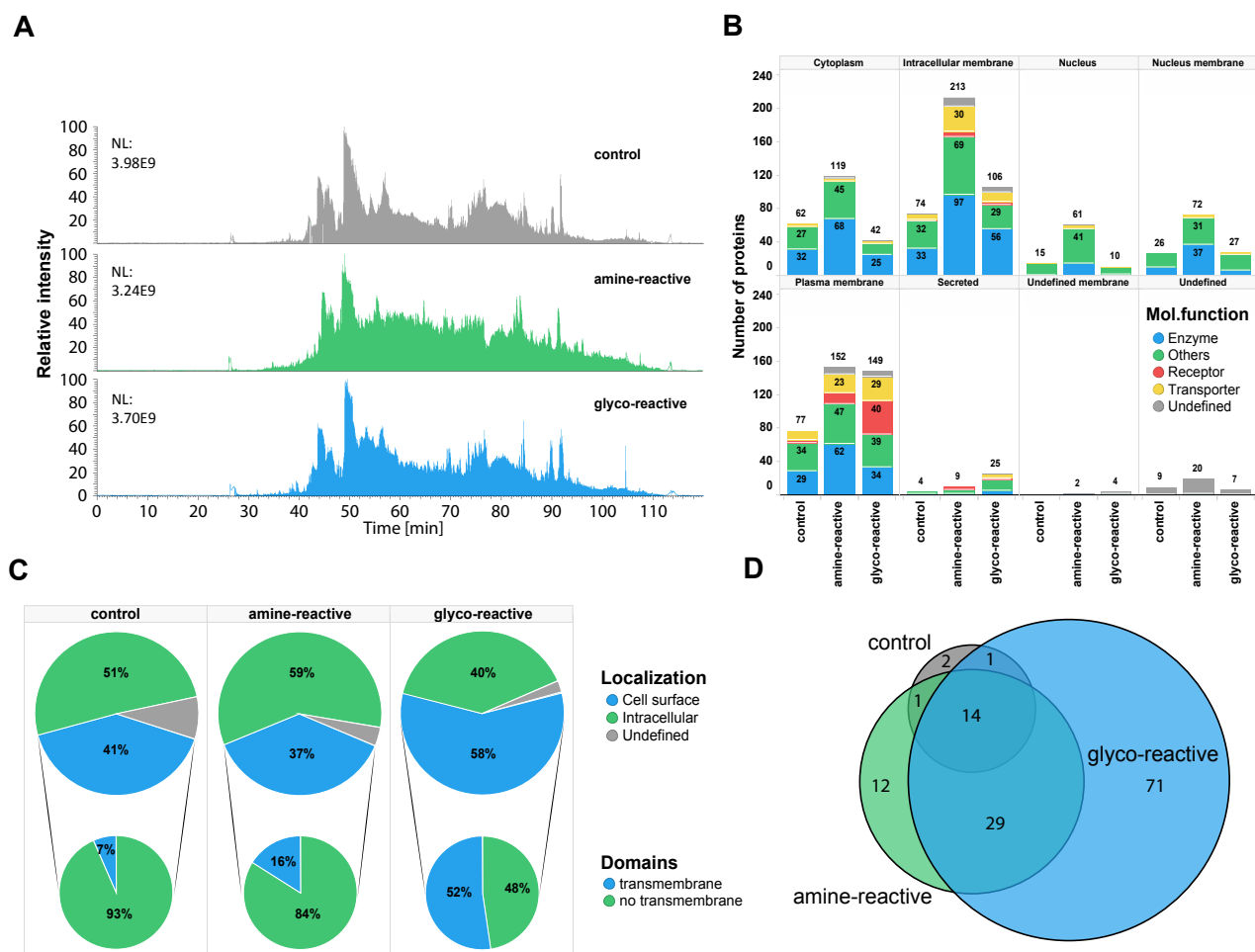
Fig. 19 Mass spectrometric analysis of enriched proteins after elution from streptavidin-coated beads by boiling. Lysates of 1×10^7 YT-cells biotinylated with sulfo-NHS-LC-LC-biotin (amine-reactive) or with alkoxyamine-PEG$_4$-biotin (glyco-reactive) were incubated for 60 min with 15 µL streptavidin-coated beads. Untreated cells were used as control. After washing, bound proteins were eluted by boiling the beads in 4 % SDS containing 10 mM biotin and 50 mM DTT. Subsequently, 25 % of the samples were subjected to in-gel digestion and 50 % of the resulting peptide mixtures were analyzed by LC-MS/MS on a LTQ Orbitrap XL mass spectrometer using a 120 min gradient. Identified proteins were filtered for PSM ≥ 2. (**A**) Total ion chromatogram (TIC) of biotinylated and control samples. (**B**) Number of identified proteins grouped by annotated subcellular localization and colored by annotated molecular function (UniProt) (**C**) MS1Intensity-based estimation of fractional abundances of identified proteins grouped by their annotated subcellular localization (large cake diagram). Fractional abundances of plasma membrane proteins grouped by number of annotated transmembrane domains are shown in the small cake diagram. (**D**) Overlap of identified plasma membrane associated proteins with annotated transmembrane domains (UniProt) in the respective samples.

However, the low TIC, the overall low numbers of identified proteins and the previous blotting results implied an inefficient elution of bound proteins from streptavidin-coated beads by boiling. A common alternative elution strategy in proteomic workflows utilizes protease cleavage on the affinity resin as also applied for elution of cell surface biotinylated proteins (Weekes et al., 2012). This on-bead digestion was evaluated for both cell surface biotinylation strategies by repeating the previous experiment with on-bead digestion using the protease trypsin. Subsequently, collected peptide mixtures were desalted and 30 % of the samples were analyzed by LC-MS/MS on a LTQ Orbitrap XL mass spectrometer using a 120 min gradient (Fig. 20). Untreated cells were used as control. Total ion chromatograms of both biotinylation samples showed comparable signal intensities and equal sample loadings. In turn, the control on-bead digestion sample showed a much less complex chromatogram. Glycosylation-directed biotinylation resulted in the highest number of identified plasma membrane proteins with about

50 % more cell surface proteins after on-bead digestion compared to elution by boiling (221 versus 149 plasma membrane proteins). Furthermore, the glycosylation-directed biotinylation sample was less contaminated with intracellularly localized proteins compared to the amine-directed strategy according to absolute numbers and fractional abundances. In this sample, more than 60 % of the total protein abundance was associated to cell surface proteins predominantly containing transmembrane domains. In summary, the glycosylation-directed biotinylation resulted in the highest number of identified plasma membrane receptors and transporters, the best overall coverage of cell surface annotated proteins as well as the highest number of uniquely identified cell surface transmembrane proteins. Based on this outcome, the glycosylation-directed biotinylation was selected for all further experiments.
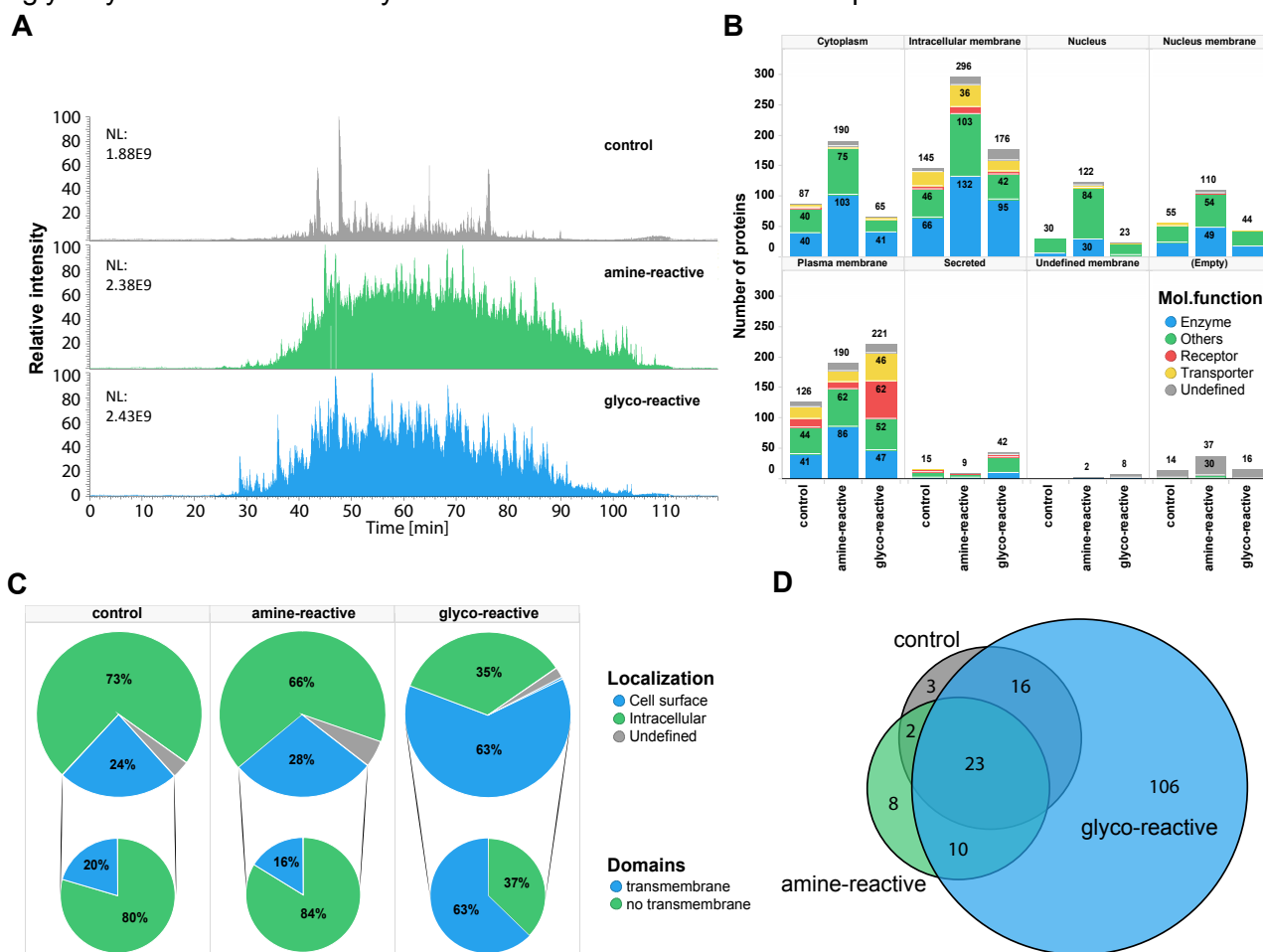
Fig. 20 Mass spectrometry analysis of enriched proteins after on-bead digestion from streptavidin-coated beads. Lysates of 1×10^7 YT-cells biotinylated with sulfo-NHS-LC-LC-biotin (amine-reactive) or with alkoxyamine-PEG$_4$-biotin (glyco-reactive) were incubated for 60 min with 15 µL streptavidin-coated beads. Untreated cells were used as control. After washing, bound proteins were eluted by on-bead digestion with 800 ng trypsin for 16 h. The samples were desalted and 30 % of the resulting peptide mixtures were analyzed by LC-MS/MS on a LTQ Orbitrap XL mass spectrometer using a 120 min gradient. Identified proteins were filtered for PSM $\geq$ 2. (**A**) Total ion chromatogram (TIC) of biotinylated and control samples. (**B**) Number of identified proteins grouped by annotated subcellular localization and colored by annotated molecular function (UniProt). (**C**) MS1Intensity-based estimation of fractional abundances of identified proteins grouped by their annotated subcellular localization (large cake diagram). Fractional abundances of plasma membrane proteins grouped by number of annotated transmembrane domains are shown in the small cake diagram. (**D**) Overlap of identified plasma membrane associated proteins with annotated transmembrane domains (UniProt) in the respective samples.

Previously published protocols for glycosylation-directed biotinylation and enrichment of cell surface proteins (Wollscheid et al., 2009) commonly utilize the endoglycosidase PNGase F for selective elution after streptavidin-based enrichment. This enzyme cleaves asparagine-linked (N-linked) oligosaccharides from glycoproteins liberating the biotinylated sugar chain and converting the asparagine into aspartic acid. Due to the intrinsic selectivity of PNGase F cleavage, this elution procedure was tested as an alternative for the on-bead digestion potentially increasing selectivity for cell surface proteins. Cells were labeled with alkoxyamine-PEG$_4$-biotin and biotinylated proteins were enriched with streptavidin-coated beads. After stringent washing, beads were incubated over 3 h at 37 °C with PNGase F at various enzyme activities and eluates were subjected to in-gel digestion. Subsequently, 30 % of the resulting peptide mixtures were analyzed by LC-MS/MS on a Q Exactive Hybrid-Quadrupole-Orbitrap mass spectrometer using a 270 min gradient (Fig. 21A and C). Elution of glycosylated proteins with 0.25, 0.5 and 1 U of PNGase F resulted in low total numbers of identified proteins and the enrichment of cell surface proteins was low according to fractional abundances. Due to these results, the experiment was repeated with higher units of PNGase F as well as trypsin on-bead digestion as positive control after PNGase F elution (Fig. 21B and D).
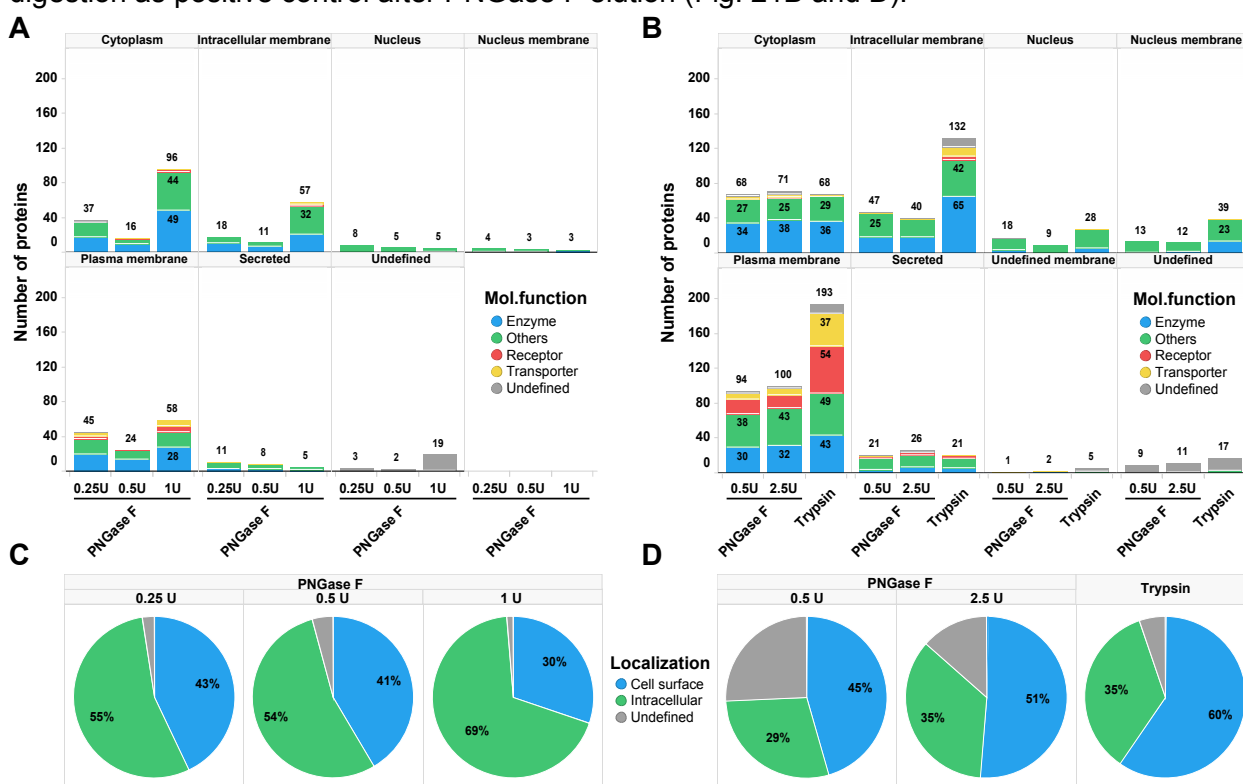
Fig. 21 Elution of biotinylated proteins from streptavidin-coated beads by deglycosylation with PNGase F. Lysates of 1x10^7 YT-cells biotinylated with 1 mM alkoxyamine-PEG$_4$-biotin were incubated for 60 min with 15 µL streptavidin-coated beads. After washing, bound proteins were eluted over 3 h at 37 °C by cleavage with PNGase F at indicated enzyme activities. A tryptic on-bead digestion after incubation with 0.5 U PNGase F was used as positive control. PNGase F eluates were subjected to in-gel digestion and 30 % of the resulting peptide mixtures were analyzed by LC-MS/MS on a Q Exactive Hybrid-Quadrupole-Orbitrap mass spectrometer using a 270 min gradient. The peptide mixture after on-bead digestion was desalted and 30 % of the resulting peptide mixture was analyzed with a 120 min gradient on a LTQ Orbitrap mass spectrometer. Identified proteins were filtered for PSM ≥ 2. (**A**) Number of identified proteins after elution with 0.25, 0.5 and 1 U of PNGase F grouped by annotated subcellular localization and colored by annotated molecular function (UniProt). (**B**) As in (A) but comparing samples after elution with 0.5 and 2.5 U of PNGase F as well as after tryptic on-bead digestion following elution with 0.5 U of PNGase F. (**C**) MS1Intensity-based estimation of fractional abundances of identified proteins in (A) grouped by their annotated subcellular localization. (**D**) As in (C) but using samples of (B).

Similarly, the elution with 2.5 U of PNGase F resulted in low numbers of identified proteins. Tryptic on-bead digestion as positive control after elution with PNGase F resulted in a comparable number and fractional abundance of identified cell surface proteins as compared to previous on-bead digestion experiments. These results confirmed the inefficient elution of enriched proteins by PNGase F. However, published protocols utilize PNGase F after enrichment of already in-solution digested biotinylated glycoproteins. Thus, in an additional experiment two cell lines (Ramos, THP-1) were cell surface labeled in two biological replicates and biotinylated proteins were enriched. Following tryptic on-bead digestion and stringent washing, remaining bound glycopeptides were eluted with 0.5 U of PNGase F. Subsequently, 30 % of the resulting peptide mixtures were analyzed by LC-MS/MS on a Q Exactive Hybrid-Quadrupole-Orbitrap mass spectrometer using a 270 min gradient (Fig. 22). These experiments resulted in high numbers of identified cell surface proteins. Fractional abundances between 86 % and 95 % for cell surface proteins suggested highly selective enrichments and elutions of proteins of this subcellular localization. However, as the majority of proteotypic peptides are removed by the preceding on-bead digestion, the performance of this approach had to be compared to tryptic on-bead digestion. This comparison was performed after further optimizations for the cell surface biotinylation approach were applied.
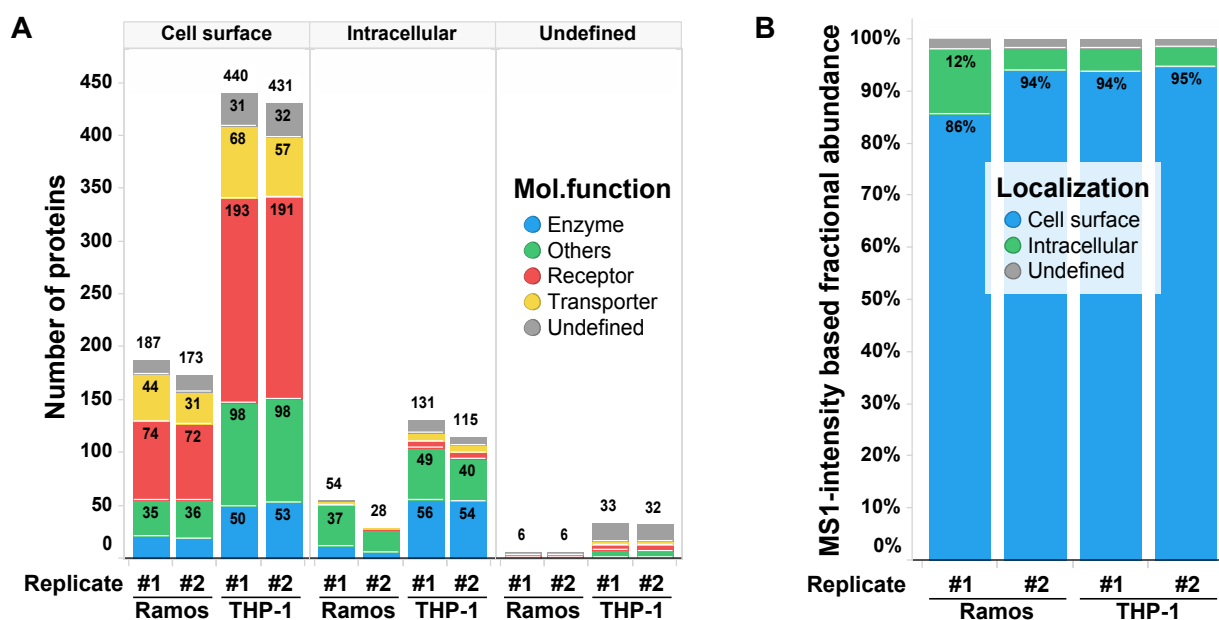
Fig. 22 Selective elution of biotinylated peptides by deglycosylation with PNGase F after on-bead digestion. Enriched biotinylated cell surface proteins of two biological replicates of Ramos and THP-1 cells were eluted first by on-bead digestion with trypsin followed by selective elution of still bound glycopeptides by deglycosylation with PNGase F. Samples were analyzed by LC-MS/MS on a Q Exactive Hybrid-Quadrupole-Orbitrap mass spectrometer using a 270 min gradient. Identified proteins were filtered for Mascot score ≥ 20. (**A**) Number of identified proteins grouped by annotated subcellular localization and colored by annotated molecular function (UniProt). (**B**) MS1-intensity-based estimation of fractional abundances of identified proteins grouped by their annotated subcellular localization.

Aniline is described as a catalyst for oxime ligations by accelerating reactions between periodate-induced aldehydes and alkoxyamine-containing biotinylation reagents and thereby enabling efficient and fast labeling of viable cells under physiological conditions (Zeng et al., 2009). Thus, aniline catalysis was evaluated as an additional optimization for cell surface proteome biotinylation (Fig. 23). For that purpose, cell surface proteins were labeled in presence of absence of aniline with two biotinylation reagent concentrations (0.1 mM and 1 mM) and enriched proteins were eluted from streptavidin-coated beads by tryptic on-bead digestion. In

both cases, labeling in the presence of 10 mM aniline resulted in an increase in the number of identified plasma membrane proteins by 15 to 20 %. Furthermore, biotinylation with 0.1 mM alkoxyamine-PEG$_4$-biotin in presence of aniline led to an increased fractional abundance for cell surface proteins compared to biotinylation without aniline. Therefore, aniline catalysis was used for all further cell surface biotinylation experiments.
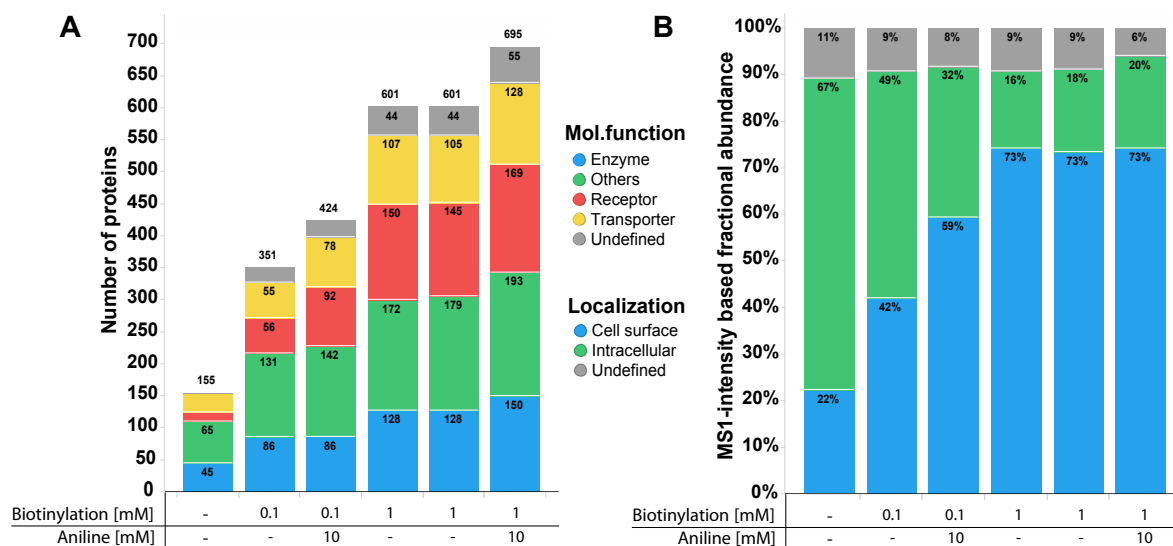
Fig. 23 Aniline catalysis of glycosylation-directed cell surface proteome mapping. K562 cells were labeled with 0.1 mM or 1 mM alkoxyamine-PEG$_4$-biotin in presence or absence of 10 mM aniline and biotinylated proteins were enriched with streptavidin-coated beads. Untreated cells were used as control. After washing, bound proteins were eluted by tryptic on-bead digestion and 30 % of the resulting peptide mixtures were analyzed by LC-MS/MS on a Q Exactive Hybrid-Quadrupole-Orbitrap mass spectrometer using a 270 min gradient. Identified proteins were filtered for PSM ≥ 2. (**A**) Number of identified plasma membrane associated proteins colored by annotated molecular function (UniProt). (**B**) MS1-intensity-based estimation of fractional abundances of identified proteins grouped by their annotated subcellular localization.

The cell surface proteome mapping approach was intended to be utilized for the comprehensive analysis of cell surface proteomes with low mass spectrometry resource consumption. This requires a robust method enabling good coverage of cell surface proteins and reproducible results. Thus, the cell surface proteome mapping method was tested for both aspects based on two suspension and two adherent cell lines each in four biological replicates (Fig. 24). Highly reproducible cell surface proteome maps were observed for all four cell lines as indicated by high coefficients of correlation between replicates for ms1intensity-based abundance estimations (Fig. 24A) and tight clustering of replicates for each cell line in a principal component analysis (Fig. 24B). Analysing the cumulative increase in identified cell surface proteins per number of replicates suggested that saturation is almost reached after two replicates (Fig. 24C). Whilst the second replicate on average added 9 % coverage, the third and fourth replicate only added 3 % and 2 %, respectively. Based on these results all further cell surface proteome mappings were performed in two biological replicates.
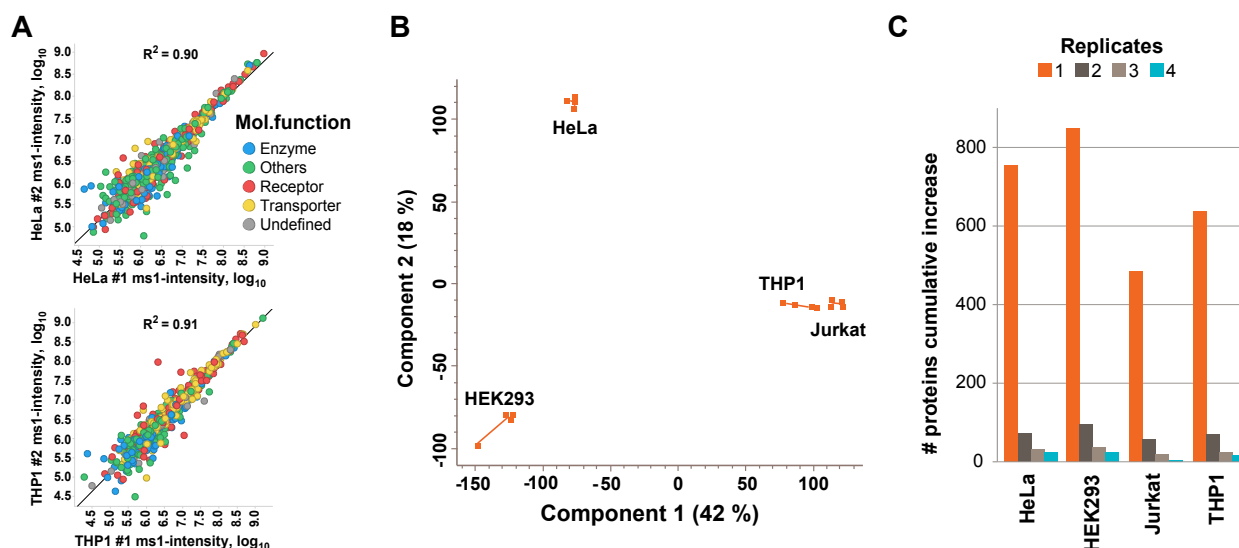
Fig. 24 Reproducibility and protein coverage of the cell surface proteome mapping. Cell surface proteome mappings of the adherent cell lines HeLa and HEK293 as well as of the suspension cell lines Jurkat and THP-1 in four biological replicates. Samples were analyzed by LC-MS/MS on a Q Exactive Hybrid-Quadrupole-Orbitrap mass spectrometer using a 270 min gradient. Identified proteins were filtered for PSM ≥ 2. (**A**) Scatter plot comparison of ms1-intensity based abundance estimations of identified cell surface proteins in two biological replicates of the cell surface proteome mappings on HeLa (top) and THP-1 (bottom) cells. Proteins colored according to annotated molecular function (UniProt). (**B**) Principal component analysis based on identified cell surface proteins and their estimated abundances. Replicates are linked by lines. (**C**) Cumulative increase in numbers of identified cell surface proteins per number of replicates.

Finally, tryptic on-bead digestion and PNGase F elution were compared based on cell surface proteome biotinylations of 11 cell lines and primary cells in two biological replicates. Isolation of primary cell types from human blood were evaluated by immunoblotting for cell type specific cell surface markers as well as by comparing ms1intensity-based abundance estimations of these markers in trypsin samples (supplemental Fig. 1). After streptavidin-based enrichment, biotinylated proteins were eluted by tryptic on-bead digestion followed by glycopeptide elution with PNGase F. Resulting peptide mixtures were analyzed by LC-MS/MS on a Q Exactive Hybrid-Quadrupole-Orbitrap mass spectrometer using a 270 min gradient (Fig. 25).

Fig. 25 Comparison of tryptic on-bead digestion and PNGase F based glycopeptide elution. Cell surface proteomes of cell lines and primary cells were biotinylated in two biological replicates and labeled proteins were enriched with streptavidin-coated beads. Bound proteins were eluted consecutively by tryptic on-bead digestion and by deglycosylation with PNGase F. Samples were analyzed by LC-MS/MS on a Q Exactive Hybrid-Quadrupole-Orbitrap mass spectrometer using a 270 min gradient. Identified proteins in tr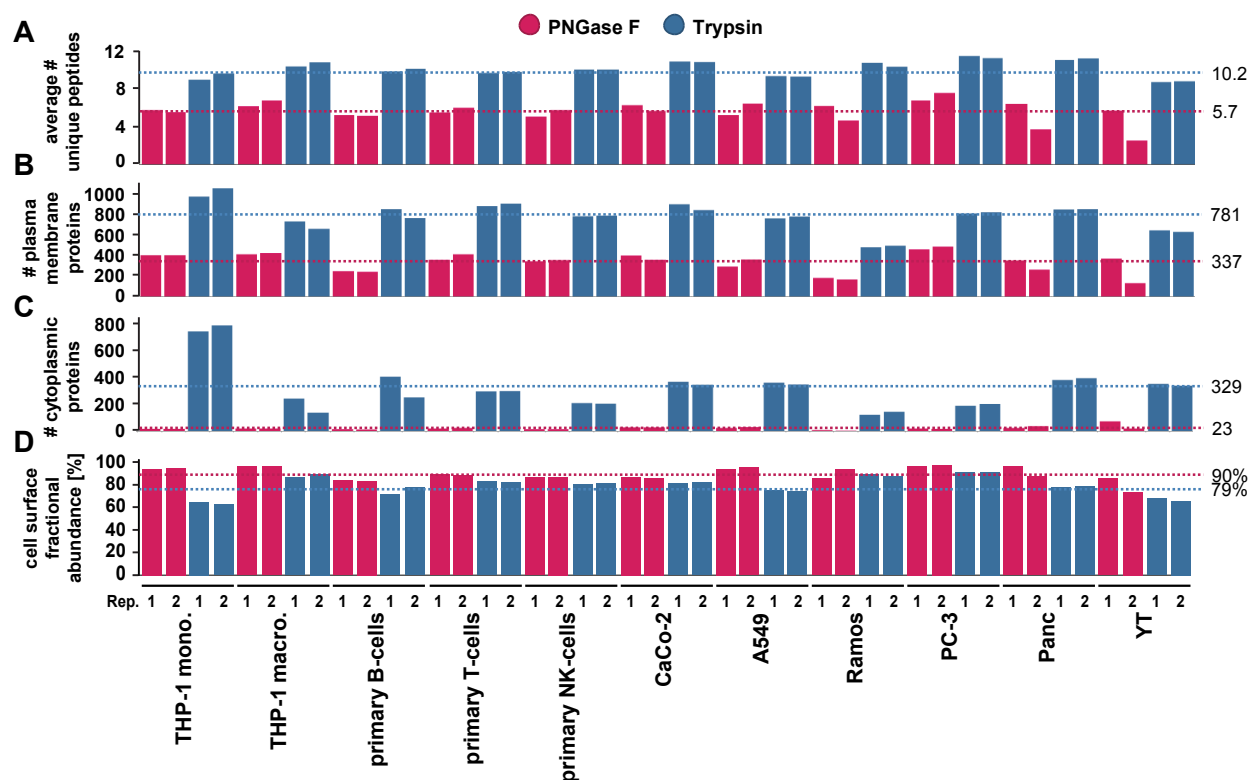ypsin samples were filtered for PSM ≥ 2. Identified proteins in PNGase F samples were filtered for Mascot score ≥ 20. Dashed lines indicate average numbers for trypsin and PNGase F samples. (**A**) Average numbers of identified unique peptides for plasma membrane associated proteins (UniProt). (**B**) Numbers of identified plasma membrane associated proteins. (**C**) Numbers of identified cytoplasmic proteins. (**D**) MS1-intensity-based estimation of fractional abundances of identified cell surface proteins.

Both approaches were compared based on selectivity, sensitivity and protein coverage. Proteins associated with the plasma membrane were the most abundant proteins for all tested cell lines and primary cells, indicating an efficient enrichment strategy for both approaches. In case of tryptic on-bead digestion, on average 79% of the total protein abundance was attributed to cell surface associated proteins, while in case of PNGase F samples, fractional abundances of proteins of this subcellular localization were on average 11% higher (Fig. 25D). In line with these results, more proteins with cytoplasmic annotation were identified in on-bead digestion samples compared to PNGase F samples (on average 329 vs. 23, Fig. 25C). However, tryptic on-bead digestion yielded more than twice as many plasma membrane proteins as the PNGase F strategy (on average 781 vs. 337, Fig. 25B) and protein identifications were based on nearly twice as many unique peptides (on average 10.2 vs. 5.7, Fig. 25A). Because of the substantially higher coverage achieved and the modest loss in specificity, the PNGase F digestion step was omitted in the following experiments and analyses were focused on the complete sets of tryptic peptides generated by on-bead proteolysis from individual samples.

With all optimizations, the cell surface proteome mapping approach was benchmarked against deep whole proteome analysis which enables comprehensive coverage of even low abundant proteins. However, the disadvantage of this method is its high mass spectrometry resource consumption. Here, the plasma membrane proteome coverage of the glycoproteome

enrichment strategy was compared to published full expression proteomics analyses for three cell lines (Jurkat, MCF7, HeLa, Geiger et al., 2012, Fig. 26).
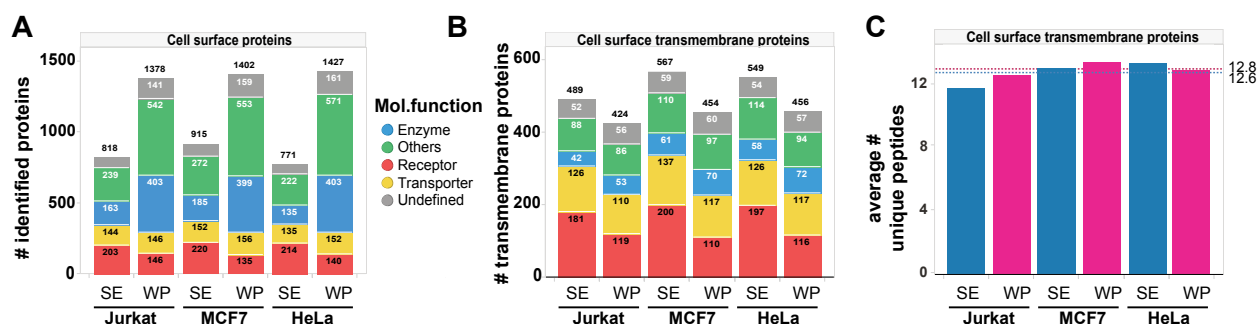

Fig. 26 Comparison of cell surface proteome mapping and whole proteome analysis. Cell surface proteome enrichments (SE) and published whole proteome analyses (WP, Geiger et al., 2012) of Jurkat, MCF7 and HeLa cells. Cell surface enrichment samples were analyzed with a single 270 min gradient. Whole proteome data was based on 3 replicates each fractionated into 6 fractions corresponding to 60 h total analysis time per cell line. Cell surface enrichment data was filtered for PSM ≥ 2. (**A**) Number of identified cell surface associated proteins (UniProt). (**B**) Number of identified cell surface associated proteins with annotated transmembrane domains (UniProt). (**C**) Average number of identified unique peptides for cell surface associated proteins with annotated transmembrane domains.

While cell surface enriched samples were analyzed in a single 4 h LC-MS/MS run, the published whole proteome data was based on 3 replicates each fractionated into 6 fractions corresponding to 60 h total analysis time per cell line. On average, whole proteome analyses yielded 7520 proteins of which 1402 were annotated to be plasma membrane associated compared to on average 835 plasma membrane associated proteins identified with the cell surface protein enrichment strategy (Fig. 26A). However, the majority of the plasma membrane associated proteins found in the expression proteomics analyses are not integral membrane proteins but include enzymes and other proteins that are localized at the cytosolic side of the plasma membrane. In contrast, for proteins with annotated transmembrane domains, the cell surface labeling strategy achieved on average a 20 % higher coverage (445 expression proteomics vs. 535 cell surface enrichment) including 40 % more plasma membrane receptors and transporters (230 expression proteomics vs. 322 cell surface enrichment, Fig. 26B). In summary, due to the significantly lower complexity of the cell surface enriched samples, a higher cell surface presented plasma membrane proteome coverage (with comparable sequence coverage according to average number of identified unique peptides per protein, Fig. 26C) was achieved with less than 10% of the MS analysis time compared to whole proteome analysis. Furthermore, whole proteome analysis does not allow for the distinction of cell surface presented from intracellularly stored fractions of a protein preventing e.g. the detection of ligand or compound induced internalization events of cell surface proteins.

4.2. Cell surface proteome mapping of cell lines and primary cells

To demonstrate the applicability of the cell surface labeling strategy for large scale studies and to generate a cell line-specific inventory of the plasma membrane proteome, 15 commonly used human cell lines and three primary cell types isolated from human blood were analyzed (Table 1). This selection included ten adherent epithelial cell lines from various tissue origins, four lymphoblastic suspension cell lines and one monocytic cell line (THP-1) that can be differentiated into macrophage- and osteoclast-like adherent cells (Schwende et al., 1996; Park et al., 2012). For comparison to primary cells, B-cells, T-cells and NK-cells were isolated from human blood and compared to the lymphoblastic cell lines Ramos, Jurkat and YT, respectively. Each cell line and primary cell type was analyzed in two biological replicates by LC-MS/MS on a Q Exactive Hybrid-Quadrupole-Orbitrap mass spectrometer using a 270 min gradient.

Cell line	Morphology	Tissue/Cells
A549	epithelial	Lung
HeLa	epithelial	Cervix
HepG2	epithelial	Liver
HEK293	epithelial	Kidney
Panc	epithelial	Pancreas
PC-3	epithelial	Prostate
MCF7	epithelial	Mammary breast gland
U87MG	epithelial	Brain
CaCo2	epithelial	Colon
Saos2	epithelial	Bone
Ramos	lymphoblastic	B-cells
K562	lymphoblastic	B-cells
YT	lymphoblastic	NK-cells
Jurkat	lymphoblastic	T-cells
THP1 mono.	monocytic	Monocyte
THP1 macro.	macrophage-like	Macrophage
THP1 osteo.	osteoclast-like	Osteoclast
THP1 PMA+Dasa	-	-
primary B	lymphoblastic	B-cells
primary T	lymphoblastic	T-cells
primary NK	lymphoblastic	NK-cells

Table 1 List of cell lines and primary cell types for cell surface proteome mapping
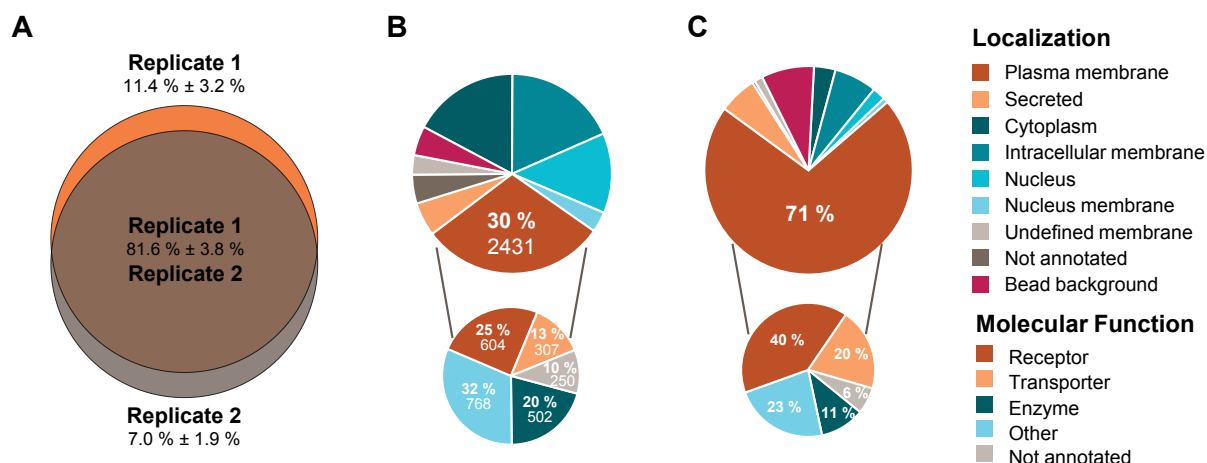
Fig. 27 Cell surface proteome mapping of primary cell types and standard laboratory human cell lines. Cell surface proteome mappings were conducted in two biological replicates for 15 standard laboratory human cell lines and 3 primary human cell types. Data was filtered for PSM ≥ 2. (**A**) Average overlap of identified proteins in two biological replicates of plasma membrane proteome mappings of cell lines and primary cell types (n=18, standard deviation in percentage). (**B**) Total number of identified proteins (large cake diagram) grouped by their annotated subcellular localization (UniProt) and annotated common bead background proteins (CRAPome). Plasma membrane proteins grouped by their annotated molecular function are shown in the small cake diagram. (**C**) As in (B), but based on estimated fractional abundance of identified proteins.

Cell surface proteome profiling experiments yielded on average 855 plasma membrane and secreted proteins with high reproducibility and high overlap in identified proteins between replicates (Fig. 27A). In the combined dataset a total of 2431 plasma membrane proteins were identified including 604 receptors, 307 transporters, 502 enzymes, 768 proteins with other molecular functions such as GTPase activation, developmental protein, cytokine or chaperone and 250 proteins with no annotated molecular function (Fig. 27B). In total, 192 out of 397 known SLC transporters and 29 out of 47 known ABC transporters were identified. Fractional abundance estimations revealed that on average 77 % of the total protein abundance per sample could be attributed to plasma membrane associated and secreted proteins and less than 10 % was derived from common bead background binding proteins, as annotated by the contaminant repository of affinity purifications (CRAPome, Mellacheruvu et al., 2013, Fig. 27C). The majority of the remaining 15 % were derived from proteins with intracellular membrane or unknown membrane localization. Potentially these proteins have a missing cell surface annotation. Finally, other non-membrane proteins could be co-enriched by association to cytosolic parts of cell surface transmembrane proteins.
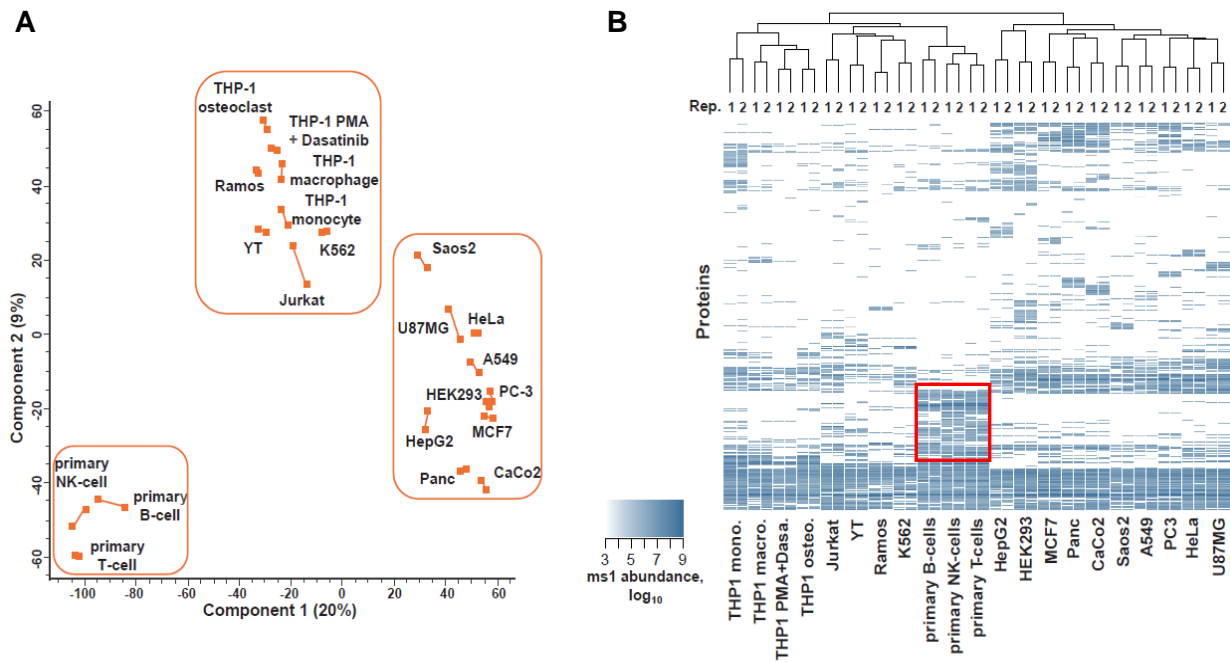
Fig. 28 Comparison of plasma membrane proteomes of cell lines and primary cells. Cell lines and primary cell types were compared based on identified cell surface proteomes and ms1-intensity based abundance estimations. (**A**) Principal component analysis of cell line and primary cell surface proteomes in two biological replicates. The first two principal components account for 29 % of the total variation. Axes are labeled with the percent total variance of the corresponding principal component. Biological replicates are connected by lines. Epithelial, lymphoblastic and primary cells are grouped in boxes. (**B**) Heat map representation of the cell surface proteomes based on protein abundances and average linkage clustering using a Euclidian distance matrix.

Principal component analysis based on the measured plasma membrane protein abundances clustered cell surface mapping replicates in close proximity along the first and the second principle component axes (Fig. 28A). On the first principal component, cell systems were grouped in three distinct clusters separating epithelial from lymphoid cell lines as well as primary cells from cell lines typically used as a model for these primary cells (e.g., Jurkat cells are a model for T-cells, Ramos cells are a model for B-cells, etc.). The second principal component further separates cells within each cluster, e.g. the osteoclast and macrophage-like cell lines derived from the monocytic cell line THP-1. Hierarchical clustering yielded similar grouping of cell lines (Fig. 28B). This clustering on protein level identified differential presentation of surface proteins. A distinct protein cluster (red box) was common to the tested primary cells and included chemokine receptors, clusters of differentiation, interleukin receptors, integrins and also a number of solute carrier proteins e.g. SLC18A2 (amine transporter), SLC2A5 (fructose transporter) and SLC2A9 (fructose and glucose transporter). GO-term s of biological processes for immune response, inflammatory response or platelet activation were enriched amongst the significantly higher expressed proteins (p-value < 0.05) in primary cells as compared to cell lines while GO-term s for transmembrane transport processes were enriched amongst the significantly higher expressed proteins in cell lines (supplemental Fig. 2). Differences between cell lines and primary cells were also observed when comparing protein abundances of selected protein families like ATP binding cassette-transporters (ABC), clusters of differentiation (CD), G-protein coupled receptors (GPCR), integrins and solute carrier (SLC) transporters (Fig. 29 and supplemental Fig. 3).
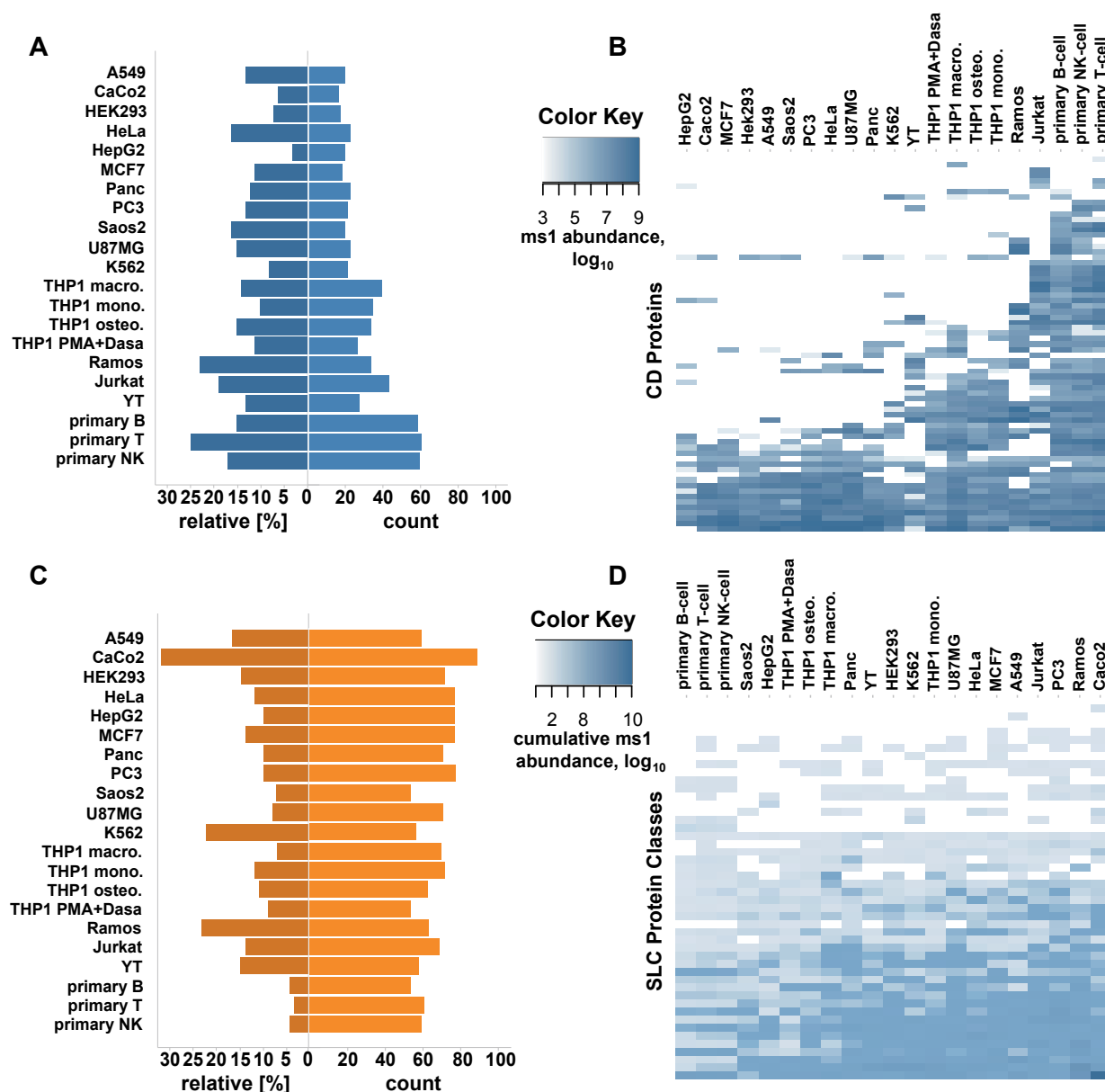
Fig. 29 Comparison of cell surface proteomes based on CD proteins and SLC transporters. Cell lines and primary cell types were compared based on identified cell surface protein groups and ms1-intensity based abundance estimations. (**A**) Relative abundance and absolute number of identified CD proteins. Relative abundance is defined as the sum of ms1 signal intensity of CD proteins divided by the ms1 signal intensity summed over all plasma membrane proteins. (**B**) Heat map representation based on CD protein abundances and average linkage clustering using a Euclidian distance matrix. (**C**) As in (A) but based on SLC transporters. (**D**) as in (B) but based on SLC transporter classes.

For primary cell types on average 59 CD proteins were detected compared to 34 in the corresponding cell lines but the cumulative relative abundance was similar among the different cells (Fig. 29A and B). In contrast, primary and immortalized cells on average showed similar numbers of expressed SLC proteins (58 vs. 64) but their cumulative relative abundance was much lower in primary cells compared to their cognate cell lines (4 % vs. 18 %, Fig. 29C and D). Exceptions are the facilitative GLUT transporters (SLC2, Mueckler and Thorens, 2013), the choline-like transporters (SLC44, Traiffort et al., 2013) and the SLC25 mitochondrial carrier family (Palmieri, 2013) which were present with similar abundances on all selected cell lines and primary cells. Other SLC transporter groups like the amino acid and nucleoside transporters SLC1, SLC7, SLC38 and SLC29 (Fotiadis et al., 2013; Kanai et al., 2013; Schiöth et al., 2013;

Young et al., 2013) were substantially more abundant in cell lines. Furthermore, primary cells showed more GPCRs (56 vs. 23) (supplemental Fig. 3) which is in line with previously published transcriptomic profiles (Groot-Kormelink et al., 2012) and a higher relative cumulative abundance of integrins (17 % vs. 9 %).

4.3. An interactive tool for visualization of the cell surface proteome compendium and associated annotations

Protein databases play a crucial role in biological data analysis. The most widely used protein database is UniProt (Xu, 2004). Its web-accessible portal offers a wide variety of protein information, including annotations of protein function, topology, domains and post-translational modifications. Other tools and databases like Phobius (Käll et al., 2004), STRING (Jensen et al., 2009), PhosphoSitePlus (Hornbeck et al., 2012) and iHOP (Hoffmann and Valencia, 2004) offer additional information about transmembrane topology, protein-protein interaction networks, post-translational modifications as well as phenotypes, pathologies and gene functions, respectively. In addition, databases like DrugBank (Wishart et al., 2008) and ChEMBL (Gaulton et al., 2012) provide valuable information about drugs, drug targets, binding affinities and selectivities of compounds. Incorporation of multiple databases for biological data analysis often supports data interpretation and deciphering biological rationales (Xu, 2004). However, gathering multiple database annotations on a proteome-wide scale can be tedious and difficult to integrate. For that purpose, an interactive tool was developed and programmed in C# which combines annotations from UniProt with information from Phobius, STRING, PhosphoSitePlus, ChEMBL, DrugBank and iHOP. This tool enables a well-structured visualization of annotated information as well as a two-dimensional illustration of protein topologies and domains inspired by the web-tool Protter (Omasits et al., 2014). Furthermore, visualization of the generated compendium of cell surface proteome maps facilitates easy selection of the most relevant *in vitro* cell systems which express cell surface proteins of interest. The main interface of the application showing annotated information for a protein of interest is illustrated in Fig. 30.
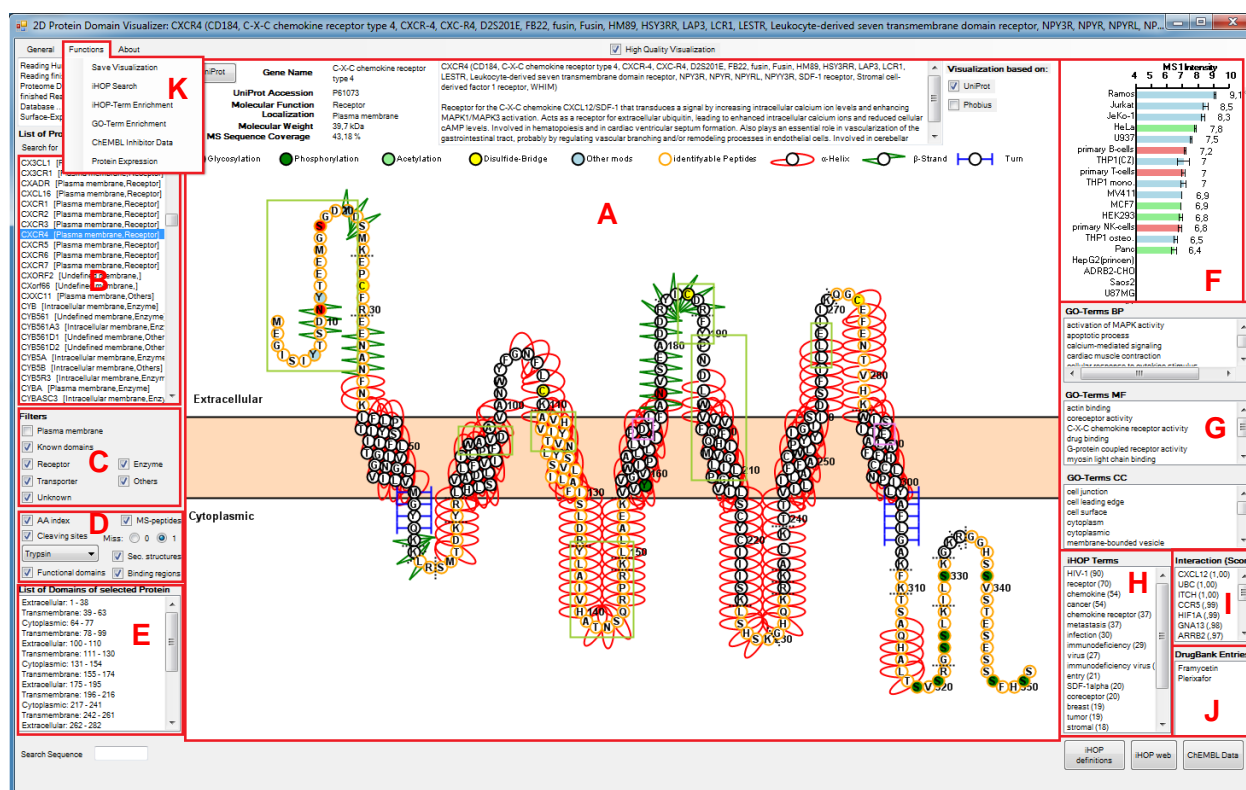
Fig. 30 Main interface of the database-integrating tool. The application is written in C# and uses data provided by several databases like UniProt. (**A**) Two dimensional illustration of amino acid sequence with protein topology (based on UniProt or Phobius) indicating e.g. extracellular, transmembrane and cytoplasmic domains as well as secondary structures like alpha helices, beta sheets and turns. Locations of common post-translational modifications like phosphorylations or glycosylations are highlighted. Annotated functional domains and binding regions are marked by green and pink boxes, respectively. MS compatible peptides are colored in orange. Protein name aliases and a functional description are shown in a textbox. (**B**) Interface for protein search and selection. (**C**) Filters for protein search. (**D**) Settings for visualizations like cleavage sites of common proteases (e.g. trypsin), MS compatible peptides, secondary structures and protein domains. (**E**) List of protein domains with amino acid indices which can be highlighted in the visualization. (**F**) Estimated ms1intensity-based protein abundances from the generated cell surface proteome mapping compendium. (**G**) UniProt annotated gene ontology terms. (**H**) Keywords occurring in iHOP terms for the selected protein ranked by frequency. (**I**) List of interaction partners with scores annotated by STRING. (**J**) List of DrugBank-annotated drugs for the selected protein. (**K**) Additional functionalities of the application like iHOP reverse search, browsing ChEMBL inhibitor data or visualization of cell surface protein expression.

The main interface enables searching for human proteins and filtering according to annotated subcellular localization or molecular function. Upon protein selection, the application visualizes the annotated topology of the protein in a two-dimensional graphical illustration. If topology annotation is incomplete, the application predicts missing topology information based on existing annotations. For example, if transmembrane domains are annotated in addition to at least one extramembrane domain, missing domains are alternately predicted on one side of the membrane as illustrated in supplemental Fig. 4. The tool furthermore allows visualization of annotated secondary structures. Alpha-helical structures are indicated by red "helices", beta-sheets are indicated as green "zigzags" and turns are indicated as blue "Ts". Annotated post-translational modifications like glycosylations, phosphorylations and disulfide-bridges are shown as red, green and yellow-colored amino acids. Clicking on the amino acids highlights additional available details about the respective post-translational modification like the biological effect of a phosphorylation or linkage of cysteins by disulfide-bridges. Annotated functional domains and binding regions can be highlighted as green and pink boxes, respectively.

Descriptions for these domains and regions are displayed when the mouse is hovered over them. An *in-silico* digestion with a selected protease can be performed to illustrate cleavage sites as well as resulting mass spectrometry-compatible peptides (orange-circled amino acids). Based on the compatible peptides, a theoretical sequence coverage is calculated. The tool also enables searching for specific amino acid sequences with regular expressions. An example is the search for the N-linked glycosylation motif N-X-S/T (X representing any amino acid). Entering "NXS" or "NXT" to the sequence search field highlights all possible N-linked glycosylation motifs in the selected protein sequence. MS1intensity-based expression level estimations of the protein observed in the compendium of cell surface proteome maps are visualized in a bar plot. Lymphoid cell lines are colored in blue, epithelial cell lines are colored in green and primary cell types are colored in red. Besides additional GO-term annotations and DrugBank-linked drugs, protein interaction partners are listed ranked by STRING-derived scores. The web-tool iHOP provides information about phenotypes, pathologies and functions of a protein of interest by summarizing sentences which are originating from scientific literature in PubMed. This enables an initial and quick overview about the biological relevance of a protein. The summarized iHOP sentences for the selected protein can be accessed within the application in a new window. The application further condenses this information by listing recurrently occurring terms in the iHOP sentences ranked by frequency. These "iHOP terms" are displayed in the main interface. In case of the example protein CXCR4, the terms HIV-1, chemokine receptor, cancer and metastasis are most frequently occurring terms in PubMed literature about this protein. In addition to the original use of the iHOP information for an overview about a single protein, the developed application also enables a reversed search which can be accessed in a subwindow (Fig. 31). This reversed search allows identification of proteins for which iHOP entries are recurrently containing a term of interest. This enables identification of potential proteins of interest e.g. involved in a biological question.
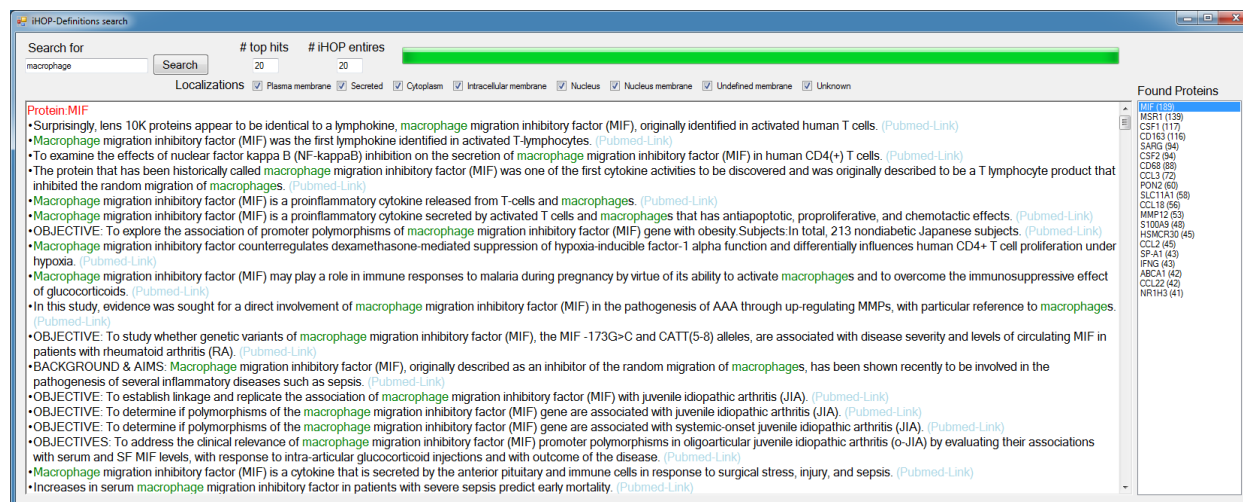
Fig. 31 iHOP reverse-search interface. This subwindow interface allows a reversed iHOP search to identify proteins for which iHOP entries frequently contain a searched term. The tool enables quick identification of proteins filtered by subcellular localization, which are frequently described with a relation to a searched term.

In this example, the iHOP reverse search function of the application was used to identify proteins which are recurrently occurring in the literature with a link to the search term "macrophage". Proteins are sorted by occurrence of the search term in their iHOP sentences and can be filtered for subcellular localization. Proteins and the respective iHOP entries containing the search term with weblinks to the original publication are listed. The top3 results of

the example search were the macrophage migration inhibitory factor (MIF), the macrophage scavenger receptor (MSR1) and the macrophage colony-stimulating factor 1 (CSF1).

The ChEMBL database provides information about drug targets, binding affinities and selectivities of compounds. The application enables the search for inhibitors of a protein of interest. Results can be sorted by half maximal inhibitory concentrations (IC_{50}). To estimate the selectivity of compounds, a reversed search lists all additional proteins inhibited by the compounds. Results can be filtered for an IC_{50} cutoff and protein subcellular localization (Fig. 32).

Fig. 32 ChEMBL inhibitor interface. This subwindow interface allows quick identification of described inhibitors for a specific protein or determination of described protein targets for a selected drug. Results can be filtered for drug potencies based on IC_{50} values and for proteins according to their annotated subcellular localization.

In the example, ChEMBL entries were searched for the multidrug-resistance transporter ABCB1. Among the many inhibitors, the four commercially available inhibitors verapamil, elacridar, vinblastine and zosuquidar were selected for a reversed search. Results were filtered for an IC_{50} lower than 1 µM. Results are displayed in a table or can be visualized as a heatmap.

The cell surface proteome mapping compendium provides guidance for selection of cell systems expressing a protein of interest. The data of the compendium is visualized in an additional subwindow in the application (Fig. 33). Proteins of interest can be selected and their ms1intensity-based expression level estimations are displayed in a heatmap. Hierarchical clustering of the heatmap enables quick identification of commonalities, and furthermore cell systems can be selected for improved clarity.
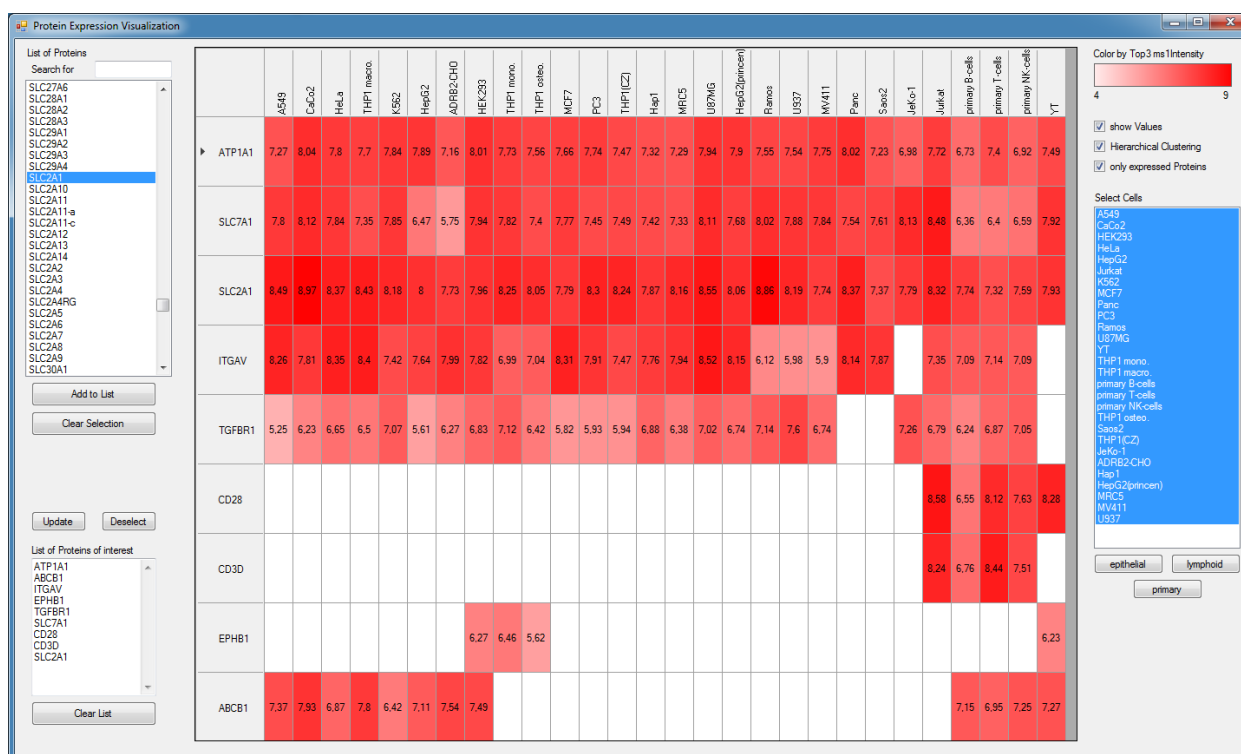
Fig. 33 Visualization of the cell surface proteome mapping compendium. This subwindow allows comparison of protein expression levels determined in cell surface proteome mappings. The tool can be used to identify suitable cell systems which are expressing proteins of interest. Average ms1intensity-based abundance estimations for respective proteins are colored from white (low expression) to red (high expression). Proteins and cell systems can be clustered based on the observed protein expression.

In summary, the developed application combines information from multiple databases and web-accessible tools with the compendium of cell surface proteome maps generated in this thesis. This integration of annotated protein information can assist the design of experimental setups and can support biological data interpretation as well as deciphering biological rationales.

4.4. Monitoring the cell surface proteome of differentiating monocytes

Human biology is determined by dynamic processes, in which environmental changes or external stimuli induce cellular adaptation or differentiation. To monitor dynamic processes occurring at the cell surface during such transitions, a tandem mass tag (TMT)-based cell surface proteomics strategy was devised which enabled multiplexed measurements of up to ten samples without missing values (Werner et al., 2012). This strategy was applied for the time-resolved analysis of dynamic processes of the cell surface proteome of THP-1 cells during phorbol-12-myristate-13-acetate (PMA) induced differentiation from monocytic into macrophage-like cells. Morphological changes during the differentiation time course were monitored by light microscopy (Fig. 34). Monocytic suspension THP-1 cells showed cellular adhesion to the tissue culture plate already after four hours and cells were completely adherent after eight hours. Cellular morphology showed transition from small, globular monocytic suspension cells to large, flat and tightly adherent macrophage-like cells.
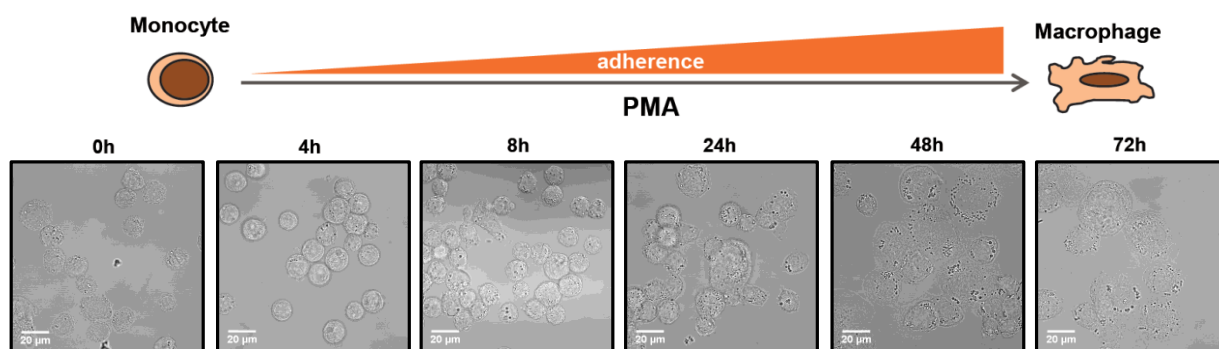
Fig. 34 Morphological changes during PMA-stimulated monocyte to macrophage differentiation.
Morphological changes of suspension monocytic THP-1 cells to adherent macrophage-like cells during differentiation in presence of 100 nM PMA monitored by light microscopy (Zeis LSM 780, 65x oil).

For monitoring cell surface proteome changes during this differentiation process, two experimental designs were combined to achieve high precision for short as well as late time points: In the first experiment block (denoted as experimental group 1) the differentiation process was split into two separate experiments, one covering the short incubation times (0, 4 and 8 h, each in biological triplicates, TMT9) and the second experiment covering the long incubation times (0, 24, 48 and 72 h, each in biological duplicates, TMT8). Differentiation was validated by immunoblot analysis for known markers of monocyte to macrophage differentiation such as CD11b (Schwende et al., 1996; Sintiprungrat et al., 2010) and CD4 (Auwerx et al., 1992) (Fig. 35A). After cell surface proteome enrichment and isobaric mass tagging, the resulting pooled peptide mixtures of both experiment blocks were separated each into nine fractions using reversed-phase chromatography at pH 12 as previously described (Kruse et al., 2011). Fractions were analyzed by LC-MS/MS on a Q Exactive Hybrid-Quadrupole-Orbitrap mass spectrometer using a 120 min gradient. For statistical data analysis, p-values were calculated using a modified t-test (Smyth, 2004) and Benjamini-Hochberg corrected. A combined fold-change and p-value cut-off was applied to determine significant outliers: $\log_2$ relative abundances ≥ 2 or ≤ -2 at least once between 24 h and 72 h of the time course and p-values < 0.01. For further confirmation of results, the differentiation was repeated in two additional experiments (denoted as experimental group 2 and experimental group 3) covering all six time points in single TMT experiments.
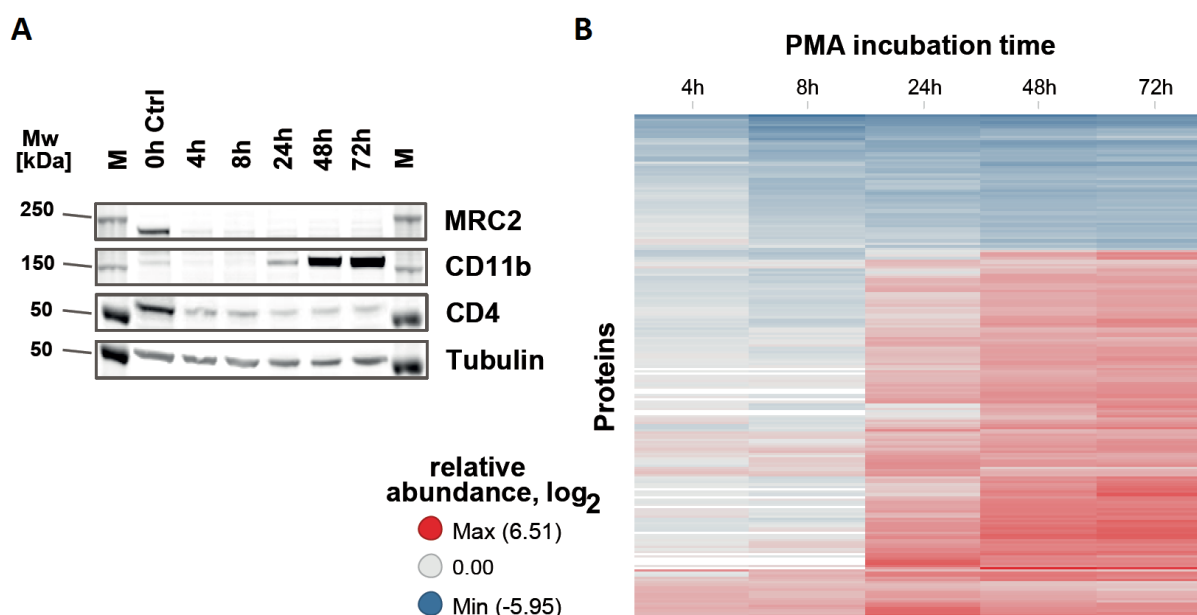
Fig. 35 Time-dependent monitoring of the cell surface proteome during monocyte to macrophage differentiation. For each time point cells were differentiated in at least three biological replicates which were analyzed by MS in three experimental groups after labeling with TMT reagents. A p-value < 0.01 and an abundance change ≥ 4-fold in at least one of the three late time points (24, 48 or 72 h) was defined as significance cutoff. (**A**) Immunoblot of regulated cell surface markers during differentiation of monocytic THP-1 cells to macrophage-like cells by PMA. (**B**) Heat map of relative abundances for significantly regulated plasma membrane proteins during differentiation.

Immunoblot analysis for CD11b composed of ITGAM and ITGB2 showed marked increase in abundance after 24 h of PMA-induced differentiation while CD4 down-regulation was observed already after four hours of differentiation. Significant regulation of both markers was also detected by the cell surface proteomic approach (Fig. 36). Furthermore, among others MRC2 was identified as a new marker of monocyte to macrophage differentiation by the cell surface proteomic approach. This protein showed significant down-regulation also validated by immunoblot read out. Overall, significant changes between undifferentiated and differentiated THP-1 cells were detected for 20 % of the cell surface proteome (230 out of 1106 quantified plasma membrane and secreted proteins, Fig. 35B and Fig. 36).
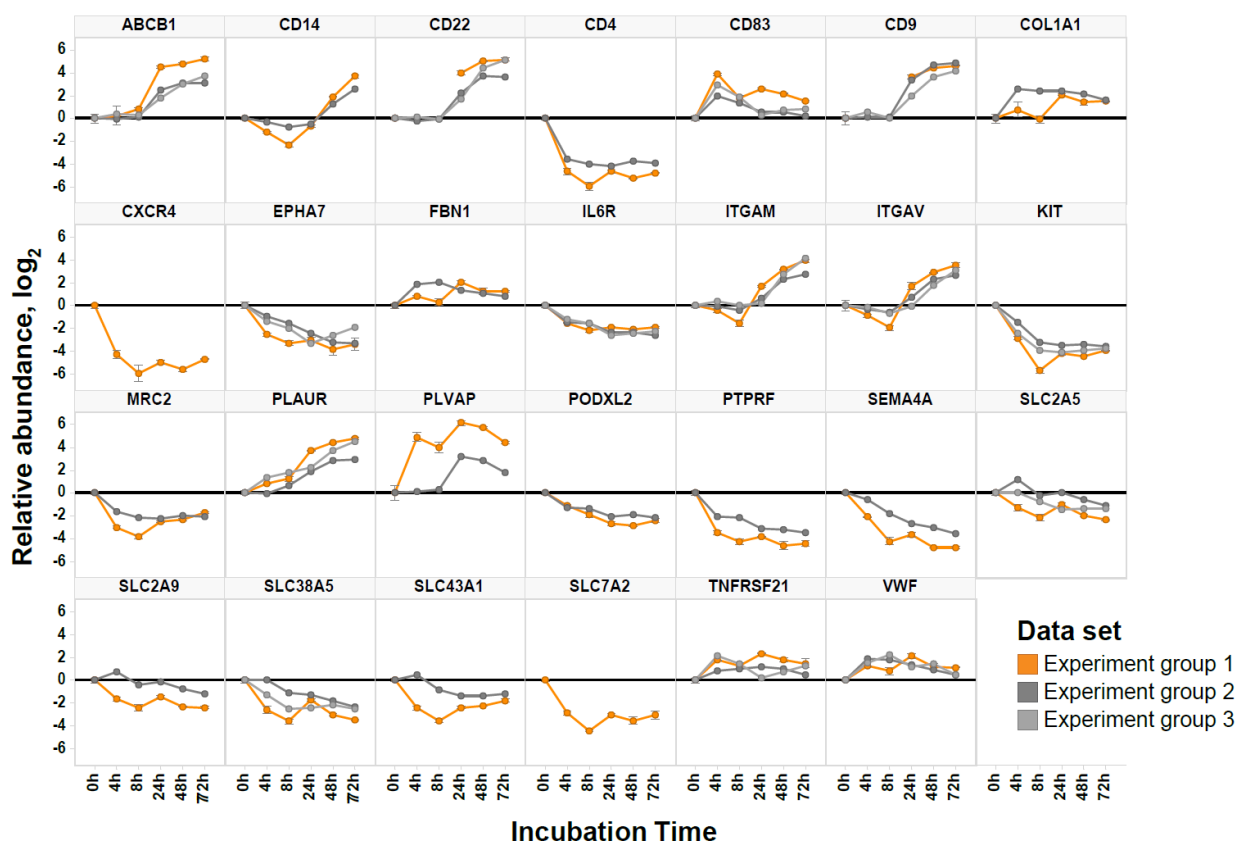
Fig. 36 Changes in the THP-1 cell surface proteome during differentiation with PMA. Examples for significantly regulated proteins during PMA-induced differentiation of monocytic THP-1 cells to macrophage-like cells in a time course of 72 h. Log$_2$ transformed abundance changes relative to 0 h are shown for three independent experiments.

Changes in the cell surface proteome correlated with functional differences between monocytes and macrophages: Macrophages invade into tissue, and in line with this function e.g. down-regulation of PODXL2 (-8-fold) was observed which is necessary for leukocyte rolling over vascular surfaces (Kerr et al., 2008) as well as up-regulation of cell adhesion proteins like CD9 (+24-fold), CD22 (+32-fold) and ITGAV (+12-fold) (Cook et al., 2002; Sgroi and Stamenkovic, 1994; Sims et al., 2000). After differentiation, the macrophage-like THP-1 cells are non-dividing. Consequently, proteins involved in the control of cell growth and cell differentiation like PTPRF, SEMA4A and EPHA7 are significantly down-regulated. Altered display of cell surface transporters included down-regulated sugar (SLC2A5, SLC2A9) and amino acid transporters (SLC38A5, SLC43A1, SLC7A2) probably reflecting the lower nutrient demand of differentiated and resting cells. The multidrug-resistance transporter ABCB1 was also strongly up-regulated (+37-fold up) enabling ATP-hydrolysis driven efflux of small molecules. Furthermore, functional dependencies between proteins could also be observed: for example, the urokinase plasminogen activator surface receptor PLAUR was found 28-fold up-regulated whereas its negative regulator, the c-type mannose receptor MRC2 which controls the extracellular level of PLAUR (Messaritou et al., 2009) was 5-fold reduced during differentiation.

Based on all regulated cell surface proteins, the entire differentiation process could be clustered into three time-dependent major phases: rapid presentation/ secretion, concurrent internalization and delayed presentation of new cell surface proteins (Fig. 37).
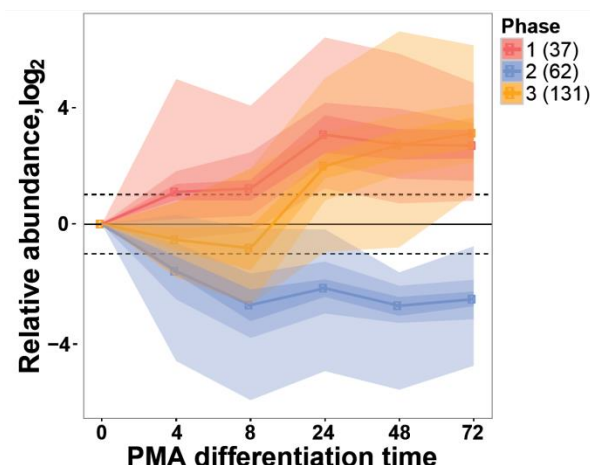
Fig. 37 PMA-induced differentiation of THP-1 cells grouped into three time-dependent major phases. Abundance changes of significantly regulated plasma membrane proteins during THP-1 differentiation grouped into three phases. Color shadings indicate data density. The numbers of proteins in each cluster are indicated.

In the first phase, immediately after stimulation with PMA, cells start to secrete ECM proteins including collagens COL1A1 and COL1A2, von Willebrand factor and Fibrillin-1 thus priming the cells for settling and cell adhesion (Fig. 36). A rapid and substantial increase was also observed for the transmembrane proteins CD83, PLVAP and tumor necrosis factor receptor superfamily member 21, which is involved in B-cell activation and vascular permeability (Fig. 36). The second phase comprises internalization of a large set of proteins including nutrient transporters and proteins involved in regulation of cell differentiation like PTPRF, IL6R and KIT reflecting the transition from dividing to non-dividing cells (Fig. 36). Finally, the *de novo* synthesis of cell surface proteins leads to the presentation of a new subset of the plasma membrane proteome beginning 24 h after the onset of differentiation (Fig. 35B and Fig. 37). These proteins like ITGAM and MSR1 fulfill macrophage-specific functions such as cell adhesion and phagocytosis. GO-term and INTERPRO domain enrichment analyses were in line with the differentiation induced cellular transition (Fig. 38).
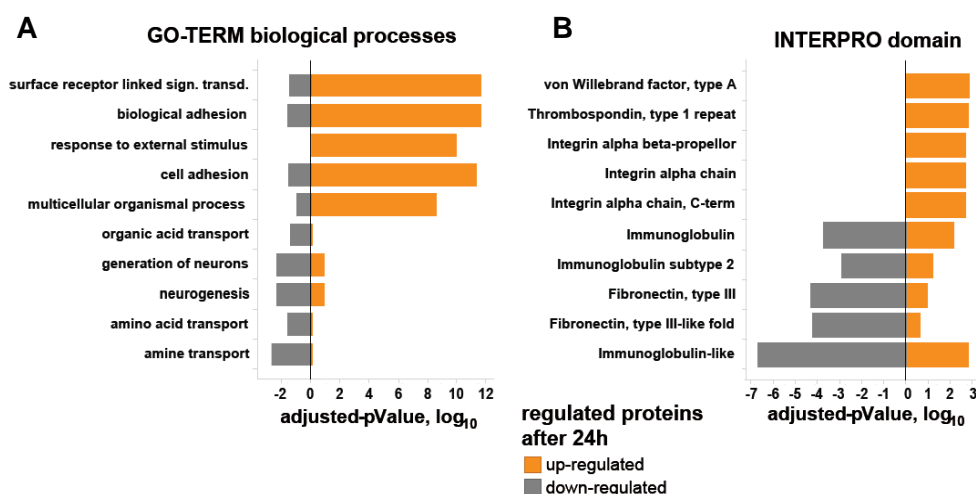
Fig. 38 GO-term and INTERPRO-domain enrichment analysis based on regulated proteins during differentiation. (**A**) GO-term enrichment analysis of up- and down-regulated proteins after 72 h. Bars indicate logarithmic Benjamini-Hochberg corrected p-values of top5 results. (**B**) INTERPRO domain enrichment analysis of up- and down-regulated proteins after 72 h. Bars indicate logarithmic Benjamini-Hochberg corrected p-values of top5 results.

For up-regulated proteins, cell surface receptor linked signal transduction, biological adhesion and response to external stimulus were identified as most significant processes while down-regulated proteins are involved in amine transport or amino acid transport (Fig. 38A). Protein domain enrichment analysis suggested up-regulation of mainly integrin-domain containing proteins while proteins with immunoglobulin-like or fibronectin domains were down-regulated (Fig. 38B).

To analyze PMA-induced differentiation in more detail, the regulation of cell surface proteins was also monitored on phosphopeptide level. For this purpose, an additional TMT-based cell surface proteomics strategy was devised which combines cell surface proteome enrichment with immobilized metal ion affinity chromatography (IMAC)-based phosphopeptide enrichment. THP-1 cells were differentiated with PMA for 0, 15, 30 and 60 min followed by cell surface proteome enrichment and isobaric mass tagging. After pooling, a small fraction of the sample was used to monitor cell surface proteome abundance changes within the selected differentiation time window. The remaining sample was subjected to phosphopeptide enrichment and the resulting peptide mixture was analyzed by LC-MS/MS on a Q Exactive Hybrid-Quadrupole-Orbitrap mass spectrometer using a 270 min gradient. Data was filtered for cell surface proteins with qusm ≥ 2 and peptide identifications with Mascot score ≥ 15. Phosphopeptides with an abundance change ≥ 2-fold in at least one time point with a p-value < 0.05 were regarded as significantly regulated (Fig. 39).
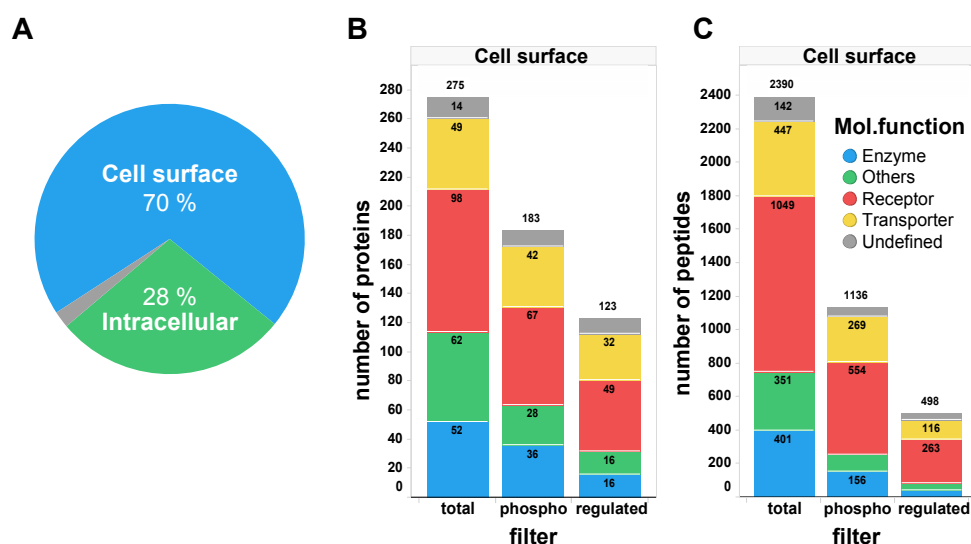
Fig. 39 Monitoring cell surface proteome phosphorylation changes by cell surface phosphoproteomics. THP-1 cells were differentiated by PMA for 0, 15, 30 and 60 min in two biological replicates. Cell surface proteins were enriched and resulting peptide mixtures were pooled after TMT labeling. Of this sample, 90 % were further subjected to phosphopeptide enrichment by IMAC followed by MS analysis while the remaining 10 % were directly analyzed. Samples were analyzed by LC-MS/MS on a Q Exactive Hybrid-Quadrupole-Orbitrap mass spectrometer using a 270 min gradient. Three data filters were used: total (protein qusm ≥ 2, peptide Mascot score ≥ 15 and cell surface localization), phospho (the total filter and in addition filtering for the peptide modification phosphorylation) and regulated (the phospho filter and in addition abundance change ≥ 2-fold in at least one time point with a p-value < 0.05). (**A**) MS1intensity based fractional abundance of identified proteins grouped by their annotated subcellular localization (UniProt). Proteins without annotated localization are colored in grey. (**B**) Number of all quantified cell surface proteins (total), cell surface proteins identified with phospho peptides (phospho) and cell surface proteins with significantly regulated phosphorylations (regulated). (**C**) As in (B) but showing numbers of peptides.

Cell surface proteins had high fractional abundances indicating efficient enrichment (Fig. 39A). In total, 275 good quantified cell surface proteins with 2390 good quantified peptides were identified of which 183 proteins and 1136 peptides were identified with phosphorylations representing a phosphopeptide enrichment efficiency of about 50 % (Fig. 39B and C). Of these peptides, 498 were detected to be significantly regulated within 60 min of PMA-induced differentiation. A selection of proteins with significantly regulated phosphorylation sites but with unaffected total protein abundance is shown in Fig. 40. All proteins with significantly regulated phosphopeptides are shown in supplemental Fig. 5.

Fig. 40 Regulated phosphorylation sites of selected cell surface proteins. Effects of PMA-induced differentiation on the cell surface phosphoproteome of THP-1 cells were monitored by combining enrichment of cell surface proteins with IMAC. Samples were analyzed by LC-MS/MS on a Q Exactive Hybrid-Quadrupole-Orbitrap mass spectrometer using a 270 min gradient and data was filtered for cell surface proteins with protein qusm ≥ 2, peptide Mascot score ≥ 15, phosphorylation as peptide modification and peptide abundance change ≥ 2-fold in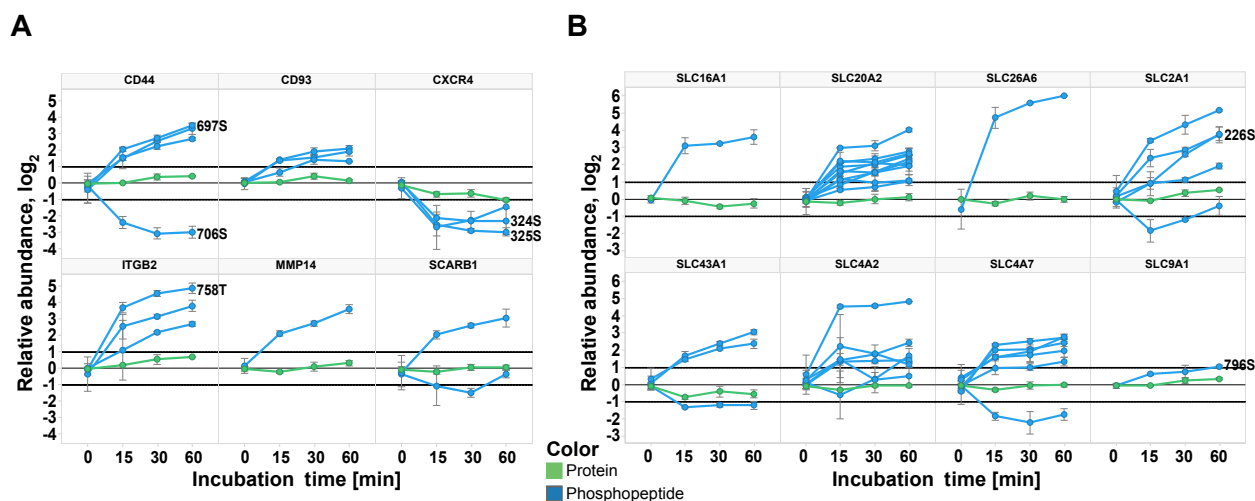 at least one time point with a p-value < 0.05. Amino acid index of selected phosphorylation sites are indicated with numbers. (**A**) Time courses of selected cell surface proteins. The overall protein abundances are indicated as green lines. Phosphopeptide abundances are indicated as blue lines. Data points indicate means of two replicates. Error bars indicate standard deviations. (**B**) As in (A) but showing selected time courses of regulated SLC transporters.

Cell surface phosphoproteomics enabled monitoring of early regulations of cell surface proteins during PMA-induced differentiation. For example, phosphorylation at 324S and 325S of CXCR4, known to be involved in the regulation of the activity, internalization and degradation of this protein (Bhandari et al., 2009), was found to be significantly down-regulated. Interestingly, this protein was detected to be significantly internalized already at the four hours' time point of the previous 72 h cell surface proteome mapping time course (Fig. 36). Other examples of regulated proteins are SCARB1, CD93 and MMP14 which are involved in macrophage functions like phagocytosis. Furthermore, the cell adhesion proteins ITGB2 and CD44 both showed significant regulation of phosphorylation sites known to be involved in cellular motility (ITGB2: 758T (Takala et al., 2008) and CD44: 697S, 706S (Tzircotis et al., 2006; Desai et al., 2009)). Overall, GO-term enrichment analysis for significantly regulated proteins revealed biological adhesion, cell migration and cell motility as the most significantly enriched biological processes (Fig. 41). These results were in line with the previous observation that one of the first steps of PMA-induced differentiation is priming the cells for settling and cell adhesion. Besides phosphorylation changes of cell surface receptors also significant regulation of cell surface transporters was observed. For example the glucose transporter SLC2A1 showed down-regulation of several phosphorylation sites comprising 226S known to induce transporter activity (Lee et al., 2015). Other examples are the amino acid transporters SLC43A1, SLC1A5 and SLC38A1, the phosphate transporter SLC20A2 as well as the intracellular pH regulating transporters SLC16A1, SLC26A6, SLC4A2, SLC4A7 and SLC9A1. These results suggested an increased nutrient demand and cellular metabolism early during the differentiation process probably correlating with the *de novo* synthesis of macrophage cell surface markers. As several of these transporters were found to be down-regulated in the course of the 72 h differentiation, this enhanced metabolism might be only necessary during the early events of the process.
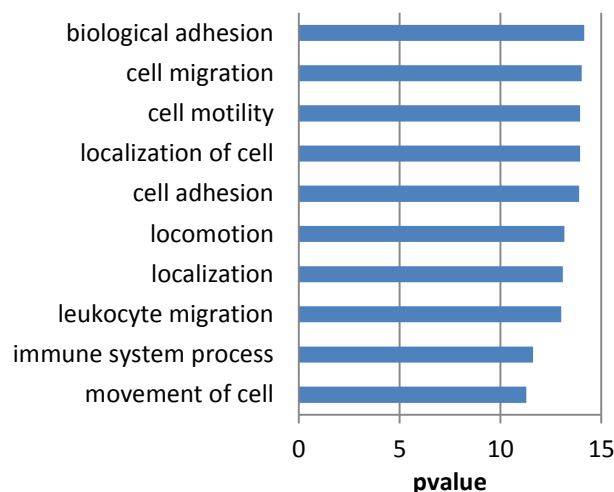
Fig. 41 GO-term enrichment analysis for biological processes of regulated cell surface proteins. GO-term enrichment analysis for biological processes based on proteins with significantly regulated phosphorylation sites. Bars indicate logarithmic p-values of top10 results.

4.5. Influence of kinase inhibitors on the cell surface proteome of differentiating monocytes

Phorbol esters have been shown to mimic endogenous signaling cascades and activate protein kinase C (PKC) (Farrar and Anderson, 1985; Tahara et al., 2009). Monitoring cell surface proteome changes during PMA-induced monocyte to macrophage differentiation resulted in significant regulation of 14 out of 68 quantified plasma membrane associated kinases including KIT and ephrin receptors EPHA3, EPHA7 and EPHB1 (supplemental Fig. 6) suggesting rewiring of signaling networks. Thus, perturbation of signaling processes specific to the monocyte to macrophage differentiation was tested with small molecule kinase inhibitors. Treatment of THP-1 cells with the BCR-Abl inhibitor imatinib (Capdeville et al., 2002), the broad-specificity inhibitor sunitinib (Sun et al., 2003) and the Abl and Src family kinase inhibitor dasatinib (Kantarjian et al., 2006) did not affect the morphology, viability and proliferation of undifferentiated THP-1 cells within 48 h (Fig. 42). However, dasatinib but none of the other two inhibitors induced severe morphological changes when present for 48 h during PMA-induced differentiation leading to cells being more dendritic, less flat and less adherent. In contrast, when dasatinib was applied to already differentiated cells, it had no influence on the morphology.
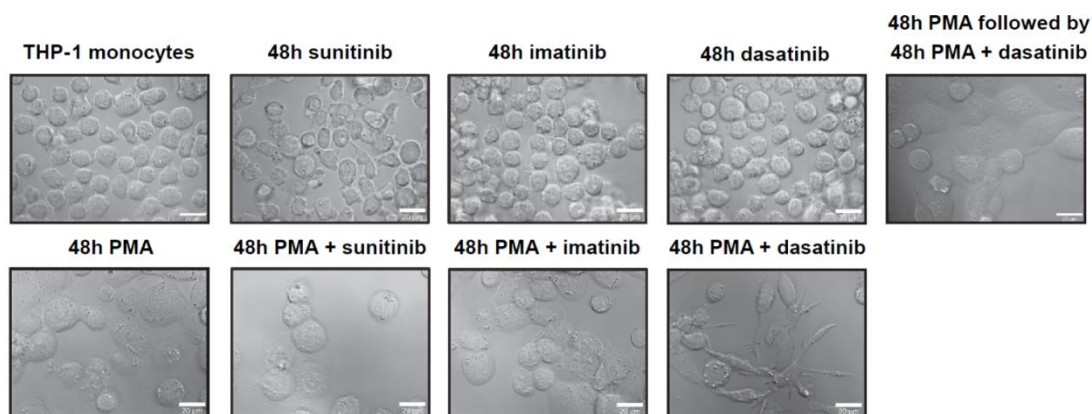
Fig. 42 Morphological changes during PMA-stimulated differentiation in presence of tyrosine kinase inhibitors. Monocytic THP-1 cells were differentiated with 100 nM PMA for 48 h in presence or absence of the tyrosine kinase inhibitors sunitinib, imatinib or dasatinib at 1 µM concentration. As controls, THP-1 cells were incubated without PMA for 48 h with the respective tyrosine kinase inhibitor. The influence of dasatinib on already differentiated cells was tested by differentiating cells for 48 h with PMA followed by additional 48 h in presence of PMA and dasatinib. Morphological changes were monitored by light microscopy (Zeis LSM 780, 65x oil).

Based on these results, the effects of dasatinib and sunitinib on the surface proteomes of monocytic or macrophage-like THP-1 cells as well as during PMA-induced differentiation were compared using a TMT-based quantitative mass spectrometry strategy and immunoblotting. Sunitinib did not induce any significant changes when applied during cell differentiation (Fig. 43, Fig. 44A and supplemental Fig. 7). In contrast, when dasatinib was present during differentiation, up-regulation of CD11b was blocked while MRC2 down-regulation was not affected (Fig. 43).
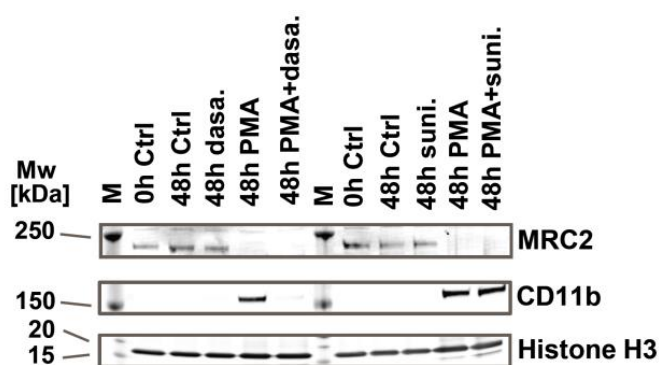
Fig. 43 Effects of kinase inhibitors on regulation of cell surface markers during PMA-induced differentiation. Immunoblots for cell surface markers regulated during differentiation of THP-1 cells by 100 nM PMA in presence or absence of 1 µM dasatinib or 1 µM sunitinib. Untreated cells and cells incubated for 48 h in presence or absence of the kinase inhibitors without PMA-stimulation were used as controls.

In total, abundances of 56 cell surface proteins were significantly altered after differentiation in the presence of dasatinib compared to control differentiation experiments (Fig. 44).
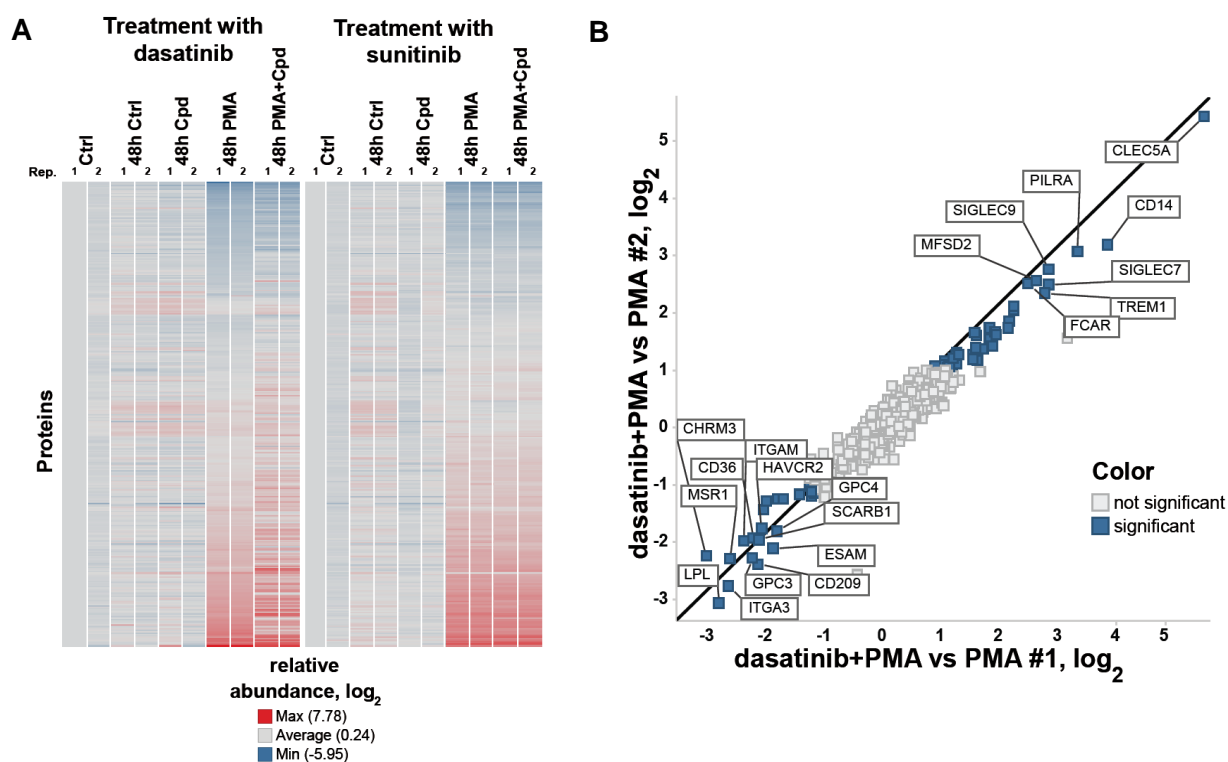
Fig. 44 Effects of kinase inhibitors on cell surface proteomes during PMA-induced differentiation. THP-1 cells were differentiated in presence or absence of 1 μM dasatinib or 1 μM sunitinib in two biological replicates. Resulting peptide mixtures after cell surface proteome enrichment were isobaric mass tagged, pooled and analyzed by LC-MS/MS on a Q Exactive Hybrid-Quadrupole-Orbitrap mass spectrometer using a 270 min gradient. Untreated cells and cells incubated for 48 h in presence or absence of the kinase inhibitors without PMA-stimulation were used as controls. Data was filtered for cell surface proteins quantified with at least three qusm and at least two qupm. Significance was defined as a combined fold-change and p-value cut-off between cells differentiated in presence and cells differentiated in absence of the kinase inhibitors with log_2 relative abundances ≥ 1 or ≤ -1 in both replicates and t-test p-values < 0.05. (**A**) Heat map representation of quantified plasma membrane associated proteins during differentiation in presence of dasatinib or sunitinib. Colors represent log_2 relative abundance to untreated controls. (**B**) Proteins with significantly altered abundance in THP-1 cells differentiated in presence versus cells differentiated in absence of dasatinib.

Pronounced up-regulation was observed for 35 proteins including CLEC5a (47-fold up), a positive regulator of osteoclastogenesis (Inui et al., 2009) as well as TREM1, PILRA and CD14 which together with CLEC5a are markers for mature myeloid cells (Fournier et al., 2000; Gingras et al., 2002; Ritter et al., 2006). Substantial down-regulation of 21 proteins was observed including macrophage markers like CD209, CD22, HAVCR2 and TLR4 suggesting compromised macrophage-specific functions. Up-regulation of cell adhesion proteins like ESAM, ITGA3, ITGAE and ITGAM during differentiation from monocytes to macrophages was reduced or completely blocked in presence of dasatinib in line with a less adherent cellular morphology. In addition, reduced expression was observed for SCARB1, MSR1, CD36 and LPL which are involved in phagocytosis as well as fatty acid, cholesterol and lipid endocytosis. In agreement with these findings, the phagocytotic activity of THP1 cells differentiated in the presence of dasatinib was reduced by > 40 % but was not significantly changed for cells differentiated in presence of sunitinib (Fig. 45). Addition of the phagocytosis inhibitor cytochalasin D (2 μM) resulted in partial but significant reduction of the phagocytotic activity in all samples.
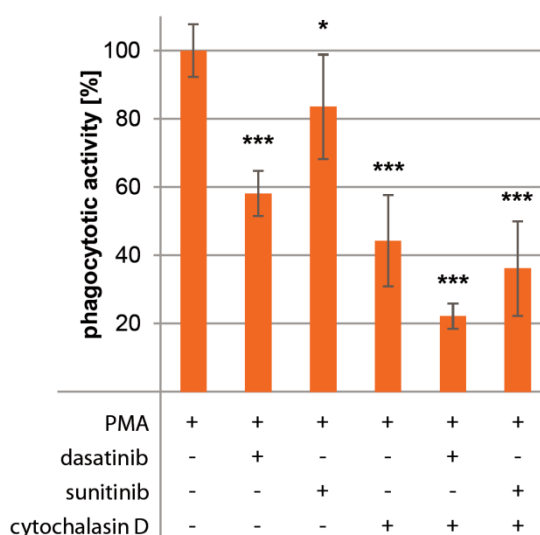
Fig. 45 Comparison of phagocytotic activities after differentiation in presence or absence of dasatinib or sunitinib. Phagocytosis assay based on the determination of the amount of engulfed nonopsonized zymosan particles in presence or absence of 2 µM of the phagocytosis inhibitor cytochalasin D. Bars represent mean of 4 replicates. Error bars represent standard deviations. Stars indicate statistical significance (* < 0.1; ** < 0.05; *** < 0.01).

CLEC5A was found to be most significantly changed in abundance after PMA-induced differentiation in presence of dasatinib. Since this protein has a role in osteoclastogenesis, the cell surface proteome of these cells was compared to osteoclast-like THP-1 cells obtained by differentiation using vitamin D_3 (Park et al., 2012) as well as to monocytic and macrophage-like THP-1 cells. Principal component analysis of plasma membrane protein abundances showed cells differentiated with PMA in the presence of dasatinib to be related to both, osteoclast-like and macrophage-like THP-1 cells (Fig. 28A).

For identification of targets involved in the dysregulation of THP-1 cell differentiation, a differential analysis of the selectivity profiles for the tested kinase inhibitors imatinib, sunitinib and dasatinib was conducted using kinobeads (Bantscheff et al., 2007, Fig. 46). Results showed a limited selectivity of the marketed BCR-ABL inhibitor dasatinib suggesting that neither ABL kinase inhibition nor any of the other kinases affected by imatinib or sunitinib are responsible for the observed dysregulation of the differentiation program. However, among others ephrin receptor tyrosine kinases are potently inhibited by dasatinib but not by imatinib or sunitinib probably hinting at an involvement of these receptors in the dysregulation.
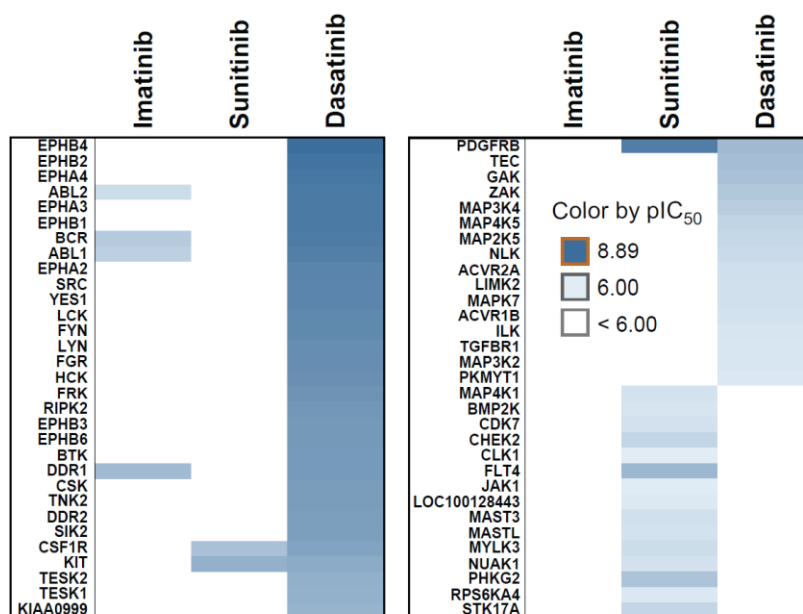
Fig. 46 Selectivity profiles of kinase inhibitors assessed by kinobeads competition assay. Lysate mixes were pre-incubated with defined concentrations of the compounds followed by incubation with kinobeads. After washing, bound proteins were eluted with SDS sample buffer, fractionated by SDS gel electrophoresis, in-gel digested, TMT labeled and analyzed by mass spectrometry. Compound pIC_{50} values were calculated based on dose-dependent binding inhibition curves. Heat map represents targeted kinases by the kinase inhibitors imatinib, sunitinib and dasatinib with $pIC_{50} \geq 6$.

4.6. Establishing a cell surface selective thermal proteome profiling approach

The recently published thermal proteome profiling enables monitoring of protein-ligand interactions in live cells (Savitski et al., 2014). It is based on ligand-binding induced changes in protein thermal stability and requires accurate proteome quantification by multiplexed isobaric mass tags. In the initial approach, cell lysis was performed by freeze-thawing without addition of detergents to avoid solubilization of protein aggregates. However, this resulted in inefficient solubilization of membrane proteins. A revised method incorporated the mild detergent IGEPAL CA-630 for an improved solubilization of membrane proteins while keeping protein aggregates unaffected (Reinhard et al., 2015). But, also this method is hampered by the generally low abundance of many membrane and cell surface proteins. Here, the previously established selective enrichment of plasma membrane proteins was combined with thermal proteome profiling. For establishing this cell surface selective thermal proteome profiling, several parameters had to be defined and optimized. For this approach it is important to quantitatively remove protein aggregates that formed upon incubation at any given temperature. Thus for first simplified evaluations, the remaining soluble fraction of the representative cell surface transmembrane receptor ITGAV after heat treatment (HT) at high temperatures (typically inducing complete protein denaturing, e.g. 70 °C, Savitski et al., 2014) was monitored by immunoblotting. As the HT incubation is a core step in thermal proteome profiling, the influence of the HT incubation time was evaluated by comparing a prolonged and a pulsed HT with the previously described 3 min incubation. The results did not show an observable difference on thermal protein aggregation of ITGAV (supplemental Fig. 8), thus the HT incubation time was kept at 3 min. Another important factor on protein aggregation is the post-HT incubation time. This parameter was previously defined to be 3 min at RT and was now compared with a

post-HT incubation time of 5 min at RT (Fig. 47). The shorter incubation resulted in a less efficient protein aggregation. About 30 % of the initial ITGAV abundance was still present in the 70 °C sample. In turn, the residual abundance of ITGAV after high temperature treatment could be reduced to less than 10 % in case of a prolonged post-HT incubation of 5 min. Additionally, it was important to evaluate the influence of cell surface proteome biotinylation on protein aggregation. For that purpose, heat treated cells were biotinylated by 10 min oxidation and 10 min aniline-catalyzed alkoxyamine-based biotinylation at RT (Fig. 47). This process resulted in a total post-HT incubation time of 30 min and showed an even lower residual ITGAV abundance compared to 5 min of post-HT incubation. Thus, thermal proteome aggregation was unaffected by the biotinylation procedure and in summary, post-HT incubation times longer than 3 min were identified to be beneficial for efficient removal of protein aggregates. Based on these observations, in all following experiments the cell surface proteome biotinylation was performed, after 3 min of post-HT incubation at RT, by periodate oxidation for 10 min at RT and 10 min aniline-catalyzed alkoxyamine-based biotinylation at 4 °C.
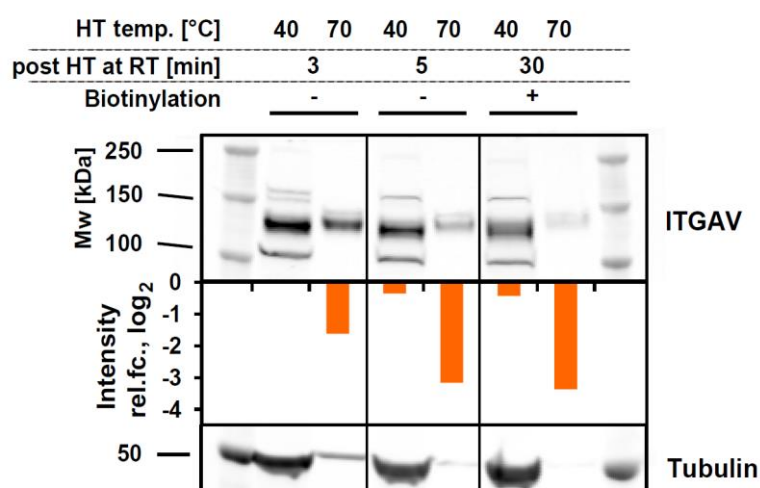
Fig. 47 Influence of post-HT incubation time and cell surface biotinylation on protein aggregation. K562 cells (3×10^6 per condition) were incubated for 3 min at 40 or 70 °C followed by a post-HT incubation time of 3 or 5 min at RT. To evaluate the influence of cell surface protein biotinylation on protein aggregation, cells were biotinylated at RT after 3 min of post-HT incubation resulting in a total post-HT incubation time of 30 min at RT. Subsequently, cells were lysed and 30 µg lysate were subjected to immunoblotting for ITGAV. Band signal intensities relative to the 40 °C sample with 3 min post-HT incubation are shown. Staining of tubulin was used as loading control for 40 °C samples.

In a next step, the influence of detergents on membrane protein solubilization and thermal proteome profiling was evaluated. The previous protocol used the mild detergent IGEPAL CA-630, capable of solubilizing membrane proteins without affecting protein aggregates. For further evaluation, the performance of the cell surface thermal proteome profiling with the mild detergents CHAPS (3-[(3-cholamidopropyl)dimethylammonio]-1-propanesulfonate), DDM (n-dodecyl-β-D-maltopyranoside) and digitonin were compared to IGEPAL CA-630. Cells heat treated with a gradient of 10 temperatures were surface biotinylated, lysed with the respective detergent in two replicates and samples were analyzed by LC-MS/MS on a Q Exactive Hybrid-Quadrupole-Orbitrap mass spectrometer using a 270 min gradient after TMT-labeling and sample pooling (Fig. 48). The performance of the assay with the respective detergent was compared on the one hand based on the numbers of identified cell surface proteins and on the other hand based on the number of proteins with good-quality melting curves. Calculation of melting curves was performed as described (Franken et al., 2015) by fitting relative protein abundances at the respective temperatures of the selected temperature gradient to sigmoidal

curves. These curve fits then enabled determination of protein melting points representing the temperature at which 50 % of the protein was aggregated and precipitated. Important performance criteria for this melting-curve based data analysis are the coefficient of determination R^2 and the reproducibility of calculated melting points ΔT_M between replicates.
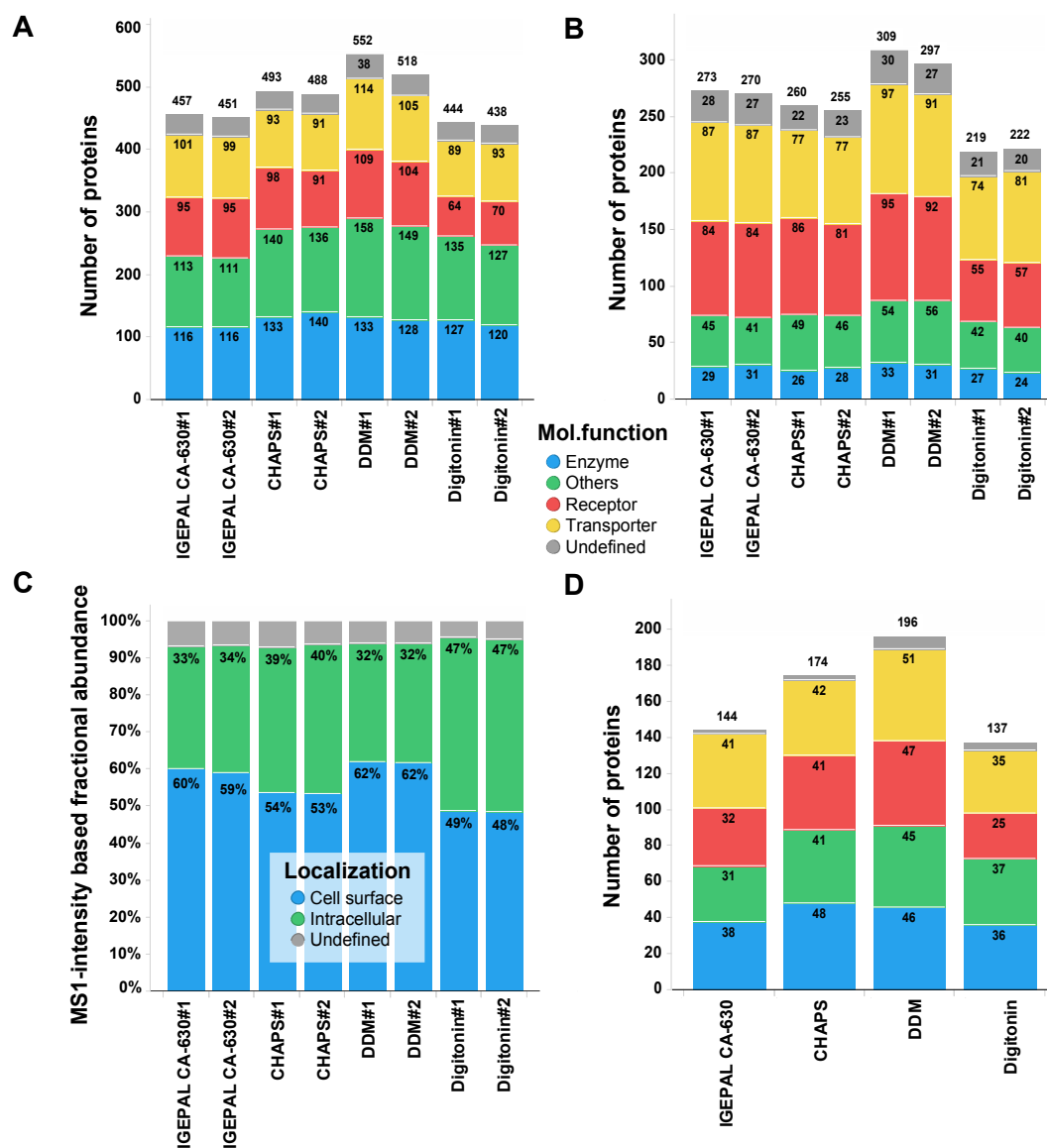
Fig. 48 Influence of detergents on cell surface protein identification and thermal proteome profiling. The influence of the detergents IGEPAL CA-630, CHAPS, DDM and digitonin on cell surface thermal proteome profiling was evaluated. K562 cells (3x10^6 cells per temperature) were heated to different temperatures followed by cell surface biotinylation. Subsequently, cells were lysed in PBS containing 1 % IGEPAL CA-630, CHAPS, DDM or digitonin. Protein aggregates were removed by filtration and a volume of lysate, corresponding to 100 µg protein in the reference temperature sample, were subjected to streptavidin-based enrichment for 60 min. Enriched proteins were eluted by tryptic on-bead digestion for 16 h. Resulting peptide mixtures were TMT-labeled, cleaned by C18-SCX STAGE tips and 25 % of the final mixtures were analyzed by LC-MS/MS on a Q Exactive Hybrid-Quadrupole-Orbitrap mass spectrometer using a 270 min gradient. Identified proteins were filtered for PSM ≥ 2. For melting curve calculations data was normalized and filtered for cell surface proteins with qusm ≥ 3, qupm ≥ 2, $R^2 \geq 0.6$ and $\Delta T_M \leq 3\,°C$ in both of the respective replicates. (**A**) Number of identified cell surface proteins colored by their annotated molecular function (UniProt). (**B**) As in (A) but showing numbers of identified cell surface transmembrane proteins. (**C**) MS1-intensity based fractional abundance of identified proteins grouped by annotated subcellular localization. (**D**) Number of cell surface proteins fulfilling all defined filter criteria for proper quantification and melting behavior.

The use of DDM resulted in the highest number of identified cell surface proteins with an increase of about 20 % compared to IGEPAL CA-630. This detergent also enabled identification of a higher number of cell surface transmembrane proteins, a slightly higher enrichment efficiency for proteins of this subcellular localization and the highest number of cell surface proteins with defined good-quality melting curves (qusm ≥ 3, qupm ≥ 2, R^2 of curve fit ≥ 0.6 and melting point differences ≤ 3 °C between respective replicates). Based on these results, DDM was defined as detergent for all following experiments.

Up to that point, the optimized protocol for cell surface thermal proteome profiling involved protein biotinylation after the heat treatment. However, hyperthermia can lead to changes in cell membrane dynamics (Bischof et al., 1995). Thus, biotinylation after HT can result in artificial protein melting behaviors. To circumvent this problem, biotinylation was tested to be performed prior to the HT. However, this resulted in an overall reduced number of quantified cell surface proteins as well as a reduced number of cell surface proteins with good-quality melting curves (supplemental Fig. 9). In another approach, aldehydes were introduced by periodate oxidation prior to HT followed by biotinylation after the HT thus circumventing artifacts resulting from HT-induced changes in cell surface proteome presentation. However, as elevated temperatures might quench introduced aldehydes, the influence of hyperthermia on the stability of induced aldehydes was investigated. For that purpose, cells were periodate-treated, incubated at 4, 40, and 70 °C and subsequently biotinylated. To be able to neglect thermally induced protein aggregation between experiments, cells were lysed in 4 % SDS for efficient solubilization of also aggregated membrane proteins. Finally, samples were compared by immunoblot-derived signal intensities of biotinylated proteins as well as by TMT-based quantitative proteomics comparing relative abundances of cell surface proteins (supplemental Fig. 10). The results showed a slightly reduced overall protein biotinylation signal intensity and a generally reduced protein abundance for cell surface proteins after HT at 70 °C compared to 4 and 40 °C. An additional thermal proteome profiling experiment with this approach also showed a lower number of identified cell surface proteins and a lower number of cell surface proteins with good-quality melting curves compared to the previous approach (supplemental Fig. 11). According to these results, the previously tested biotinylation after HT was used for all following experiments.

Based on the optimizations for the cell surface proteome mapping approach, streptavidin-based enrichment of biotinylated proteins with subsequent quantitative elution by on-bead digestion was also used for the cell surface thermal proteome profiling approach. However, as the on-bead digestion can result in a marked contamination of the resulting peptide mixture with streptavidin peptides, a streptavidin-coated bead titration experiment was conducted to determine the minimal necessary bead volume for efficient capturing of biotinylated proteins (supplemental Fig. 12). Furthermore, the influence of a prolonged incubation time (120 min instead of 60 min) on capturing efficiency was assessed. Results were evaluated by comparing residual signal intensities of blotted biotinylated proteins after streptavidin-coated bead incubation. An optimal ratio for the bead volume to captured proteins was observed between 3 and 5 µL of the affinity resin per sample and 2 h of incubation. According to these results, 4 µL of streptavidin-coated beads were used for following experiments. Besides the bead amount, the on-bead digestion incubation time as well has an influence on the contamination of the sample with streptavidin peptides. Thus in a next step, the on-bead digestion incubation time was evaluated. For that purpose, TIC signal intensities of streptavidin peptides and numbers of PSMs for streptavidin identification were compared after 1 h, 4 h and 16 h (overnight, o.n.) digestion (Fig. 49). In addition, numbers of identified cell surface proteins as well as enrichment efficiencies for proteins of this subcellular localization were examined.
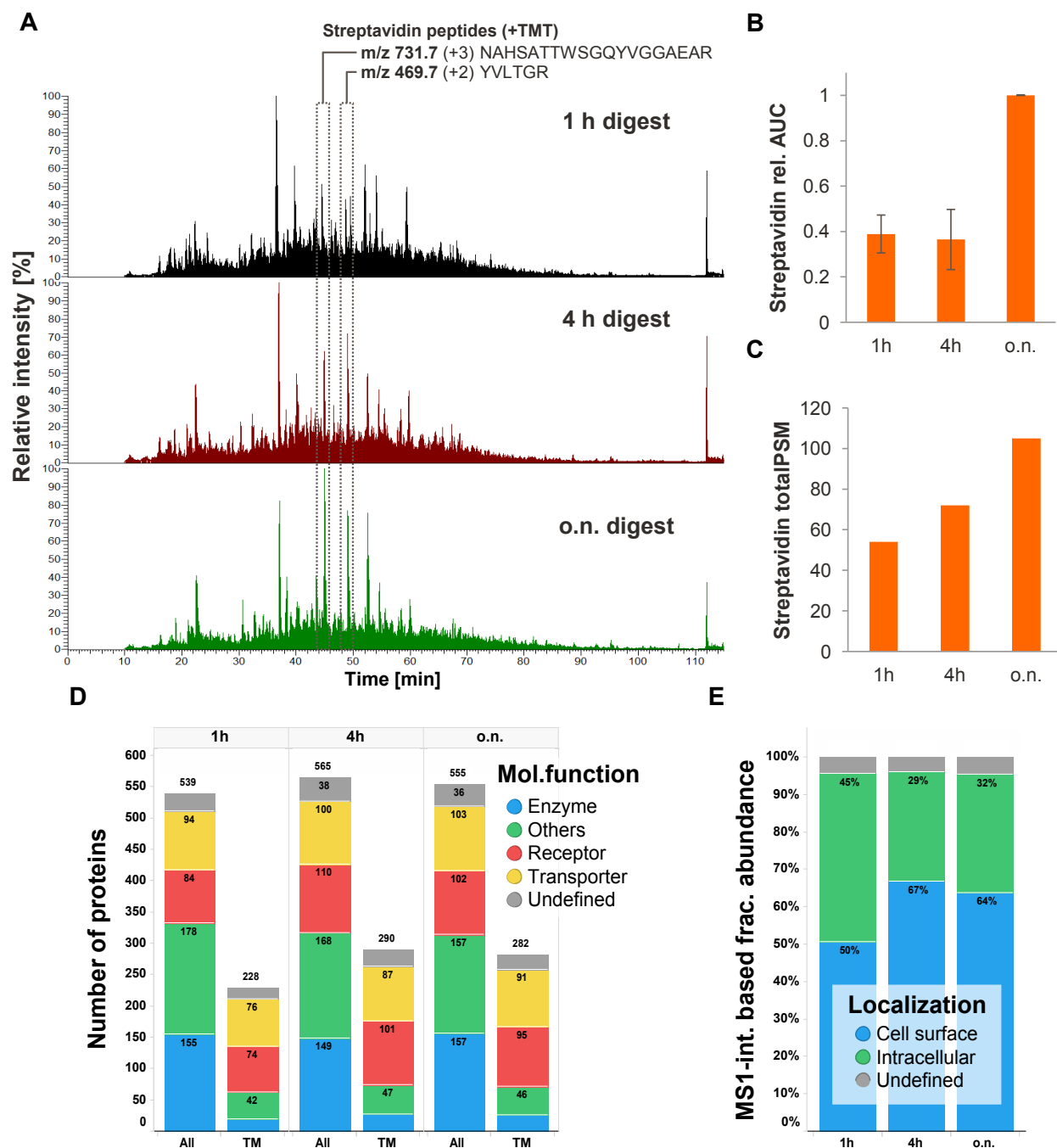
Fig. 49 Comparison of on-bead digestion incubation times. K562 cells were cell surface biotinylated and lysed. Subsequently, in three replicates 150 µg lysate were incubated for 2 h with streptavidin-coated beads. Enriched proteins were eluted by tryptic on-bead digestion either for 1 h, 4 h or 16 h (overnight, o.n.). Resulting peptide mixtures were TMT-labeled, cleaned by C18-SCX STAGE tips and separately analyzed by LC-MS/MS on a Q Exactive Hybrid-Quadrupole-Orbitrap mass spectrometer using a 120 min gradient. Identified proteins were filtered for PSM ≥ 2. (**A**) Total ion chromatograms of the samples. The 2 most intense out of 5 identified streptavidin peptide ions are labeled. (**B**) Comparison of the AUCs of streptavidin peptides between samples relative to o.n. digestion. (**C**) Number of PSM with Mascot score ≥ 20 for streptavidin. (**D**) Number of identified cell surface proteins (All) and cell surface transmembrane proteins (TM) colored by their annotated molecular function (UniProt). (**E**) MS1-intensity based fractional abundance of identified proteins grouped by annotated subcellular localization.

Relative comparison of the area under the curve (AUC) of the two most intense streptavidin peptides with *m/z* 731.7 (+3 charged, NAHSATTWSGQYVGGAEAR) and *m/z* 469.7 (+2 charged, YVLTGR) showed a markedly higher contamination of samples with these peptides

after o.n. on-bead digestion compared to 1 h or 4 h on-bead digestion. Furthermore, the total number of identified peptide spectra matched (PSM) for streptavidin correlated with the incubation time. Since a comparable number of identified cell surface proteins with a comparable cell surface enrichment efficiency but a markedly lower contamination with streptavidin peptides was observed after 4 h on-bead digestion compared to o.n. digestion, the on-bead digestion incubation time was set to 4 h for all following experiments. Nevertheless, the most intense streptavidin peptides were highly abundant and are eluting around the center of the liquid chromatography gradient. Besides streptavidin, neutravidin is an alternative affinity resin for selective biotin enrichment. Thus, beads coated with this deglycosylated form of avidin were compared to the streptavidin resin in an additional experiment (Fig. 50). The results showed a comparable efficiency in capturing cell surface biotinylated proteins with neutravidin-coated beads. However, the two most intense avidin peptides were eluting at the end of the LC gradient and identification of avidin was based on less total PSMs compared to streptavidin (-20 to -30 % after 4 h or o.n. on-bead digestion, respectively). Thus, neutravidin-coated beads were defined to be used for cell surface thermal proteome profiling.

Finally, after incorporating all modifications and optimizations, the cell surface thermal proteome profiling approach was evaluated for monitoring target engagement to cell surface proteins. The effect of the three compounds cyclo-RGDfK, ouabain and elacridar targeting integrin adhesion proteins, Na^+-K^+-ATPases and the multidrug-resistance transporter ABCB1 were investigated, respectively (Fig. 51). Treatments were conducted in two replicates with 10 µM cyclo-RGDfK, 1 µM ouabain or 1 µM elacridar and cell surface protein melting curves were compared to vehicle treated cells. Significances were calculated by student´s t-test. Significance cut offs were defined as described in methods section incorporating a maximal accepted significance level of 0.05 and a minimal accepted melting point shift defined by the standard deviation between replicates.
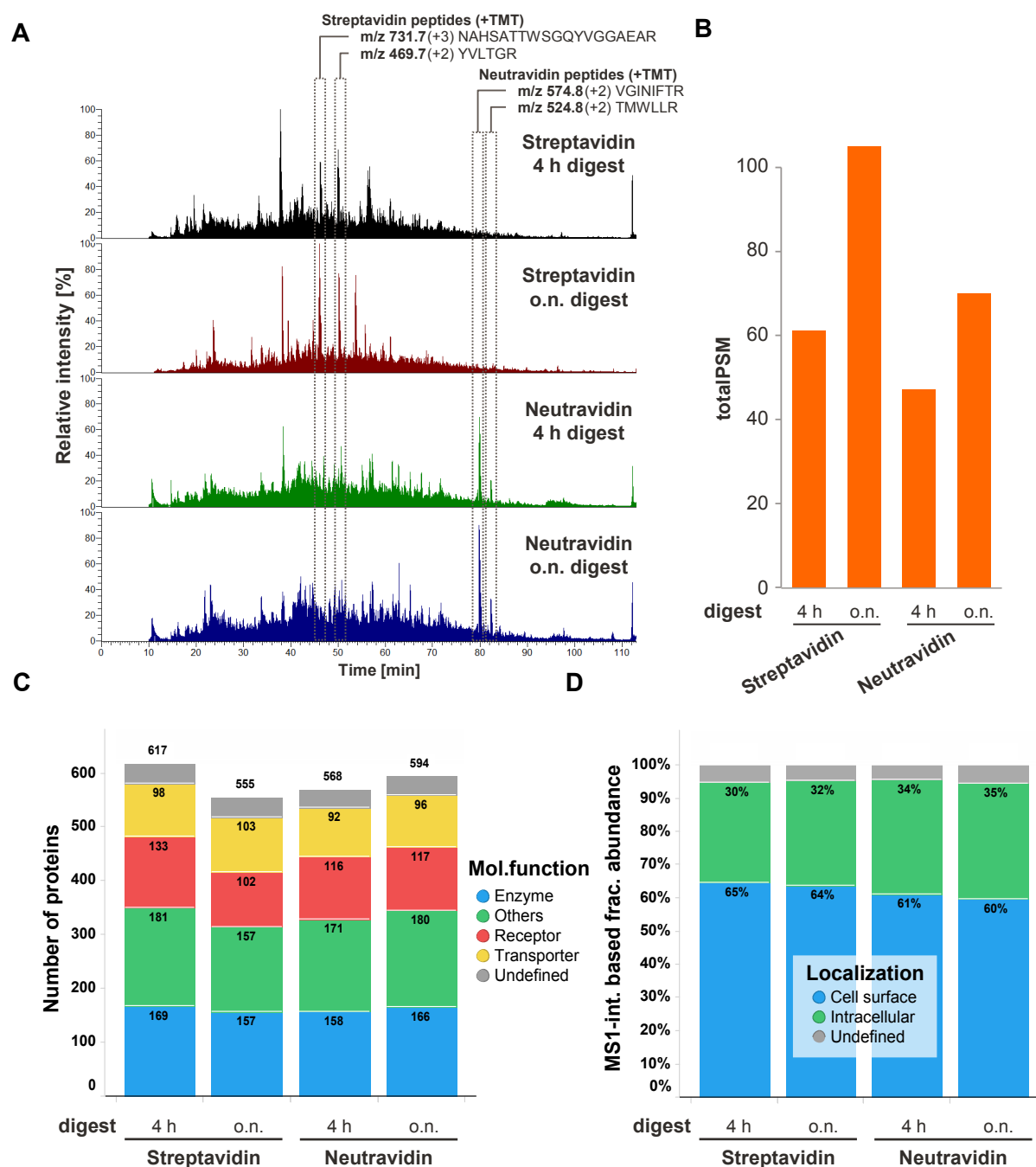
Fig. 50 Comparison of streptavidin- and neutravidin-coated beads. K562 cells were cell surface biotinylated and lysed. Subsequently, 150 μg lysate were incubated for 2 h with streptavidin- or neutravidin-coated beads each in two replicates. Enriched proteins were eluted by on-bead digestion for 4 h or 16 h (overnight, o.n.). Resulting peptide mixtures were TMT-labeled, cleaned by C18-SCX STAGE tips and separately analyzed by LC-MS/MS on a Q Exactive Hybrid-Quadrupole-Orbitrap mass spectrometer using a 120 min gradient. Identified proteins were filtered for PSM $\geq$ 2. (**A**) Total ion chromatograms of the samples. The two most intense streptavidin and neutravidin peptide ions are labeled. (**B**) Number of PSMs with Mascot score $\geq$ 20 for streptavidin and neutravidin, respectively. (**C**) Number of identified cell surface proteins colored by their annotated molecular function (UniProt). (**D**) MS1-intensity based fractional abundance of identified proteins grouped by annotated subcellular localization.
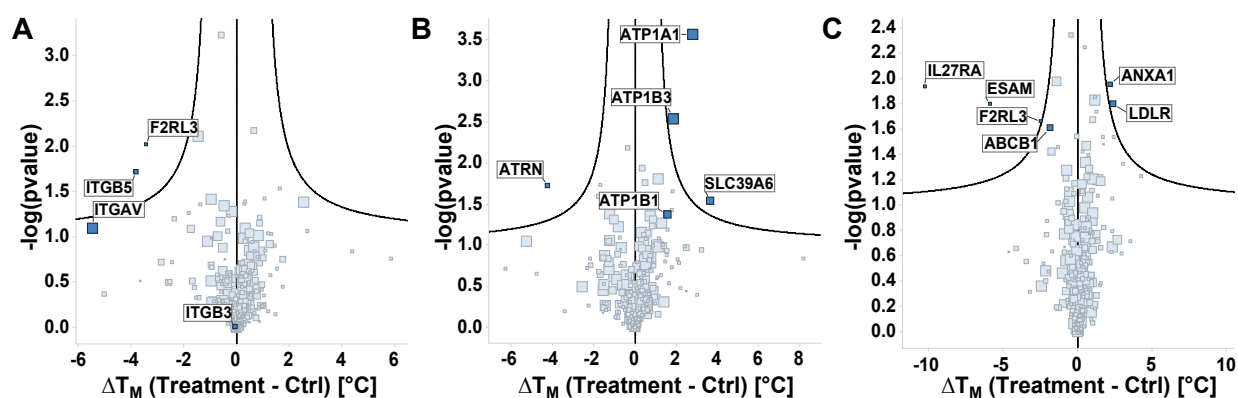
Fig. 51 Evaluation of the modified thermal proteome profiling for identification of target engagement. K562 cells (50x10^6 cells per experiment) were treated in two replicates with 10 µM cyclo-RGDfK, 1 µM ouabain or 1 µM elacridar. Vehicle treated cells were used as controls. Cells were heated to a temperature range between 43 and 73 °C, surface biotinylated and lysed. Protein aggregates were removed and 150 µg lysate per condition were subjected to enrichment with neutravidin-coated beads. Enriched proteins were eluted by on-bead digestion. Resulting peptide mixtures were TMT-labeled, cleaned by C18-SCX STAGE tips and analyzed by LC-MS/MS on a Q Exactive Hybrid-Quadrupole-Orbitrap mass spectrometer using a 120 min gradient. Data was filtered for proteins with qusm ≥ 2, qupm ≥ 2 and R^2 ≥ 0.6 in both of the respective treatment and control samples as well as with cell surface annotated localization. The significance cut-off was defined based on the median standard deviation of melting points between replicates. Data points are sized by the average qusm in respective experiment. (**A**) Significantly shifted proteins after cyclo-RGDfK treatment. Median standard deviation of melting points: 0.47 °C. (**B**) Significantly shifted proteins after ouabain treatment. Median standard deviation of melting points: 0.46 °C. (**C**) Significantly shifted proteins after elacridar treatment. Median standard deviation of melting points: 0.44 °C.

Treatment with the integrin inhibitor cyclo-RGDfK resulted in a significant thermal destabilization of ITGB5 forming an RGD-motif binding integrin with ITGAV. This alpha subunit also showed a pronounced but not significant thermal destabilization while the other expected beta subunit ITGB3 was not influenced. Ouabain treatment resulted in significant thermal stabilization of the alpha subunit ATP1A1 and of the beta subunit ATP1B3 but not of ATP1B1, all forming a functional Na$^+$/K$^+$-transporting ATPase. Elacridar resulted in a slight but non-significant thermal destabilization of ABCB1. The observed melting curves of expected protein targets are shown in supplemental Fig. 13.

Besides expected targets, in all three experiments significant thermal shifts of other proteins were observed as well. These are probably false positive results due to inappropriate data normalization which was based on only few proteins (supplemental Fig. 14). Furthermore, fitting of observed relative protein abundances to sigmoidal melting curves might not be accurate for plasma membrane proteins. To address these points, a different experimental set-up was explored that compared protein abundances between treatments and controls (Fig. 52). Instead of analyzing both cell populations at ten temperatures in separate TMT10 experiments, the new approach enables temperature-wise precise protein abundance comparisons between controls and treatments by combining both samples in single TMT10 experiments. In that way, data normalization and data analysis is independent from fitting data points into sigmoidal melting curves and just relies on accurate relative quantification of proteins. In addition, besides monitoring thermal stability changes, this approach also allows simultaneous evaluation of treatment-induced cell surface accessibility changes. Furthermore, usage of a reference temperature between separate TMT10 experiments enables combination of an unlimited number of experiments for data analysis depending on the required temperature resolution.
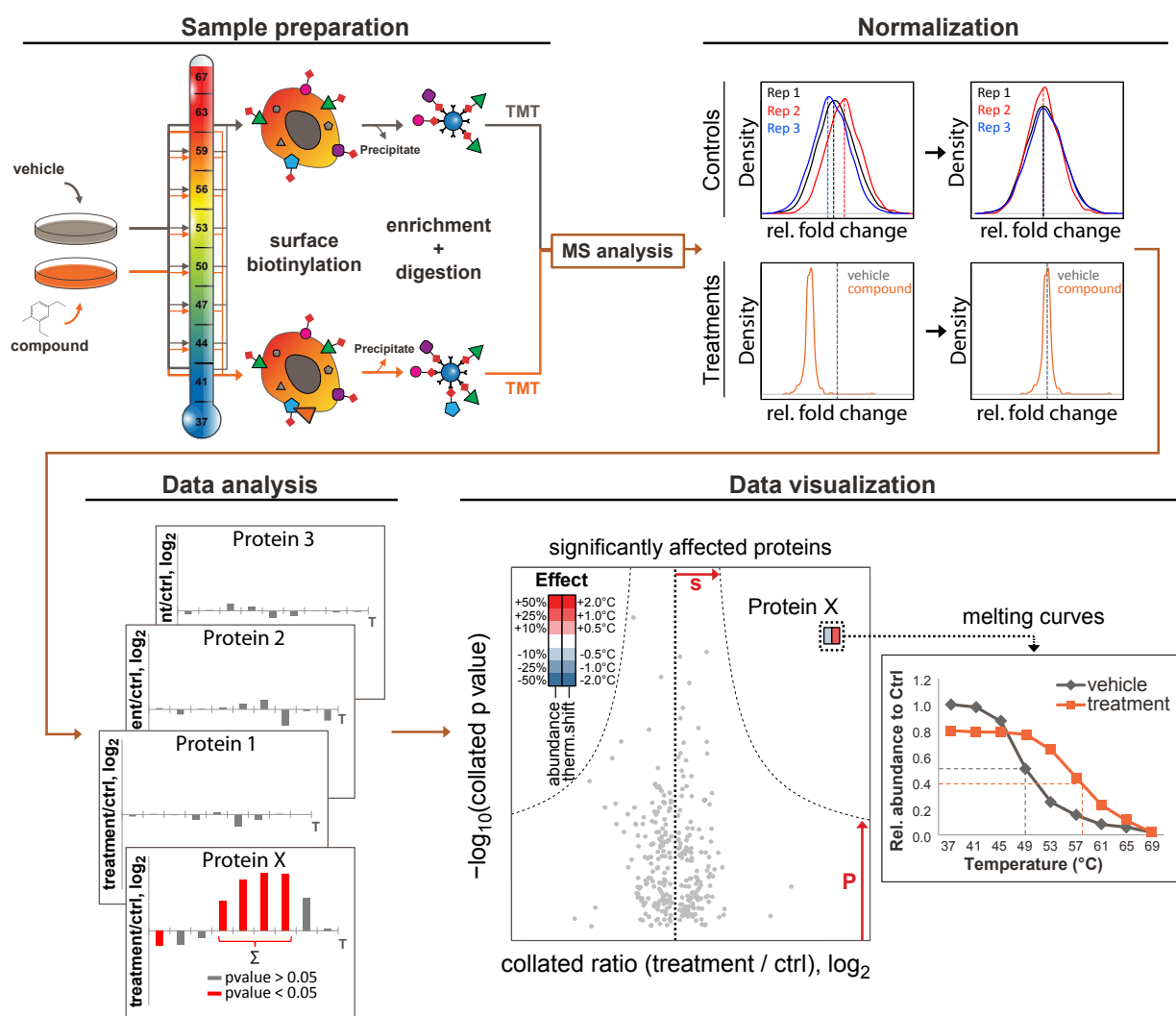
Fig. 52 Schematic illustration of the abundance ratio-based thermal proteome profiling approach. Cells are treated with a compound or vehicle followed by HT and surface biotinylation. Subsequently, cells are lysed, protein aggregates removed and biotinylated proteins enriched. After tryptic on-bead digestion, peptide mixtures are TMT-labeled, controls and treatments pooled and analyzed by mass spectrometry. For each temperature, protein abundances in controls are normalized between replicates followed by normalization of protein abundances in treatments towards their controls. Data analysis is performed by determining the temperature range with most significant differences (p-value < 0.05) in protein abundances for each individual protein between treatments and controls. The observed abundance ratios at temperatures within this temperature range are summed and p-values are combined. Finally, significant proteins exceeding minimal accepted ratio and minimal accepted significance are determined and plotted. Treatment-induced effects on cell surface abundance and thermal stability are distinguished.

Following density distribution-based data normalization for each individual temperature, data analysis is performed by determining, for each individual protein, the temperature range with most significant differences (p-value < 0.05) in protein abundances between treatments and controls. The observed abundance ratios at temperatures within this temperature range are summed and p-values are combined by Brown´s method (Brown, 1975). Plotting cumulated p-values over $\log_2$ transformed abundance ratios allows detection of proteins significantly affected by the treatment. Similar to the melting curve-based approach, a significance cut off was defined by incorporating a maximal accepted significance level (0.01 instead of 0.05) and a minimal accepted cumulative abundance ratio (instead of a minimal melting point shift) based on the standard deviation between replicates. For significantly affected proteins,

treatment-induced changes in cell surface abundance are detected by comparing relative abundances at the reference temperature (37 °C). Furthermore, thermal stability changes are detected by fitting melting curves and comparing melting points. For a first evaluation, this abundance ratio-based analysis approach with a resolution of 9 temperatures in two TMT10 experiments per replicate was compared to melting curve-based data analysis. Monitoring target engagement to Na$^+$/K$^+$-ATPases upon cellular treatment with ouabain in three biological replicates was selected as a case study (Fig. 53). Data of the melting curve-based analysis was normalized based on 58 proteins (supplemental Fig. 15) while temperature-wise normalization for ratio-based analysis was based on average on 339 cell surface proteins (lowest temperature: 427 proteins, highest temperature: 233 proteins).
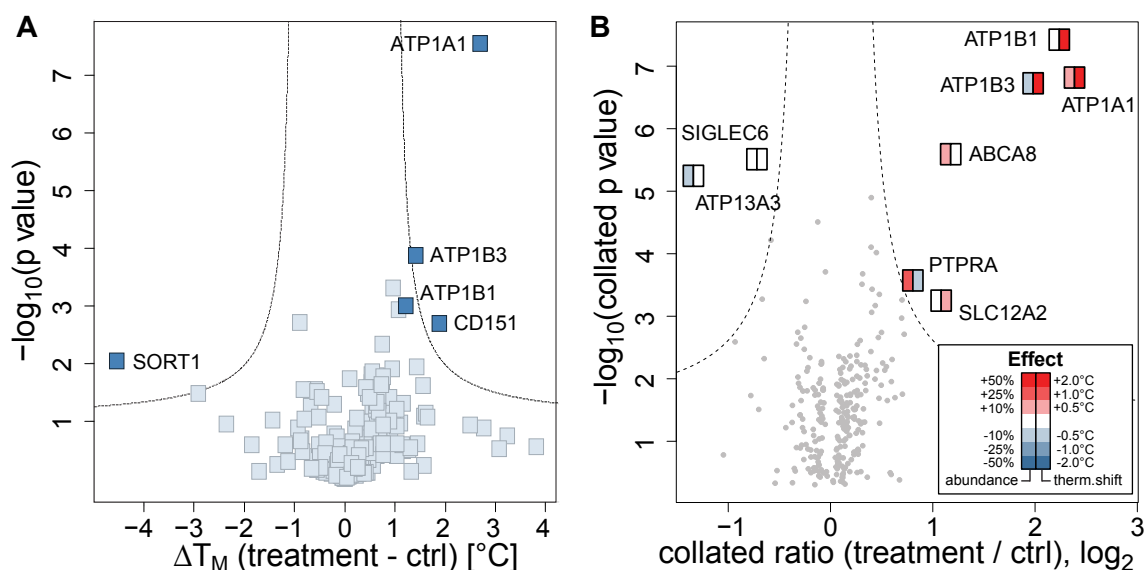

Fig. 53 Comparison of melting curve- and ratio-based cell surface thermal proteome profiling. K562 cells were treated with 1 µM ouabain in six replicates with three replicates for melting curve-based analysis and three replicates for ratio-based analysis. Vehicle treated cells were used as controls. After heat-treatment, surface biotinylation, lysis, enrichment and on-bead digestion, resulting peptide mixtures were TMT-labeled. For melting curve-based analysis, treatments and controls were analyzed in separate TMT10 experiments while for ratio-based analysis treatments and controls were pooled and analyzed together. Samples were analyzed by LC-MS/MS on a Q Exactive Hybrid-Quadrupole-Orbitrap mass spectrometer using a 270 min gradient. (**A**) Melting curve-based analysis of significantly thermally shifted proteins upon ouabain treatment (n = 3). Significant proteins are labeled. Median standard deviation between replicates: 0.49 °C. (**B**) Ratio-based analysis of significantly influenced proteins upon ouabain treatment (n = 3). Significant proteins are labeled. Left half of squares indicate abundance changes while right half of squares indicate thermal shifts. Median standard deviation between replicates: 0.13.

Melting curve-based analysis resulted in detection of a significant thermal stabilization of ATP1A1. ATP1B3 showed only a barely significant thermal stabilization while ATP1B1 was not significantly affected. In contrast to that, ratio-based analysis resulted in detection of highly significant changes in thermal stability of all three expected ATPase subunits. Furthermore, an increased surface abundance of the multidrug-resistance transporter ABCA8, described to be involved in the efflux of digitalis-like (e.g. ouabain) compounds (Tsuruoka et al., 2002; Wakaumi et al., 2005), was detected and a thermal stabilization of the Na$^+$/K$^+$/2Cl$^-$ co-transporter SLC12A2, mediating ouabain-insensitive K+ efflux, was observed (Gagnon and Delpire, 2013). In addition, a marked increase in surface abundance of the Src family kinase activator PTPRA (Pallen, 2003) was detected, in line with described Src activation upon ouabain-induced inhibition of Na$^+$/K$^+$-ATPases (Haas et al., 2002). Reduced abundance of the calcium-homeostasis transporter ATP13A3 is consistent with described intracellular calcium accumulation upon ouabain treatment (Roevens and de Chaffoy de Courcelles, 1990).

Comparisons of melting curves of significantly affected proteins in both approaches are shown in supplemental Fig. 16. In summary, ratio-based thermal proteome profiling enabled a more robust detection of target engagement to cell surface proteins as well as distinction of treatment-induced changes in thermal stability and surface abundance. Based on these results, the ratio-based data analysis was defined to be used for cell surface thermal proteome profiling.

4.7. Mapping target engagement to the cell surface proteome

The cell surface thermal proteome profiling approach was evaluated with 17 small molecule compounds, 9 native ligands and antibodies as well as 3 cellular stimuli all with known cell surface protein target classes resulting in a total number of 34 individual experiments with at least three biological replicates each. On average, about 380 plasma membrane annotated proteins were identified with good quantification (qusm ≥ 3 and qupm ≥ 2) and a mean fractional abundance for cell surface proteins of about 70 % (supplemental Fig. 17).

After first assessment of cell surface thermal proteome profiling for monitoring target engagement to the target class of Na^+/K^+-ATPases, this approach was further evaluated for monitoring small molecule binding to single pass transmembrane receptor tyrosine kinases. For that purpose, cellular treatment with the tyrosine kinase inhibitor dasatinib was conducted in three biological replicates on THP-1 cells (Fig. 54 and supplemental Fig. 18). Results showed target engagement to expected receptor tyrosine kinases CSF1R, KIT, EPHA2 and EPHB3. While dasatinib treatment resulted in thermal stabilization of KIT and both ephrin receptors, it induced thermal destabilization and increased surface presentation (+22%, -log(p) 3.4) in case of CSF1R. Furthermore, an increased surface presentation (+16%, -log(p) 4.8) of the ATPase flippase ATP11C and an undefined effect on VLDLR were observed. EPHB1, an additional dasatinib target expressed on the surface of THP-1 cells, was not affected by treatment with dasatinib although it is among the most potently hit ephrin receptors according to the kinobeads competition assay (pIC_{50} 2.6 nM, Fig. 46). The effect of dasatinib on VLDLR was validated in an additional experiment by treating cells with VLDL in presence or absence of dasatinib resulting in a thermal stabilization of this receptor (supplemental Fig.19). This treatment also resulted in an internalization of KIT and IL6R, effects only detected during co-treatment with human VLDL but not with dasatinib alone.

Fig. 54 Monitoring target engagement to receptor tyrosine kinases with dasatinib on THP-1 cells. Cells were treated in three biological replicates with 1 µM dasatinib or vehicle as control followed by a heat treatment with a temperature gradient between 37 °C to 66 °C. (**A**) Significantly affected proteins upon dasatinib treatment are labeled. Left half of squares indicate significant abundance changes while right half of squares indicate significant thermal shifts. Median standard deviation between replicates: 0.10. (**B-E**) Mean melting curves in controls and treatments of significantly affected proteins. Error bars indicate standard deviations. Selected data points for cumulation are highlighted with dashed boxes. Treatment-induced thermal shifts and abundance changes are indicated with statistical significances.

To determine cellular pEC_{50} values of dasatinib, isothermal dose response experiments were conducted in three biological replicates. For this purpose, THP-1 cells were incubated with increasing concentrations of dasatinib followed by HT at a selected temperature for which high abundance ratios between treatments and controls for proteins of interest were detected. Here, HT was performed at 51.5 °C for EPHB3 and 53.9 °C for KIT (Fig. 55). Data analysis was performed as described (Savitski et al., 2014; Franken et al., 2015) by fitting normalized data to sigmoidal dose-response curves enabling determination of half-maximal effective concentrations. These experiments revealed pEC_{50} values in the nanomolar range for EPHB3 (16.6 ± 5.8 nM) and KIT (0.7 ± 0.5 nM) in line with previously determined potencies with the kinobeads competition assay (EPHB3: 13 nM, KIT: 36 nM, Fig. 46).
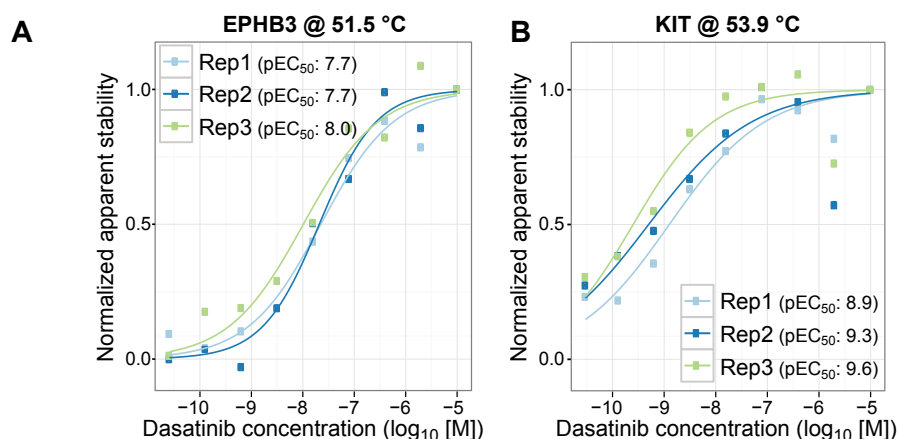
Fig. 55 Isothermal dose response of dasatinib on live cells. THP-1 cells were treated with increasing concentrations of dasatinib followed by HT at 51.5 °C or 53.9 °C. Experiments were conducted in three biological replicates. Dose response curves were fitted to normalized apparent stabilities and half-maximal effective concentrations were determined (pEC$_{50}$).

To increase the observable cell surface target space of dasatinib, cellular treatment with this inhibitor was repeated for the additional cell line model system K562 (Fig. 56).
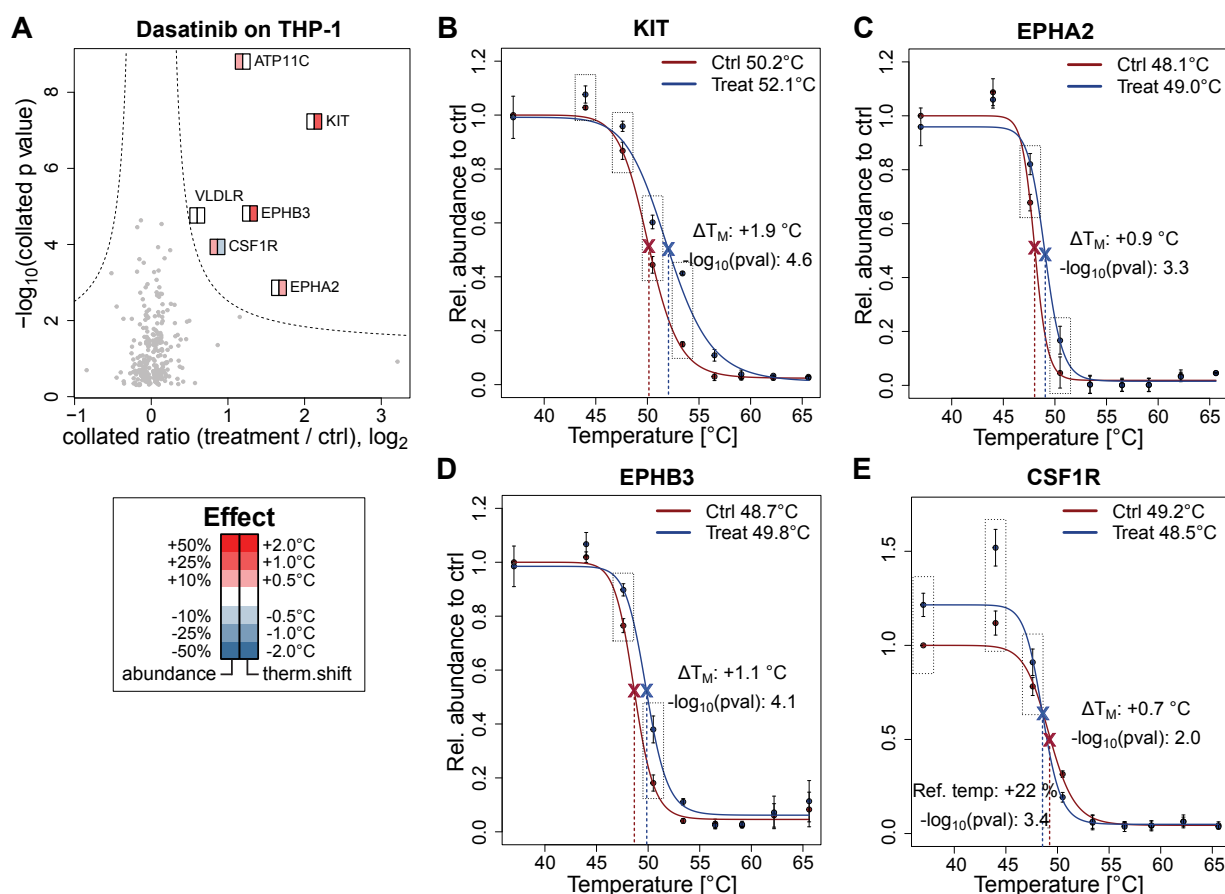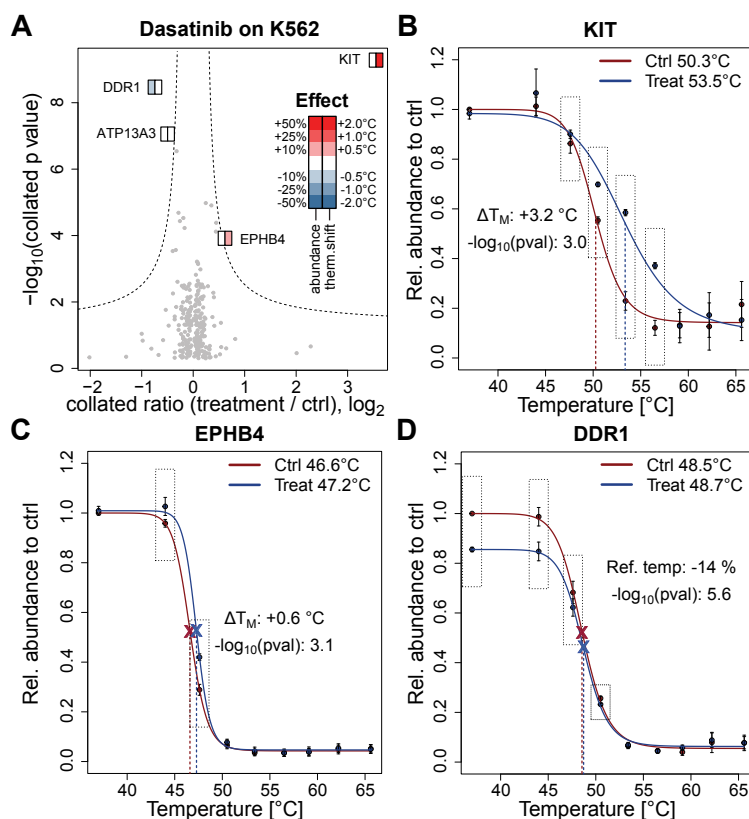

Fig. 56 Monitoring target engagement to receptor tyrosine kinases with dasatinib on K562 cells. Cells were treated in three biological replicates with 1 µM dasatinib or vehicle as control followed by heat treatment with a temperature gradient between 37 °C to 66 °C. (**A**) Significantly affected proteins upon dasatinib treatment are labeled. Left half of squares indicate significant abundance changes while right half of squares indicate significant thermal shifts. Median standard deviation between replicates: 0.09. (**B-D**) Mean melting curves in controls and treatments of significantly affected proteins. Error bars indicate standard deviations. Selected data points for cumulation are highlighted with dashed boxes. Treatment-induced thermal shifts and abundance changes are indicated with statistical significances.

The results showed thermal stabilization of KIT and of the additional ephrin receptor EPHB4. Discoidin domain receptor tyrosine kinase 1 (DDR1), another expected target of dasatinib (Fig. 46), showed a decreased surface abundance (-14 %, -log(p) 5.6) upon dasatinib treatment.

In a next step, cell surface thermal proteome profiling was used to monitor target engagement to integrins, the principal class of cell adhesion proteins. For that purpose, cells were treated with the two RGD-motif binding integrin inhibitors SB273005 (Fig. 57) and cyclo-RGDfK (supplemental Fig. 20).
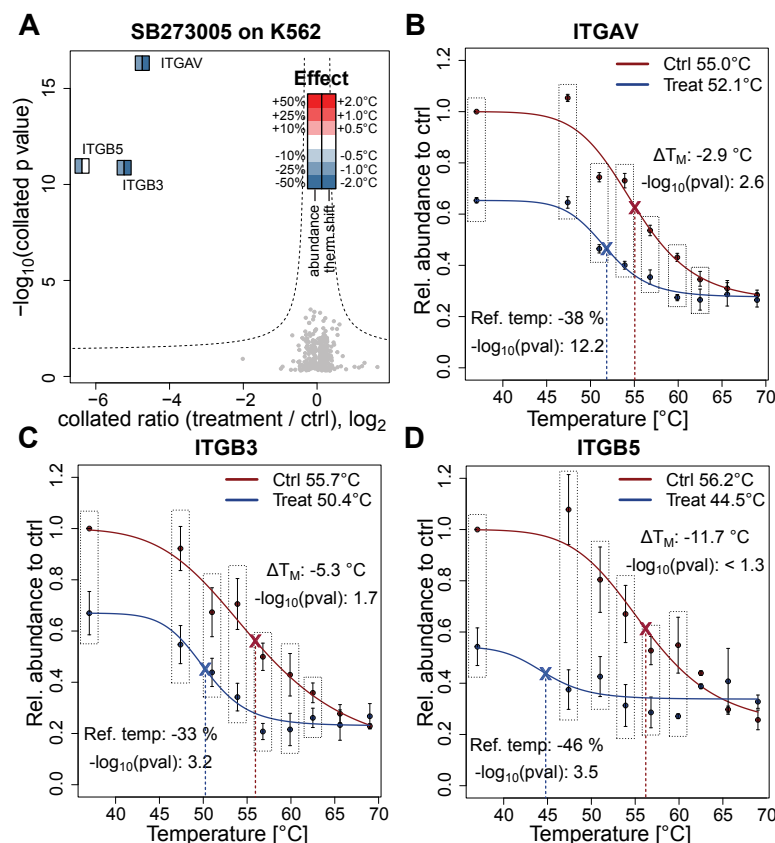
Fig. 57 Monitoring target engagement of SB273005 to RGD-binding integrins. K562 cells were treated in three biological replicates with 1 µM SB273005 or vehicle as control followed by a heat treatment with a temperature gradient between 37 °C to 69 °C. (**A**) Significantly affected proteins upon SB273005 treatment are labeled. Left half of squares indicate significant abundance changes while right half of squares indicate significant thermal shifts. Median standard deviation between replicates: 0.14. (**B-D**) Mean melting curves in controls and treatments of significantly affected proteins. Error bars indicate standard deviations. Selected data points for cumulation are highlighted with dashed boxes. Treatment-induced thermal shifts and abundance changes are indicated with statistical significances.

Both small molecule RGD-mimetics induced a significant thermal destabilization and internalization of the three integrin subunits ITGAV, ITGB3 and ITGB5 which are described to form functional RGD-binding integrin complexes (Humphries, 2006). Another beta subunit expressed on the surface of K562 cells, ITGB1, was neither affected by SB273005 nor by cyclo-RGDfK although it can also form a functional RGD-binding complex with ITGAV. This result was also observed when treating another cell line (Jurkat) with SB273005 (supplemental Fig. 21). Besides the two small molecule inhibitors, also a monoclonal antibody (mAb) directed against an extracellular epitope of ITGAV was tested (supplemental Fig. 22). The results showed the integrin alpha subunit ITGAV to be selectively affected and thus demonstrated the applicability of cell surface thermal proteome profiling for monitoring target engagement to plasma membrane proteins with biopharmaceuticals like antibodies (supplemental Fig. 22).

Additional evaluation experiments were conducted with the small molecule inhibitors elacridar, SB431542 and luminespib directed against ABCB1, TGFBR1 and HSP90 proteins, respectively (Fig 58 and supplemental Fig. 23-25).
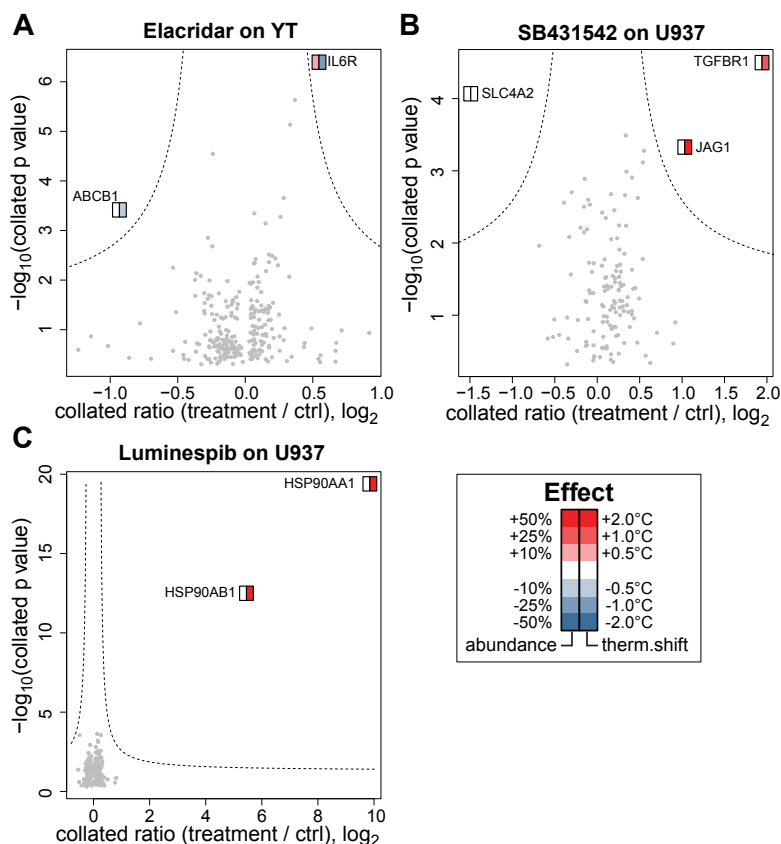
Fig. 58 Monitoring target engagement to several cell surface protein classes. Cells were treated in three biological replicates with 1 µM elacridar, 10 µM SB431542, 1 µM luminespib or vehicle as control. (**A**) Significantly affected proteins upon elacridar treatment are labeled. Left half of squares indicate significant abundance changes while right half of squares indicate significant thermal shifts. Median standard deviation between replicates: 0.11. (**B**) As in (A) but showing results of SB431542 treatment. Median standard deviation between replicates: 0.11. (**C**) As in (A) but showing results of luminespib treatment. Median standard deviation between replicates: 0.11.

For all three inhibitors, significant treatment-induced effects for the expected cell surface proteome targets were observed. In case of SB431542, besides TGFBR1 also JAG1, described to be required for a subset of TGFB1 responses (Nyhan et al., 2010; Zavadil et al., 2004), was thermally stabilized. When also focusing on slight treatment-induced cell surface abundance changes, a significant reduction in the cell surface presentation of the monocarboxylate transporters SLC16A1 (MCT1, -25%, -log(p) 2.9) and SLC16A3 (MCT3, -18%, -log(p) 5.2) was observed (supplemental Fig. 24D). This observation is in line with the described complete blockage of MCT1-mediated activities by SB431542 (Xu et al., 2017).

Besides small molecule inhibitors, cell surface thermal proteome profiling was evaluated for monitoring native ligand binding to cell surface receptors. In line with the increasing evidence for a relationship between cell signaling and endocytic membrane trafficking for attenuation of signaling pathways (Sorkin and von Zastrow, 2009), treatments with human IL2, IL6, CXCL12 and VLDL resulted in reduced cell surface abundances of the respective receptors and receptor complexes (Fig. 59 and supplemental Fig. 26-29).

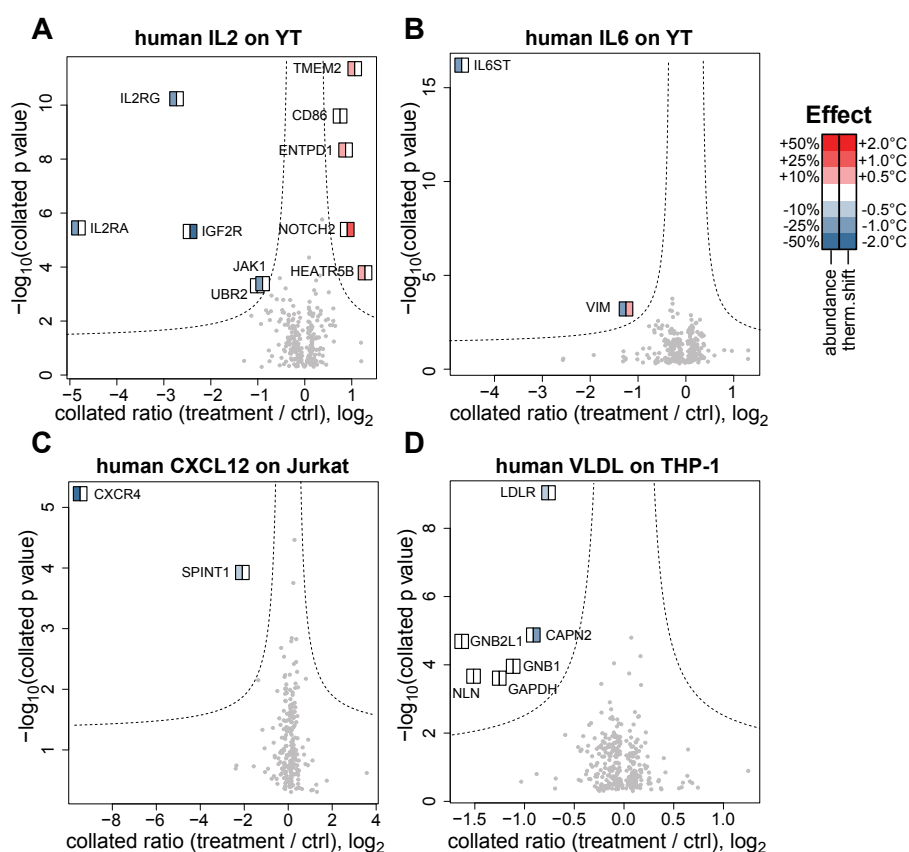**Fig. 59 Monitoring target engagement with native ligands.** Cells were treated in three biological replicates with 10 nM IL2, 20 nM IL6, 20 nM CXCL12, 100 µg VLDL or vehicle as control. (**A**) Significantly affected proteins upon IL2 treatment are labeled. Left half of squares indicate significant abundance changes while right half of squares indicate significant thermal shifts. Median standard deviation between replicates: 0.15. (**B**) As in (A) but showing results of IL6 treatment. Median standard deviation between replicates: 0.15. (**C**) As in (A) but showing results of CXCL12 treatment. Median standard deviation between replicates: 0.17. (**D**) As in (A) but showing results of VLDL treatment. Median standard deviation between replicates: 0.09.

Treatment of the natural killer model cell line YT with 10 nM human IL2 resulted in pronounced internalization of all three subunits of the interleukin 2 receptor, IL2RA, IL2RB and IL2RG (IL2RB significant at reference temperature only, see supplemental Fig. 26) as well as the interleukin 2 receptor associated protein JAK1 involved in the interleukin signaling cascade (Zhu et al., 1998). Other effects were observed on the E3 ubiquitin-protein ligase UBR2, involved in ubiquitination, internalization and degradation of transmembrane proteins (d'Azzo et al., 2005), on CD86, which is described to show an increased expression as a side effect of IL2 therapy (Paine et al., 2012) and a thermal stabilization of NOTCH2, described to be activated by inflammatory cytokines (Wang et al., 2013). IL2 signaling involves membrane-association and activation of PKC proteins (Lu et al., 1999). Since activation of these kinases plays an important role in the negative regulation of receptor signaling as also described for IGF1R (Zheng et al., 2000), the observed pronounced thermal destabilization of IGF2R could be the result from a negative feedback from IL-2 activated PKC. In comparison to these results, treatment with an IL2RA directed mAb did not result in detection of significantly affected proteins (supplemental Fig. 30). Treatment of the same cell line with human IL6 resulted in pronounced internalization of the IL6 receptor complex formed by the alpha subunit IL6R and the beta subunit IL6ST (IL6R quantified in one replicate only, supplemental Fig. 27). Furthermore, vimentin (VIM) described to be differentially regulated by interleukins (Hornbeck et al., 1993; Weidle et al., 2010), was found to be internalized upon IL6 treatment. Treating Jurkat cells with human CXCL12 resulted in profound internalization of its receptor CXCR4. In addition, SPINT1, an inhibitor of HGF

activator (Kirchhofer et al., 2003) which in turn is involved in regulation of CXCR4 expression (Maroni et al., 2007), was found to be internalized upon CXCL12 treatment (supplemental Fig. 28). Lastly, stimulation of serum starved THP-1 cells with human VLDL resulted in slight but significant internalization of LDLR but not of VLDLR (supplemental Fig. 29). LDLR activation and internalization is described to activate protein kinase C (PKC, Lara et al., 1997). In line with this, the receptor for activated C kinase (GNB2L1, Park et al., 2004), the calpain CAPN2, described to be associated to PKC (Savart et al., 1987), and the PKC target GAPDH (Zhang et al., 2015) were found to be affected by VLDL treatment.

In addition to the observed receptor internalization, native ligands can also induce thermal stability changes in their receptors (Fig. 60).
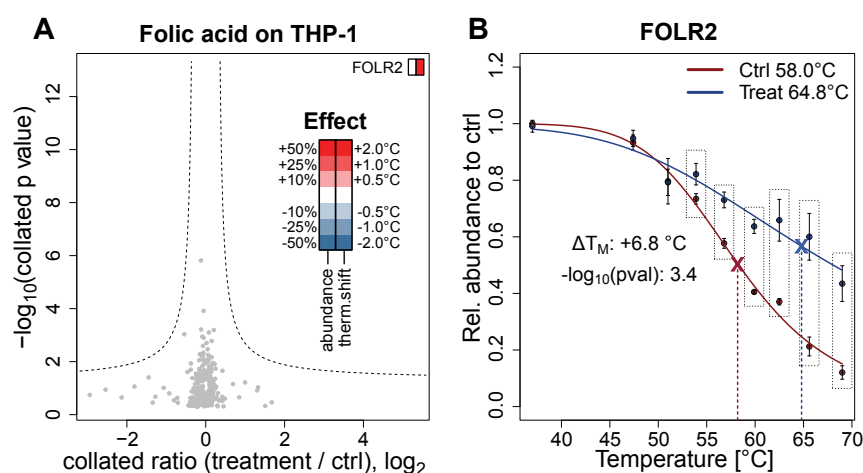

Fig. 60 Monitoring target engagement with folic acid. Starved cells were treated in three biological replicates with 20 µM folic acid or vehicle as control. (**A**) Significantly affected proteins upon treatment are labeled. Left half of squares indicate significant abundance changes while right half of squares indicate significant thermal shifts. Median standard deviation between replicates: 0.14. (**B**) Mean melting curves of significantly affected FOLR2. Error bars indicate standard deviations. Selected data points for cumulation are highlighted with dashed boxes. Treatment-induced thermal shift is indicated with statistical significances.

Treating serum and folate starved THP-1 cells with 20 µM folic acid resulted in a profound thermal stabilization of FOLR2. However, treatment of cells with the folic acid analogue methotrexate did not affect this receptor (supplemental Fig. 31). Instead, an increased surface accessibility and a thermal destabilization of CORO1B, involved in actin cytoskeleton organization (Cai et al., 2008), was observed. In line with this observation, methotrexate treatment is described to induce changes in actin filament organization (Otrocka et al., 2001) and cytoskeletal morphology probably involved in the lethal effects of this chemotherapeutic drug (Jackson et al., 1989). Nevertheless, both treatments with folic acid and methotrexate did not significantly affect the reduced folate carrier SLC19A1, one of the major facilitative membrane folate transporters (Hou and Matherly, 2014), making this transporter a false-negative drug target.

It is important to understand which proteins can be altered in thermal stability upon binding of small or large molecule ligands and for which proteins false negative results might be expected. Target binding could be detected for different plasma membrane target classes with small molecules and native ligands. However, there were also multiple cases for which expected targets did not show significant changes in thermal stability or in cell surface abundance. For example, cell surface thermal proteome profiling was unable to detect target engagement to respective cell surface receptors after treatment of serum starved cells with 100 nM insulin-like

growth factor 1 (IGF-1) or insulin (INS) as shown in supplemental Fig. 32. Furthermore, negative results were observed in case of cellular treatment with the loop diuretic furosemide (NKCC1 (SLC12A2) and NKCC2 (SLC12A1) inhibitor, César-Razquin et al., 2015), the SLC22 family inhibitor probenecid (César-Razquin et al., 2015) and the nucleoside transporter inhibitor dipyridamole (SLC29A1 inhibitor, César-Razquin et al., 2015) as shown in supplemental Fig. 33. Likewise, cellular treatment with the broad-spectrum matrix metalloproteinase inhibitor ilomastat (supplemental Fig. 34) as well as with the BCR-ABL tyrosine kinase inhibitor nilotinib (supplemental Fig. 35) did not result in identification of target engagement with the cell surface thermal proteome profiling approach. Furthermore, the approach was inappropriate to directly detect target engagement with the small molecule inhibitors WZ811 (supplemental Fig. 36) and IT1t (Fig. 61), both targeting the GPCR CXCR4. However, as these small molecule inhibitors bind to the same binding site on CXCR4 like its native ligand CXCL12, measuring a reduced CXCL12-dependent CXCR4 internalization in presence of IT1t enabled monitoring of target engagement to this GPCR by small molecule inhibitors (Fig. 61).
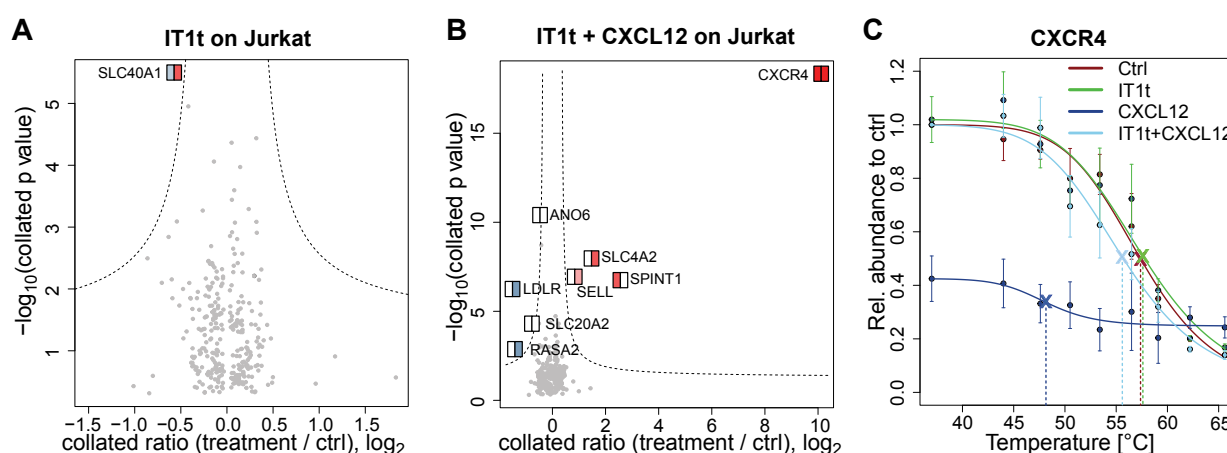

Fig. 61 Monitoring target engagement to CXCR4 by competition binding. (**A**) Jurkat cells were treated in three biological replicates with 1 µM IT1t or vehicle as control. Significantly affected proteins upon treatment are labeled. Left half of squares indicate significant abundance changes while right half of squares indicate significant thermal shifts. Median standard deviation between replicates: 0.11. (**B**) As in (A) but cells were treated for 30 min with 1 µM IT1t followed by treatment for 15 min with 20 nM CXCL12 or cells were only treated for 15 min with 20 nM CXCL12 as control. Median standard deviation between replicates: 0.16. (**C**) Mean melting curves for CXCR4 in untreated (Ctrl), IT1t-treated (IT1t), CXCL12-treated (CXCL12) or IT1t and CXCL12-treated (IT1t+CXCL12) cells. Error bars indicate standard deviations.

Programmed cell death is a biological process for targeted clearance of unwanted or malfunctioning cells. Dysregulation of this apoptotic process can disrupt the delicate balance between cell proliferation and cell death and can lead to diseases such as cancer (Fesik, 2005). Drug discovery often aims at developing small molecules that restore the normal apoptotic pathways leading to selective death of such aberrant cells. However, there is often a delay before any morphological or biochemical changes on apoptotic cells can be detected (Chin et al., 2006). Since programmed cell death is often accompanied by changes in the cell surface proteome (Elmore, 2007), cell surface thermal proteome profiling was tested to study effects of apoptosis-inducing small molecules. For that purpose, THP-1 cells were treated for 60 min with 1 µM of the broad spectrum kinase inhibitor staurosporine (Fig. 62 and supplemental Fig. 37-40) described to induce rapid apoptosis (Chin et al., 2006; Namgaladze et al., 2008). Furthermore, Jurkat cells were treated with 1 µM digitoxin and 1 µM ouabain, both described to induce apoptosis in this cell line but not in K562 cells (Ihenetu et al., 2007). The different susceptibility of Jurkat and K562 cells towards these digitalis-like compounds can be explained by the differential expression of the two multidrug resistance transporters ABCB1 and ABCA8, both

described to allow intracellular clearance of digitalis-like compounds (Gozalpour et al., 2016; Tsuruoka et al., 2002; Wakaumi et al., 2005). Both transporters were observed to be expressed in K562 but not in Jurkat cells.
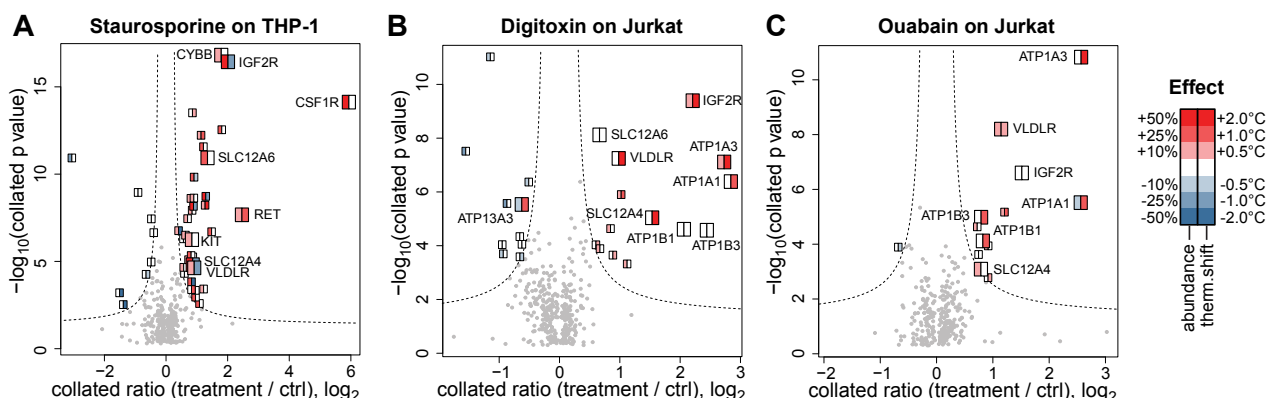

Fig. 62 Monitoring effect of apoptosis-inducing compounds. Cells were treated in three biological replicates with 1 µM staurosporine, 1 µM digitoxin, 1 µM ouabain or vehicle as control. Respectively used cell lines are indicated (**A**) Selection of significantly affected proteins upon treatment with staurosporine are labeled. Left half of squares indicate significant abundance changes while right half of squares indicate significant thermal shifts. Median standard deviation between replicates: 0.10. (**B**) As (A) but showing significantly affected proteins after treatment with digitoxin. Median standard deviation between replicates: 0.11. (**C**) As (A) but showing significantly affected proteins after treatment with ouabain. Median standard deviation between replicates: 0.10.

In case of staurosporine treatment, the expected direct targets CSF1R, RET and KIT as well as CYBB, described to mediate the staurosporine-induced apoptotic death (Guemez-Gamboa and Morán, 2009), were detected to be significantly affected. In addition to these, 39 other proteins like IGF2R and VLDLR showed significant treatment-induced effects which were probably primarily triggered by secondary events, in line with the broad spectrum effect of this inhibitor on several cellular signaling pathways. Treatment of Jurkat cells with digitoxin and ouabain, two Na^+/K^+-ATPase inhibitors, resulted in detection of target engagement to their direct ATPase alpha and beta subunit targets ATP1A1, ATP1A3, ATP1B1 and ATP1B3. Furthermore as already observed for the treatment of K562 cells with ouabain, also ATP13A3 and SLC12 members were significantly affected. In addition to these, significant effects were detected for 17 and 8 other proteins for digitoxin and ouabain treatments, respectively. The list of these other proteins again comprised IGF2R and VLDLR making these proteins potential markers for detection of early cellular stress response.

In a final approach, cell surface thermal proteome profiling was evaluated for monitoring cellular responses to environmental stimuli like T-cell activation, hypercupremia and hyperthermia. T-cell activation by co-stimulation of CD3 and CD28 with antibodies partially mimics physiologic stimulation by antigen-presenting cells (Trickett and Kwan, 2003). Stimulation for 30 min resulted in reduction of the surface abundances of CD28 and the T-cell receptor comprising the T-cell receptor alpha and beta subunits TCRA, TRBC1 and TRBV12-3 as well as CD3D, CD3E and CD3G by on average 61 % (Fig. 63 and supplemental Fig. 41-42). Furthermore, internalization of the L-selecting SELL (-70%, -log(p) 11.8), described to be associated with the T-cell receptor (Szabo et al., 1994), along with the SELL-cleaving metalloprotease ADAM17 (Wang et al., 2009, -31%, -log(p) 7.5), was observed. In addition, a marked increase in surface accessibility was detected for ATRN (+43%, -log(p) 5.4), known to be rapidly presented on activated T-cells (Pozzi et al., 2001), for ITGAL and ITGB2, described to be up-regulated upon T-cell activation (Bose et al., 2013), for ANO6, involved in cell volume regulation (Sirianant et al., 2016) as T-cell activation results in increased cell volume (June et al., 1987) as well as for

CD2 and CD48, whose interaction is described to be critical during T cell activation (Musgrave et al., 2003). CORO1A, observed to be thermally stabilized upon co-stimulation, is described to link cytoskeleton dynamics to T-cell receptor induced cell signaling (Mugnier et al., 2008). In addition, along with thermal stabilization, a marked increase in surface accessibility was detected for the complement receptor CR2 (+35%, -log(p) 8.0) and for the flippases ATP11A (+46%, -log(p) 8.4) and ATP11B (+39%, -log(p) 2.9).
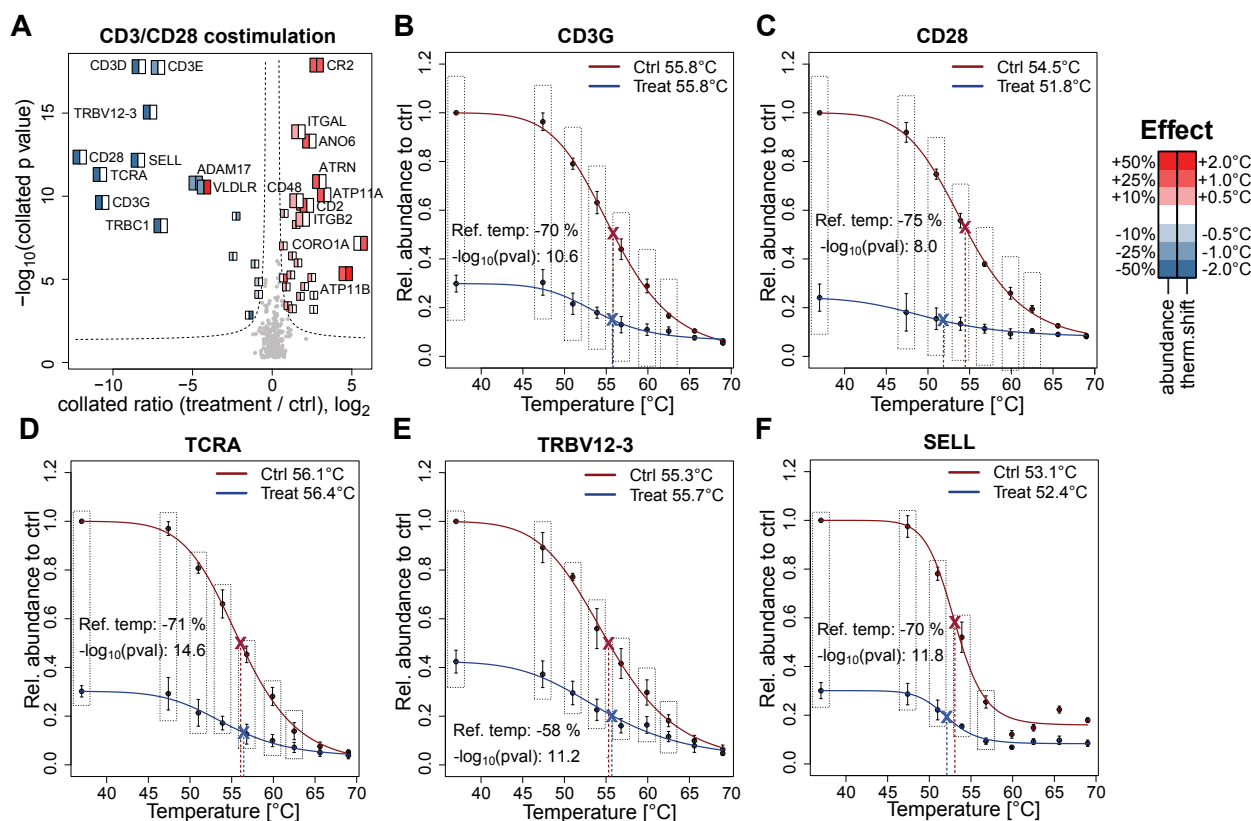

Fig. 63 Monitoring T-cell activation by CD3 and CD28 co-stimulation. Cells were treated in four biological replicates with 20 μg anti-CD3 mAB and 20 μg anti-CD28 mAb crosslinked with 50 μg anti-mouse mAb or vehicle as control. (**A**) Selection of significantly affected proteins upon treatment are labeled. Left half of squares indicate significant abundance changes while right half of squares indicate significant thermal shifts. Median standard deviation between replicates: 0.18. (**B-F**) Mean melting curves in controls and treatments of significantly affected proteins. Error bars indicate standard deviations. Selected data points for cumulation are highlighted with dashed boxes. Treatment-induced thermal shifts and abundance changes are indicated with statistical significances.

Hypercupremia was simulated by treating K562 cells with 20 μM CuSO4 for 60 min. This resulted in internalization and thermal destabilization of the copper influx transporter SLC31A1 as well as an increased surface presentation and thermal stabilization of the copper efflux transporter ATP7A (Fig. 64 and supplemental Fig. 43-44). Furthermore, internalization of the zinc-influx transporter SLC39A6, described to be able to transport copper (Taylor et al., 2007), thermal destabilization of the cation channel P2RX7 described to be inhibited by copper (Virginio et al., 1997) and an increased surface presentation of the cation channel TRPM4 involved in copper-induced membrane depolarization (Gómez et al., 2016), was observed. In addition, an increased surface presentation and thermal stabilization of ANXA2, described to co-localize with ATP7A (Matsuzaki et al., 2014), and of the divalent cation transporter ATP2B4 was detected. Hypercupremia also affected several other transporters involved in amino acid (SLC38A5, SLC43A1), nucleoside (SLC29A2), bicarbonate (SLC4A), multivitamin (SLC5A6) and ion (ATP1A1, ATP1B1, SLC12A6, CLCN3) transport suggesting an overall altered cellular metabolism.
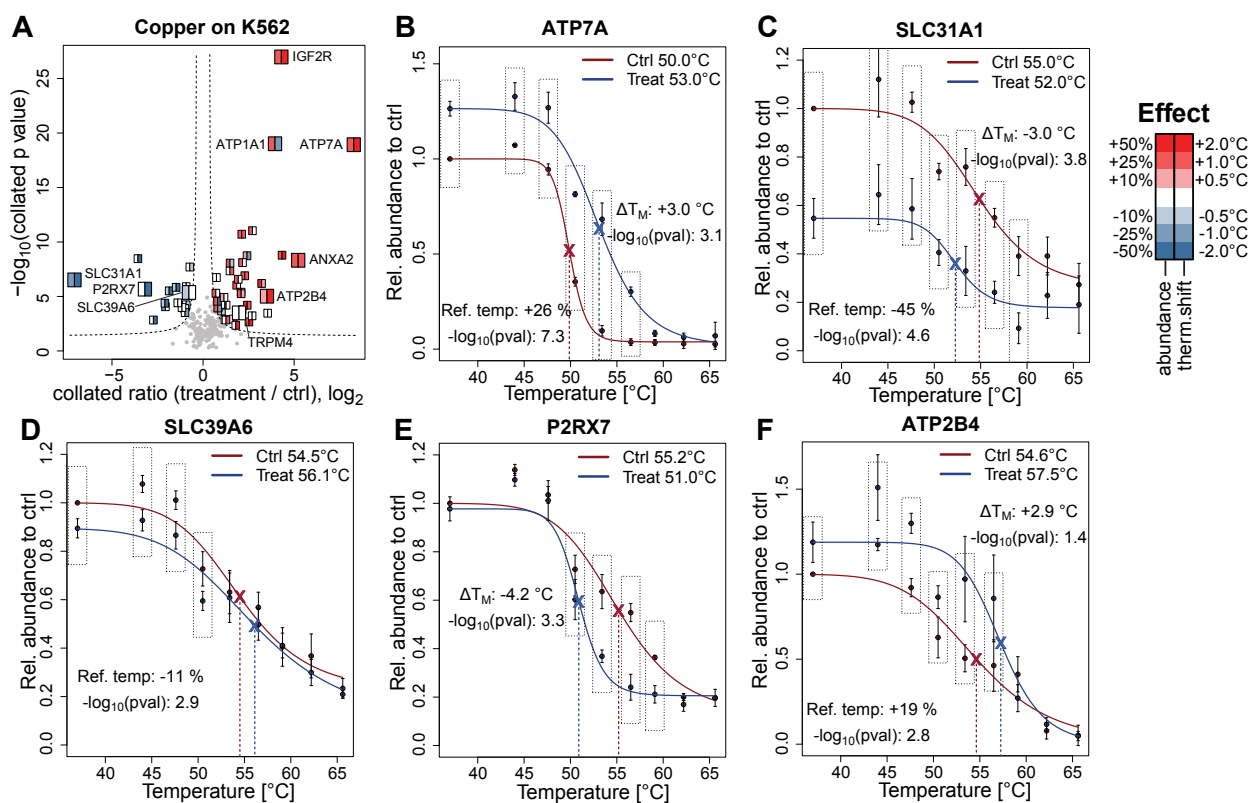
Fig. 64 Monitoring cellular stimulation by hypercupremia. K562 cells were treated in three biological replicates with 20 µM $CuSO_4$ or vehicle as control. (**A**) Selection of significantly affected proteins upon treatment are labeled. Left half of squares indicate significant abundance changes while right half of squares indicate significant thermal shifts. Median standard deviation between replicates: 0.17. (**B-F**) Mean melting curves in controls and treatments of significantly affected proteins. Error bars indicate standard deviations. Selected data points for cumulation are highlighted with dashed boxes. Treatment-induced thermal shifts and abundance changes are indicated with statistical significances.

Finally, cell surface thermal proteome profiling was evaluated for identification of HSP90 protein clients. For that purpose, cells were exposed to hyperthermia at 42 °C for 30 min in presence or absence of the HSP90 inhibitor luminespib. After additional 60 min in the incubator at 37 °C for recovery, the cell surface thermal proteome profiling approach was applied. Treatment with luminespib led to thermal stabilization of HSP90AA1 and HSP90AB1 as already previously observed (Fig. 65, supplemental Fig. 45 and Fig 58C). As most of the HSP90 client proteins belong to the families of tyrosine kinases and related tyrosine kinase-like proteins (Citri et al., 2006; Den and Lu, 2012), inhibition of the HSP90 proteins during hyperthermia resulted in reduced cell surface abundances of the receptor tyrosine kinases IGF1R and INSR. Other clients of HSP90 are non-receptor tyrosine kinases. Although these kinases cannot be directly analyzed with the cell surface thermal proteome profiling approach as they are not cell surface proteins, their reduced stability upon HSP90 inhibition still affected the stability of cell surface receptors to which they are associated. An example is the non-receptor tyrosine kinase TYK2 described to be constitutively associated to IL10RB (Shouval et al., 2014) and to be rapidly degraded upon HSP90 inhibition (Akahane et al., 2016). Similarly, janus kinases (JAKs), described to be associated with the interferon gamma receptor IFNGR1 (Sakatsume et al., 1995) as well as with the common gamma chain IL2RG (Kawahara et al., 1995), are clients of HSP90 proteins (Fridman and Sarlis, 2012; Bhagwat et al., 2014; Shang and Tomasi, 2006). Accordingly, these receptors, which are described to rely on associated non-receptor tyrosine kinases for signal transduction, were found with reduced cell surface abundances upon hyperthermia in presence of luminespib.
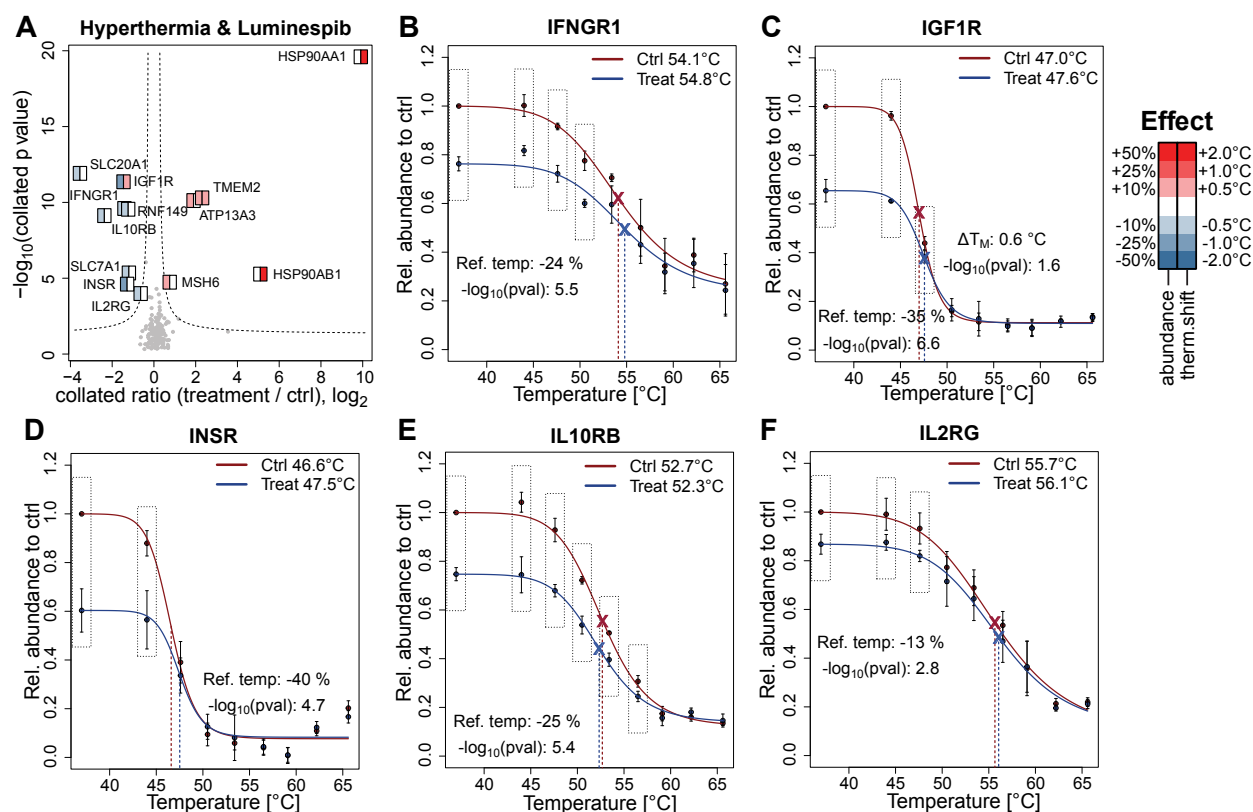
Fig. 65 Cell surface thermal proteome profiling for identification of HSP90-targeted proteins. U937 cells were treated in three biological replicates for 30 min with 1 µM luminespib or vehicle as control. Subsequently, cells were exposed to hyperthermia at 42 °C for 30 min followed by additional 60 min at 37 °C for recovery. (**A**) Significantly affected proteins upon treatment are labeled. Left half of squares indicate significant abundance changes while right half of squares indicate significant thermal shifts. Median standard deviation between replicates: 0.12. (**B-F**) Mean melting curves in controls and treatments of significantly affected proteins. Error bars indicate standard deviations. Selected data points for cumulation are highlighted with dashed boxes. Treatment-induced thermal shifts and abundance changes are indicated with statistical significances.

5. Discussion

5.1. Cell surface proteome mapping of cell lines and primary cells

Covalent tagging of glycoproteins on the cell surface is a commonly used approach for the analysis of the plasma membrane proteome by enabling selective enrichment of a major fraction of this subproteome. An advantage of this method is its remarkable selectivity (Zhang et al., 2014). This can be explained by the fact that most cytosolic proteins are not glycosylated thus making the approach intrinsically selective for cell surface proteins. Accordingly, glycosylation-directed cell surface proteome biotinylation outperformed an amine-directed covalent tagging strategy. In addition, it is also frequently applied e.g. for identifying cell surface markers or to map the cell surface proteome of cell lines (Wollscheid et al., 2009; Bausch-Fluck et al., 2015). Incorporation of the oxime-ligation catalyst aniline into the protocol enabled even increased speed and efficiency at low temperatures while maintaining high cell viability (Zeng et al., 2009) and reducing cellular responses induced by the biotinylation procedure. However, published glycoproteome tagging protocols usually focus on the identification of glycosylated peptides rather than on identifying all proteotypic peptides. Although this enables reduced sample complexities and increased selectivities for cell surface presented proteins, it is accompanied with a decreased mass spectrometry-based protein identification and quantification confidence as both are based on only few glycopeptides. Furthermore, since the commonly used protocols utilize a selective elution of enriched N-linked glycopeptides from the affinity resin by the endoglycosidase PNGase F, other O-linked cell surface glycoproteins might be missed. For that reason, the glycoproteome tagging strategy was intended to be optimized by incorporating all proteotypic peptides for qualitative and quantitative investigation of cell surface proteins. This enabled a more than two-fold increase in the number of identified plasma membrane annotated proteins and a two-fold increase in on average identified unique peptides. Utilization of PNGase F instead of tryptic on-bead digestion for a more selective elution of enriched cell surface glycoproteins from the affinity resin was not efficient. As this enzyme is typically used for cleavage at the N-linked glycosylation sites of enriched glycopeptides rather than complete proteins, this inefficiency might be explained by steric hindrances due to dense packing of the affinity resin and bound biotinylated proteins. Elution with PNGase F was only efficient after previous tryptic on-bead digestion. Analysis of the PNGase F elution fraction in addition to the tryptic on-bead digestion fraction added on average less than 5 % more plasma membrane proteins (supplemental Fig. 46). Thus, PNGase F elution was omitted. Alternative proteases for elution of enriched proteins were evaluated by *in-silico* digestion of UniProt-annotated plasma membrane proteins. Results suggested only chymotrypsin as a protease with comparable performance to trypsin with even slightly higher theoretical sequence coverages for transmembrane proteins (supplemental Fig. 47). Nevertheless, trypsin was selected as protease due to its efficiency, specificity and compatibility with electro spray ionization. With all incorporated optimizations, the cell surface proteome mapping technique outperformed the whole proteome analysis by achieving a 20 % higher coverage of cell surface transmembrane proteins while requiring less than 10% of the MS analysis time.

Plasma membrane proteome mapping was applied to chart the cell surface proteomes of commonly used model cell line systems and primary cells at a hitherto unprecedented depth detecting on average >800 plasma membrane proteins per cell type and >2400 distinct cell surface proteins in 21 different cell systems. These numbers compared very favorably to the 300 proteins per cell type and in total 1492 cell surface proteins from 41 human cell types detected in a recent publication (Bausch-Fluck et al., 2015). The achieved increase in cell surface proteome coverage can be attributed to more efficient labeling of surface proteins by

including aniline as catalyst, enrichment on protein level rather than on peptide level and improved MS instrumentation. The generated cell surface compendium can facilitate selecting the appropriate cell system in which proteins of interest are expressed in sufficient amounts to monitor responsiveness to external stimuli, cell signaling or drug transport. The marked differences observed in surface proteome composition between primary cell systems and corresponding cell lines of similar origin reflect a loss in functional specialization of cell lines due to a deprivation of cell surface antigens (Gedye et al., 2014) and are in line with altered responsiveness to many stimuli as well as differences in drug sensitivity (Dobson-Belaire et al., 2011; Lidington et al., 1999; Thonemann et al., 2002). Furthermore, lymphoid cell lines were observed to display a higher expression of transporters than corresponding primary cells. This can be explained by the fact that growth rate is an intrinsic selection criterion for cell lines in culture favoring elevated metabolism with the demand for higher nutrient uptake e.g. achieved by increased transporter expression (McCracken and Edinger, 2013). Solute carrier proteins represent a major group of such nutrient transporters which, in turn, can be hijacked for transporter-mediated drug uptake (Dobson and Kell, 2008; Kell et al., 2013; Winter et al., 2014). These observations suggest that data on drug uptake and drug potency for such cell lines might not be predictive for the *in vivo* situation and that candidate drug molecules should be tested in primary systems resembling the *in vivo* state as closely as possible (Cree et al., 2010).

5.2. Monitoring cell surface proteome dynamics and kinase inhibitor disturbances during cellular differentiation

Cell surface proteome maps are typically static representations of cellular states. However, human biology is determined by dynamic processes in which environmental changes or external stimuli induce cellular adaptation or differentiation. Monocytes, for example, circulate in the bloodstream and upon recruitment to damaged or infected tissues differentiate into macrophages (Daigneault et al., 2010). Previous studies (Wollscheid et al., 2009), as well as the data presented in this thesis, demonstrated major changes in the cell surface proteome between the end points of cellular differentiation. However, relatively little is known about the mechanisms underlying such differentiation processes and published studies are mainly based on transcript profiling (Martinez et al., 2006). Here, plasma membrane proteome changes during monocyte to macrophage differentiation were analyzed in a time resolved manner by making use of the high multiplexing capabilities of tandem mass tag based quantitative mass spectrometry. This approach for the first time enabled the comprehensive analysis of the dynamic remodeling processes of the cell surface proteome during differentiation of THP-1 cells into macrophages and provides unique insights into the underlying mechanisms. Remodeling on the cell surface occurs in three major steps. In a first step, collagens and other extracellular matrix proteins are secreted and proteins such as CD83, that are stored intracellularly, are relocalized to the plasma membrane (Cao et al., 2005). Due to the rapid response to the differentiation stimulus, this process must be to a large extent independent of *de novo* protein synthesis. Morphologically, the initial step manifests as the cells start to become adherent, suggesting that remodeling of the ECM and relocalization of PLAVB, CD83 and other proteins induce initial adherence of THP-1 cells. The second phase that partially overlaps with the first phase is dominated by internalization or degradation of no longer required surface markers, transporters and proteins regulating cell proliferation. While the internalization of some monocyte markers such as CD4 is very fast, abundances of some receptor tyrosine kinases such as the ephrin receptors steadily decrease over the course of two days. The third phase is dominated by delayed presentation of newly synthesized proteins at the plasma membrane that reflect altered nutritional requirements and functions of non-dividing macrophages. The delayed

de novo synthesis following degradation of no longer needed proteins suggests a highly energy efficient process that enables differentiation without temporarily increasing the biomass.

Differentiation of monocytes in the presence of the marketed kinase inhibitor dasatinib resulted in a major change of cellular morphology and impaired macrophage function. Dasatinib has been suggested to influence differentiation processes *in vitro* and *in vivo*, e.g. by enhancing megakaryocyte differentiation, by inhibiting platelet formation in mice (Mazharian et al., 2011) as well as by promoting retinoic acid-induced differentiation of AML cells (Kropf et al., 2010). The data presented here provides a detailed description of alterations in the cell surface proteome when monocytes are differentiated in the presence of dasatinib. Up-regulation of CLEC5A, described to be involved in osteoclastogenesis (Inui et al., 2009), was the most prominent change observed. Interestingly, dasatinib has already been described to affect osteoclasts by acting as a bone-modifying agent through enhancing the differentiation and function of osteoblasts while inhibiting osteoclast differentiation (Garcia-Gomez et al., 2012). These observations suggest that patients treated with dasatinib might suffer from a weakened immune system due to impaired replenishment with newly differentiated functional macrophages. As only some of the classic macrophage cell surface markers are affected, this drug effect might not be identified with targeted methods such as immunostaining or fluorescence-activated cell sorting (FACS). Sunitinib and imatinib, two other marketed kinase inhibitors, did not elicit this response. Since imatinib and dasatinib are both marketed ABL kinase inhibitors, an off-target activity of dasatinib must be responsible for the impaired differentiation. Ephrin receptors, which are potently inhibited by dasatinib, are expressed in monocytes and their presentation is regulated during monocyte to macrophage differentiation. This data and the known role of ephrin receptor tyrosine kinases in differentiation processes (Wilkinson, 2014) are suggestive for these proteins being the dasatinb off-targets responsible for the observed dysregulation of the monocyte to macrophage differentiation. As no selective ephrin receptor inhibitors are currently available, it is difficult to further investigate this hypothesis. However, RNA interference experiments could potentially aid in elucidating this dysregulation by inducing a temporary suppression of ephrin receptor expression. In summary, these findings suggest including cell differentiation assays more rigorously in preclinical testing of candidate drugs to detect such adverse drug effects at an early stage in drug discovery.

The presented qualitative and quantitative cell surface mapping technique allows detailed analyses of time and stimulus-dependent effects on the plasma membrane proteome to a depth of more than 1000 cell surface proteins in a single experiment. In contrast to methods monitoring transcript levels of known surface proteins, the plasma membrane proteome mapping approach enables the detection of altered subcellular localization and proteins presented from intracellular vesicles. The coverage of the cell surface proteome achieved with this mass spectrometry-based strategy greatly exceeds multiplexed immunohistochemistry-based approaches (Levenson et al., 2015) and in addition the approach is unbiased in nature. Using conventional fluorescence-based detection methods such as FACS, depletion of a specific cell population upon drug treatment can hardly be distinguished from perturbations in the cell surface proteome masking detection. However, it is important to note that this approach is primarily (Wollscheid et al., 2009) based on selective enrichment of sialylated cell surface proteins. Thus, non-sialylated glycoproteins may be missed. Furthermore, potential stimulus-dependent effects or modifications on protein sialylation as described e.g. for cellular differentiation processes (Wang et al., 2016; Keppler et al., 1999) might influence results. However, for most human glycosylated proteins the glyco structure is described to carry a sialic acid at the end of the glycan chain (Varki, 2007) and proper glycosylation has been previously shown to be necessary for surface delivery of proteins (Gahmberg and Tolvanen,

1996). In addition, it was shown that despite major changes in glycosylation during the differentiation of monocytic THP-1 cells into macrophage-like cells, no significant change in overall sialylation was observed (Delannoy et al., 2017).

5.3. Cell surface thermal proteome profiling for monitoring target engagement to plasma membrane proteins

Membrane proteins are important therapeutic targets, however, the discovery and analysis of drug interactions with membrane targets still represents a challenging task. Most approaches like differential scanning fluorimetry (Hofmann et al., 2016) or surface plasmon resonance spectroscopy (Patching, 2014) are performed in lysates or from purified proteins and as such require extraction of proteins from their native cellular environment often resulting in denaturation and inactivation of membrane proteins (Seddon et al., 2004). Furthermore, these approaches usually only monitor predefined protein targets and drugs under investigation often need to be chemically modified to attach, for example, an enrichment handle or a fluorophore. In contrast, the recently described thermal proteome profiling approach (TPP, Savitski et al., 2014) enables an unbiased identification of protein targets of small molecules in live cells and does not require chemical modifications of these molecules. TPP has been successfully applied for the identification of intracellular drug targets. However, frequent targets for pharmaceutical intervention are transmembrane proteins containing cell surface accessible domains. A revised TPP protocol incorporating the mild detergent IGEPAL CA-630 extended the target space of this approach towards integral membrane proteins (Reinhard et al., 2015; Huber et al., 2015). Nevertheless, the analysis of transmembrane proteins and their interactions is still challenging especially due to their low abundances compared to many cytosolic proteins. As a result, long mass spectrometry analysis times are required to achieve sufficient proteome coverage. Reinhard et al. invested a total MS analysis time of 60 hours per experimental TPP replicate (one control and one treatment) for analyzing the effects of pervanadate treatment on the T-cell receptor pathway in Jurkat cells. On average, 1200 plasma membrane annotated proteins were identified with good quantification per sample. However, similar to the previous comparison of the cell surface mapping technology with deep whole proteome analysis, the majority of these proteins were not integral membrane proteins but included enzymes and other proteins that are localized to the cytosolic side of the plasma membrane. When focusing on proteins with annotated transmembrane domains, on average 380 annotated integral membrane cell surface proteins were quantified per sample in this study. Furthermore, due to the total lysis of the cells, this approach does not distinguish between cell surface presented and intracellularly stored fractions of plasma membrane annotated proteins. As often only the fraction of the protein pool accessible on the cell surface is therapeutically relevant, this spatial averaging might mask effects.

To specifically analyze cell surface presented proteins, thermal proteome profiling was combined with the above described selective enrichment of glycosylated plasma membrane proteins. The enrichment of cell surface proteins reduces sample complexity thus less MS analysis time is required while still enabling an extensive coverage of this subproteome. Furthermore, the approach only focuses on the cell surface presented fraction of plasma membrane proteins. This cell surface thermal proteome profiling (CSTPP) approach enabled quantification of on average 380 plasma membrane associated proteins and 225 cell surface transmembrane proteins with 2 hours of total MS analysis time per sample and 4h per experimental replicate from Jurkat cells. Thus, the CSTPP approach allows the quantification of almost ten times more cell surface transmembrane proteins per utilized MS analysis time compared to the previously published TPP protocol (113 proteins/h in CSTPP vs. 13 proteins/h

in TPP). For evaluation of the CSTPP approach, the short analysis time of 2 hours per sample was kept although this only allowed a robust quantification of about 45 % (225 vs 503 proteins in cell surface mapping) of the theoretical observable cell surface transmembrane target space.

Melting curves of transmembrane proteins have been shown to deviate from cytosolic proteins (Reinhard et al., 2015) and the experimental design using melting curves suffers from low sensitivity for detecting small changes in thermal stability (Savitski et al., 2014). Initial CSTPP experiments using melting curve-based data analysis as applied for TPP did not consistently result in a robust detection of thermal shifts for positive controls. Furthermore, an increased false positive rate was observed. A crucial part of the TPP data analysis is the normalization of melting curves to reduce variability between parallel experiments (Franken et al., 2015). However, in case of the CSTPP experiments, only few proteins fulfilled the selection criteria to be used for determining normalization factors thus resulting in inaccurate data normalization. In addition, the melting behavior of several plasma membrane proteins could not be accurately described by sigmoidal curves. To address these weaknesses, a new sample and data analysis scheme which does not depend on the fitting of melting curves, was introduced. This new data analysis approach vastly improved data quality and enabled more robust detection of treatment-induced effects. Furthermore, whereas the previous approach only fitted melting curves and failed to detect protein abundance changes, the new analysis strategy also precisely quantifies these treatment-induced effects. Especially for cell surface membrane proteins, the additional information about protein spatial changes is of great importance, as e.g. receptor internalization upon ligand binding is a common cellular mechanism for the attenuation of signaling pathways (Sorkin and von Zastrow, 2009).

The cell surface thermal proteome profiling approach was benchmarked with a total of 31 different cellular treatments (small molecules, native ligands, antibodies) targeting plasma membrane proteins. These experiments were conducted in 5 different non-adherent cell lines selected according to the observed expression of expected cell surface protein targets in the compendium of cell surface proteome mappings. In total, 1200 plasma membrane proteins (about 300 receptors and 160 transporters) were quantified (supplemental Fig. 48) with an average fractional abundance of about 70 % for cell surface proteins which indicated good enrichment efficiency. A general data analysis revealed correlation of determined melting points with physicochemical properties of cell surface proteins (Fig. 66).
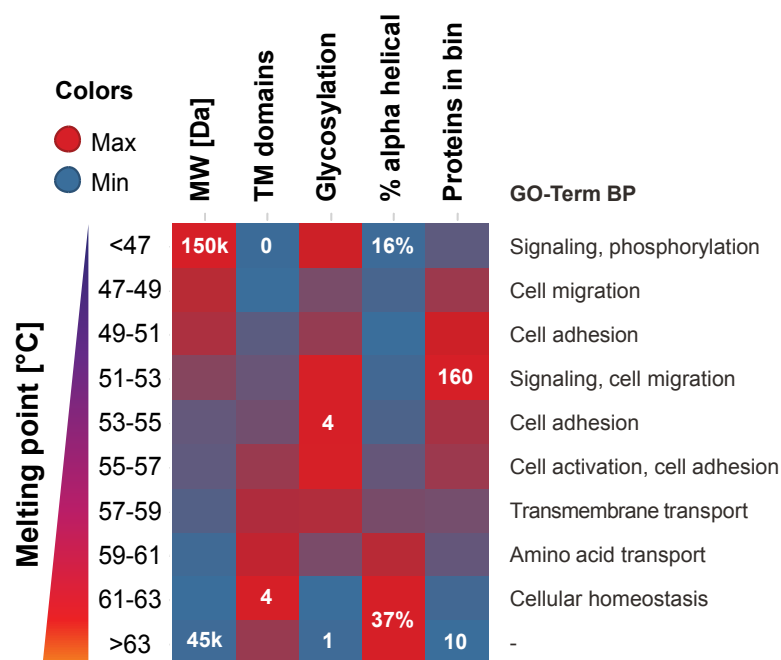
Fig. 66 Correlation of thermal stability with physicochemical properties of cell surface proteins. Overall analysis of identified plasma membrane proteins based on the physicochemical properties (as annotated by UniProt) molecular weight (MW), transmembrane (TM) domains, glycosylations and relative content of alpha helical structures. Data was filtered for proteins quantified in at least 2 replicates of at least 2 experiments with $R^2 \geq 0.8$ of melting curves and standard deviations of determined melting points < 3 °C. Proteins are binned by their determined average melting points. Average values for each bin of the physicochemical properties are color shaded between blue (min) and red (max). Minimal and maximal values are indicated. Numbers of proteins per melting point bin are shown in the last column of the heat map. Enriched GO-terms of biological processes (Benjamini-Hochberg corrected p-value < 0.05) for proteins in each melting point bin are indicated.

The observed protein thermal stability increased with decreasing molecular weight, increasing numbers of transmembrane domains and an increasing content of alpha helical secondary structures. In line with these observations, Leuenberger et al. recently described an inverse correlation between protein length and thermal stability (Leuenberger et al., 2017). Furthermore, the alpha helical structure of transmembrane domains is described to be highly thermostable (Haltia and Freire, 1995) suggesting an increasing protein thermal stability with increasing numbers of transmembrane domains or in general increasing content of alpha helical secondary structures. Accordingly, GO-term enrichment analysis of biological processes for proteins binned by observed melting points showed the terms "transport" and "amino acid transport" as most significantly enriched (Benjamini-Hochberg corrected p-value < 0.05) for proteins with high melting points. The number of annotated glycosylation sites revealed no obvious correlation with determined melting points.

In 70 % of the conducted validation experiments, significant effects were detected for expected direct targets, interactors or downstream targets. Besides the detection of target engagement with small molecule inhibitors, native ligands and biopharmaceuticals, CSTPP also enabled the monitoring of cellular stimulations like T-cell activation or hypercupremia as well as identification of client proteins for HSP90 chaperones. Furthermore, CSTPP enabled identification of two new potential markers for early detection of cellular stress responses. Treatments with different toxins resulted in the detection of a common effect on VLDLR and IGF2R with the latter being already described to be involved in the regulation of apoptosis (Chu et al., 2009). The remaining 30 % of the conducted validation experiments produced false negative outcomes. A major group of these experiments involved cellular treatments with small molecule inhibitors targeting SLC

transporters or GPCRs. These protein classes typically have a high number of alpha helical transmembrane (TM) domains (SLCs: 10-14 TM domains (Schlessinger et al., 2013), GPCR: 7 TM domains (Kobilka, 2007)). Furthermore, the binding sites of the tested compounds are described to be located within these membrane spanning domains. TM domains are highly thermal stable regions and retain most of their secondary structure even at elevated temperatures. Consequently, thermal denaturation of transmembrane proteins is predominantly driven by their extramembrane domains (Haltia and Freire, 1995). As GPCRs and SLCs mainly consist of TM domains while the extracellular parts are also primarily of alpha helical structure, protein thermal stability can only be negligibly affected by ligand-binding thus explaining the false negative observations. These results suggest that SLCs and GPCRs might in general not be accessible for thermal proteome profiling. However, many cell surface receptors are internalized upon ligand binding (Sorkin and von Zastrow, 2009). Thus, competition experiments monitoring reduced ligand-induced receptor internalization demonstrated the ability of CSTPP to also detect target engagement to GPCRs as exemplified for CXCR4, its ligand CXCL12 and the inhibitor IT1t.

In addition to target classes which are prone to produce false negative outcomes, some members of protein classes which were demonstrated to be accessible to the approach and are known to bind to the tested compound, showed no significant effect. For example, the integrin ITGB1 was not affected by cellular treatments with integrin inhibitors, whereas other integrins (e.g. ITGAV, ITGB3) showed a clear effect. Integrins form functional heterodimers composed of an alpha and a beta subunit thereby defining their binding specificity for endogenous ligands often containing a specific amino acid recognition sequence (Humphries, 2006). Both tested small molecule RGD-mimetics resulted in the detection of target engagement to the alpha subunit ITGAV as well as the beta subunits ITGB3 and ITGB5. Besides these integrins described to form RGD-binding heterodimers, ITGAV is also described to form RGD-binding complexes with ITGB1 (Humphries, 2006). Nevertheless, CSTPP failed to detect treatment-induced effects on this integrin beta subunit. This outcome could be explained either by the absence of functional complexes between ITGAV and ITGB1 on both tested cell lines (K562 and Jurkat cells) or by a stoichiometry issue caused by highly different expression levels of both receptors. For the latter case: if one complex partner is present with a much higher copy number although complexes are formed in a 1:1 ratio, this results in a low fraction of this protein to be actually forming the functional heterodimer while the remainder of the protein population is for example forming other complexes. Interestingly, when comparing protein abundances estimated from the signal intensities in the mass spectrometric analyses, ITGAV represents only 9 % of the total abundance of ITGB1. Consequently, only these 9 % of ITGB1 are able to form a functional RGD-binding complex and can show a treatment-induced effect. However, as proteomics does not distinguish between subpopulations of a protein and thus quantifies the average response of the entire protein population, a treatment-induced effect on this small fraction of ITGB1 cannot be detected. As ITGB3 and ITGB5 together represent only about 10 % of the total ITGAV abundance and since ITGAV showed highly significant treatment-induced effects, the majority of the remaining 90 % of ITGAV have to be in a RGD-binding functional complex (supplemental Fig. 49). The only other interaction partner at sufficient abundance and capable of forming a RGD-binding complex with ITGAV is ITGB1 suggesting that functional complexes between both are present. In summary, these results demonstrate that only those proteins are accessible for a thermal proteome profiling approach for which the majority of the protein pool is accessible for compound binding.

Thermal proteome profiling is a target engagement assay. The lack of an observed thermal shift for proteins with a proven ability to be accessible for the assay can thus also indicate that no

target engagement occurred in the analyzed cell system. An example is the receptor tyrosine kinase EPHB1 which was not affected by cellular treatment with dasatinib although this kinase is among the most potently hit targets of the tested inhibitor in the kinobeads competition assay (pIC_{50} 2.6 nM, see figure 46). The successful detection of target engagement with CSTPP to other members of this group of receptor tyrosine kinases as well as the high structural similarity within this class of proteins suggests that ephrin receptors in general can be accessed with the methodology. Thus, the lack of an observed treatment-induced effect on EPHB1 with dasatinib suggests a blocked target engagement in live THP-1 cells rather than a false negative result. Dasatinib is a type-1 kinase inhibitor that targets kinase domains in their active form (Kothiwale et al., 2015). The activity of RTKs is in general regulated by phosphorylation of the kinase activation loop which, in the inactive non-phosphorylated state, blocks the active site of the kinase (Huse and Kuriyan, 2002). A special mechanism for ephrin receptor inactivation involves inhibitory lateral cis interactions between ephrin receptors and ephrin ligands co-expressed on the same cell (Falivelli et al., 2013). Interestingly, EFNB1, a ligand of EPHB1, but no other ephrin ligand was identified on the surface of THP-1 cells. These findings suggest inaccessibility of the active site of the EPHB1 kinase domain for dasatinib due to cis-inhibition by EFNB1 as a likely reason for the reduced binding affinity of dasatinib. These results underline the importance and benefits of cell-based methodologies as lysate-based experiments might abrogate such interactions and thus could be non-predictive for phenotypic effects in live cells.

In addition to target engagement, thermal proteome profiling has also been applied to monitor downstream effects of cellular treatments. Savitski et al. demonstrated thermal destabilization of CRKL, a downstream effector of BCR-ABL signaling, upon dasatinib treatment (Savitski et al., 2014) most likely triggered by phosphorylation changes in the protein. Similarly, Reinhard et al. observed changes on downstream effectors upon cellular treatment with the unspecific protein-tyrosine phosphatase inhibitor pervanadate (Reinhard et al., 2015). Equally, downstream effects can be observed by CSTPP induced by changes in post-translational modification or changes in protein-protein interactions. However, beyond that, CSTPP also enables the detection of downstream effects which affect protein cell surface abundance either by changes in the overall protein turnover or by internalization as well as presentation. An example for the detection of downstream effects is the observed thermal stabilization of JAG1 in addition to TGFBR1 upon cellular treatment with the TGF-beta 1 receptor inhibitor SB431542. JAG1 is required for a subset of TGFB1 responses (Nyhan et al., 2010; Zavadil et al., 2004) and its induction by TGFB1 is down-regulated by TGF receptor inhibitors (Zhang et al., 2010). Furthermore, this experiment revealed a treatment-induced internalization of MCT1 (SLC16A1) and MCT3 (SLC16A3). Interestingly, SB431542 has been described to block oncogenic activities mediated by the monocarboxylate transporter MCT1. This transporter is related to the enhanced glycolytic flux (Warburg effect, Warburg, 1956) in cancer cells by enabling the export of the increased formation of intracellular lactate (Xu et al., 2017) which otherwise results in toxic intracellular acidification (Doherty and Cleveland, 2013). CSTPP explains the therapeutic effect of SB431542 on MCT1 by pinpointing it to the internalization of the monocarboxylate transporters. These results are further validated by an observed treatment-induced effect on the bicarbonate transporter SLC4A2 which is involved in the regulation of intracellular pH (Romero et al., 2013) counteracting intracellular acidification.

Another example for an observed biologically relevant downstream effect is the stabilization of the very-low-density-lipoprotein receptor VLDLR upon treatment with the kinase inhibitor dasatinib. The lack of a nucleotide binding domain in VLDLR as well as the fact that chemoproteomic profilings have not shown VLDLR as a dasatinib target (Li et al., 2010; Rix et al., 2007; Shi et al., 2012) makes this protein an unlikely direct target of dasatinib. However,

clinical studies with receptor tyrosine kinase (RTK) inhibitors showed increased blood lipid levels in treated chronic myeloid leukemia patients (Iizuka et al., 2016; Iurlo et al., 2015) suggesting a connection between dasatinib treatment and blood lipid homeostasis. A ligand of VLDLR is VLDL which is composed of cholesterol, triglycerides and apolipoproteins. In CSTPP experiments, stimulation of THP-1 cells with VLDL showed no observable effect on VLDLR. In line with this finding, the observed thermal stabilization of VLDLR by dasatinib was not affected by the presence of VLDL. However, this co-treatment revealed other effects of dasatinib only observed during VLDL stimulation. These included receptor internalization of KIT, already observed to be thermally stabilized upon cellular treatment with dasatinib, as well as receptor internalization and thermal destabilization of IL6R. Interestingly, the cytokine IL6 has been described to be involved in the regulation of the lipid metabolism by inducing expression of VLDLR and LDLR, thereby resulting in increased uptake and degradation of lipoproteins (Gierens et al., 2000; Hashizume et al., 2010). Furthermore, antibody-based blockade of IL6R in rheumatoid arthritis patients resulted in increased blood lipid levels (Hashizume et al., 2010). Thus, the observed effects of dasatinib in monocytes on VLDLR and the removal of IL6R from the cell surface can be related to the dysregulated lipid metabolism observed in RTK inhibitor therapy.

In summary, cell surface thermal proteome profiling allows thermal profiling analysis of cell surface presented proteins. This method offers a more comprehensive characterization of treatment-induced effects on this subproteome while reducing required MS analysis time. An optimized sample and data analysis scheme vastly improved data quality and allows detection of treatment-induced protein thermal stability changes along with cell surface presentation changes. The combined analysis of these effects provides an unbiased measure of drug-target occupancy, enables the investigation of treatment-induced downstream effects on the cell surface and thus facilitates the identification of markers for drug efficacy and toxicity.

6. Future perspectives

The plasma membrane proteome is a prominent target for pharmaceutical intervention due to its fundamental roles in many biological processes bearing opportunities for identification of novel therapeutic targets and therapies. Consequently, techniques facilitating the unbiased work with this subproteome have a major impact on basic science and drug discovery. This thesis aimed at developing techniques targeting the plasma membrane proteome to enable novel insights into biology and to facilitate analysis of drug effects. The utility of these techniques was demonstrated on selected examples, e.g. for monitoring cellular differentiation as well as perturbation of this process by dasatinib. However, there is a plethora of further applications awaiting to be further explored. For example, this thesis just scratched the surface of the plasma membrane proteomes of common cell line model systems and primary cells. An expansion of the generated compendium of cell surface proteome maps to more cell lines and primary cell types would be a step towards comprehensive description of plasma membrane proteomes. This would facilitate the selection of the most relevant *in vitro* cell system to address biological questions. Interestingly, several cell types like immune cells are characterized by a large cell population heterogeneity (Satija and Shalek, 2014). Expression proteomics of cell subpopulations is a powerful approach to analyze this heterogeneity (Rieckmann et al., 2017). However, the coverage of cell surface proteins with conventional proteomic approaches has been limited so far. Utilizing FACS to isolate cell subpopulations followed by cell surface proteomics has the potential to enhance characterization of these populations. Furthermore, the extension of the cell surface proteome mapping to primary tissues, in contrast to pure cell populations as described so far, would broaden the scope towards even more physiologically relevant specimen and has the potential to facilitate modern biomarker discovery (Longuespée et al., 2014). Monitoring of dynamic processes during cellular differentiation revealed major rearrangements on the cell surface proteome. Yet, the impact of such dynamic processes for drug discovery has so far been neglected. For example, analyzing plasma membrane proteome changes during lineage differentiation of stem cells offers enormous potential for the identification of novel therapeutic targets and therapies (Nagano et al., 2008).

Cell surface selective thermal proteome profiling fills a gap in analyzing target engagement to the cell surface proteome. Despite the large number of successful examples, the here established methodology still has opportunities for further improvements. CSTPP has so far been evaluated for lymphoid and monocytic cell line model systems, but e.g. epithelial and primary cell systems have not been analyzed, yet. Furthermore, the CSTPP approach encountered false negative observations, similar to other target engagement assays. For example, no effect was detected for small molecules targeting GPCRs. In this specific case, this impairment could be circumvented by competition experiments in which ligand-induced receptor internalization in presence of a small molecule inhibitor was reduced. To obtain an unbiased GPCR-focused target engagement assay, a mixture of known native ligands of the GPCRome (Kroeze et al., 2015) could be utilized for simultaneous analysis of reduced ligand-induced receptor internalization in the presence of a molecule of interest. GPCRs are the most frequently targeted protein class by FDA approved drugs (Overington et al., 2006) and such a GPCR-focused CSTPP-based target engagement assay could further advance and facilitate the drug discovery process. Beyond the application of CSTPP in drug discovery, this methodology could be used for a more comprehensive analysis of stimulus-induced effects on the cell surface proteome. Changes in thermal stability or surface presentation of this subproteome upon a treatment or stimulation may be indicative for alterations in protein activity, complex partners or changes in PTMs and thus could point towards hitherto unidentified effects. The opportunities of such novel analysis strategies have been demonstrated e.g. by the utilization of limited proteolysis for a global analysis of protein structural changes during metabolic transition (Feng et al., 2014). Similarly, CSTPP could shed new light on many cellular processes and could enable novel insights into systems biology.

7. References

Aebersold, R., and Mann, M. (2003). Mass spectrometry-based proteomics. Nature *422*, 198–207.

Akahane, K., Sanda, T., Mansour, M.R., Radimerski, T., DeAngelo, D.J., Weinstock, D.M., and Look, A.T. (2016). HSP90 inhibition leads to degradation of the TYK2 kinase and apoptotic cell death in T-cell acute lymphoblastic leukemia. Leukemia *30*, 219–228.

Alberts, B., Johnson, A., Lewis, J., Raff, M., Roberts, K., and Walter, P. (2002). Molecular biology of the cell (New York: Garland Science).

Alexa, A., and Rahnenfuhrer, J. (2015). topGO: Enrichment analysis for Gene Ontology.

Anderle, P., Huang, Y., and Sadée, W. (2004). Intestinal membrane transport of drugs and nutrients: genomics of membrane transporters using expression microarrays. Eur. J. Pharm. Sci. Off. J. Eur. Fed. Pharm. Sci. *21*, 17–24.

Auwerx, J., Staels, B., Van Vaeck, F., and Ceuppens, J.L. (1992). Changes in IgG Fc receptor expression induced by phorbol 12-myristate 13-acetate treatment of THP-1 monocytic leukemia cells. Leuk. Res. *16*, 317–327.

d'Azzo, A., Bongiovanni, A., and Nastasi, T. (2005). E3 ubiquitin ligases as regulators of membrane protein trafficking and degradation. Traffic Cph. Den. *6*, 429–441.

Bantscheff, M. (2012). Mass spectrometry-based chemoproteomic approaches. Methods Mol. Biol. Clifton NJ *803*, 3–13.

Bantscheff, M., and Drewes, G. (2012). Chemoproteomic approaches to drug target identification and drug profiling. Bioorg. Med. Chem. *20*, 1973–1978.

Bantscheff, M., Eberhard, D., Abraham, Y., Bastuck, S., Boesche, M., Hobson, S., Mathieson, T., Perrin, J., Raida, M., Rau, C., et al. (2007). Quantitative chemical proteomics reveals mechanisms of action of clinical ABL kinase inhibitors. Nat. Biotechnol. *25*, 1035–1044.

Bantscheff, M., Hopf, C., Savitski, M.M., Dittmann, A., Grandi, P., Michon, A.-M., Schlegl, J., Abraham, Y., Becher, I., Bergamini, G., et al. (2011). Chemoproteomics profiling of HDAC inhibitors reveals selective targeting of HDAC complexes. Nat. Biotechnol. *29*, 255–265.

Bantscheff, M., Lemeer, S., Savitski, M.M., and Kuster, B. (2012). Quantitative mass spectrometry in proteomics: critical review update from 2007 to the present. Anal. Bioanal. Chem. *404*, 939–965.

Bausch-Fluck, D., Hofmann, A., Bock, T., Frei, A.P., Cerciello, F., Jacobs, A., Moest, H., Omasits, U., Gundry, R.L., Yoon, C., et al. (2015). A mass spectrometric-derived cell surface protein atlas. PloS One *10*, e0121314.

Becher, I., Savitski, M.M., Savitski, M.F., Hopf, C., Bantscheff, M., and Drewes, G. (2013). Affinity profiling of the cellular kinome for the nucleotide cofactors ATP, ADP, and GTP. ACS Chem. Biol. *8*, 599–607.

Bhagwat, N., Koppikar, P., Keller, M., Marubayashi, S., Shank, K., Rampal, R., Qi, J., Kleppe, M., Patel, H.J., Shah, S.K., et al. (2014). Improved targeting of JAK2 leads to increased therapeutic efficacy in myeloproliferative neoplasms. Blood *123*, 2075–2083.

Bhandari, D., Robia, S.L., and Marchese, A. (2009). The E3 ubiquitin ligase atrophin interacting protein 4 binds directly to the chemokine receptor CXCR4 via a novel WW domain-mediated interaction. Mol. Biol. Cell *20*, 1324–1339.

Bischof, J.C., Padanilam, J., Holmes, W.H., Ezzell, R.M., Lee, R.C., Tompkins, R.G., Yarmush, M.L., and Toner, M. (1995). Dynamics of cell membrane permeability changes at supraphysiological temperatures. Biophys. J. *68*, 2608–2614.

Boersema, P.J., Raijmakers, R., Lemeer, S., Mohammed, S., and Heck, A.J.R. (2009). Multiplex peptide stable isotope dimethyl labeling for quantitative proteomics. Nat. Protoc. *4*, 484–494.

Boisvert, F.-M., Lam, Y.W., Lamont, D., and Lamond, A.I. (2010). A quantitative proteomics analysis of subcellular proteome localization and changes induced by DNA damage. Mol. Cell. Proteomics MCP *9*, 457–470.

Bose, T.O., Pham, Q.-M., Jellison, E.R., Mouries, J., Ballantyne, C.M., and Lefrançois, L. (2013). CD11a regulates effector CD8 T cell differentiation and central memory development in response to infection with Listeria monocytogenes. Infect. Immun. *81*, 1140–1151.

Bowie, J.U. (2005). Solving the membrane protein folding problem. Nature *438*, 581–589.

Brönstrup, M. (2004). Absolute quantification strategies in proteomics based on mass spectrometry. Expert Rev. Proteomics *1*, 503–512.

Brown, M.B. (1975). A Method for Combining Non-Independent, One-Sided Tests of Significance. Biometrics *31*, 987.

Burbaum, J., and Tobal, G.M. (2002). Proteomics in drug discovery. Curr. Opin. Chem. Biol. *6*, 427–433.

Burkhart, J.M., Schumbrutzki, C., Wortelkamp, S., Sickmann, A., and Zahedi, R.P. (2012). Systematic and quantitative comparison of digest efficiency and specificity reveals the impact of trypsin quality on MS-based proteomics. J. Proteomics *75*, 1454–1462.

Cabodi, S., Di Stefano, P., Leal, M. del P.C., Tinnirello, A., Bisaro, B., Morello, V., Damiano, L., Aramu, S., Repetto, D., Tornillo, G., et al. (2010). Integrins and signal transduction. Adv. Exp. Med. Biol. *674*, 43–54.

Cai, L., Makhov, A.M., Schafer, D.A., and Bear, J.E. (2008). Coronin 1B antagonizes cortactin and remodels Arp2/3-containing actin branches in lamellipodia. Cell *134*, 828–842.

Cao, W., Lee, S.H., and Lu, J. (2005). CD83 is preformed inside monocytes, macrophages and dendritic cells, but it is only stably expressed on activated dendritic cells. Biochem. J. *385*, 85–93.

Capdeville, R., Buchdunger, E., Zimmermann, J., and Matter, A. (2002). Glivec (STI571, imatinib), a rationally developed, targeted anticancer drug. Nat. Rev. Drug Discov. *1*, 493–502.

Cech, N.B., and Enke, C.G. (2001). Practical implications of some recent studies in electrospray ionization fundamentals. Mass Spectrom. Rev. *20*, 362–387.

César-Razquin, A., Snijder, B., Frappier-Brinton, T., Isserlin, R., Gyimesi, G., Bai, X., Reithmeier, R.A., Hepworth, D., Hediger, M.A., Edwards, A.M., et al. (2015). A Call for Systematic Research on Solute Carriers. Cell *162*, 478–487.

References

Cha, S.H., Sekine, T., Fukushima, J.I., Kanai, Y., Kobayashi, Y., Goya, T., and Endou, H. (2001). Identification and characterization of human organic anion transporter 3 expressing predominantly in the kidney. Mol. Pharmacol. *59*, 1277–1286.

Chait, B.T. (2006). Chemistry. Mass spectrometry: bottom-up or top-down? Science *314*, 65–66.

Chakraborty, A.B., and Berger, S.J. (2005). Optimization of reversed-phase peptide liquid chromatography ultraviolet mass spectrometry analyses using an automated blending methodology. J. Biomol. Tech. JBT *16*, 327–335.

Chattopadhyay, S., and Sen, G.C. (2014). Tyrosine phosphorylation in Toll-like receptor signaling. Cytokine Growth Factor Rev. *25*, 533–541.

Cheng, Y., and Prusoff, W.H. (1973). Relationship between the inhibition constant (K1) and the concentration of inhibitor which causes 50 per cent inhibition (I50) of an enzymatic reaction. Biochem. Pharmacol. *22*, 3099–3108.

Chin, S., Hughes, M.P., Coley, H.M., and Labeed, F.H. (2006). Rapid assessment of early biophysical changes in K562 cells during apoptosis determined using dielectrophoresis. Int. J. Nanomedicine *1*, 333–337.

Choudhary, C., and Mann, M. (2010). Decoding signalling networks by mass spectrometry-based proteomics. Nat. Rev. Mol. Cell Biol. *11*, 427–439.

Christiansen, M.N., Chik, J., Lee, L., Anugraham, M., Abrahams, J.L., and Packer, N.H. (2014). Cell surface protein glycosylation in cancer. Proteomics *14*, 525–546.

Chu, C.-H., Tzang, B.-S., Chen, L.-M., Liu, C.-J., Tsai, F.-J., Tsai, C.-H., Lin, J.A., Kuo, W.-W., Bau, D.-T., Yao, C.-H., et al. (2009). Activation of insulin-like growth factor II receptor induces mitochondrial-dependent apoptosis through G(alpha)q and downstream calcineurin signaling in myocardial cells. Endocrinology *150*, 2723–2731.

Citri, A., Harari, D., Shohat, G., Ramakrishnan, P., Gan, J., Lavi, S., Eisenstein, M., Kimchi, A., Wallach, D., Pietrokovski, S., et al. (2006). Hsp90 Recognizes a Common Surface on Client Kinases. J. Biol. Chem. *281*, 14361–14369.

Cook, G.A., Longhurst, C.M., Grgurevich, S., Cholera, S., Crossno, J.T., and Jennings, L.K. (2002). Identification of CD9 extracellular domains important in regulation of CHO cell adhesion to fibronectin and fibronectin pericellular matrix assembly. Blood *100*, 4502–4511.

Cooper, G.M. (2000). The cell: a molecular approach (Washington, DC: ASM Press [u.a.]).

Cordwell, S.J., and Thingholm, T.E. (2010). Technologies for plasma membrane proteomics. Proteomics *10*, 611–627.

Cox, J., and Mann, M. (2009). Computational principles of determining and improving mass precision and accuracy for proteome measurements in an Orbitrap. J. Am. Soc. Mass Spectrom. *20*, 1477–1485.

Cravatt, B.F., Wright, A.T., and Kozarich, J.W. (2008). Activity-based protein profiling: from enzyme chemistry to proteomic chemistry. Annu. Rev. Biochem. *77*, 383–414.

Cree, I.A., Glaysher, S., and Harvey, A.L. (2010). Efficacy of anti-cancer agents in cell lines versus human primary tumour tissue. Curr. Opin. Pharmacol. *10*, 375–379.

Cummings, R.D. (2009). The repertoire of glycan determinants in the human glycome. Mol. Biosyst. *5*, 1087–1104.

Daigneault, M., Preston, J.A., Marriott, H.M., Whyte, M.K.B., and Dockrell, D.H. (2010). The identification of markers of macrophage differentiation in PMA-stimulated THP-1 cells and monocyte-derived macrophages. PloS One *5*, e8668.

De Baets, M.H. (1994). Autoimmune diseases against cell surface receptors: myasthenia gravis, a prototype anti-receptor disease. Neth. J. Med. *45*, 294–301.

Deeb, S.J., D'Souza, R.C.J., Cox, J., Schmidt-Supprian, M., and Mann, M. (2012). Super-SILAC allows classification of diffuse large B-cell lymphoma subtypes by their protein expression profiles. Mol. Cell. Proteomics MCP *11*, 77–89.

Delannoy, C.P., Rombouts, Y., Groux-Degroote, S., Holst, S., Coddeville, B., Harduin-Lepers, A., Wuhrer, M., Elass-Rochard, E., and Guérardel, Y. (2017). Glycosylation Changes Triggered by the Differentiation of Monocytic THP-1 Cell Line into Macrophages. J. Proteome Res. *16*, 156–169.

Den, R.B., and Lu, B. (2012). Heat shock protein 90 inhibition: rationale and clinical potential. Ther. Adv. Med. Oncol. *4*, 211–218.

Dengjel, J., Kratchmarova, I., and Blagoev, B. (2010). Mapping protein-protein interactions by quantitative proteomics. Methods Mol. Biol. Clifton NJ *658*, 267–278.

Desai, B., Ma, T., Zhu, J., and Chellaiah, M.A. (2009). Characterization of the expression of variant and standard CD44 in prostate cancer cells: identification of the possible molecular mechanism of CD44/MMP9 complex formation on the cell surface. J. Cell. Biochem. *108*, 272–284.

Di, L., Artursson, P., Avdeef, A., Ecker, G.F., Faller, B., Fischer, H., Houston, J.B., Kansy, M., Kerns, E.H., Krämer, S.D., et al. (2012). Evidence-based approach to assess passive diffusion and carrier-mediated drug transport. Drug Discov. Today *17*, 905–912.

Dobson, P.D., and Kell, D.B. (2008). Carrier-mediated cellular uptake of pharmaceutical drugs: an exception or the rule? Nat. Rev. Drug Discov. *7*, 205–220.

Dobson-Belaire, W.N., Cochrane, A., Ostrowski, M.A., and Gray-Owen, S.D. (2011). Differential response of primary and immortalized CD4+ T cells to Neisseria gonorrhoeae-induced cytokines determines the effect on HIV-1 replication. PloS One *6*, e18133.

Doherty, J.R., and Cleveland, J.L. (2013). Targeting lactate metabolism for cancer therapeutics. J. Clin. Invest. *123*, 3685–3692.

Elmore, S. (2007). Apoptosis: A Review of Programmed Cell Death. Toxicol. Pathol. *35*, 495–516.

Falivelli, G., Lisabeth, E.M., Rubio de la Torre, E., Perez-Tenorio, G., Tosato, G., Salvucci, O., and Pasquale, E.B. (2013). Attenuation of eph receptor kinase activation in cancer cells by coexpressed ephrin ligands. PloS One *8*, e81445.

Farrar, W.L., and Anderson, W.B. (1985). Interleukin-2 stimulates association of protein kinase C with plasma membrane. Nature *315*, 233–235.

Feng, Y., De Franceschi, G., Kahraman, A., Soste, M., Melnik, A., Boersema, P.J., de Laureto, P.P., Nikolaev, Y., Oliveira, A.P., and Picotti, P. (2014). Global analysis of protein structural changes in complex proteomes. Nat. Biotechnol. *32*, 1036–1044.

References

Fesik, S.W. (2005). Promoting apoptosis as a strategy for cancer drug discovery. Nat. Rev. Cancer *5*, 876–885.

Fonslow, B.R., Carvalho, P.C., Academia, K., Freeby, S., Xu, T., Nakorchevsky, A., Paulus, A., and Yates, J.R. (2011). Improvements in proteomic metrics of low abundance proteins through proteome equalization using ProteoMiner prior to MudPIT. J. Proteome Res. *10*, 3690–3700.

Fotiadis, D., Kanai, Y., and Palacín, M. (2013). The SLC3 and SLC7 families of amino acid transporters. Mol. Aspects Med. *34*, 139–158.

Fournier, N., Chalus, L., Durand, I., Garcia, E., Pin, J.J., Churakova, T., Patel, S., Zlot, C., Gorman, D., Zurawski, S., et al. (2000). FDF03, a novel inhibitory receptor of the immunoglobulin superfamily, is expressed by human dendritic and myeloid cells. J. Immunol. Baltim. Md 1950 *165*, 1197–1209.

Franken, H., Mathieson, T., Childs, D., Sweetman, G.M.A., Werner, T., Tögel, I., Doce, C., Gade, S., Bantscheff, M., Drewes, G., et al. (2015). Thermal proteome profiling for unbiased identification of direct and indirect drug targets using multiplexed quantitative mass spectrometry. Nat. Protoc. *10*, 1567–1593.

Fridman, J.S., and Sarlis, N.J. (2012). The interplay between inhibition of JAK2 and HSP90. JAK-STAT *1*, 77–79.

Gagnon, K.B., and Delpire, E. (2013). Physiology of SLC12 transporters: lessons from inherited human genetic mutations and genetically engineered mouse knockouts. Am. J. Physiol. Cell Physiol. *304*, C693-714.

Gahmberg, C.G., and Tolvanen, M. (1996). Why mammalian cell surface proteins are glycoproteins. Trends Biochem. Sci. *21*, 308–311.

Garcia-Gomez, A., Ocio, E.M., Crusoe, E., Santamaria, C., Hernández-Campo, P., Blanco, J.F., Sanchez-Guijo, F.M., Hernández-Iglesias, T., Briñón, J.G., Fisac-Herrero, R.M., et al. (2012). Dasatinib as a bone-modifying agent: anabolic and anti-resorptive effects. PloS One *7*, e34914.

Gaulton, A., Bellis, L.J., Bento, A.P., Chambers, J., Davies, M., Hersey, A., Light, Y., McGlinchey, S., Michalovich, D., Al-Lazikani, B., et al. (2012). ChEMBL: a large-scale bioactivity database for drug discovery. Nucleic Acids Res. *40*, D1100–D1107.

Gedye, C.A., Hussain, A., Paterson, J., Smrke, A., Saini, H., Sirskyj, D., Pereira, K., Lobo, N., Stewart, J., Go, C., et al. (2014). Cell surface profiling using high-throughput flow cytometry: a platform for biomarker discovery and analysis of cellular heterogeneity. PloS One *9*, e105602.

Geiger, T., Wehner, A., Schaab, C., Cox, J., and Mann, M. (2012). Comparative proteomic analysis of eleven common cell lines reveals ubiquitous but varying expression of most proteins. Mol. Cell. Proteomics MCP *11*, M111.014050.

Gerber, S.A., Rush, J., Stemman, O., Kirschner, M.W., and Gygi, S.P. (2003). Absolute quantification of proteins and phosphoproteins from cell lysates by tandem MS. Proc. Natl. Acad. Sci. *100*, 6940–6945.

Giannone, G., and Sheetz, M.P. (2006). Substrate rigidity and force define form through tyrosine phosphatase and kinase pathways. Trends Cell Biol. *16*, 213–223.

Giansanti, P., Tsiatsiani, L., Low, T.Y., and Heck, A.J.R. (2016). Six alternative proteases for mass spectrometry-based proteomics beyond trypsin. Nat. Protoc. *11*, 993–1006.

Gibb, S. (2015). Cleaver - Package for cleavage of polypeptide sequences.

Gierens, H., Nauck, M., Roth, M., Schinker, R., Schürmann, C., Scharnagl, H., Neuhaus, G., Wieland, H., and März, W. (2000). Interleukin-6 stimulates LDL receptor gene expression via activation of sterol-responsive and Sp1 binding elements. Arterioscler. Thromb. Vasc. Biol. *20*, 1777–1783.

Gingras, M.-C., Lapillonne, H., and Margolin, J.F. (2002). TREM-1, MDL-1, and DAP12 expression is associated with a mature stage of myeloid development. Mol. Immunol. *38*, 817–824.

Godl, K., Wissing, J., Kurtenbach, A., Habenberger, P., Blencke, S., Gutbrod, H., Salassidis, K., Stein-Gerlach, M., Missio, A., Cotten, M., et al. (2003). An efficient proteomics method to identify the cellular targets of protein kinase inhibitors. Proc. Natl. Acad. Sci. U. S. A. *100*, 15434–15439.

Gómez, M., González, A., Sáez, C.A., and Moenne, A. (2016). Copper-Induced Membrane Depolarizations Involve the Induction of Mosaic TRP Channels, Which Activate VDCC Leading to Calcium Increases in Ulva compressa. Front. Plant Sci. *7*, 754.

Gottesman, M.M., Fojo, T., and Bates, S.E. (2002). Multidrug resistance in cancer: role of ATP-dependent transporters. Nat. Rev. Cancer *2*, 48–58.

Gozalpour, E., Wilmer, M.J., Bilos, A., Masereeuw, R., Russel, F.G.M., and Koenderink, J.B. (2016). Heterogeneous transport of digitalis-like compounds by P-glycoprotein in vesicular and cellular assays. Toxicol. In Vitro *32*, 138–145.

Graessel, A., Hauck, S.M., von Toerne, C., Kloppmann, E., Goldberg, T., Koppensteiner, H., Schindler, M., Knapp, B., Krause, L., Dietz, K., et al. (2015). A Combined Omics Approach to Generate the Surface Atlas of Human Naive CD4+ T Cells during Early T-Cell Receptor Activation. Mol. Cell. Proteomics MCP *14*, 2085–2102.

Groot-Kormelink, P.J., Fawcett, L., Wright, P.D., Gosling, M., and Kent, T.C. (2012). Quantitative GPCR and ion channel transcriptomics in primary alveolar macrophages and macrophage surrogates. BMC Immunol. *13*, 57.

Gross, J.H. (2013). Massenspektrometrie: ein Lehrbuch (Berlin Heidelberg: Springer Spektrum).

Guemez-Gamboa, A., and Morán, J. (2009). NOX2 mediates apoptotic death induced by staurosporine but not by potassium deprivation in cerebellar granule neurons. J. Neurosci. Res. *87*, 2531–2540.

Gygi, S.P., Rist, B., Gerber, S.A., Turecek, F., Gelb, M.H., and Aebersold, R. (1999). Quantitative analysis of complex protein mixtures using isotope-coded affinity tags. Nat. Biotechnol. *17*, 994–999.

Haas, M., Wang, H., Tian, J., and Xie, Z. (2002). Src-mediated inter-receptor cross-talk between the Na+/K+-ATPase and the epidermal growth factor receptor relays the signal from ouabain to mitogen-activated protein kinases. J. Biol. Chem. *277*, 18694–18702.

Hahne, H., Pachl, F., Ruprecht, B., Maier, S.K., Klaeger, S., Helm, D., Médard, G., Wilm, M., Lemeer, S., and Kuster, B. (2013). DMSO enhances electrospray response, boosting sensitivity of proteomic experiments. Nat. Methods *10*, 989–991.

Haltia, T., and Freire, E. (1995). Forces and factors that contribute to the structural stability of membrane proteins. Biochim. Biophys. Acta *1228*, 1–27.

Hanahan, D., and Weinberg, R.A. (2000). The hallmarks of cancer. Cell *100*, 57–70.

Hanke, S., Besir, H., Oesterhelt, D., and Mann, M. (2008). Absolute SILAC for accurate quantitation of proteins in complex mixtures down to the attomole level. J. Proteome Res. *7*, 1118–1130.

References

Harburger, D.S., and Calderwood, D.A. (2009). Integrin signalling at a glance. J. Cell Sci. *122*, 159–163.

Harding, M.W., Galat, A., Uehling, D.E., and Schreiber, S.L. (1989). A receptor for the immunosuppressant FK506 is a cis-trans peptidyl-prolyl isomerase. Nature *341*, 758–760.

Hashizume, M., Yoshida, H., Koike, N., Suzuki, M., and Mihara, M. (2010). Overproduced interleukin 6 decreases blood lipid levels via upregulation of very-low-density lipoprotein receptor. Ann. Rheum. Dis. *69*, 741–746.

Ho, C.S., Lam, C.W.K., Chan, M.H.M., Cheung, R.C.K., Law, L.K., Lit, L.C.W., Ng, K.F., Suen, M.W.M., and Tai, H.L. (2003). Electrospray ionisation mass spectrometry: principles and clinical applications. Clin. Biochem. Rev. *24*, 3–12.

Hoffmann, R., and Valencia, A. (2004). A gene network for navigating the literature. Nat. Genet. *36*, 664–664.

Hofmann, L., Gulati, S., Sears, A., Stewart, P.L., and Palczewski, K. (2016). An effective thiol-reactive probe for differential scanning fluorimetry with a standard RT-PCR device. Anal. Biochem. *499*, 63–65.

Hörmann, K., Stukalov, A., Müller, A.C., Heinz, L.X., Superti-Furga, G., Colinge, J., and Bennett, K.L. (2016). A Surface Biotinylation Strategy for Reproducible Plasma Membrane Protein Purification and Tracking of Genetic and Drug-Induced Alterations. J. Proteome Res. *15*, 647–658.

Hornbeck, P.V., Garrels, J.I., Capetanaki, Y., and Heimer, S. (1993). Vimentin expression is differentially regulated by IL-2 and IL-4 in murine T cells. J. Immunol. Baltim. Md 1950 *151*, 4013–4021.

Hornbeck, P.V., Kornhauser, J.M., Tkachev, S., Zhang, B., Skrzypek, E., Murray, B., Latham, V., and Sullivan, M. (2012). PhosphoSitePlus: a comprehensive resource for investigating the structure and function of experimentally determined post-translational modifications in man and mouse. Nucleic Acids Res. *40*, D261–D270.

Hou, Z., and Matherly, L.H. (2014). Biology of the Major Facilitative Folate Transporters SLC19A1 and SLC46A1. Curr. Top. Membr. *73*, 175–204.

Hu, J., Qin, H., Li, C., Sharma, M., Cross, T.A., and Gao, F.P. (2007). Structural biology of transmembrane domains: efficient production and characterization of transmembrane peptides by NMR. Protein Sci. Publ. Protein Soc. *16*, 2153–2165.

Huang, D.W., Sherman, B.T., and Lempicki, R.A. (2009). Systematic and integrative analysis of large gene lists using DAVID bioinformatics resources. Nat. Protoc. *4*, 44–57.

Hubbard, S.R., and Miller, W.T. (2007). Receptor tyrosine kinases: mechanisms of activation and signaling. Curr. Opin. Cell Biol. *19*, 117–123.

Huber, K.V.M., Olek, K.M., Müller, A.C., Tan, C.S.H., Bennett, K.L., Colinge, J., and Superti-Furga, G. (2015). Proteome-wide drug and metabolite interaction mapping by thermal-stability profiling. Nat. Methods *12*, 1055–1057.

Humphries, J.D. (2006). Integrin ligands at a glance. J. Cell Sci. *119*, 3901–3903.

Huse, M., and Kuriyan, J. (2002). The conformational plasticity of protein kinases. Cell *109*, 275–282.

Ihenetu, K., Qazzaz, H.M., Crespo, F., Fernandez-Botran, R., and Valdes, R. (2007). Digoxin-like immunoreactive factors induce apoptosis in human acute T-cell lymphoblastic leukemia. Clin. Chem. *53*, 1315–1322.

Iizuka, K., Niwa, H., Kato, T., and Takeda, J. (2016). Dasatinib improves insulin sensitivity and affects lipid metabolism in a patient with chronic myeloid leukaemia. BMJ Case Rep. *2016*.

Inui, M., Kikuchi, Y., Aoki, N., Endo, S., Maeda, T., Sugahara-Tobinai, A., Fujimura, S., Nakamura, A., Kumanogoh, A., Colonna, M., et al. (2009). Signal adaptor DAP10 associates with MDL-1 and triggers osteoclastogenesis in cooperation with DAP12. Proc. Natl. Acad. Sci. U. S. A. *106*, 4816–4821.

Iurlo, A., Orsi, E., Cattaneo, D., Resi, V., Bucelli, C., Orofino, N., Sciumè, M., Elena, C., Grancini, V., Consonni, D., et al. (2015). Effects of first- and second-generation tyrosine kinase inhibitor therapy on glucose and lipid metabolism in chronic myeloid leukemia patients: a real clinical problem? Oncotarget *6*, 33944–33951.

Jackson, D.A., Pearson, C.K., Fraser, D.C., Prise, K.M., and Wong, S.Y. (1989). Methotrexate-induced morphological changes mimic those seen after heat shock. J. Cell Sci. *92 (Pt 1)*, 37–49.

Jedrychowski, M.P., Huttlin, E.L., Haas, W., Sowa, M.E., Rad, R., and Gygi, S.P. (2011). Evaluation of HCD- and CID-type fragmentation within their respective detection platforms for murine phosphoproteomics. Mol. Cell. Proteomics MCP *10*, M111.009910.

Jensen, L.J., Kuhn, M., Stark, M., Chaffron, S., Creevey, C., Muller, J., Doerks, T., Julien, P., Roth, A., Simonovic, M., et al. (2009). STRING 8--a global view on proteins and their functional interactions in 630 organisms. Nucleic Acids Res. *37*, D412-416.

June, C.H., Ledbetter, J.A., Gillespie, M.M., Lindsten, T., and Thompson, C.B. (1987). T-cell proliferation involving the CD28 pathway is associated with cyclosporine-resistant interleukin 2 gene expression. Mol. Cell. Biol. *7*, 4472–4481.

Käll, L., Krogh, A., and Sonnhammer, E.L.L. (2004). A combined transmembrane topology and signal peptide prediction method. J. Mol. Biol. *338*, 1027–1036.

Kanai, Y., Clémençon, B., Simonin, A., Leuenberger, M., Lochner, M., Weisstanner, M., and Hediger, M.A. (2013). The SLC1 high-affinity glutamate and neutral amino acid transporter family. Mol. Aspects Med. *34*, 108–120.

Kantarjian, H., Jabbour, E., Grimley, J., and Kirkpatrick, P. (2006). Dasatinib. Nat. Rev. Drug Discov. *5*, 717–718.

Kanter, I., and Kalisky, T. (2015). Single cell transcriptomics: methods and applications. Front. Oncol. *5*, 53.

Karas, M., Bachmann, D., Bahr, U., and Hillenkamp, F. (1987). Matrix-assisted ultraviolet laser desorption of non-volatile compounds. Int. J. Mass Spectrom. Ion Process. *78*, 53–68.

Kawahara, A., Minami, Y., Miyazaki, T., Ihle, J.N., and Taniguchi, T. (1995). Critical role of the interleukin 2 (IL-2) receptor gamma-chain-associated Jak3 in the IL-2-induced c-fos and c-myc, but not bcl-2, gene induction. Proc. Natl. Acad. Sci. U. S. A. *92*, 8724–8728.

Kell, D.B., Dobson, P.D., Bilsland, E., and Oliver, S.G. (2013). The promiscuous binding of pharmaceutical drugs and their transporter-mediated uptake into cells: what we (need to) know and how we can do so. Drug Discov. Today *18*, 218–239.

References

Keppler, O.T., Peter, M.E., Hinderlich, S., Moldenhauer, G., Stehling, P., Schmitz, I., Schwartz-Albiez, R., Reutter, W., and Pawlita, M. (1999). Differential sialylation of cell surface glycoconjugates in a human B lymphoma cell line regulates susceptibility for CD95 (APO-1/Fas)-mediated apoptosis and for infection by a lymphotropic virus. Glycobiology *9*, 557–569.

Kerr, S.C., Fieger, C.B., Snapp, K.R., and Rosen, S.D. (2008). Endoglycan, a member of the CD34 family of sialomucins, is a ligand for the vascular selectins. J. Immunol. Baltim. Md 1950 *181*, 1480–1490.

Kimura, N., Masuda, S., Tanihara, Y., Ueo, H., Okuda, M., Katsura, T., and Inui, K.-I. (2005). Metformin is a superior substrate for renal organic cation transporter OCT2 rather than hepatic OCT1. Drug Metab. Pharmacokinet. *20*, 379–386.

Kingdon, K.H. (1923). A Method for the Neutralization of Electron Space Charge by Positive Ionization at Very Low Gas Pressures. Phys. Rev. *21*, 408–418.

Kirchhofer, D., Peek, M., Li, W., Stamos, J., Eigenbrot, C., Kadkhodayan, S., Elliott, J.M., Corpuz, R.T., Lazarus, R.A., and Moran, P. (2003). Tissue expression, protease specificity, and Kunitz domain functions of hepatocyte growth factor activator inhibitor-1B (HAI-1B), a new splice variant of HAI-1. J. Biol. Chem. *278*, 36341–36349.

Klabunde, T., and Hessler, G. (2002). Drug design strategies for targeting G-protein-coupled receptors. Chembiochem Eur. J. Chem. Biol. *3*, 928–944.

Kobilka, B.K. (2007). G protein coupled receptor structure and activation. Biochim. Biophys. Acta *1768*, 794–807.

Kohler, J.J. (2009). Aniline: a catalyst for sialic acid detection. Chembiochem Eur. J. Chem. Biol. *10*, 2147–2150.

Kothiwale, S., Borza, C.M., Lowe, E.W., Pozzi, A., and Meiler, J. (2015). Discoidin domain receptor 1 (DDR1) kinase as target for structure-based drug discovery. Drug Discov. Today *20*, 255–261.

Krey, J.F., Wilmarth, P.A., Shin, J.-B., Klimek, J., Sherman, N.E., Jeffery, E.D., Choi, D., David, L.L., and Barr-Gillespie, P.G. (2014). Accurate label-free protein quantitation with high- and low-resolution mass spectrometers. J. Proteome Res. *13*, 1034–1044.

Kroeze, W.K., Sassano, M.F., Huang, X.-P., Lansu, K., McCorvy, J.D., Giguère, P.M., Sciaky, N., and Roth, B.L. (2015). PRESTO-Tango as an open-source resource for interrogation of the druggable human GPCRome. Nat. Struct. Mol. Biol. *22*, 362–369.

Kropf, P.L., Wang, L., Zang, Y., Redner, R.L., and Johnson, D.E. (2010). Dasatinib promotes ATRA-induced differentiation of AML cells. Leukemia *24*, 663–665.

Kruse, U., Pallasch, C.P., Bantscheff, M., Eberhard, D., Frenzel, L., Ghidelli, S., Maier, S.K., Werner, T., Wendtner, C.M., and Drewes, G. (2011). Chemoproteomics-based kinome profiling and target deconvolution of clinical multi-kinase inhibitors in primary chronic lymphocytic leukemia cells. Leukemia *25*, 89–100.

Lara, L.L., Rivera, H., Perez-P, C., Blanca, I., Bianco, N.E., and De Sanctis, J.B. (1997). Low density lipoprotein receptor expression and function in human polymorphonuclear leucocytes. Clin. Exp. Immunol. *107*, 205–212.

Lee, E.E., Ma, J., Sacharidou, A., Mi, W., Salato, V.K., Nguyen, N., Jiang, Y., Pascual, J.M., North, P.E., Shaul, P.W., et al. (2015). A Protein Kinase C Phosphorylation Motif in GLUT1 Affects Glucose Transport and is Mutated in GLUT1 Deficiency Syndrome. Mol. Cell *58*, 845–853.

Leuenberger, P., Ganscha, S., Kahraman, A., Cappelletti, V., Boersema, P.J., von Mering, C., Claassen, M., and Picotti, P. (2017). Cell-wide analysis of protein thermal unfolding reveals determinants of thermostability. Science *355*.

Levenson, R.M., Borowsky, A.D., and Angelo, M. (2015). Immunohistochemistry and mass spectrometry for highly multiplexed cellular molecular imaging. Lab. Investig. J. Tech. Methods Pathol. *95*, 397–405.

Li, J., Rix, U., Fang, B., Bai, Y., Edwards, A., Colinge, J., Bennett, K.L., Gao, J., Song, L., Eschrich, S., et al. (2010). A chemical and phosphoproteomic characterization of dasatinib action in lung cancer. Nat. Chem. Biol. *6*, 291–299.

Li, Y., Massey, K., Witkiewicz, H., and Schnitzer, J.E. (2011). Systems analysis of endothelial cell plasma membrane proteome of rat lung microvasculature. Proteome Sci. *9*, 15.

Lidington, E.A., Moyes, D.L., McCormack, A.M., and Rose, M.L. (1999). A comparison of primary endothelial cells and endothelial cell lines for studies of immune interactions. Transpl. Immunol. *7*, 239–246.

Lindsley, C.W. (2015). 2014 global prescription medication statistics: strong growth and CNS well represented. ACS Chem. Neurosci. *6*, 505–506.

Liu, S., and Trapnell, C. (2016). Single-cell transcriptome sequencing: recent advances and remaining challenges. F1000Research *5*.

Lomenick, B., Hao, R., Jonai, N., Chin, R.M., Aghajan, M., Warburton, S., Wang, J., Wu, R.P., Gomez, F., Loo, J.A., et al. (2009). Target identification using drug affinity responsive target stability (DARTS). Proc. Natl. Acad. Sci. U. S. A. *106*, 21984–21989.

Longuespée, R., Fléron, M., Pottier, C., Quesada-Calvo, F., Meuwis, M.-A., Baiwir, D., Smargiasso, N., Mazzucchelli, G., De Pauw-Gillet, M.-C., Delvenne, P., et al. (2014). Tissue proteomics for the next decade? Towards a molecular dimension in histology. Omics J. Integr. Biol. *18*, 539–552.

Lu, Y., Morley, P., and Durkin, J.P. (1999). Signalling events mediating the activation of protein kinase C by interleukin-2 in cytotoxic T cells. Cell. Signal. *11*, 275–285.

Lundgren, D.H., Hwang, S.-I., Wu, L., and Han, D.K. (2010). Role of spectral counting in quantitative proteomics. Expert Rev. Proteomics *7*, 39–53.

Makarov, A., Denisov, E., and Lange, O. (2009). Performance evaluation of a high-field Orbitrap mass analyzer. J. Am. Soc. Mass Spectrom. *20*, 1391–1396.

Mann, M. (2016). Origins of mass spectrometry-based proteomics. Nat. Rev. Mol. Cell Biol. *17*, 678.

Maroni, P., Bendinelli, P., Matteucci, E., and Desiderio, M.A. (2007). HGF induces CXCR4 and CXCL12-mediated tumor invasion through Ets1 and NF-kappaB. Carcinogenesis *28*, 267–279.

Martinez, F.O., Gordon, S., Locati, M., and Mantovani, A. (2006). Transcriptional profiling of the human monocyte-to-macrophage differentiation and polarization: new molecules and patterns of gene expression. J. Immunol. Baltim. Md 1950 *177*, 7303–7311.

References

Martinez Molina, D., and Nordlund, P. (2016). The Cellular Thermal Shift Assay: A Novel Biophysical Assay for In Situ Drug Target Engagement and Mechanistic Biomarker Studies. Annu. Rev. Pharmacol. Toxicol. *56*, 141–161.

Martinez Molina, D., Jafari, R., Ignatushchenko, M., Seki, T., Larsson, E.A., Dan, C., Sreekumar, L., Cao, Y., and Nordlund, P. (2013). Monitoring drug target engagement in cells and tissues using the cellular thermal shift assay. Science *341*, 84–87.

Marx, V. (2015). Mapping proteins with spatial proteomics. Nat. Methods *12*, 815–819.

Matsuzaki, S., Enomoto, T., Serada, S., Yoshino, K., Nagamori, S., Morimoto, A., Yokoyama, T., Kim, A., Kimura, T., Ueda, Y., et al. (2014). Annexin A4-conferred platinum resistance is mediated by the copper transporter ATP7A. Int. J. Cancer *134*, 1796–1809.

Mazharian, A., Ghevaert, C., Zhang, L., Massberg, S., and Watson, S.P. (2011). Dasatinib enhances megakaryocyte differentiation but inhibits platelet formation. Blood *117*, 5198–5206.

McAlister, G.C., Nusinow, D.P., Jedrychowski, M.P., Wühr, M., Huttlin, E.L., Erickson, B.K., Rad, R., Haas, W., and Gygi, S.P. (2014). MultiNotch MS3 enables accurate, sensitive, and multiplexed detection of differential expression across cancer cell line proteomes. Anal. Chem. *86*, 7150–7158.

McCracken, A.N., and Edinger, A.L. (2013). Nutrient transporters: the Achilles' heel of anabolism. Trends Endocrinol. Metab. TEM *24*, 200–208.

Médard, G., Pachl, F., Ruprecht, B., Klaeger, S., Heinzlmeir, S., Helm, D., Qiao, H., Ku, X., Wilhelm, M., Kuehne, T., et al. (2015). Optimized chemical proteomics assay for kinase inhibitor profiling. J. Proteome Res. *14*, 1574–1586.

Megger, D.A., Pott, L.L., Ahrens, M., Padden, J., Bracht, T., Kuhlmann, K., Eisenacher, M., Meyer, H.E., and Sitek, B. (2014). Comparison of label-free and label-based strategies for proteome analysis of hepatoma cell lines. Biochim. Biophys. Acta *1844*, 967–976.

Mellacheruvu, D., Wright, Z., Couzens, A.L., Lambert, J.-P., St-Denis, N.A., Li, T., Miteva, Y.V., Hauri, S., Sardiu, M.E., Low, T.Y., et al. (2013). The CRAPome: a contaminant repository for affinity purification-mass spectrometry data. Nat. Methods *10*, 730–736.

Messaritou, G., East, L., Roghi, C., Isacke, C.M., and Yarwood, H. (2009). Membrane type-1 matrix metalloproteinase activity is regulated by the endocytic collagen receptor Endo180. J. Cell Sci. *122*, 4042–4048.

Meyer, J.G., Kim, S., Maltby, D.A., Ghassemian, M., Bandeira, N., and Komives, E.A. (2014). Expanding Proteome Coverage with Orthogonal-specificity α-Lytic Proteases. Mol. Cell. Proteomics *13*, 823–835.

Michalski, A., Damoc, E., Hauschild, J.-P., Lange, O., Wieghaus, A., Makarov, A., Nagaraj, N., Cox, J., Mann, M., and Horning, S. (2011). Mass Spectrometry-based Proteomics Using Q Exactive, a High-performance Benchtop Quadrupole Orbitrap Mass Spectrometer. Mol. Cell. Proteomics MCP *10*.

Michalski, A., Damoc, E., Lange, O., Denisov, E., Nolting, D., Müller, M., Viner, R., Schwartz, J., Remes, P., Belford, M., et al. (2012). Ultra High Resolution Linear Ion Trap Orbitrap Mass Spectrometer (Orbitrap Elite) Facilitates Top Down LC MS/MS and Versatile Peptide Fragmentation Modes. Mol. Cell. Proteomics MCP *11*.

Moharir, A., Peck, S.H., Budden, T., and Lee, S.Y. (2013). The role of N-glycosylation in folding, trafficking, and functionality of lysosomal protein CLN5. PloS One *8*, e74299.

Mohorko, E., Glockshuber, R., and Aebi, M. (2011). Oligosaccharyltransferase: the central enzyme of N-linked protein glycosylation. J. Inherit. Metab. Dis. *34*, 869–878.

Moremen, K.W., Tiemeyer, M., and Nairn, A.V. (2012). Vertebrate protein glycosylation: diversity, synthesis and function. Nat. Rev. Mol. Cell Biol. *13*, 448–462.

Mueckler, M., and Thorens, B. (2013). The SLC2 (GLUT) family of membrane transporters. Mol. Aspects Med. *34*, 121–138.

Mugnier, B., Nal, B., Verthuy, C., Boyer, C., Lam, D., Chasson, L., Nieoullon, V., Chazal, G., Guo, X.-J., He, H.-T., et al. (2008). Coronin-1A links cytoskeleton dynamics to TCR alpha beta-induced cell signaling. PloS One *3*, e3467.

Musgrave, B.L., Watson, C.L., and Hoskin, D.W. (2003). CD2-CD48 interactions promote cytotoxic T lymphocyte induction and function: anti-CD2 and anti-CD48 antibodies impair cytokine synthesis, proliferation, target recognition/adhesion, and cytotoxicity. J. Interferon Cytokine Res. Off. J. Int. Soc. Interferon Cytokine Res. *23*, 67–81.

Nagano, K., Yoshida, Y., and Isobe, T. (2008). Cell surface biomarkers of embryonic stem cells. Proteomics *8*, 4025–4035.

Namgaladze, D., Kollas, A., and Brüne, B. (2008). Oxidized LDL attenuates apoptosis in monocytic cells by activating ERK signaling. J. Lipid Res. *49*, 58–65.

Navarro, G., Cordomí, A., Zelman-Femiak, M., Brugarolas, M., Moreno, E., Aguinaga, D., Perez-Benito, L., Cortés, A., Casadó, V., Mallol, J., et al. (2016). Quaternary structure of a G-protein-coupled receptor heterotetramer in complex with Gi and Gs. BMC Biol. *14*, 26.

Neugebauer, K.M., and Reichardt, L.F. (1991). Cell-surface regulation of beta 1-integrin activity on developing retinal neurons. Nature *350*, 68–71.

Nicolson, G.L. (2014). The Fluid-Mosaic Model of Membrane Structure: still relevant to understanding the structure, function and dynamics of biological membranes after more than 40 years. Biochim. Biophys. Acta *1838*, 1451–1466.

Niesen, F.H., Berglund, H., and Vedadi, M. (2007). The use of differential scanning fluorimetry to detect ligand interactions that promote protein stability. Nat. Protoc. *2*, 2212–2221.

Nyhan, K.C., Faherty, N., Murray, G., Cooey, L.B., Godson, C., Crean, J.K., and Brazil, D.P. (2010). Jagged/Notch signalling is required for a subset of TGFβ1 responses in human kidney epithelial cells. Biochim. Biophys. Acta *1803*, 1386–1395.

Offringa, R., and Huang, F. (2013). Phosphorylation-dependent trafficking of plasma membrane proteins in animal and plant cells. J. Integr. Plant Biol. *55*, 789–808.

Olsen, J.V., Macek, B., Lange, O., Makarov, A., Horning, S., and Mann, M. (2007). Higher-energy C-trap dissociation for peptide modification analysis. Nat. Methods *4*, 709–712.

Olsen, J.V., Schwartz, J.C., Griep-Raming, J., Nielsen, M.L., Damoc, E., Denisov, E., Lange, O., Remes, P., Taylor, D., Splendore, M., et al. (2009). A Dual Pressure Linear Ion Trap Orbitrap Instrument with Very High Sequencing Speed. Mol. Cell. Proteomics MCP *8*, 2759–2769.

Omasits, U., Ahrens, C.H., Müller, S., and Wollscheid, B. (2014). Protter: interactive protein feature visualization and integration with experimental proteomic data. Bioinformatics *30*, 884–886.

Ong, S.-E., and Mann, M. (2006). A practical recipe for stable isotope labeling by amino acids in cell culture (SILAC). Nat. Protoc. *1*, 2650–2660.

Ong, S.-E., Blagoev, B., Kratchmarova, I., Kristensen, D.B., Steen, H., Pandey, A., and Mann, M. (2002). Stable isotope labeling by amino acids in cell culture, SILAC, as a simple and accurate approach to expression proteomics. Mol. Cell. Proteomics MCP *1*, 376–386.

Opekarová, M., and Tanner, W. (2003). Specific lipid requirements of membrane proteins--a putative bottleneck in heterologous expression. Biochim. Biophys. Acta *1610*, 11–22.

Otrocka, M., Verschueren, H., and Malicka-Błaszkiewicz, M. (2001). The effect of methotrexate on actin and invasiveness of hepatoma Morris 5123 cells in culture. Acta Biochim. Pol. *48*, 1051–1060.

Overington, J.P., Al-Lazikani, B., and Hopkins, A.L. (2006). How many drug targets are there? Nat. Rev. Drug Discov. *5*, 993–996.

Pagala, V.R., High, A.A., Wang, X., Tan, H., Kodali, K., Mishra, A., Kavdia, K., Xu, Y., Wu, Z., and Peng, J. (2015). Quantitative protein analysis by mass spectrometry. Methods Mol. Biol. Clifton NJ *1278*, 281–305.

Pai, M.Y., Lomenick, B., Hwang, H., Schiestl, R., McBride, W., Loo, J.A., and Huang, J. (2015). Drug affinity responsive target stability (DARTS) for small-molecule target identification. Methods Mol. Biol. Clifton NJ *1263*, 287–298.

Paine, A., Kirchner, H., Immenschuh, S., Oelke, M., Blasczyk, R., and Eiz-Vesper, B. (2012). IL-2 upregulates CD86 expression on human CD4(+) and CD8(+) T cells. J. Immunol. Baltim. Md 1950 *188*, 1620–1629.

Pallen, C.J. (2003). Protein tyrosine phosphatase alpha (PTPalpha): a Src family kinase activator and mediator of multiple biological effects. Curr. Top. Med. Chem. *3*, 821–835.

Palmieri, F. (2013). The mitochondrial transporter family SLC25: identification, properties and physiopathology. Mol. Aspects Med. *34*, 465–484.

Park, H.-Y., Wu, H., Killoran, C.E., and Gilchrest, B.A. (2004). The receptor for activated C-kinase-I (RACK-I) anchors activated PKC-beta on melanosomes. J. Cell Sci. *117*, 3659–3668.

Park, K.-Y., Li, W.A., and Platt, M.O. (2012). Patient specific proteolytic activity of monocyte-derived macrophages and osteoclasts predicted with temporal kinase activation states during differentiation. Integr. Biol. Quant. Biosci. Nano Macro *4*, 1459–1469.

Patching, S.G. (2014). Surface plasmon resonance spectroscopy for characterisation of membrane protein–ligand interactions and its potential for drug discovery. Biochim. Biophys. Acta BBA - Biomembr. *1838*, 43–55.

Pejchinovski, M., Klein, J., Ramírez-Torres, A., Bitsika, V., Mermelekas, G., Vlahou, A., Mullen, W., Mischak, H., and Jankowski, V. (2015). Comparison of higher energy collisional dissociation and collision-induced dissociation MS/MS sequencing methods for identification of naturally occurring peptides in human urine. Proteomics Clin. Appl. *9*, 531–542.

Perkins, D.N., Pappin, D.J., Creasy, D.M., and Cottrell, J.S. (1999). Probability-based protein identification by searching sequence databases using mass spectrometry data. Electrophoresis *20*, 3551–3567.

Plow, E.F., Haas, T.A., Zhang, L., Loftus, J., and Smith, J.W. (2000). Ligand binding to integrins. J. Biol. Chem. *275*, 21785–21788.

Pozzi, N., Gaetaniello, L., Martire, B., De Mattia, D., Balestrieri, B., Cosentini, E., Schlossman, S.F., Duke-Cohan, J.S., and Pignata, C. (2001). Defective surface expression of attractin on T cells in patients with common variable immunodeficiency (CVID). Clin. Exp. Immunol. *123*, 99–104.

Prabakaran, S., Lippens, G., Steen, H., and Gunawardena, J. (2012). Post-translational modification: nature's escape from genetic imprisonment and the basis for dynamic information encoding. Wiley Interdiscip. Rev. Syst. Biol. Med. *4*, 565–583.

Pshezhetsky, A.V., Fedjaev, M., Ashmarina, L., Mazur, A., Budman, L., Sinnett, D., Labuda, D., Beaulieu, J.-F., Ménard, D., Nifant'ev, I., et al. (2007). Subcellular proteomics of cell differentiation: quantitative analysis of the plasma membrane proteome of Caco-2 cells. Proteomics *7*, 2201–2215.

Rappsilber, J., Mann, M., and Ishihama, Y. (2007). Protocol for micro-purification, enrichment, pre-fractionation and storage of peptides for proteomics using StageTips. Nat. Protoc. *2*, 1896–1906.

Rayleigh, Lord (1882). On the equilibrium of liquid conducting masses charged with electricity. Philos. Mag. Ser. 5 *14*, 184–186.

Reinhard, F.B.M., Eberhard, D., Werner, T., Franken, H., Childs, D., Doce, C., Savitski, M.F., Huber, W., Bantscheff, M., Savitski, M.M., et al. (2015). Thermal proteome profiling monitors ligand interactions with cellular membrane proteins. Nat. Methods *12*, 1129–1131.

Rieckmann, J.C., Geiger, R., Hornburg, D., Wolf, T., Kveler, K., Jarrossay, D., Sallusto, F., Shen-Orr, S.S., Lanzavecchia, A., Mann, M., et al. (2017). Social network architecture of human immune cells unveiled by quantitative proteomics. Nat. Immunol. *18*, 583–593.

Ritter, M.R., Reinisch, J., Friedlander, S.F., and Friedlander, M. (2006). Myeloid cells in infantile hemangioma. Am. J. Pathol. *168*, 621–628.

Rix, U., Hantschel, O., Dürnberger, G., Rix, L.L.R., Planyavsky, M., Fernbach, N.V., Kaupe, I., Bennett, K.L., Valent, P., Colinge, J., et al. (2007). Chemical proteomic profiles of the BCR-ABL inhibitors imatinib, nilotinib, and dasatinib reveal novel kinase and nonkinase targets. Blood *110*, 4055–4063.

Roepstorff, P., and Fohlman, J. (1984). Proposal for a common nomenclature for sequence ions in mass spectra of peptides. Biomed. Mass Spectrom. *11*, 601.

Roevens, P., and de Chaffoy de Courcelles, D. (1990). Ouabain increases the calcium concentration in intracellular stores involved in stimulus-response coupling in human platelets. Circ. Res. *67*, 1494–1502.

Romero, M.F., Chen, A.-P., Parker, M.D., and Boron, W.F. (2013). The SLC4 Family of Bicarbonate (HCO3−) Transporters. Mol. Aspects Med. *34*, 159–182.

Ross, P.L., Huang, Y.N., Marchese, J.N., Williamson, B., Parker, K., Hattan, S., Khainovski, N., Pillai, S., Dey, S., Daniels, S., et al. (2004). Multiplexed protein quantitation in Saccharomyces cerevisiae using amine-reactive isobaric tagging reagents. Mol. Cell. Proteomics MCP *3*, 1154–1169.

Roth, J. (2002). Protein N-glycosylation along the secretory pathway: relationship to organelle topography and function, protein quality control, and cell interactions. Chem. Rev. *102*, 285–303.

Sakatsume, M., Igarashi, K., Winestock, K.D., Garotta, G., Larner, A.C., and Finbloom, D.S. (1995). The Jak kinases differentially associate with the alpha and beta (accessory factor) chains of the interferon

References

gamma receptor to form a functional receptor unit capable of activating STAT transcription factors. J. Biol. Chem. *270*, 17528–17534.

Satija, R., and Shalek, A.K. (2014). Heterogeneity in Immune Responses – From Populations to Single Cells. Trends Immunol. *35*, 219–229.

Savart, M., Belamri, M., Pallet, V., and Ducastaing, A. (1987). Association of calpains 1 and 2 with protein kinase C activities. FEBS Lett. *216*, 22–26.

Savitski, M.M., Fischer, F., Mathieson, T., Sweetman, G., Lang, M., and Bantscheff, M. (2010). Targeted data acquisition for improved reproducibility and robustness of proteomic mass spectrometry assays. J. Am. Soc. Mass Spectrom. *21*, 1668–1679.

Savitski, M.M., Sweetman, G., Askenazi, M., Marto, J.A., Lang, M., Zinn, N., and Bantscheff, M. (2011). Delayed fragmentation and optimized isolation width settings for improvement of protein identification and accuracy of isobaric mass tag quantification on Orbitrap-type mass spectrometers. Anal. Chem. *83*, 8959–8967.

Savitski, M.M., Mathieson, T., Zinn, N., Sweetman, G., Doce, C., Becher, I., Pachl, F., Kuster, B., and Bantscheff, M. (2013). Measuring and managing ratio compression for accurate iTRAQ/TMT quantification. J. Proteome Res. *12*, 3586–3598.

Savitski, M.M., Reinhard, F.B.M., Franken, H., Werner, T., Savitski, M.F., Eberhard, D., Martinez Molina, D., Jafari, R., Dovega, R.B., Klaeger, S., et al. (2014). Tracking cancer drugs in living cells by thermal profiling of the proteome. Science *346*, 1255784.

Schachter, H. (1991). The "yellow brick road" to branched complex N-glycans. Glycobiology *1*, 453–461.

Schellman, J.A. (1994). The thermodynamics of solvent exchange. Biopolymers *34*, 1015–1026.

Schiöth, H.B., Roshanbin, S., Hägglund, M.G.A., and Fredriksson, R. (2013). Evolutionary origin of amino acid transporter families SLC32, SLC36 and SLC38 and physiological, pathological and therapeutic aspects. Mol. Aspects Med. *34*, 571–585.

Schlessinger, A., Khuri, N., Giacomini, K.M., and Sali, A. (2013). Molecular modeling and ligand docking for Solute Carrier (SLC) transporters. Curr. Top. Med. Chem. *13*, 843–856.

Schwanhäusser, B., Busse, D., Li, N., Dittmar, G., Schuchhardt, J., Wolf, J., Chen, W., and Selbach, M. (2011). Global quantification of mammalian gene expression control. Nature *473*, 337–342.

Schwende, H., Fitzke, E., Ambs, P., and Dieter, P. (1996). Differences in the state of differentiation of THP-1 cells induced by phorbol ester and 1,25-dihydroxyvitamin D3. J. Leukoc. Biol. *59*, 555–561.

Scigelova, M., Hornshaw, M., Giannakopulos, A., and Makarov, A. (2011). Fourier transform mass spectrometry. Mol. Cell. Proteomics MCP *10*, M111.009431.

Seddon, A.M., Curnow, P., and Booth, P.J. (2004). Membrane proteins, lipids and detergents: not just a soap opera. Biochim. Biophys. Acta BBA - Biomembr. *1666*, 105–117.

Sgroi, D., and Stamenkovic, I. (1994). The B-cell adhesion molecule CD22 is cross-species reactive and recognizes distinct sialoglycoproteins on different functional T-cell sub-populations. Scand. J. Immunol. *39*, 433–438.

Shaikh, S.A., Wen, P.-C., Enkavi, G., Huang, Z., and Tajkhorshid, E. (2010). Capturing Functional Motions of Membrane Channels and Transporters with Molecular Dynamics Simulation. J. Comput. Theor. Nanosci. *7*, 2481–2500.

Shang, L., and Tomasi, T.B. (2006). The heat shock protein 90-CDC37 chaperone complex is required for signaling by types I and II interferons. J. Biol. Chem. *281*, 1876–1884.

Sharma, K., Weber, C., Bairlein, M., Greff, Z., Kéri, G., Cox, J., Olsen, J.V., and Daub, H. (2009). Proteomics strategy for quantitative protein interaction profiling in cell extracts. Nat. Methods *6*, 741–744.

Shi, H., Zhang, C.-J., Chen, G.Y.J., and Yao, S.Q. (2012). Cell-based proteome profiling of potential dasatinib targets by use of affinity-based probes. J. Am. Chem. Soc. *134*, 3001–3014.

Shouval, D.S., Ouahed, J., Biswas, A., Goettel, J.A., Horwitz, B.H., Klein, C., Muise, A.M., and Snapper, S.B. (2014). Interleukin 10 Receptor Signaling: Master Regulator of Intestinal Mucosal Homeostasis in Mice and Humans. Adv. Immunol. *122*, 177–210.

Silva, J.C., Gorenstein, M.V., Li, G.-Z., Vissers, J.P.C., and Geromanos, S.J. (2006). Absolute quantification of proteins by LCMSE: a virtue of parallel MS acquisition. Mol. Cell. Proteomics MCP *5*, 144–156.

Simons, K., and van Meer, G. (1988). Lipid sorting in epithelial cells. Biochemistry (Mosc.) *27*, 6197–6202.

Sims, M.A., Field, S.D., Barnes, M.R., Shaikh, N., Ellington, K., Murphy, K.E., Spurr, N., and Campbell, D.A. (2000). Cloning and characterisation of ITGAV, the genomic sequence for human cell adhesion protein (vitronectin) receptor alpha subunit, CD51. Cytogenet. Cell Genet. *89*, 268–271.

Singer, S.J., and Nicolson, G.L. (1972). The fluid mosaic model of the structure of cell membranes. Science *175*, 720–731.

Sintiprungrat, K., Singhto, N., Sinchaikul, S., Chen, S.-T., and Thongboonkerd, V. (2010). Alterations in cellular proteome and secretome upon differentiation from monocyte to macrophage by treatment with phorbol myristate acetate: insights into biological processes. J. Proteomics *73*, 602–618.

Sirianant, L., Ousingsawat, J., Wanitchakool, P., Schreiber, R., and Kunzelmann, K. (2016). Cellular volume regulation by anoctamin 6: Ca^{2+}, phospholipase A2 and osmosensing. Pflugers Arch. *468*, 335–349.

Smyth, G.K. (2004). Linear models and empirical bayes methods for assessing differential expression in microarray experiments. Stat. Appl. Genet. Mol. Biol. *3*, Article3.

Sorkin, A., and von Zastrow, M. (2009). Endocytosis and signalling: intertwining molecular networks. Nat. Rev. Mol. Cell Biol. *10*, 609–622.

de Sousa Abreu, R., Penalva, L.O., Marcotte, E.M., and Vogel, C. (2009). Global signatures of protein and mRNA expression levels. Mol. Biosyst. *5*, 1512–1526.

Steen, H., and Mann, M. (2004). The ABC's (and XYZ's) of peptide sequencing. Nat. Rev. Mol. Cell Biol. *5*, 699–711.

Sun, L., Liang, C., Shirazian, S., Zhou, Y., Miller, T., Cui, J., Fukuda, J.Y., Chu, J.-Y., Nematalla, A., Wang, X., et al. (2003). Discovery of 5-[5-fluoro-2-oxo-1,2- dihydroindol-(3Z)-ylidenemethyl]-2,4- dimethyl-1H-pyrrole-3-carboxylic acid (2-diethylaminoethyl)amide, a novel tyrosine kinase inhibitor targeting vascular endothelial and platelet-derived growth factor receptor tyrosine kinase. J. Med. Chem. *46*, 1116–1119.

References

Swaney, D.L., Wenger, C.D., and Coon, J.J. (2010). Value of Using Multiple Proteases for Large-Scale Mass Spectrometry-Based Proteomics. J. Proteome Res. *9*, 1323–1329.

Szabo, G., Pine, P.S., Weaver, J.L., Rao, P.E., and Aszalos, A. (1994). The L-selectin (Leu8) molecule is associated with the TcR/CD3 receptor; fluorescence energy transfer measurements on live cells. Immunol. Cell Biol. *72*, 319–325.

Tahara, E., Kadara, H., Lacroix, L., Lotan, D., and Lotan, R. (2009). Activation of protein kinase C by phorbol 12-myristate 13-acetate suppresses the growth of lung cancer cells through KLF6 induction. Cancer Biol. Ther. *8*, 801–807.

Takala, H., Nurminen, E., Nurmi, S.M., Aatonen, M., Strandin, T., Takatalo, M., Kiema, T., Gahmberg, C.G., Ylänne, J., and Fagerholm, S.C. (2008). Beta2 integrin phosphorylation on Thr758 acts as a molecular switch to regulate 14-3-3 and filamin binding. Blood *112*, 1853–1862.

Tan, S., Tan, H.T., and Chung, M.C.M. (2008). Membrane proteins and membrane proteomics. Proteomics *8*, 3924–3932.

Taunton, J., Hassig, C.A., and Schreiber, S.L. (1996). A mammalian histone deacetylase related to the yeast transcriptional regulator Rpd3p. Science *272*, 408–411.

Taylor, G. (1964). Disintegration of Water Drops in an Electric Field. Proc. R. Soc. Math. Phys. Eng. Sci. *280*, 383–397.

Taylor, K.M., Morgan, H.E., Smart, K., Zahari, N.M., Pumford, S., Ellis, I.O., Robertson, J.F.R., and Nicholson, R.I. (2007). The emerging role of the LIV-1 subfamily of zinc transporters in breast cancer. Mol. Med. Camb. Mass *13*, 396–406.

Thanka Christlet, T.H., and Veluraja, K. (2001). Database analysis of O-glycosylation sites in proteins. Biophys. J. *80*, 952–960.

Thompson, A., Schäfer, J., Kuhn, K., Kienle, S., Schwarz, J., Schmidt, G., Neumann, T., Johnstone, R., Mohammed, A.K.A., and Hamon, C. (2003). Tandem mass tags: a novel quantification strategy for comparative analysis of complex protein mixtures by MS/MS. Anal. Chem. *75*, 1895–1904.

Thonemann, B., Schmalz, G., Hiller, K.-A., and Schweikl, H. (2002). Responses of L929 mouse fibroblasts, primary and immortalized bovine dental papilla-derived cell lines to dental resin components. Dent. Mater. Off. Publ. Acad. Dent. Mater. *18*, 318–323.

Traiffort, E., O'Regan, S., and Ruat, M. (2013). The choline transporter-like family SLC44: properties and roles in human diseases. Mol. Aspects Med. *34*, 646–654.

Tran, J.C., Zamdborg, L., Ahlf, D.R., Lee, J.E., Catherman, A.D., Durbin, K.R., Tipton, J.D., Vellaichamy, A., Kellie, J.F., Li, M., et al. (2011). Mapping intact protein isoforms in discovery mode using top-down proteomics. Nature *480*, 254–258.

Trickett, A., and Kwan, Y.L. (2003). T cell stimulation and expansion using anti-CD3/CD28 beads. J. Immunol. Methods *275*, 251–255.

Tsuruoka, S., Ishibashi, K., Yamamoto, H., Wakaumi, M., Suzuki, M., Schwartz, G.J., Imai, M., and Fujimura, A. (2002). Functional analysis of ABCA8, a new drug transporter. Biochem. Biophys. Res. Commun. *298*, 41–45.

Tzircotis, G., Thorne, R.F., and Isacke, C.M. (2006). Directional sensing of a phorbol ester gradient requires CD44 and is regulated by CD44 phosphorylation. Oncogene *25*, 7401–7410.

Ulrich, S., Boturyn, D., Marra, A., Renaudet, O., and Dumy, P. (2014). Oxime ligation: a chemoselective click-type reaction for accessing multifunctional biomolecular constructs. Chem. Weinh. Bergstr. Ger. *20*, 34–41.

Varki, A. (2007). Glycan-based interactions involving vertebrate sialic-acid-recognizing proteins. Nature *446*, 1023–1029.

Virginio, C., Church, D., North, R.A., and Surprenant, A. (1997). Effects of divalent cations, protons and calmidazolium at the rat P2X7 receptor. Neuropharmacology *36*, 1285–1294.

Vogel, C., and Marcotte, E.M. (2012). Insights into the regulation of protein abundance from proteomic and transcriptomic analyses. Nat. Rev. Genet. *13*, 227–232.

Wakaumi, M., Ishibashi, K., Ando, H., Kasanuki, H., and Tsuruoka, S. (2005). Acute digoxin loading reduces ABCA8A mRNA expression in the mouse liver. Clin. Exp. Pharmacol. Physiol. *32*, 1034–1041.

Walgren, J. (2004). Application of proteomic technologies in the drug development process. Toxicol. Lett. *149*, 377–385.

Wang, D., Ozhegov, E., Wang, L., Zhou, A., Nie, H., Li, Y., and Sun, X.-L. (2016). Sialylation and desialylation dynamics of monocytes upon differentiation and polarization to macrophages. Glycoconj. J. *33*, 725–733.

Wang, H., Tian, Y., Wang, J., Phillips, K.L.E., Binch, A.L.A., Dunn, S., Cross, A., Chiverton, N., Zheng, Z., Shapiro, I.M., et al. (2013). Inflammatory cytokines induce NOTCH signaling in nucleus pulposus cells: implications in intervertebral disc degeneration. J. Biol. Chem. *288*, 16761–16774.

Wang, Y., Herrera, A.H., Li, Y., Belani, K.K., and Walcheck, B. (2009). Regulation of mature ADAM17 by redox agents for L-selectin shedding. J. Immunol. Baltim. Md 1950 *182*, 2449–2457.

Warburg, O. (1956). On the origin of cancer cells. Science *123*, 309–314.

Ward, W.H., and Holdgate, G.A. (2001). Isothermal titration calorimetry in drug discovery. Prog. Med. Chem. *38*, 309–376.

Watarai, H., Hinohara, A., Nagafune, J., Nakayama, T., Taniguchi, M., and Yamaguchi, Y. (2005). Plasma membrane-focused proteomics: dramatic changes in surface expression during the maturation of human dendritic cells. Proteomics *5*, 4001–4011.

Weber, P.C., and Salemme, F.R. (2003). Applications of calorimetric methods to drug discovery and the study of protein interactions. Curr. Opin. Struct. Biol. *13*, 115–121.

Weekes, M.P., Antrobus, R., Talbot, S., Hör, S., Simecek, N., Smith, D.L., Bloor, S., Randow, F., and Lehner, P.J. (2012). Proteomic plasma membrane profiling reveals an essential role for gp96 in the cell surface expression of LDLR family members, including the LDL receptor and LRP6. J. Proteome Res. *11*, 1475–1484.

Wegener, K.L., Partridge, A.W., Han, J., Pickford, A.R., Liddington, R.C., Ginsberg, M.H., and Campbell, I.D. (2007). Structural basis of integrin activation by talin. Cell *128*, 171–182.

References

Weidle, U.H., Klostermann, S., Eggle, D., and Krüger, A. (2010). Interleukin 6/Interleukin 6 Receptor Interaction and its Role as a Therapeutic Target for Treatment of Cachexia and Cancer. Cancer Genomics - Proteomics *7*, 287–302.

Werner, T., Becher, I., Sweetman, G., Doce, C., Savitski, M.M., and Bantscheff, M. (2012). High-resolution enabled TMT 8-plexing. Anal. Chem. *84*, 7188–7194.

Wilkinson, D.G. (2014). Regulation of cell differentiation by Eph receptor and ephrin signaling. Cell Adhes. Migr. *8*, 339–348.

Winter, G.E., Radic, B., Mayor-Ruiz, C., Blomen, V.A., Trefzer, C., Kandasamy, R.K., Huber, K.V.M., Gridling, M., Chen, D., Klampfl, T., et al. (2014). The solute carrier SLC35F2 enables YM155-mediated DNA damage toxicity. Nat. Chem. Biol. *10*, 768–773.

Wishart, D.S., Knox, C., Guo, A.C., Cheng, D., Shrivastava, S., Tzur, D., Gautam, B., and Hassanali, M. (2008). DrugBank: a knowledgebase for drugs, drug actions and drug targets. Nucleic Acids Res. *36*, D901–D906.

Wiśniewski, J.R., Hein, M.Y., Cox, J., and Mann, M. (2014). A "proteomic ruler" for protein copy number and concentration estimation without spike-in standards. Mol. Cell. Proteomics MCP *13*, 3497–3506.

Wollscheid, B., Bausch-Fluck, D., Henderson, C., O'Brien, R., Bibel, M., Schiess, R., Aebersold, R., and Watts, J.D. (2009). Mass-spectrometric identification and relative quantification of N-linked cell surface glycoproteins. Nat. Biotechnol. *27*, 378–386.

Xu, D. (2004). Protein Databases on the Internet. Curr. Protoc. Mol. Biol. *CHAPTER*, Unit-19.4.

Xu, C., and Ng, D.T.W. (2015). Glycosylation-directed quality control of protein folding. Nat. Rev. Mol. Cell Biol. *16*, 742–752.

Xu, R.-G., Cai, B., Cao, F., Huang, Q.-X., Mi, P., Wang, H.-P., Liu, W.-H., and Wang, B.-G. (2017). MCT1 promotes tumor progression through regulating epithelial-mesenchymal transition in pancreatic cancer. Int J Clin Exp Pathol *10*, 2461–3997.

Yang, Y.-H., Lee, K., Jang, K.-S., Kim, Y.-G., Park, S.-H., Lee, C.-S., and Kim, B.-G. (2009). Low mass cutoff evasion with q(z) value optimization in ion trap. Anal. Biochem. *387*, 133–135.

Young, J.D., Yao, S.Y.M., Baldwin, J.M., Cass, C.E., and Baldwin, S.A. (2013). The human concentrative and equilibrative nucleoside transporter families, SLC28 and SLC29. Mol. Aspects Med. *34*, 529–547.

Zavadil, J., Cermak, L., Soto-Nieves, N., and Böttinger, E.P. (2004). Integration of TGF-beta/Smad and Jagged1/Notch signalling in epithelial-to-mesenchymal transition. EMBO J. *23*, 1155–1165.

Zeiler, M., Straube, W.L., Lundberg, E., Uhlen, M., and Mann, M. (2012). A Protein Epitope Signature Tag (PrEST) library allows SILAC-based absolute quantification and multiplexed determination of protein copy numbers in cell lines. Mol. Cell. Proteomics MCP *11*, O111.009613.

Zeng, Y., Ramya, T.N.C., Dirksen, A., Dawson, P.E., and Paulson, J.C. (2009). High-efficiency labeling of sialylated glycoproteins on living cells. Nat. Methods *6*, 207–209.

Zhang, J.-Y., Zhang, F., Hong, C.-Q., Giuliano, A.E., Cui, X.-J., Zhou, G.-J., Zhang, G.-J., and Cui, Y.-K. (2015). Critical protein GAPDH and its regulatory mechanisms in cancer cells. Cancer Biol. Med. *12*, 10–22.

Zhang, Y., Zhang, J., Navrazhina, K., Argaw, A.T., Zameer, A., Gurfein, B.T., Brosnan, C.F., and John, G.R. (2010). TGFβ1 induces Jagged1 expression in astrocytes via ALK5 and Smad3 and regulates the balance between oligodendrocyte progenitor proliferation and differentiation. Glia *58*, 964–974.

Zhang, Y., Yu, M., Zhang, C., Ma, W., Zhang, Y., Wang, C., and Lu, H. (2014). Highly Selective and Ultra Fast Solid-Phase Extraction of N-Glycoproteome by Oxime Click Chemistry Using Aminooxy-Functionalized Magnetic Nanoparticles. Anal. Chem. *86*, 7920–7924.

Zheng, W.-H., Kar, S., and Quirion, R. (2000). Stimulation of Protein Kinase C Modulates Insulin-like Growth Factor-1-induced Akt Activation in PC12 Cells. J. Biol. Chem. *275*, 13377–13385.

Zhu, M.H., Berry, J.A., Russell, S.M., and Leonard, W.J. (1998). Delineation of the regions of interleukin-2 (IL-2) receptor beta chain important for association of Jak1 and Jak3. Jak1-independent functional recruitment of Jak3 to Il-2Rbeta. J. Biol. Chem. *273*, 10719–10725.

Zielinska, D.F., Gnad, F., Wiśniewski, J.R., and Mann, M. (2010). Precision mapping of an in vivo N-glycoproteome reveals rigid topological and sequence constraints. Cell *141*, 897–907.

8. Appendix
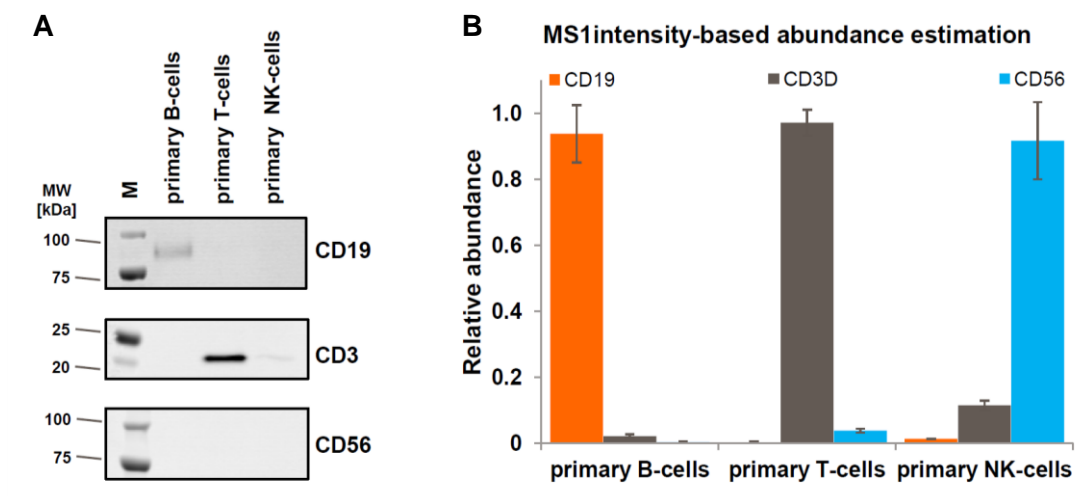
Supplemental Fig. 1 Validation of primary cell type enrichment from human blood. Human primary B-cells, T-cells and NK-cells were extracted from buffy coats of human blood by Histopaque density gradient centrifugation and the EasySep Enrichment kits according to manufacturer´s instructions in two replicates. Enriched cells were cell surface biotinylated followed by lysis in 4 % SDS. Samples were either loaded on 4-12 % SDS polyacrylamide gels with subsequent immunoblot analysis or were analyzed by LC-MS/MS on a Q Exactive Hybrid-Quadrupole-Orbitrap mass spectrometer using a 270 min gradient. (**A**) Immunoblot analysis for the B-, T- or NK-cell markers CD19, CD3 or CD56, respectively. (**B**) Comparison of relative abundances of B-, T- or NK-cell markers in enriched cell type samples after cell surface proteome enrichment according to ms1intensity-based abundance estimations. Bars indicate averages of two replicates. Error bars indicate standard deviations.
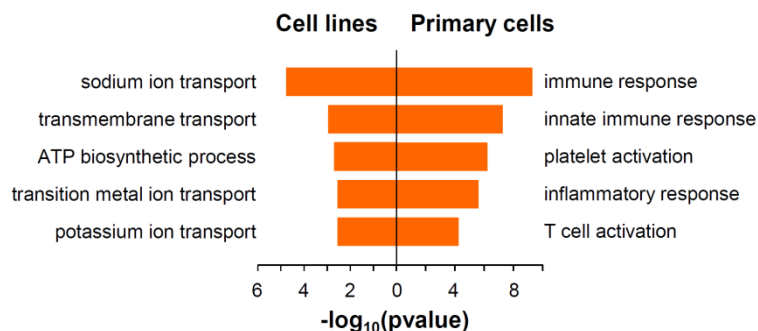
Supplemental Fig. 2 Comparison of cell lines and primary cells based on differentially expressed proteins. GO-term enrichment analysis for biological processes of proteins with significant (p-value < 0.05) higher expression on cell lines compared to primary cells (left) and vise-versa (right) in cell surface proteome mappings. Selection of top five GO-term s for biological processes.
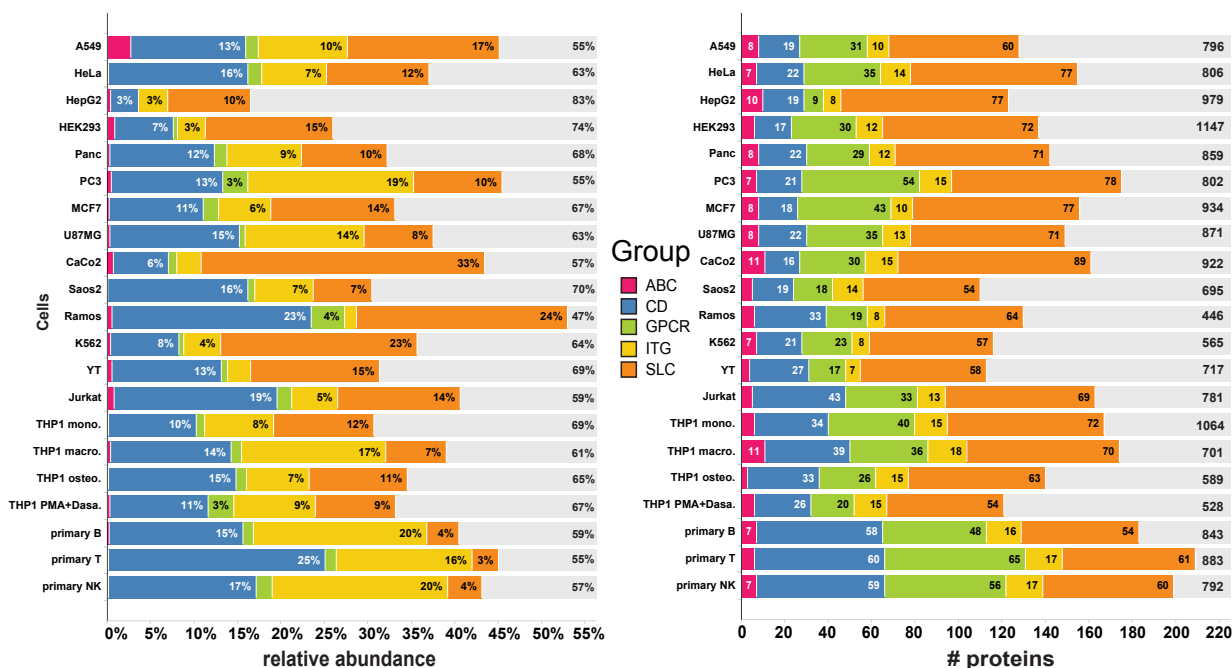
Supplemental Fig. 3 Comparison of cell lines and primary cells based on cell surface protein groups. (**A**). Fractional abundance of plasma membrane proteome subgroups on the cell surface of cell lines and primary cell types. Fractional abundances represent the summed abundance estimations for each subgroup relative to the summed abundance estimations of all identified plasma membrane proteins. Prominent plasma membrane proteome subgroups are ATP-binding cassette transporters (ABC = magenta), cluster of differentiation proteins (CD = blue), G-protein coupled receptors (GPCR = green), Integrins (ITG = yellow), solute carrier transporters (SLC = orange) and all other plasma membrane proteins in light grey. (**B**). Same data set as in A. but illustrating identified numbers of proteins.
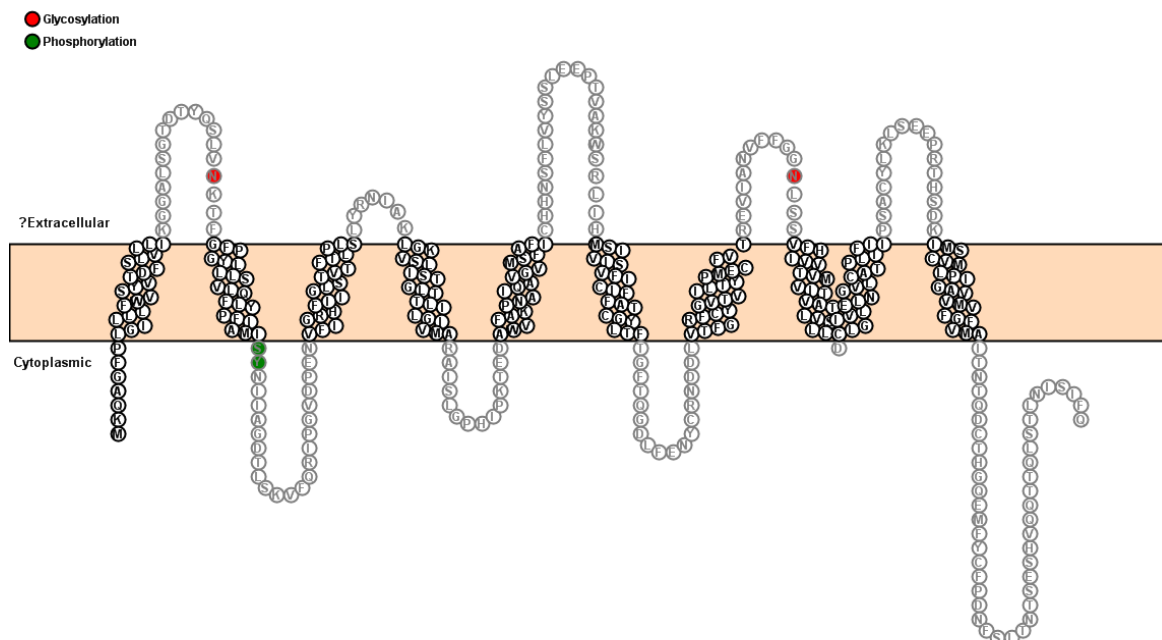
Supplemental Fig. 4 Prediction of missing protein topologies. If topology annotation is incomplete, the developed database-integrating application predicts missing topology information based on existing annotations as shown for the transmembrane protein SLC38A11. If transmembrane domains are annotated in addition to at least one extramembrane domain, the remaining missing domains will be predicted accordingly. Annotated topology information is drawn in black while predicted topologies are drawn in grey.
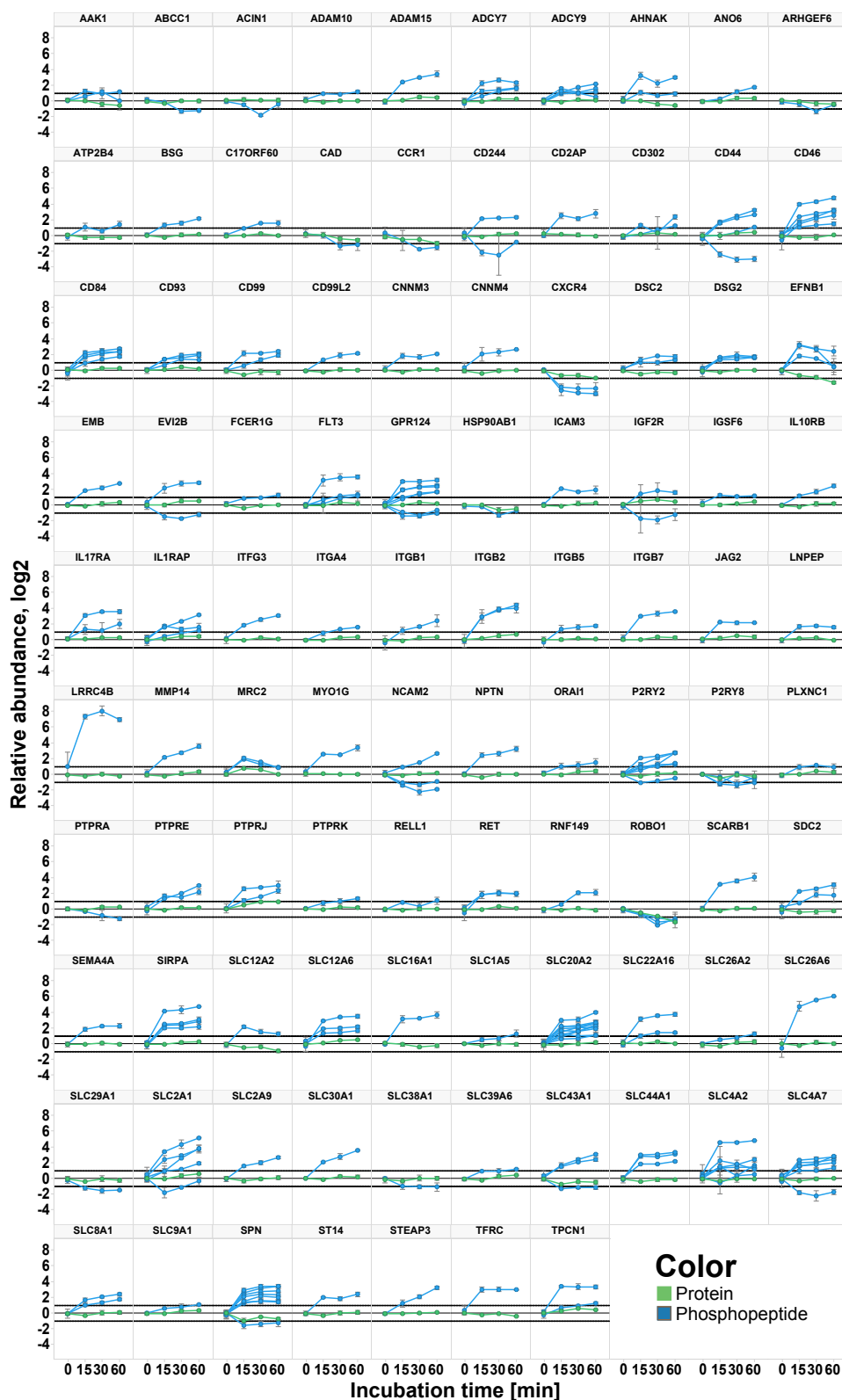
Supplemental Fig. 5 Regulated phosphorylation sites of cell surface proteins during PMA-induced differentiation. Effects of PMA-induced differentiation on the cell surface phosphoproteome of THP-1 cells were monitored by combining enrichment of cell surface proteins with IMAC. Samples were analyzed by LC-MS/MS on a Q Exactive Hybrid-Quadrupole-Orbitrap mass spectrometer using a 270 min gradient and data was filtered for cell surface proteins with protein qusm ≥ 2, peptide Mascot score ≥ 15, phosphorylation as peptide modification and peptide abundance change ≥ 2 -fold in at least one time point with a p-value < 0.05. Data was further filtered for proteins with unaffected protein abundance in the sample prior to IMAC. The overall protein abundances are indicated as green lines. Phosphopeptide abundances are indicated as blue lines. Data points indicate means of two replicates. Error bars indicate standard deviations.
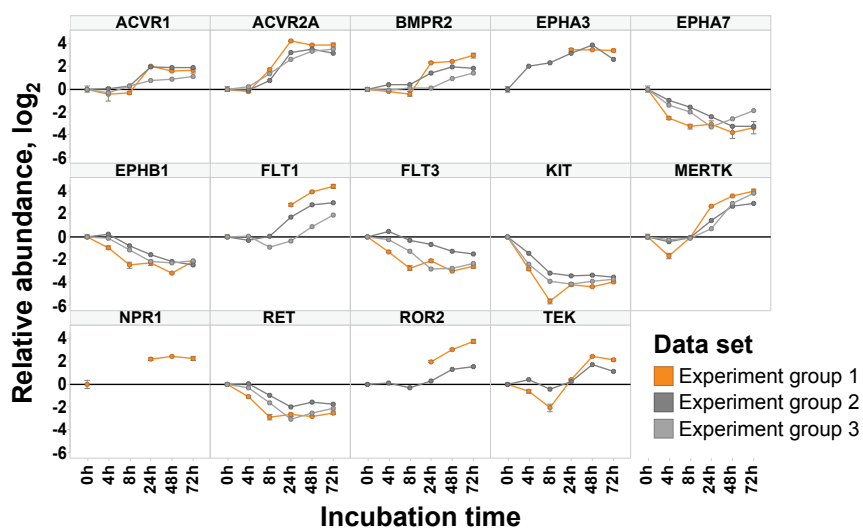
Supplemental Fig. 6 Significantly regulated plasma membrane associated kinases during differentiation. Illustration of all significantly regulated plasma membrane kinases during differentiation from monocytic to macrophage-like cells. Standard deviations in Experimental group 1 are represented as error bars. A significantly regulated protein was specified to have a Benjamini-Hochberg corrected p-value < 0.01 and a log$_2$ relative fold change $\geq$ 2 or $\leq$ -2 at least once in the time course.
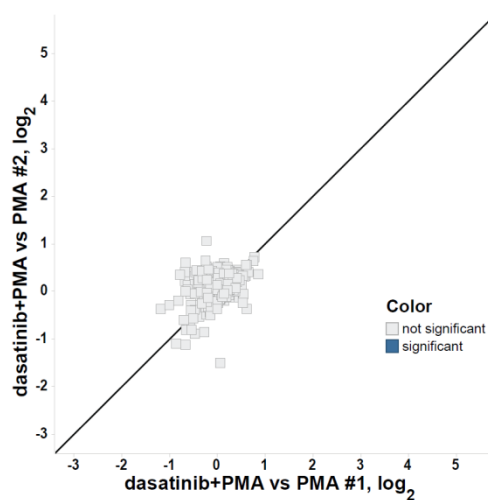
Supplemental Fig. 7 Cell surface proteome changes during differentiation in presence of sunitinib. Proteins with significantly altered abundance in THP-1 cells differentiated in presence or absence of sunitinib in two biological replicates. Significance was defined as a combined fold-change and p-value cut-off between cells differentiated in presence and cells differentiated in absence of the kinase inhibitors with log$_2$ relative abundances $\geq$ 1 or $\leq$ -1 in both replicates and t-test p-values < 0.05.
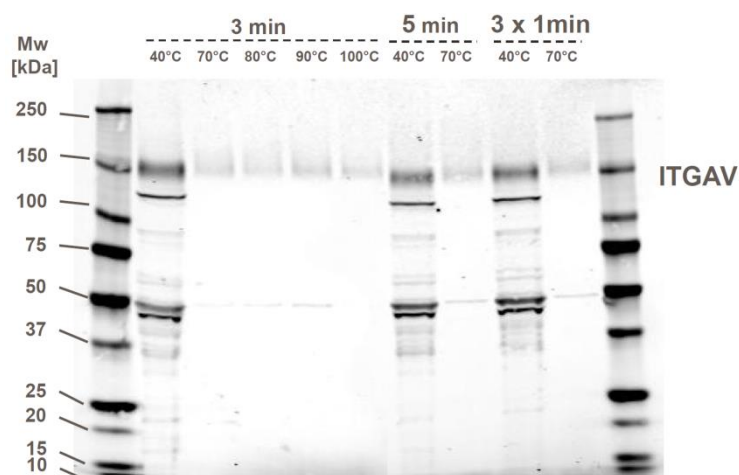
Supplemental Fig. 8 Influence of heat treatment incubation time on non-aggregated ITGAV fraction. K562 cells were incubated for 3, 5 or 3 x 1 min (1 min at RT in between) at indicated temperatures. Subsequently, cells were incubated for 3 min at RT and lysed in 0.8 % IGEPAL CA-630. Protein aggregates were removed by filtration and 30 µg of protein in flow throughs were subjected to SDS-PAGE and immunoblotting for ITGAV.
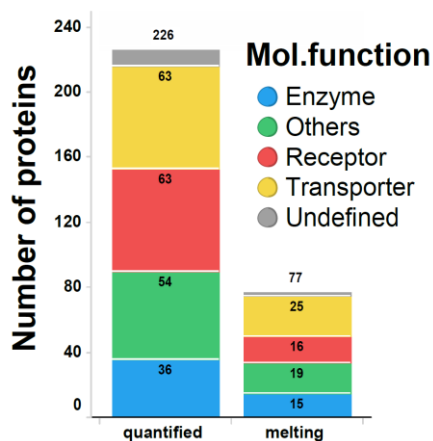
Supplemental Fig. 9 Influence of biotinylation prior to heat-treatment on thermal proteome profiling performance. K562 cells were surface biotinylated in batch and subsequently split. Cells were heated to different temperatures for 3 min followed by 3 min incubation at RT. Subsequently, cells were lysed in PBS containing 1 % IGEPAL CA-630. Protein aggregates were removed by filtration and a volume of lysate corresponding to 100 µg protein in the reference temperature sample was subjected to streptavidin-based enrichment for 60 min. Enriched proteins were eluted by tryptic on-bead digestion for 16 h. Resulting peptide mixtures were TMT-labeled, cleaned by C18-SCX STAGE tips and 25 % of the final mixtures were analyzed by LC-MS/MS on a Q Exactive Hybrid-Quadrupole-Orbitrap mass spectrometer using a 270 min gradient. Data was normalized and filtered for cell surface proteins with qusm ≥ 3, qupm ≥ 2, R^2 ≥ 0.6 and ΔT_M ≤ 3 °C in both of replicates.

Supplemental Fig. 10 Influence of periodate oxidation prior to HT on protein biotinylation and enrichment. K562 cells were oxidized in batch and subsequently split. In two replicates each, cells were incubated for 3 min at 4, 40 or 70 °C followed by 3 min at RT. Cell surface proteins were biotinylated, cells were lysed in 4 % SDS and 6 µg total protein were subjected to SDS-PAGE and immunoblotting for biotinylated proteins. Remaining 100 µg lysate were subjected to enrichment with streptavidin-resin followed by 16 h of digestions and TMT6 labeling. MS-analysis data was normalized to average relative fold-changes per condition and quantified proteins were filtered for qusm ≥ 3, qupm ≥ 2 and plasma membrane localization. (**A**) Blotting and staining of biotinylated proteins with Streptavidin DyLight800. (**B**) Abundance of cell surface proteins after HT at 40 and 70 °C relative to the 4 °C control sample.
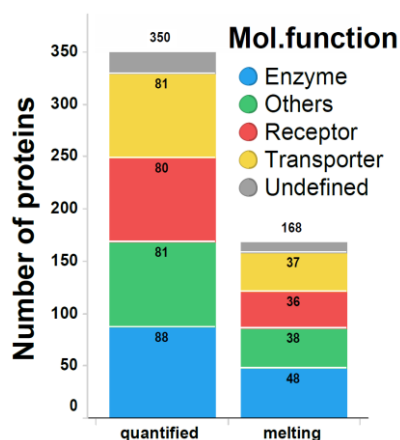
Supplemental Fig. 11 Influence of periodate oxidation prior to HT on thermal proteome profiling. K562 cells were oxidized in batch and subsequently split. Cells were heated to ten different temperatures for 3 min followed by 3 min incubation at RT. Subsequently, cells were lysed in PBS containing 1 % IGEPAL CA-630. Protein aggregates were removed by filtration and a volume of lysate corresponding to 100 µg protein in the reference temperature sample was subjected to streptavidin-based enrichment for 60 min. Enriched proteins were eluted by tryptic on-bead digestion for 16 h. Resulting peptide mixtures were TMT-labeled, cleaned by C18-SCX STAGE tips and 25 % of the final mixtures were analyzed by LC-MS/MS on a Q Exactive Hybrid-Quadrupole-Orbitrap mass spectrometer using a 270 min gradient. Data was normalized and filtered for cell surface proteins with qusm ≥ 3, qupm ≥ 2, R^2 ≥ 0.6 and ΔT_M ≤ 3 °C in both of replicates.

Supplemental Fig. 12 Streptavidin-coated bead titration for efficient capturing of biotinylated proteins. K562 cells were surface biotinylated in batch and lysed in 1 % IGEPAL CA-630. To indicated streptavidin-coated bead volumes, 150 µg lysate was added and incubated either 1 h or 2 h at RT while overhead shaking. The flow-through was collected and subjected to SDS-PAGE followed by blotting and staining of biotinylated proteins with Streptavidin DyLight800. Relative intensities were calculated towards the input (0 µL beads). (**A**) Affinity capturing for 60 min at RT. (**B**) Affinity capturing for 120 min at RT.
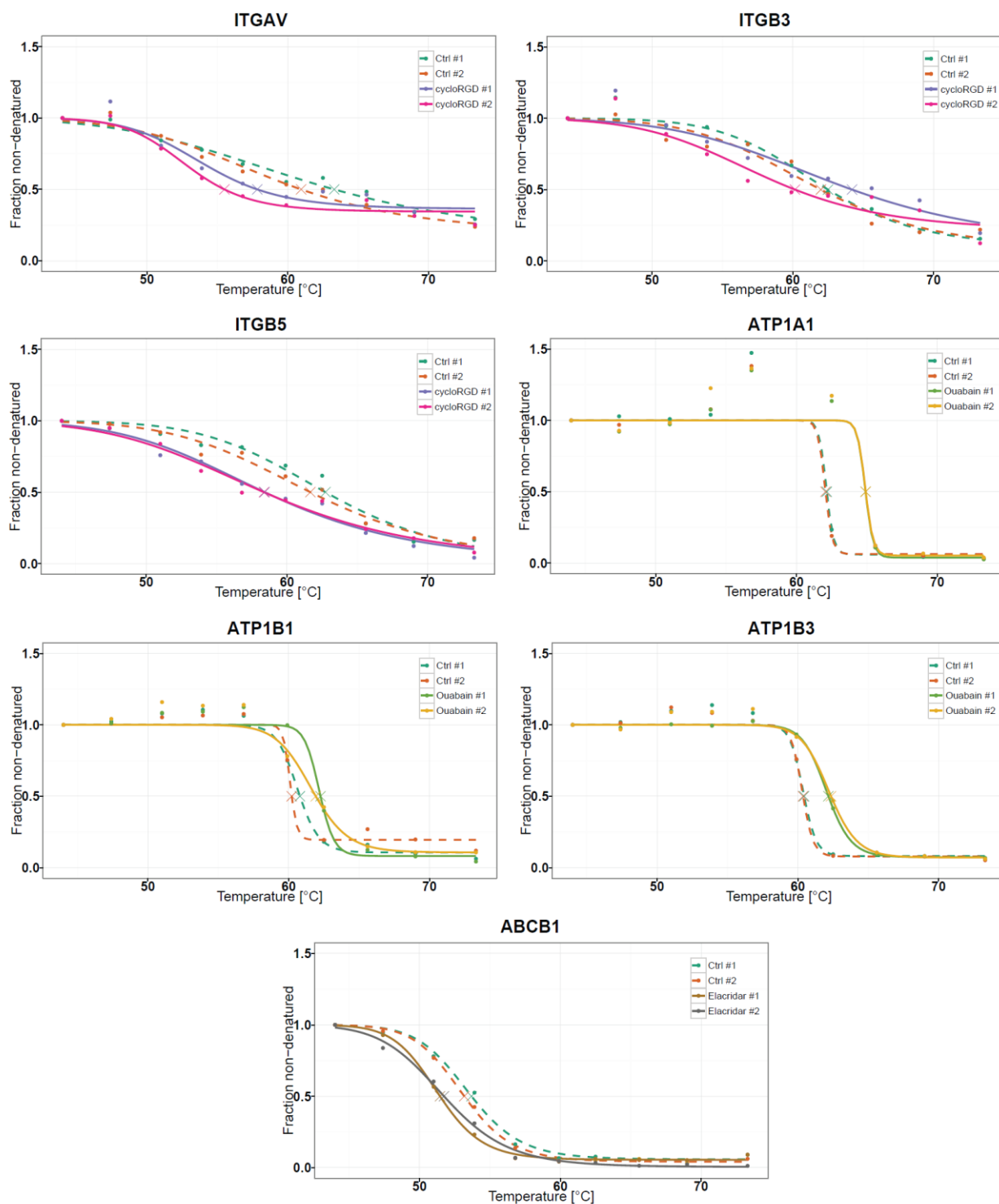
Supplemental Fig. 13 Melting curves of expected targets in evaluation experiments. K562 cells were treated in two biological replicates with 10 µM cyclo-RGDfK, 1 µM ouabain or 1 µM elacridar. Vehicle treated cells were used as controls. Expected targets are ITGAV, ITGB3 and ITGB5 for cyclo-RGD, ATP1A1, ATP1B1 and ATP1B3 for ouabain and ABCB1 for elacridar.
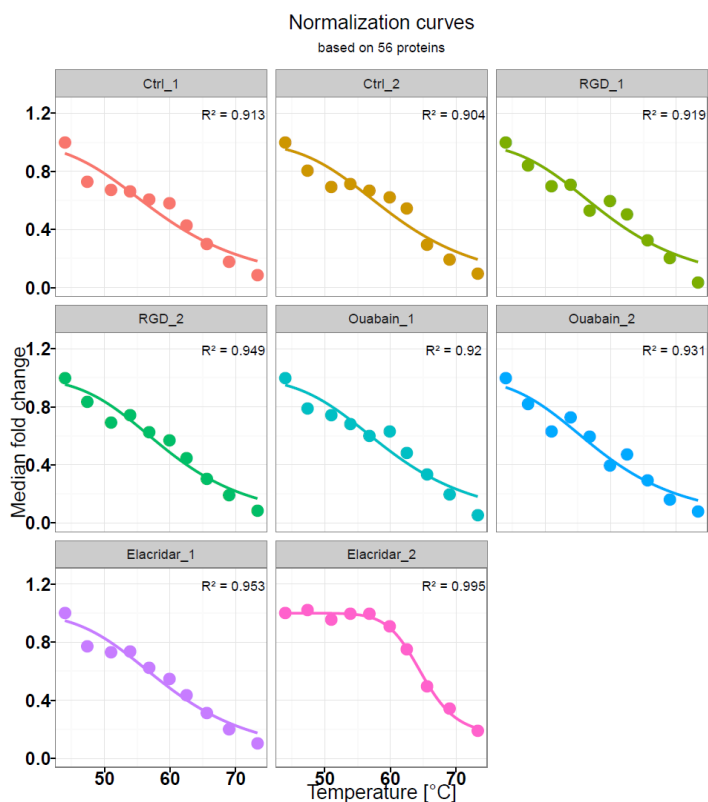
Supplemental Fig. 14 Data normalization curves for evaluation experiments. K562 cells were treated in two biological replicates with 10 µM cyclo-RGDfK, 1 µM ouabain or 1 µM elacridar. Vehicle treated cells were used as controls.
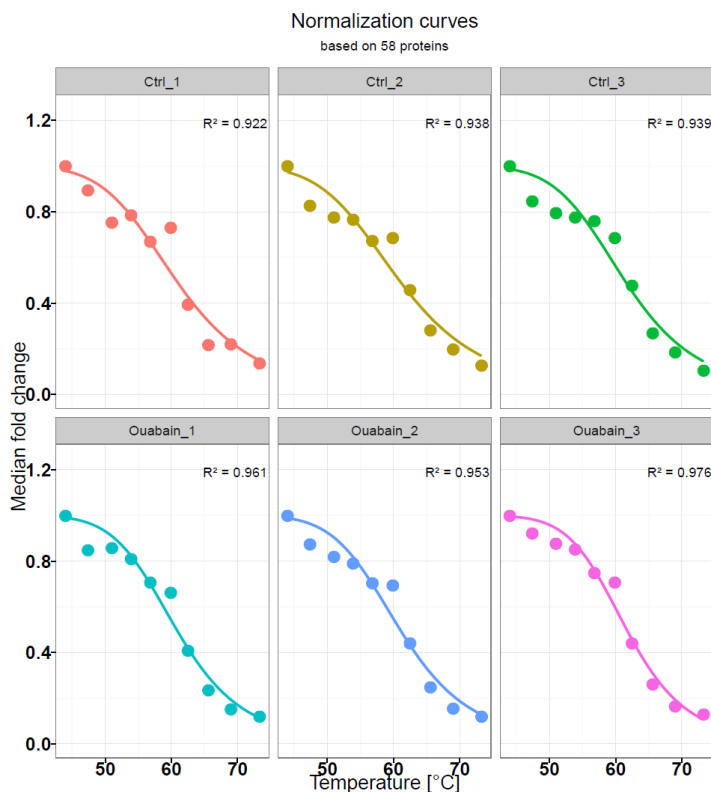
Supplemental Fig. 15 Data normalization curves for melting curve-based ouabain experiment. K562 cells were treated in three biological replicates with 1 µM ouabain. Vehicle treated cells were used as controls.
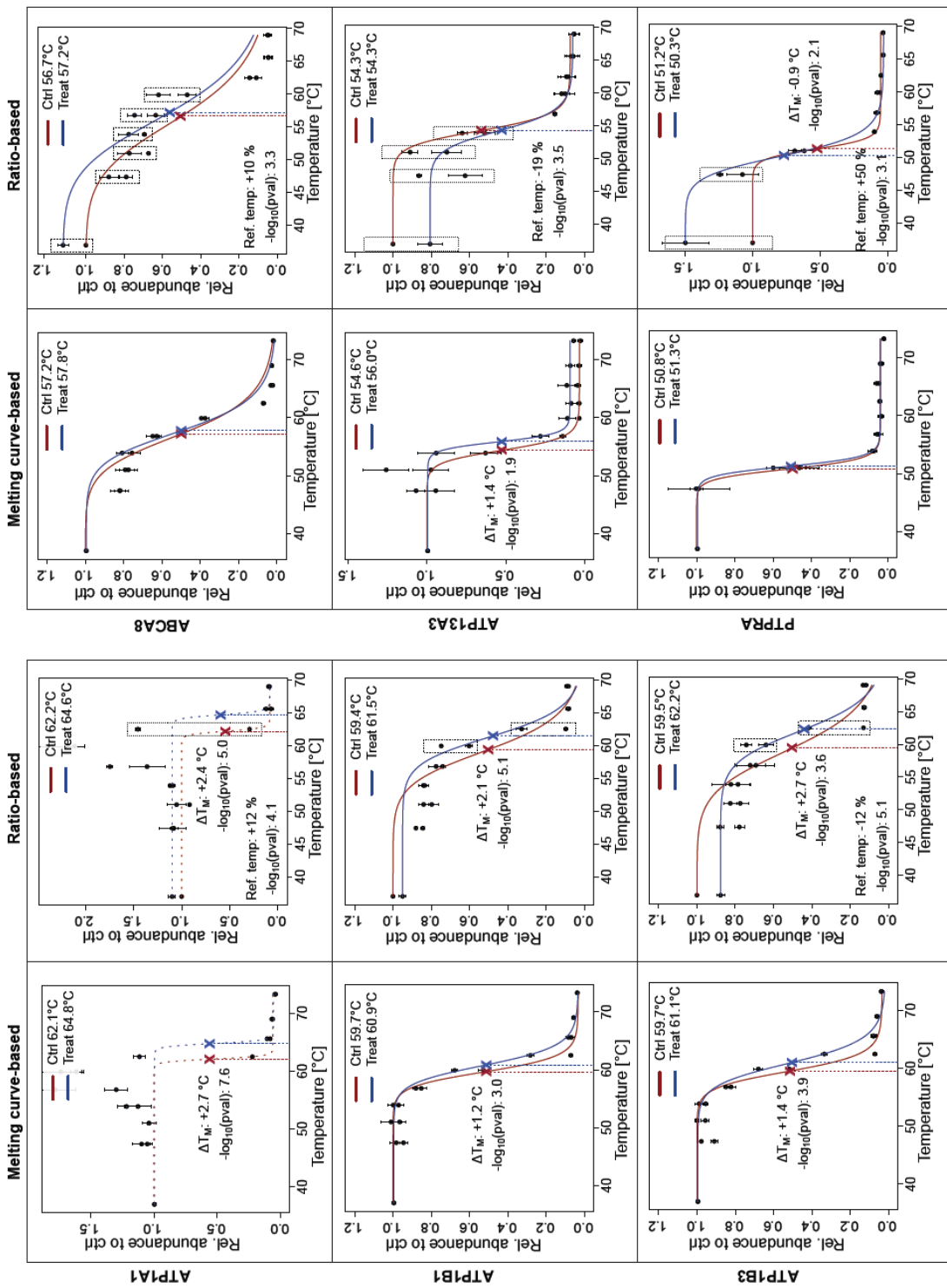
Supplemental Fig. 16 Comparison of melting curve-based and ratio-based thermal proteome profiling. Mean melting curves in controls and treatments of significantly affected proteins by ouabain treatment (n = 3). Standard deviations indicated by error bars. In case of ratio-based analysis, the cumulated data points are highlighted with dashed boxes. Treatment-induced melting point shifts and abundance changes are indicated with statistical significances.
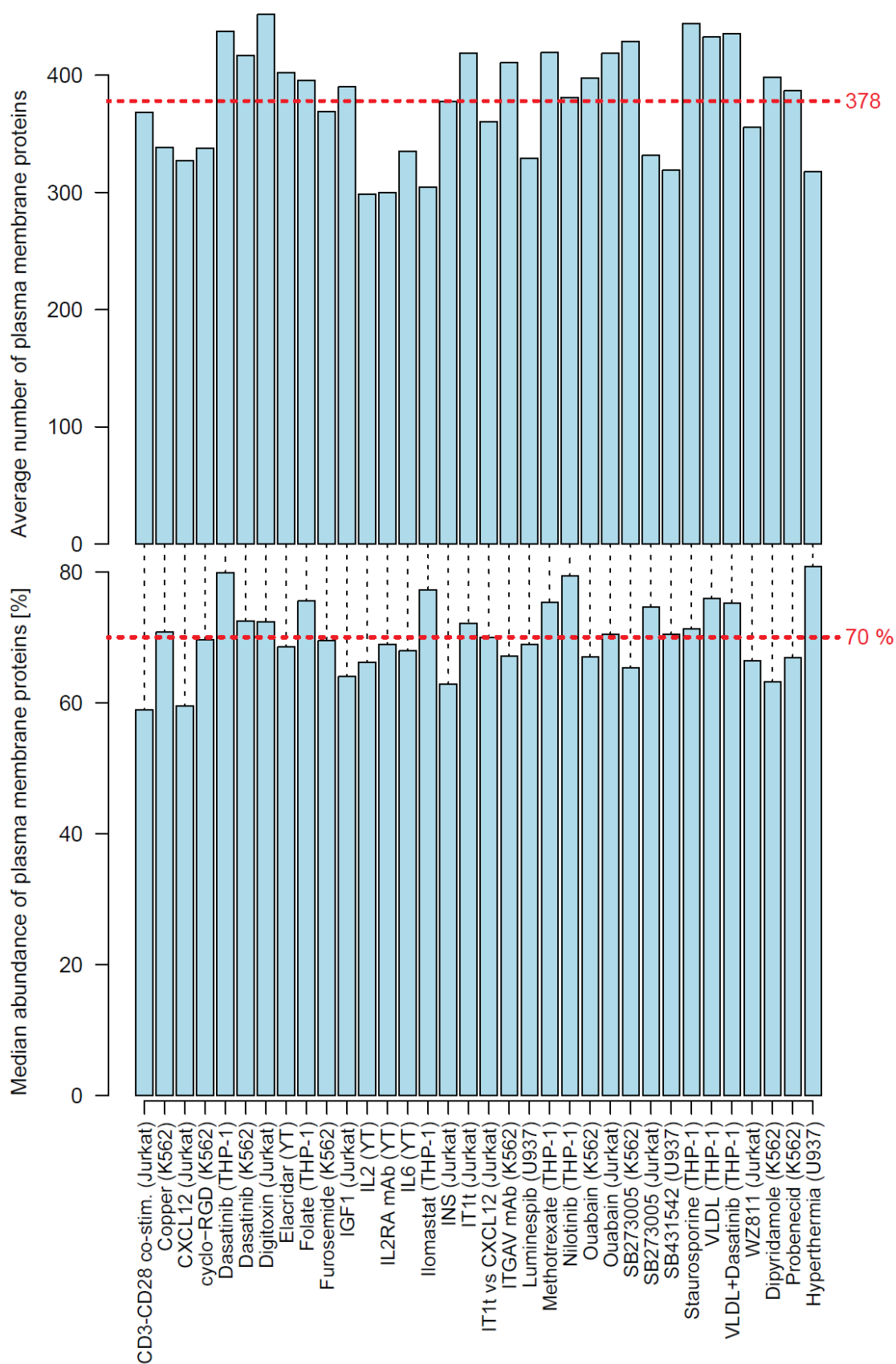
Supplemental Fig. 17 Performance indicators for cell surface thermal proteome profiling experiments. Average number (top) and median fractional abundance (bottom) of identified plasma membrane proteins in 34 cell surface thermal proteome profiling experiments each with at least three biological replicates.
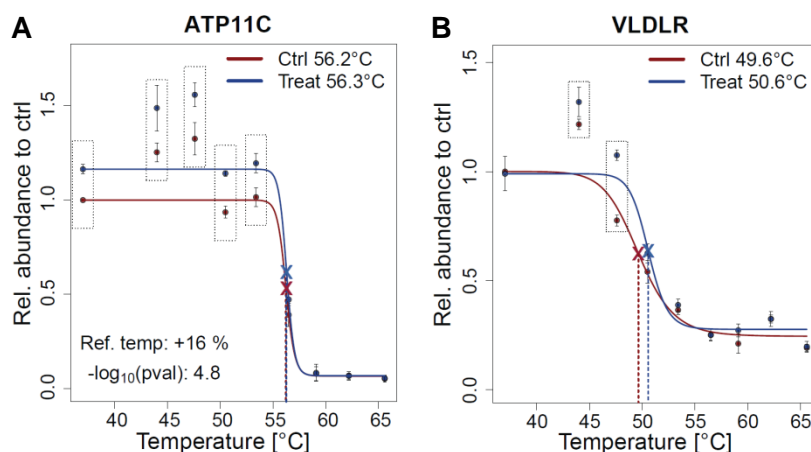
Supplemental Fig. 18 Melting curves of affected proteins by treatment of THP-1 cells with dasatinib. Cells were treated in three biological replicates with 1 μM dasatinib or vehicle as control. (**A**) Mean melting curves of ATP11C in controls and treatments. Error bars indicate standard deviations. Selected data points for cumulation are highlighted with dashed boxes. Treatment-induced thermal shifts and abundance changes are indicated with statistical significances. (**B**) As (A) but for VLDLR.
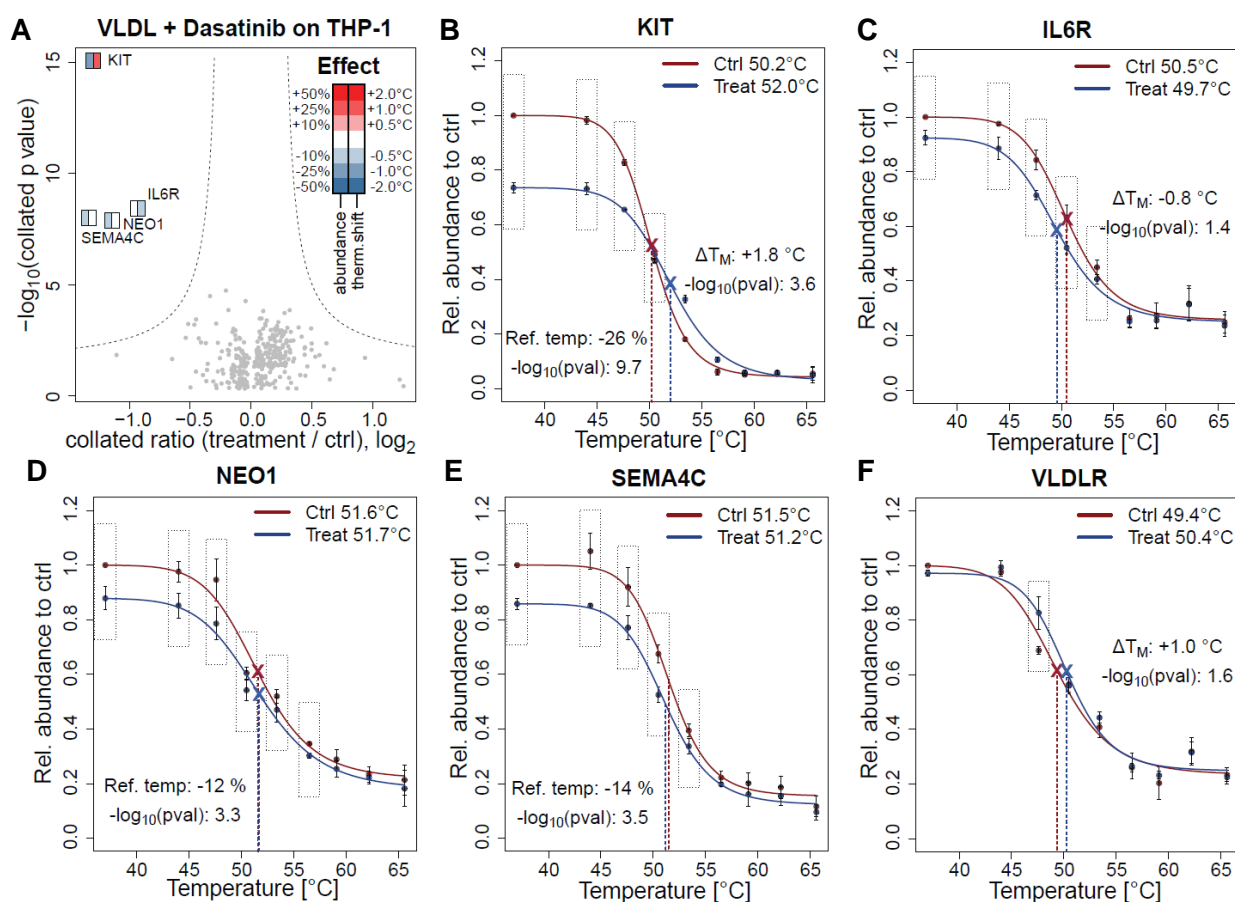

Supplemental Fig. 19 Monitoring effects of VLDL-treatment in presence of dasatinib. Serum starved THP-1 cells were treated in three biological replicates for 60 min with 1 μM dasatinib or vehicle as control followed by 60 min incubation with 100 μg human VLDL.(**A**) Significantly affected proteins upon treatment are labeled. Left half of squares indicate significant abundance changes while right half of squares indicate significant thermal shifts. Median standard deviation between replicates: 0.12. (**B-F**) Mean melting curves in controls and treatments of significantly affected proteins. Error bars indicate standard deviations. Selected data points for cumulation are highlighted with dashed boxes. Treatment-induced thermal shifts and abundance changes are indicated with statistical significances.
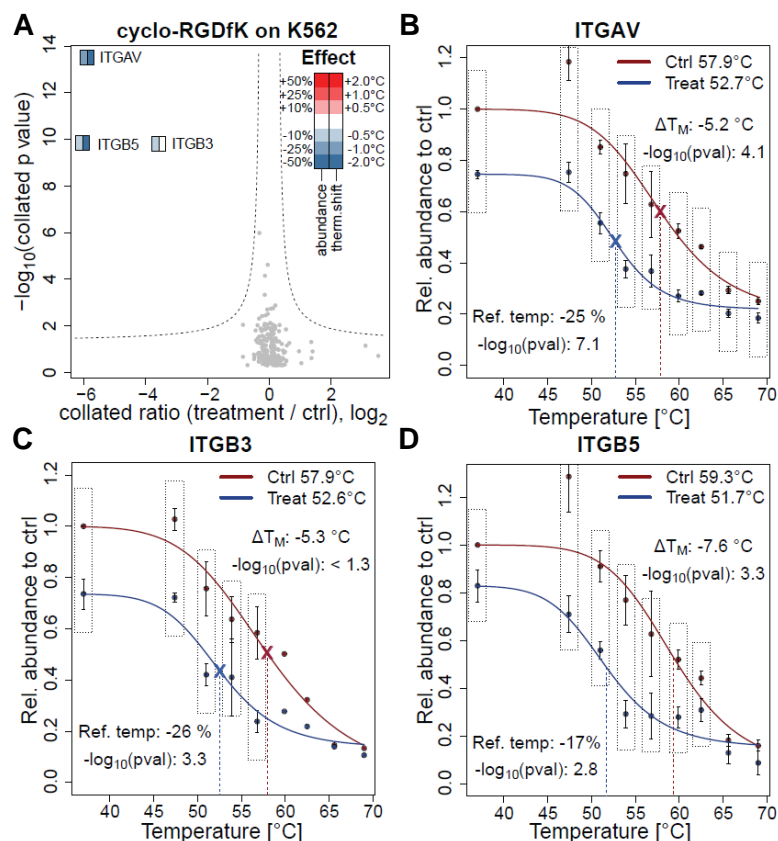
Supplemental Fig. 20 Monitoring target engagement of cyclo-RGDfK to integrins. K562 cells were treated in three biological replicates with 10 µM cyclo-RGDfK or vehicle as control followed by a heat treatment with a temperature gradient between 37 °C to 69 °C. (**A**) Significantly affected proteins upon treatment are labeled. Left half of squares indicate significant abundance changes while right half of squares indicate significant thermal shifts. Median standard deviation between replicates: 0.13. (**B-D**) Mean melting curves in controls and treatments of significantly affected proteins. Error bars indicate standard deviations. Selected data points for cumulation are highlighted with dashed boxes. Treatment-induced thermal shifts and abundance changes are indicated with statistical significances.
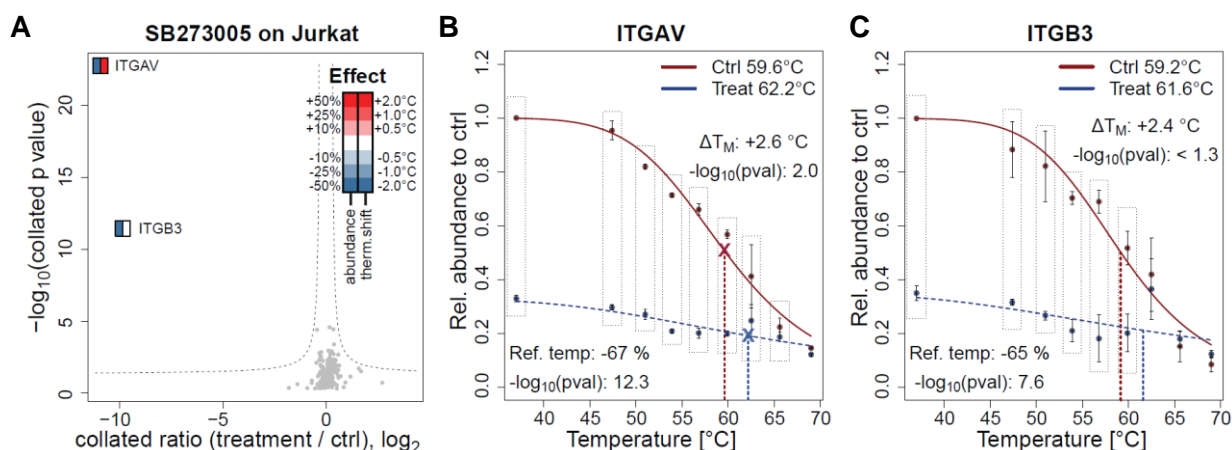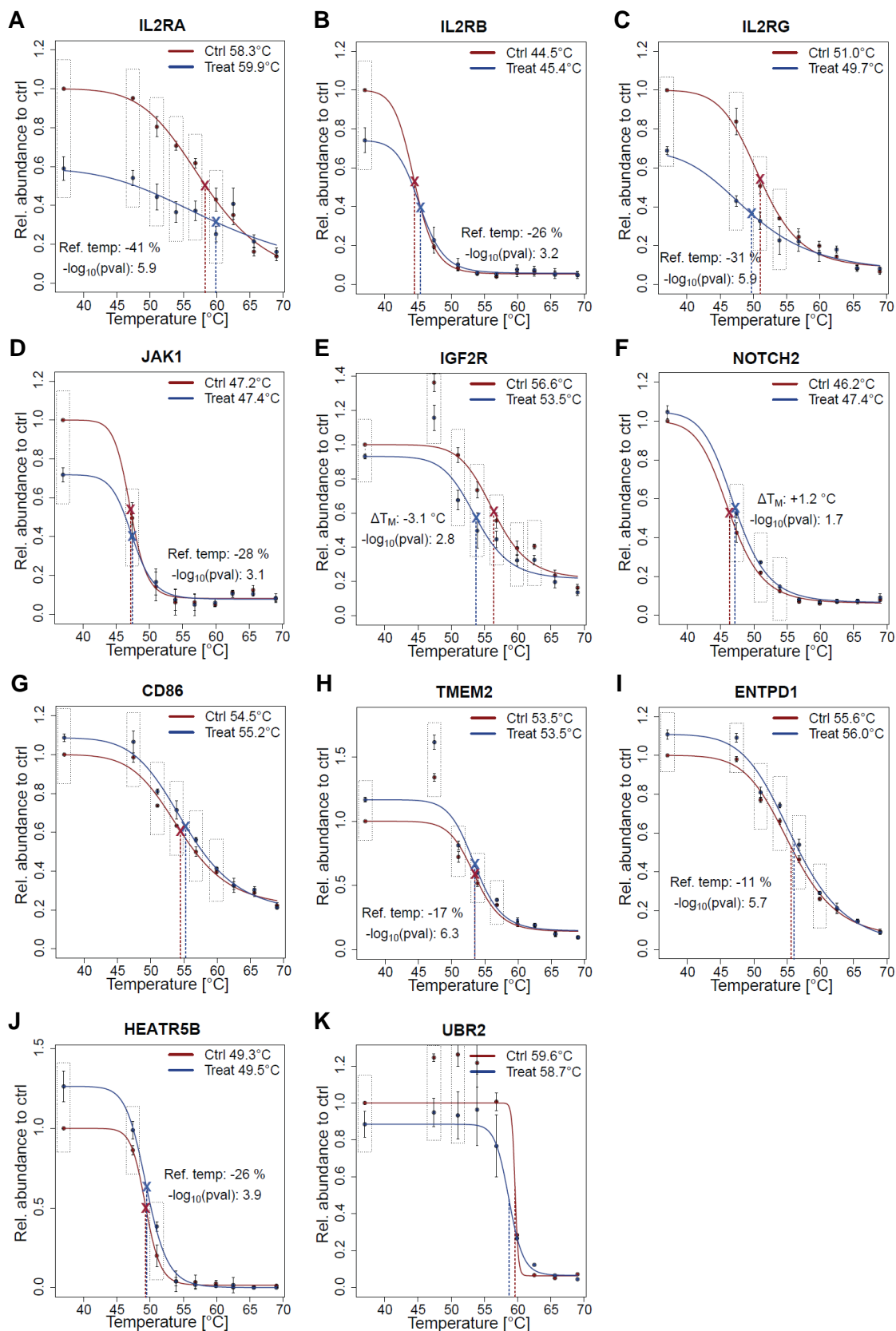
Supplemental Fig. 21 Monitoring target engagement of SB273005 to integrins on Jurkat cells. Cells were treated in three biological replicates with 1 µM SB273005 or vehicle as control followed by a heat treatment with a temperature gradient between 37 °C to 69 °C. (**A**) Significantly affected proteins upon treatment are labeled. Left half of squares indicate significant abundance changes while right half of squares indicate significant thermal shifts. Median standard deviation between replicates: 0.14. (**B**) Mean melting curves of ITGAV in controls and treatments. Dashed melting curves indicate curve fits with $R^2 < 0.85$. Error bars indicate standard deviations. Selected data points for cumulation are highlighted with dashed boxes. Treatment-induced thermal shifts and abundance changes are indicated with statistical significances. (**C**) As (**B**) but for ITGB3.
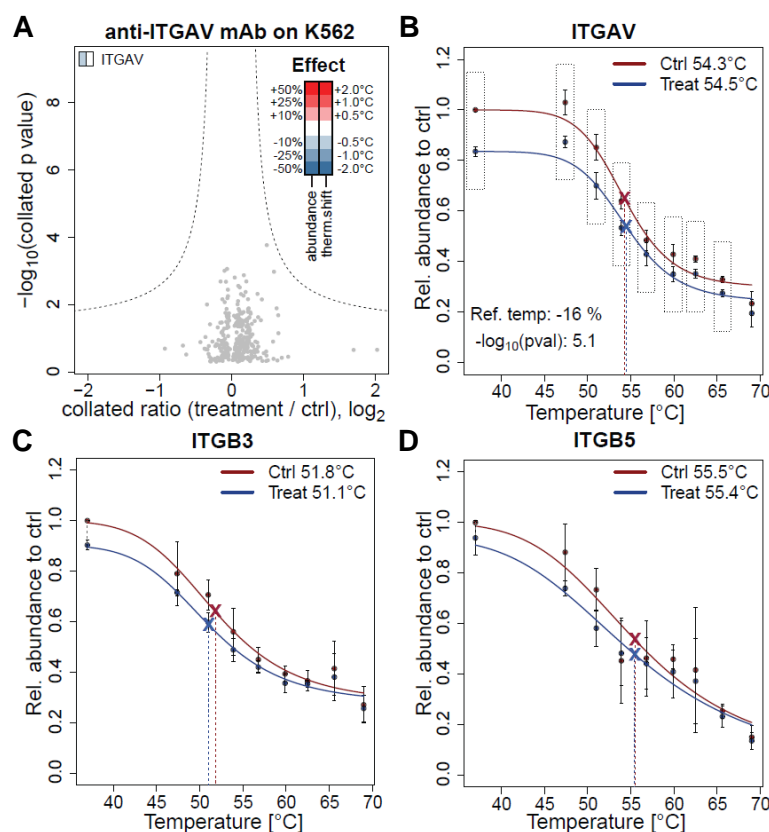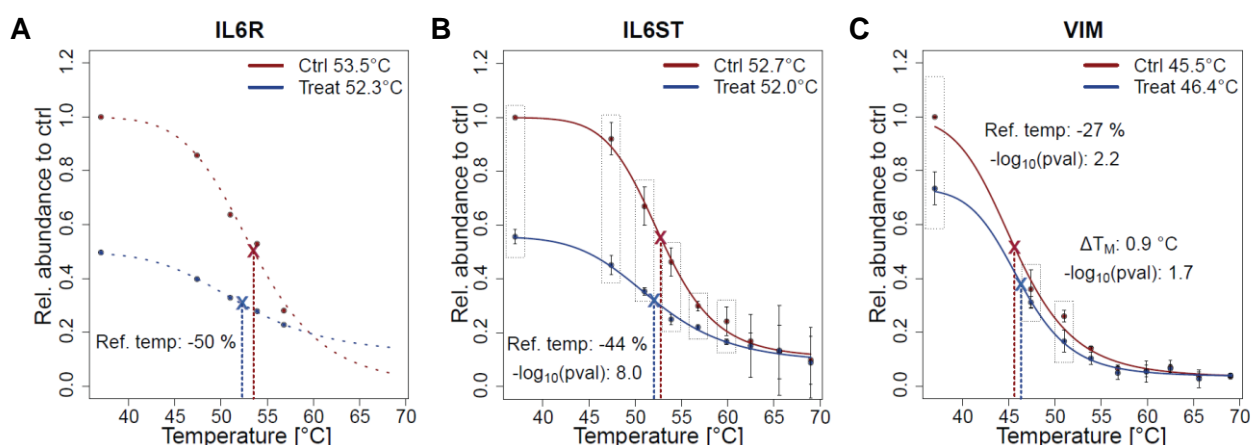

Supplemental Fig. 22 Monitoring target engagement of a mAb to integrins. K562 cells were treated in three biological replicates with 20 µg of an anti-ITGAV mAb (Sigma-Aldrich, I3783) or vehicle as control followed by heat treatment with a temperature gradient between 37 °C to 69 °C. (**A**) Significantly affected proteins upon treatment are labeled. Left half of squares indicate significant abundance changes while right half of squares indicate significant thermal shifts. Median standard deviation between replicates: 0.11. (**B-D**) Mean melting curves of significantly affected proteins in controls and treatments. Error bars indicate standard deviations. Selected data points for cumulation are highlighted with dashed boxes. Treatment-induced thermal shifts and abundance changes are indicated with statistical significances.
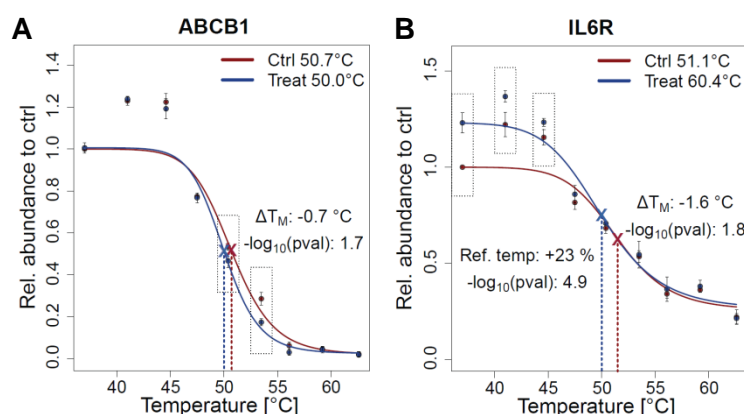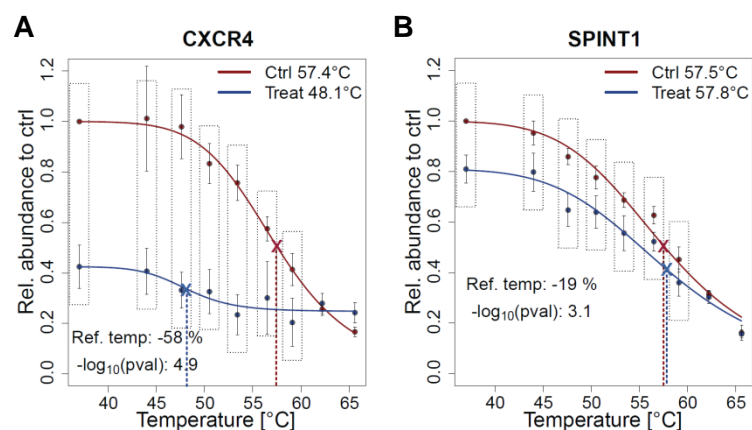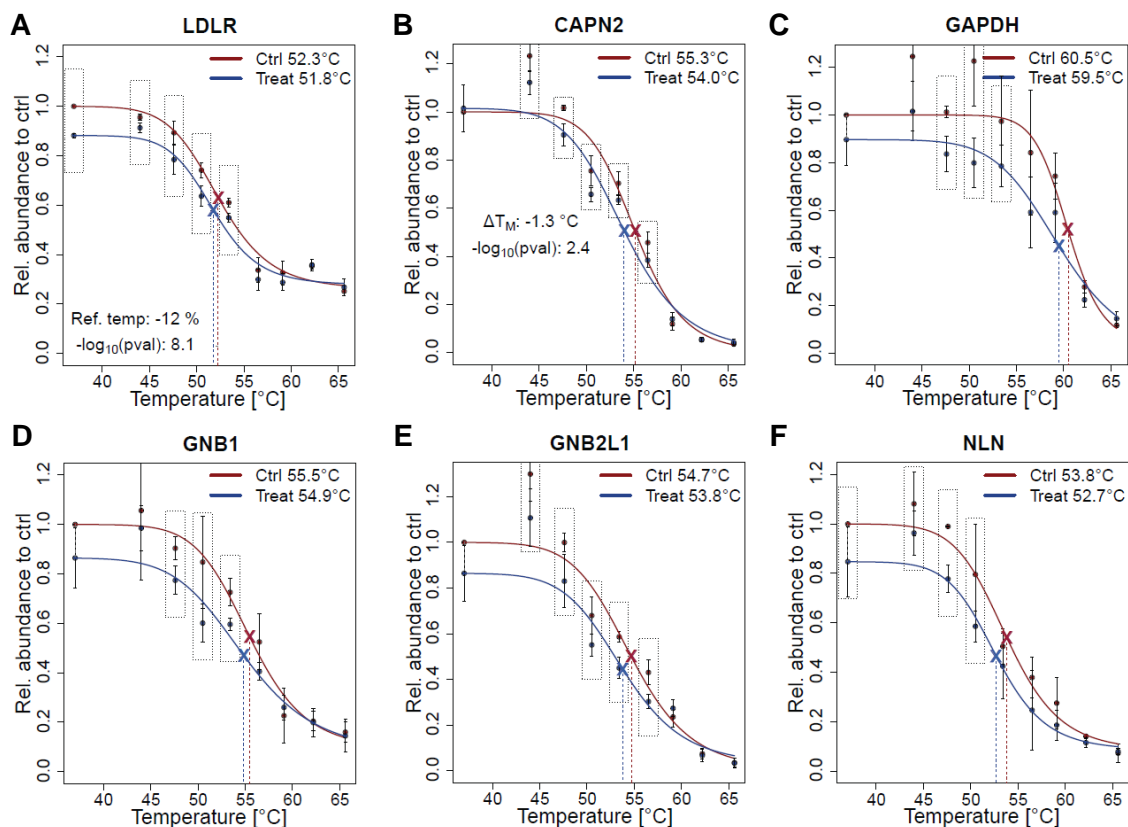
Supplemental Fig. 23 Monitoring target engagement with elacridar. Cells were treated in three biological replicates with 1 µM elacridar or vehicle as control. (**A**) Mean melting curves of ABCB1 in controls and treatments. Error bars indicate standard deviations. Selected data points for cumulation are highlighted with dashed boxes. Treatment-induced thermal shifts and abundance changes are indicated with statistical significances. (**B**) As (A) but for IL6R.
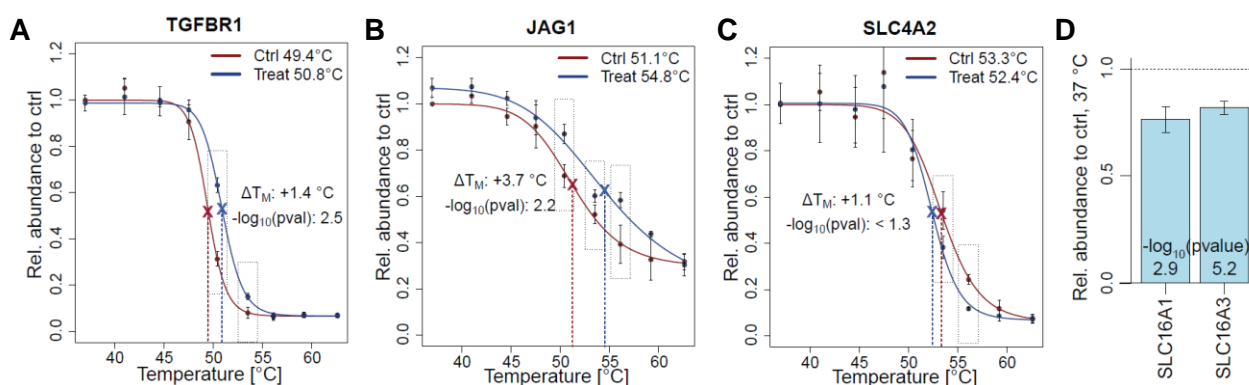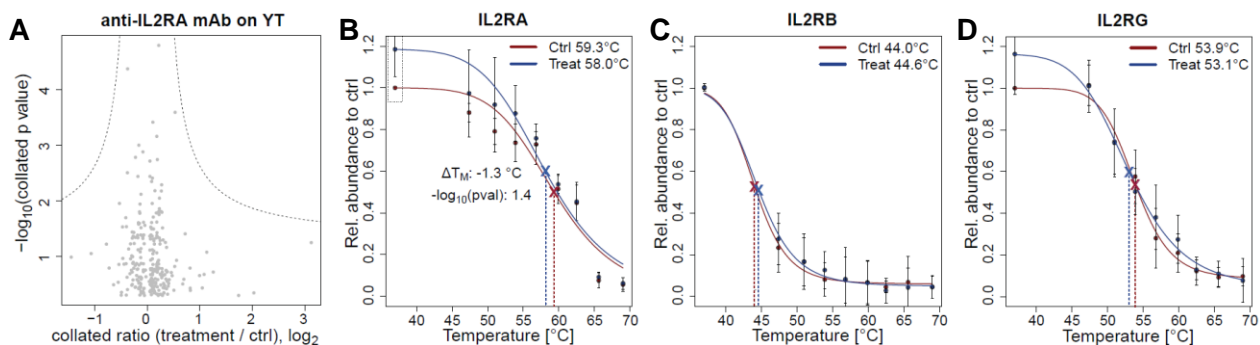

Supplemental Fig. 24 Monitoring target engagement with SB431542. Cells were treated in three biological replicates with 10 µM SB431542 or vehicle as control. (**A**) Mean melting curves of TGFBR1 in controls and treatments. Error bars indicate standard deviations. Selected data points for cumulation are highlighted with dashed boxes. Treatment-induced thermal shifts are indicated with statistical significances. (**B**) As (A) but for JAG1. (**C**) As (A) but for SLC4A2. (**D**) Average abundance at the reference temperature (37 °C) of SLC16A1 and SLC16A3 in treatments relative to controls. Error bars indicate standard deviations. Statistical significances are indicated.
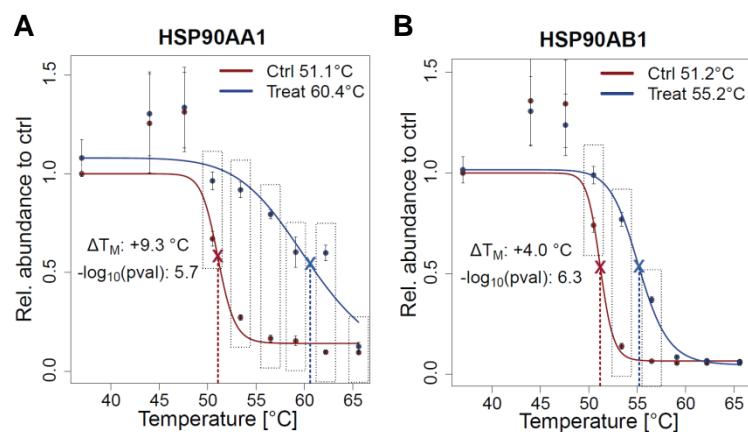
Supplemental Fig. 25 Monitoring target engagement with luminespib. Cells were treated in three biological replicates with 1 µM luminespib or vehicle as control. (**A**) Mean melting curves of HSP90AA1 in controls and treatments. Error bars indicate standard deviations. Selected data points for cumulation are highlighted with dashed boxes. Treatment-induced thermal shifts are indicated with statistical significances. (**B**) As (A) but for HSP90AB1.
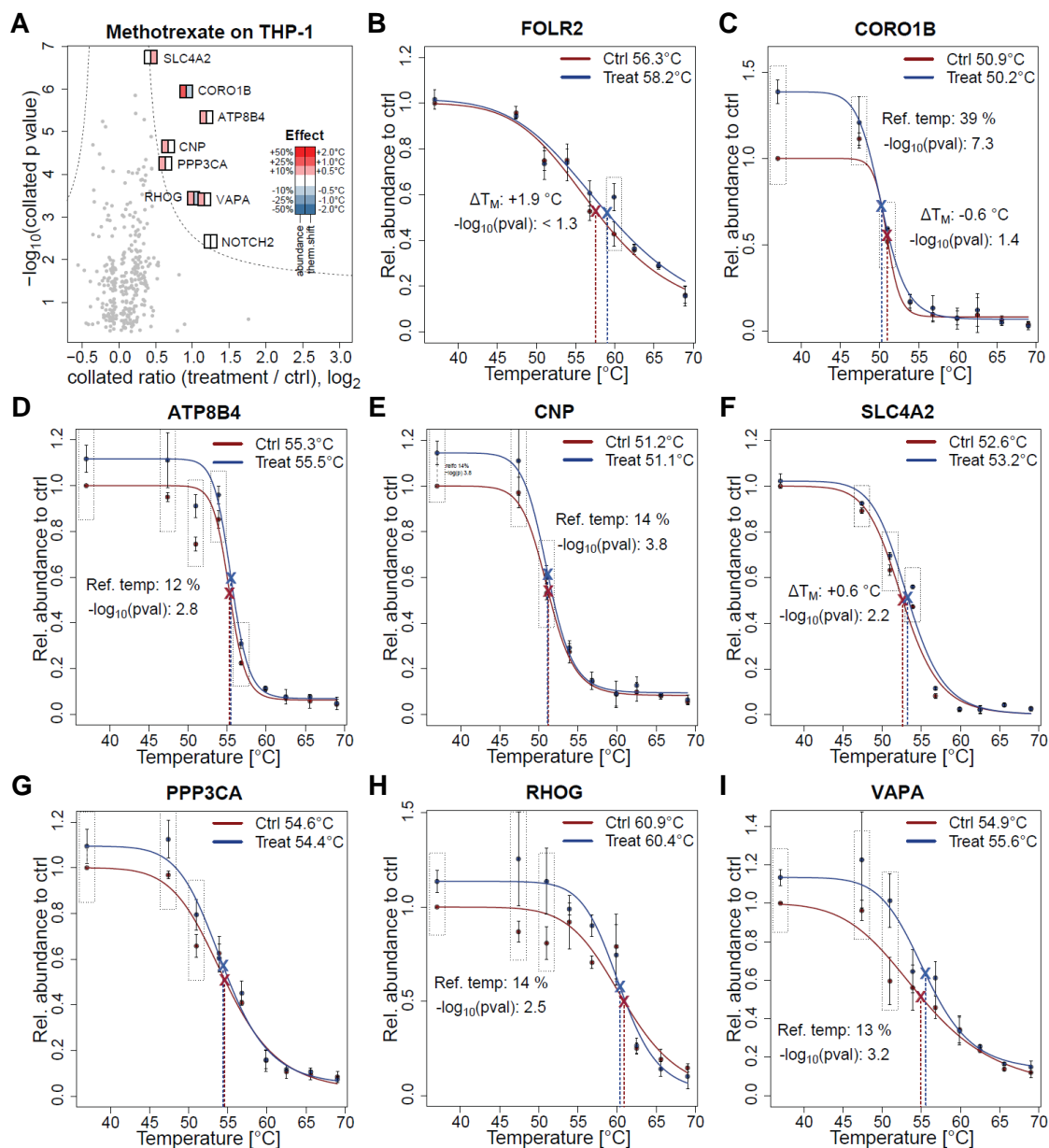
Supplemental Fig. 26 Monitoring target engagement with IL2. Cells were treated in three biological replicates with 10 nM IL2 or vehicle as control. (**A-K**) Mean melting curves in controls and treatments of significantly affected proteins. Error bars indicate standard deviations. Selected data points for cumulation are highlighted with dashed boxes. Treatment-induced thermal shifts and abundance changes are indicated with statistical significances.
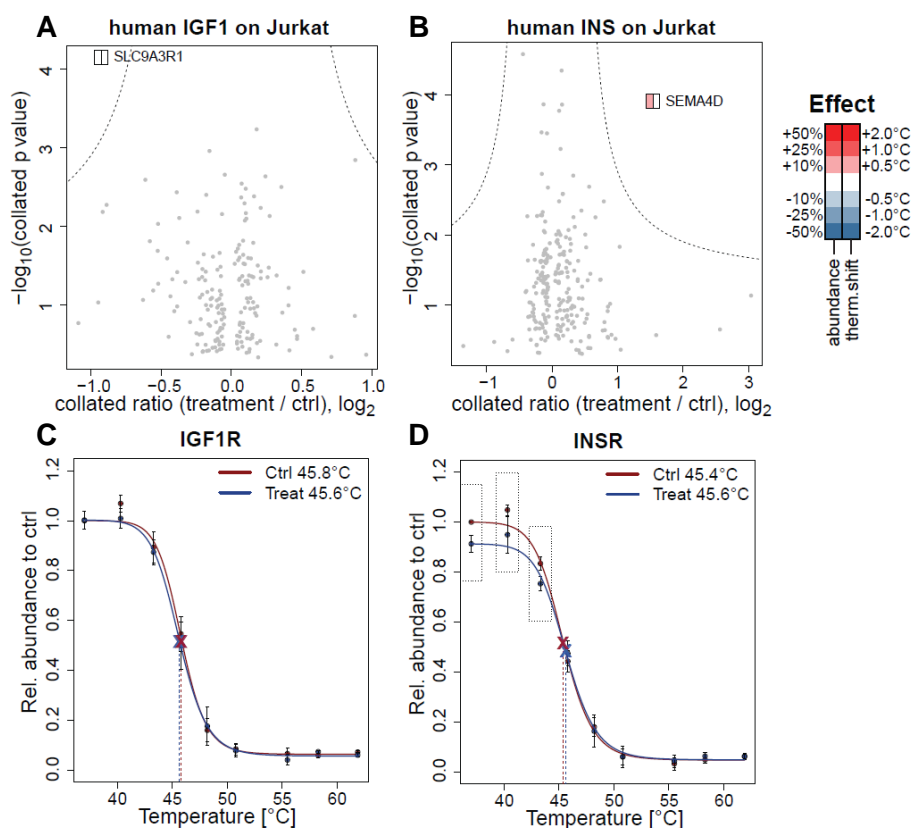
Supplemental Fig. 27 Monitoring target engagement with IL6. Cells were treated in three biological replicates with 20 nM IL6 or vehicle as control. (**A**) Melting curves of IL6R in control and treatment. Since this protein was quantified only in one replicate, fitted melting curves are indicated as dashed lines. (**B-C**) Mean melting curves in controls and treatments of significantly affected proteins. Error bars indicate standard deviations. Selected data points for cumulation are highlighted with dashed boxes. Treatment-induced thermal shifts and abundance changes are indicated with statistical significances.
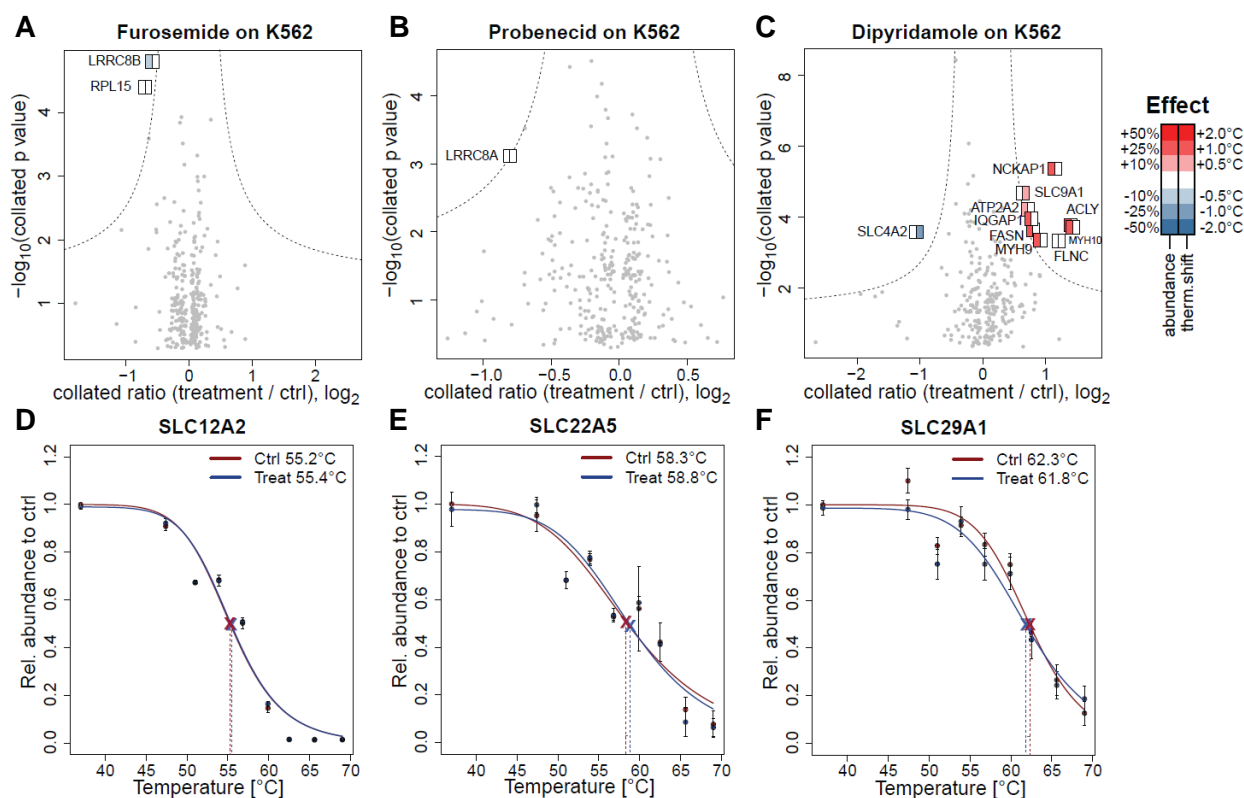

Supplemental Fig. 28 Monitoring target engagement with CXCL12. Cells were treated in three biological replicates with 20 nM CXCL12 or vehicle as control. (**A-B**) Mean melting curves in controls and treatments of significantly affected proteins. Error bars indicate standard deviations. Selected data points for cumulation are highlighted with dashed boxes. Treatment-induced thermal shifts and abundance changes are indicated with statistical significances.

Supplemental Fig. 29 Monitoring target engagement with VLDL. Cells were treated in three biological replicates with 100 µg VLDL or vehicle as control. (**A-F**) Mean melting curves in controls and treatments of significantly affected proteins. Error bars indicate standard deviations. Selected data points for cumulation are highlighted with dashed boxes. Treatment-induced thermal shifts and abundance changes are indicated with statistical significances.
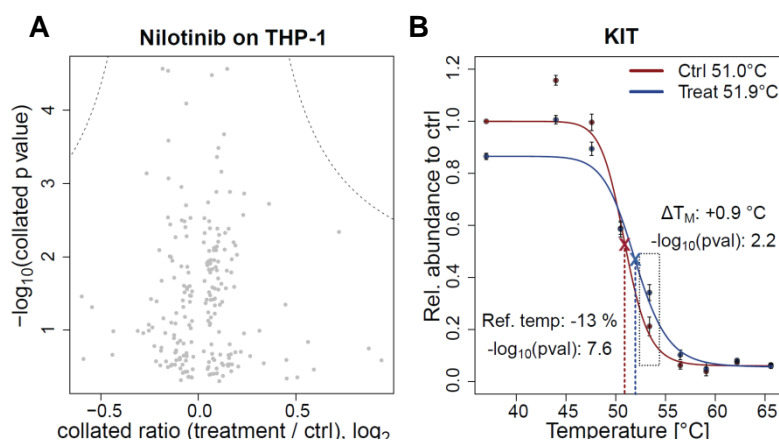

Supplemental Fig. 30 Monitoring target engagement with IL2RA direct mAb. Cells were treated in three biological replicates with 20 µg IL2RA directed mAb (SAB4700360, Sigma-Aldrich) or vehicle as control. (**A**) Significantly affected proteins upon treatment. Median standard deviation between replicates: 0.12. (**B-D**) Mean melting curves of IL2R subunits. Error bars indicate standard deviations.

Supplemental Fig. 31 Monitoring target engagement with methotrexate. Cells were treated in three biological replicates with 20 µM Methotrexate or vehicle as control. (**A**) Significantly affected proteins upon treatment are labeled. Left half of squares indicate significant abundance changes while right half of squares indicate significant thermal shifts. Median standard deviation between replicates: 0.11. (**B-I**) Mean melting curves in controls and treatments of significantly affected proteins. Error bars indicate standard deviations. Selected data points for cumulation are highlighted with dashed boxes. Treatment-induced thermal shifts and abundance changes are indicated with statistical significances.
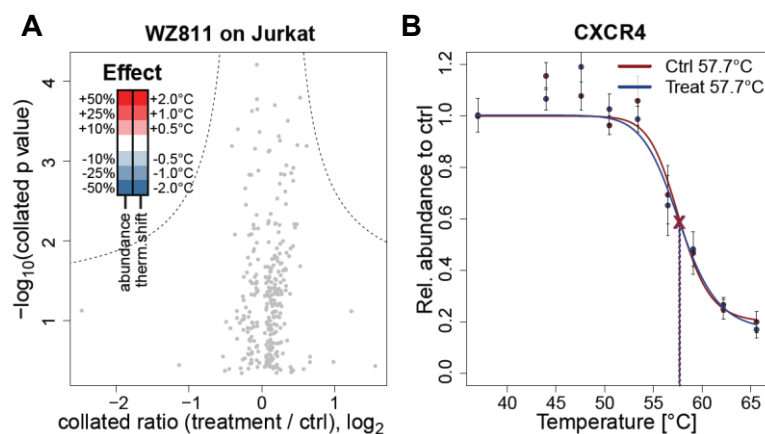
Supplemental Fig. 32 Monitoring target engagement with IGF1 and INS. Cells were treated in three biological replicates with 100 nM IGF1, 100 nM INS or vehicle as control. (**A**) Significantly affected proteins upon IGF1 treatment are labeled. Left half of squares indicate significant abundance changes while right half of squares indicate significant thermal shifts. Median standard deviation between replicates: 0.19. (**B**) As in (A) but showing results of INS treatment. Median standard deviation between replicates: 0.20. (**C**) Mean melting curves of IGF1R in IGF1-treatment experiment. Error bars indicate standard deviations. Selected data points for cumulation are highlighted with dashed boxes. (**D**) as in (C) but for INSR in INS-treatment experiment.

Supplemental Fig. 33 Monitoring target engagement with SLC inhibitors. Cells were treated in three biological replicates with 100 µM furosemide, 1 µM probenecid, 1 µM dipyridamole or vehicle as control. (**A**) Significantly affected proteins upon furosemide treatment are labeled. Left half of squares indicate significant abundance changes while right half of squares indicate significant thermal shifts. Median standard deviation between replicates: 0.11. (**B**) As in (**A**) but showing results of probenecid treatment. Median standard deviation between replicates: 0.12. (**C**) As in (**A**) but showing results of dipyridamole treatment. Median standard deviation between replicates: 0.16. (**D-F**) Mean melting curves of SLC12A2 in furosemide-treatment experiment, of SLC22A5 in probenecid-treatment experiment and of SLC29A1 in dipyridamole-treatment experiment, respectively. Error bars indicate standard deviations.
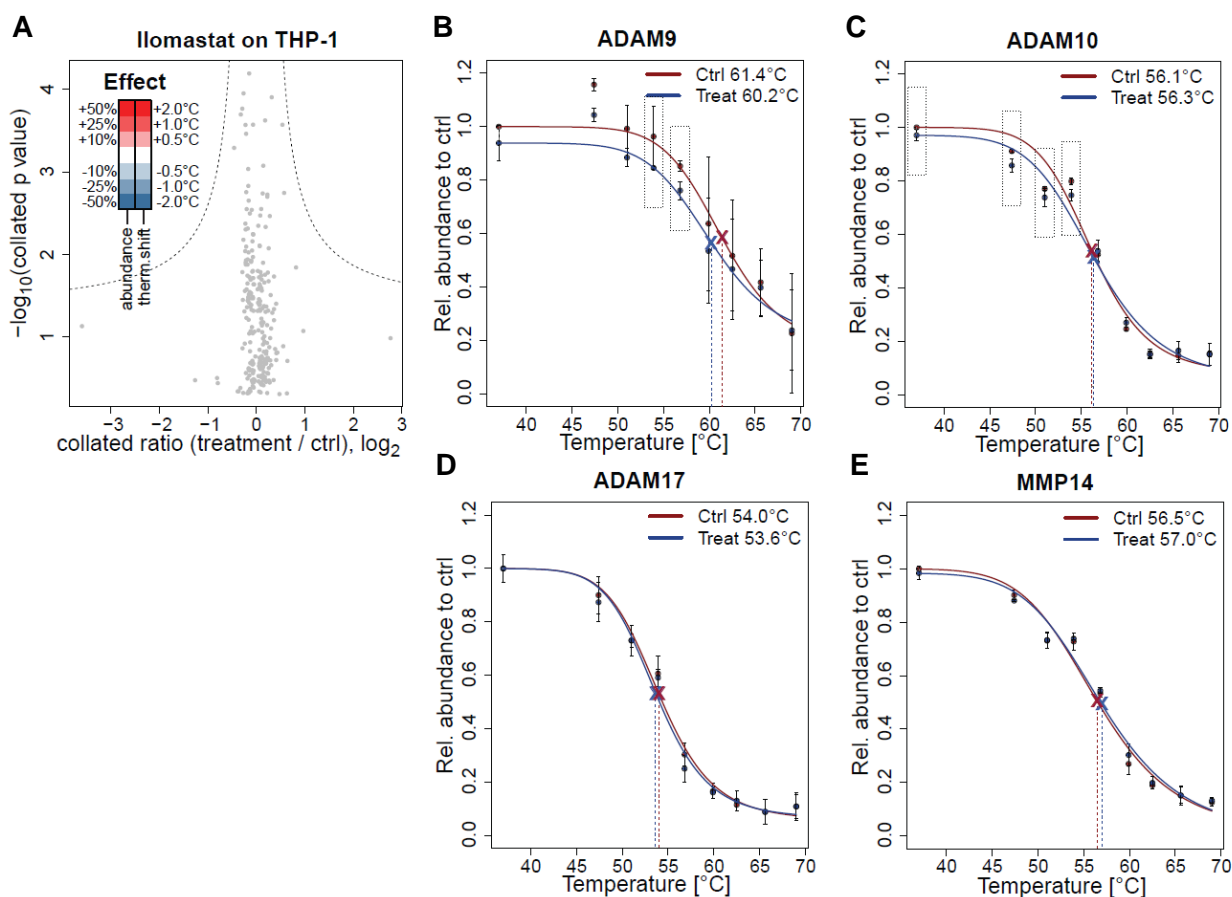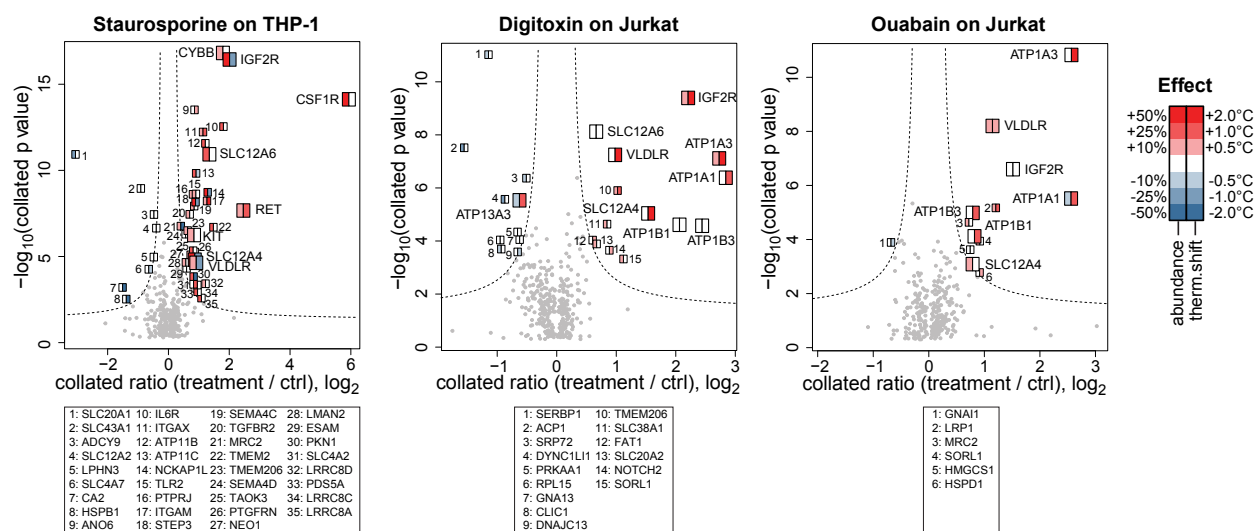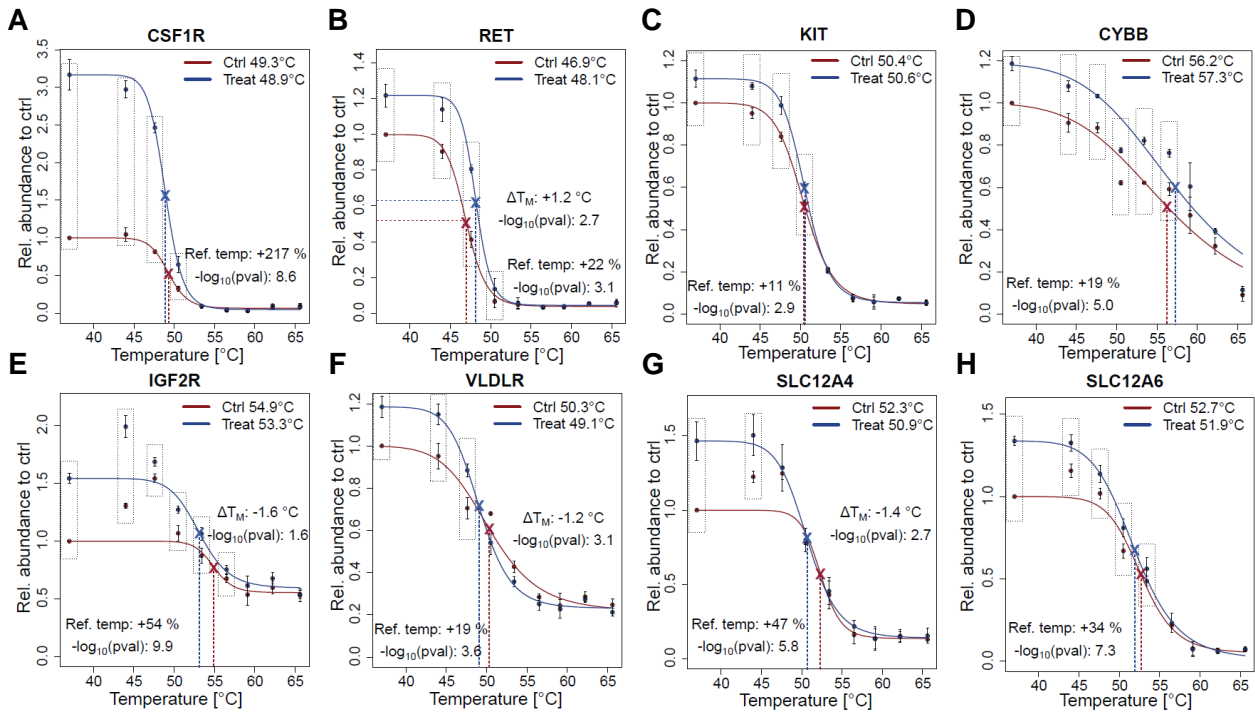
Supplemental Fig. 34 Monitoring target engagement with ilomastat. THP-1 cells were treated in three biological replicates with 1 µM ilomastat or vehicle as control. (**A**) Significantly affected proteins upon treatment. Median standard deviation between replicates: 0.12. (**B-E**) Mean melting curves of expected ilomastat targets ADAM9, ADAM10, ADAM17 and MMP14, respectively. Error bars indicate standard deviations. Selected data points for cumulation are highlighted with dashed boxes.

Supplemental Fig. 35 Monitoring target engagement with nilotinib. THP-1 cells were treated in three biological replicates with 1 µM nilotinib or vehicle as control. (**A**) Significantly affected proteins upon treatment. Median standard deviation between replicates: 0.09. (**B**) Mean melting curves of expected nilotinib target KIT. Error bars indicate standard deviations.
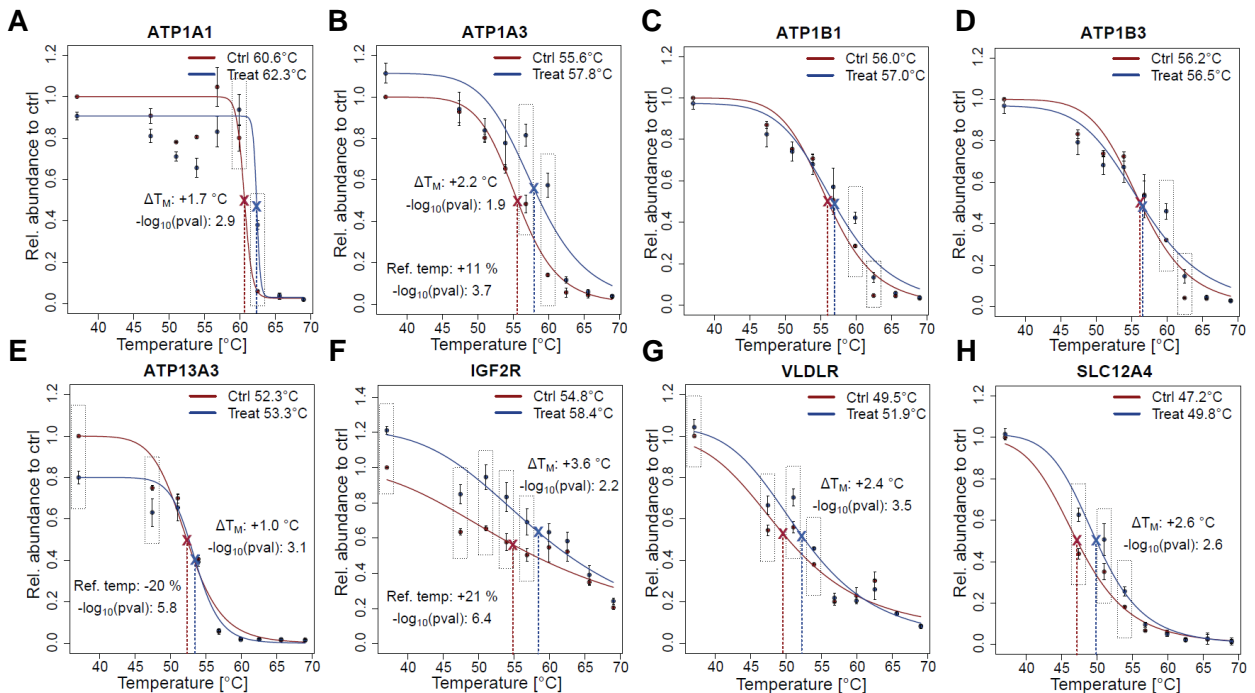
Supplemental Fig. 36 Monitoring target engagement with WZ811. Jurkat cells were treated in three biological replicates with 1 µM WZ811 or vehicle as control. (**A**) Significantly affected proteins upon treatment. Median standard deviation between replicates: 0.13. (**B**) Mean melting curves of expected WZ811 target CXCR4. Error bars indicate standard deviations.
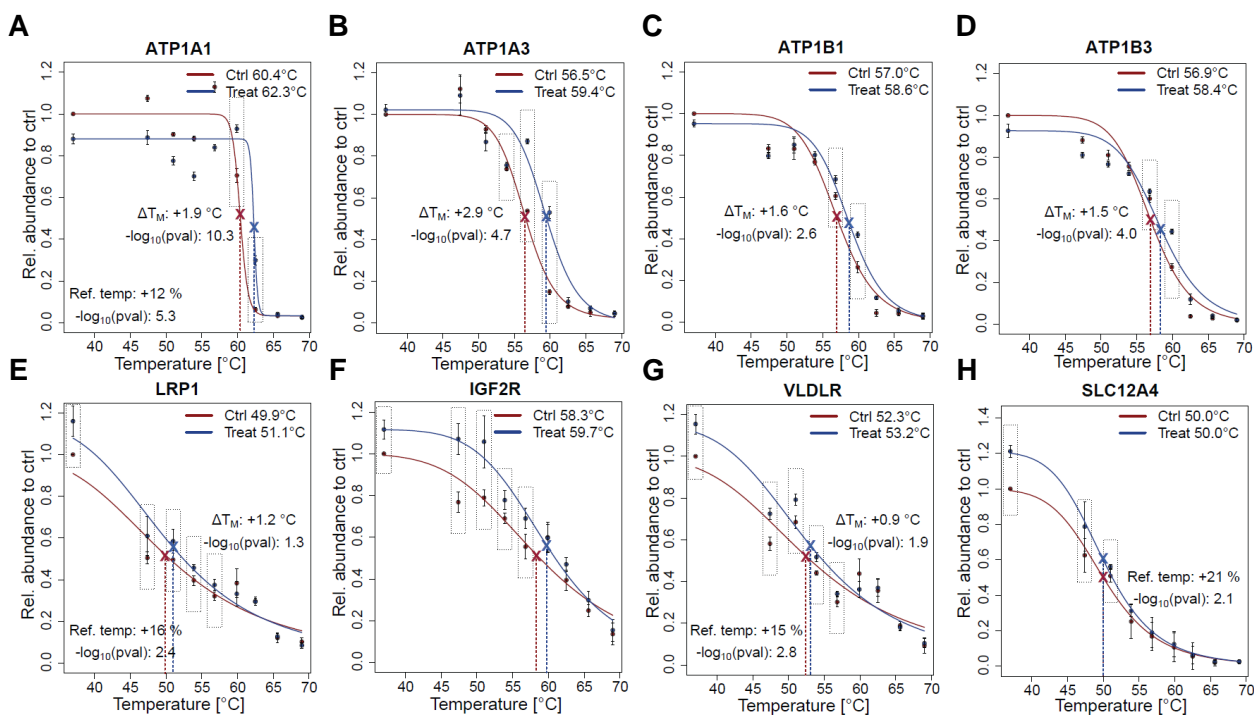

Supplemental Fig. 37 Monitoring effect of apoptosis-inducing compounds. Cells were treated in three biological replicates with 1 µM staurosporine, 1 µM digitoxin, 1 µM ouabain or vehicle as control. Respectively used cell lines are indicated (**A**) List of all significantly affected proteins upon treatment with staurosporine are labeled. Left half of squares indicate significant abundance changes while right half of squares indicate significant thermal shifts. Median standard deviation between replicates: 0.10. (**B**) As (A) but showing significantly affected proteins after treatment with digitoxin. Median standard deviation between replicates: 0.11. (**C**) As (A) but showing significantly affected proteins after treatment with ouabain. Median standard deviation between replicates: 0.10

Supplemental Fig. 38 Monitoring effect of apoptosis-inducing kinase inhibitor staurosporine. THP-1 cells were treated in three biological replicates with 1 µM staurosporine or vehicle as control. (**A-H**) Mean melting curves in controls and treatments of significantly affected proteins. Error bars indicate standard deviations. Selected data points for cumulation are highlighted with dashed boxes. Treatment-induced thermal shifts and abundance changes are indicated with statistical significances.
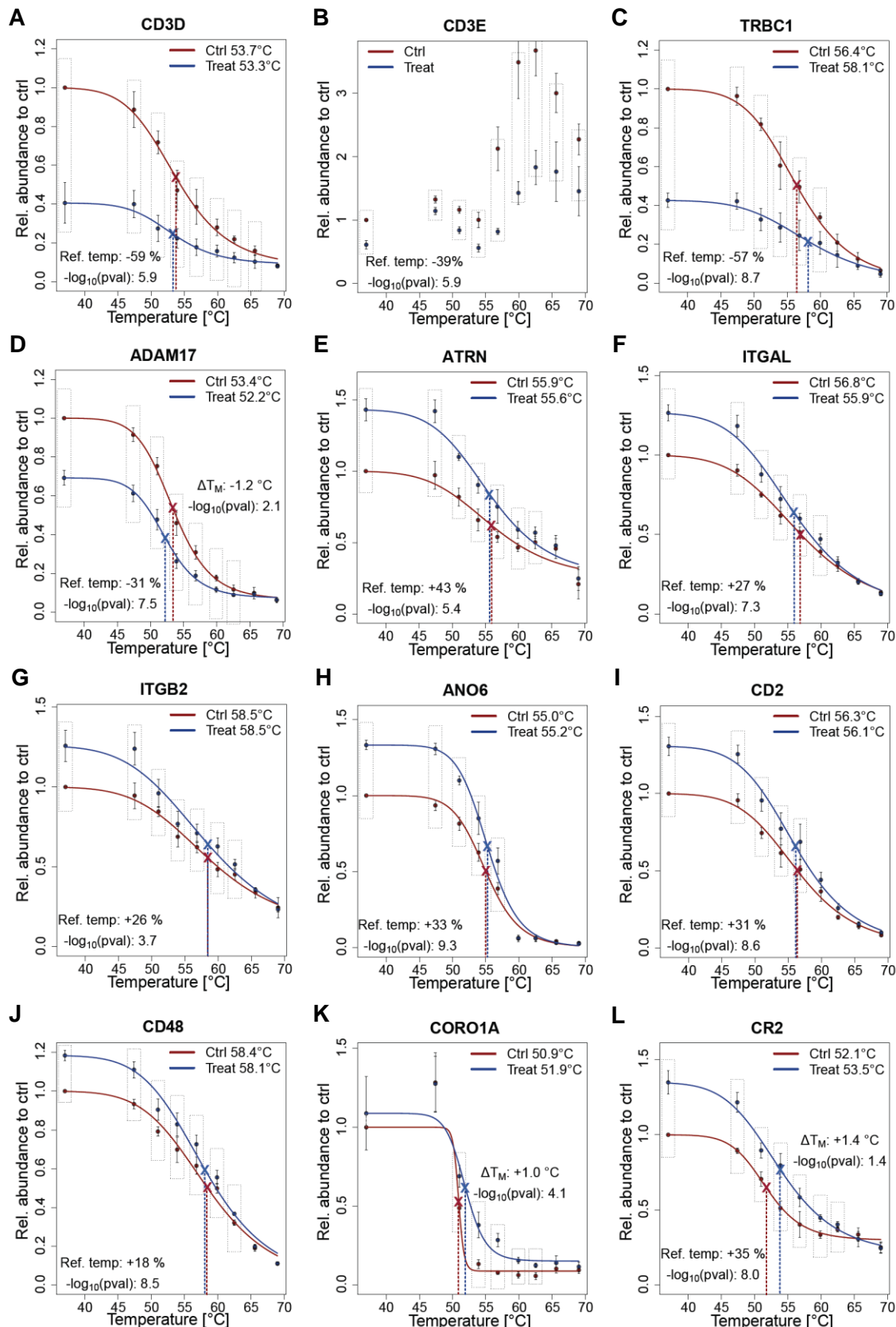

Supplemental Fig. 39 Monitoring effect of digitoxin. Jurkat cells were treated in three biological replicates with 1 µM digitoxin or vehicle as control. (**A-H**) Mean melting curves in controls and treatments of significantly affected proteins. Error bars indicate standard deviations. Selected data points for cumulation are highlighted with dashed boxes. Treatment-induced thermal shifts and abundance changes are indicated with statistical significances.
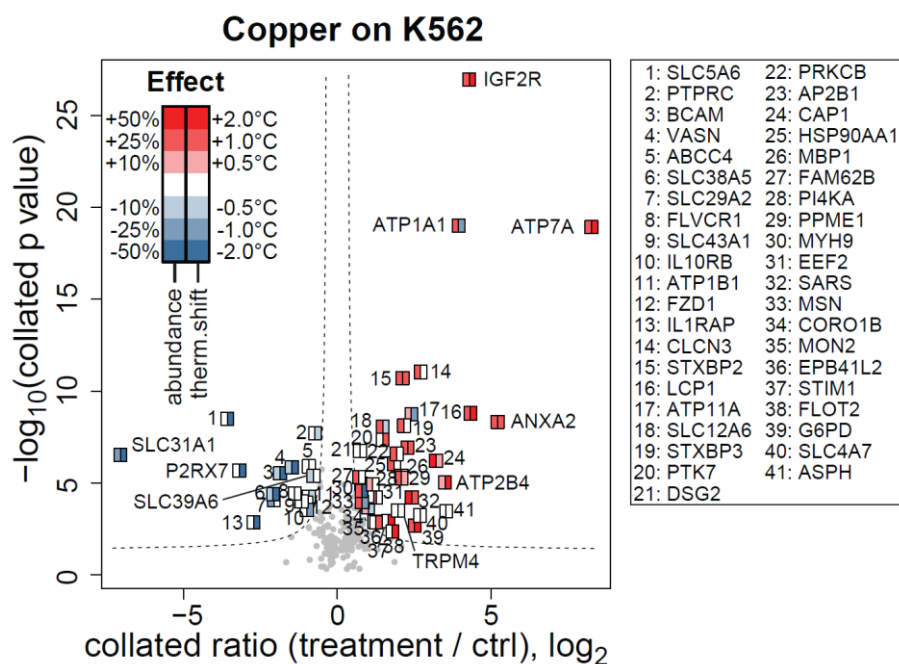
Supplemental Fig. 40 Monitoring effect of ouabain. Jurkat cells were treated in three biological replicates with 1 µM ouabain or vehicle as control. (**A-H**) Mean melting curves in controls and treatments of significantly affected proteins. Error bars indicate standard deviations. Selected data points for cumulation are highlighted with dashed boxes. Treatment-induced thermal shifts and abundance changes are indicated with statistical significances.
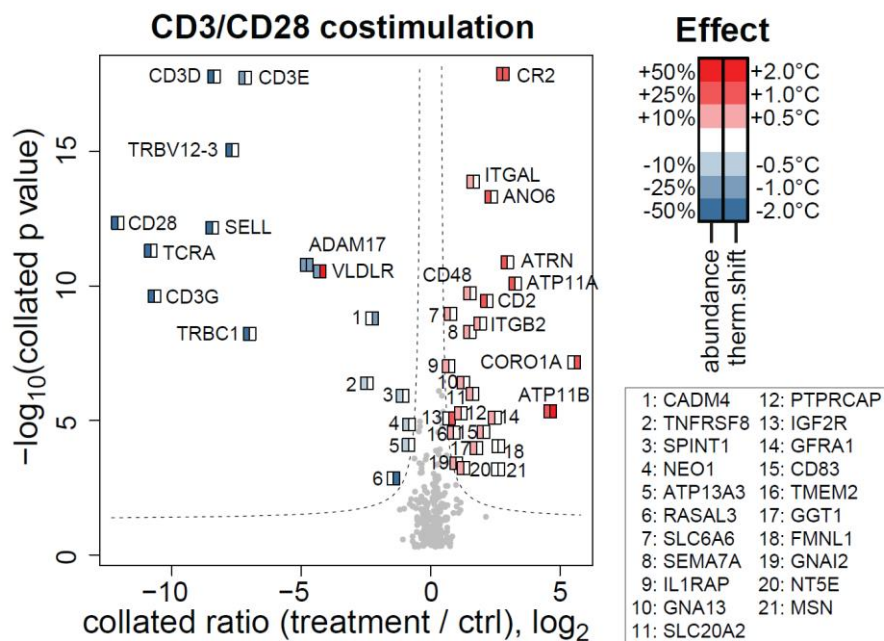

Supplemental Fig. 41 Affected proteins during T-cell activation by CD3 and CD28 co-stimulation. Cells were treated in four biological replicates with 20 µg anti-CD3 mAB and 20 µg anti-CD28 mAb crosslinked with 50 µg anti-mouse mAb or vehicle as control. List of all significantly affected proteins upon treatment. Median standard deviation between replicates: 0.18

Supplemental Fig. 42 Monitoring T-cell activation by CD3 and CD28 co-stimulation. Cells were treated in four biological replicates with 20 µg anti-CD3 mAB and 20 µg anti-CD28 mAb crosslinked with 50 µg anti-mouse mAb or vehicle as control. (**A-L**) Mean melting curves in controls and treatments of significantly affected proteins. Error bars indicate standard deviations. Selected data points for cumulation are highlighted with dashed boxes. Treatment-induced thermal shifts and abundance changes are indicated with statistical significances.

Supplemental Fig. 43 Affected proteins during hypercupremia. K562 cells were treated in three biological replicates with 20 µM CuSO4 or vehicle as control. List of all significantly affected proteins upon treatment. Median standard deviation between replicates: 0.18
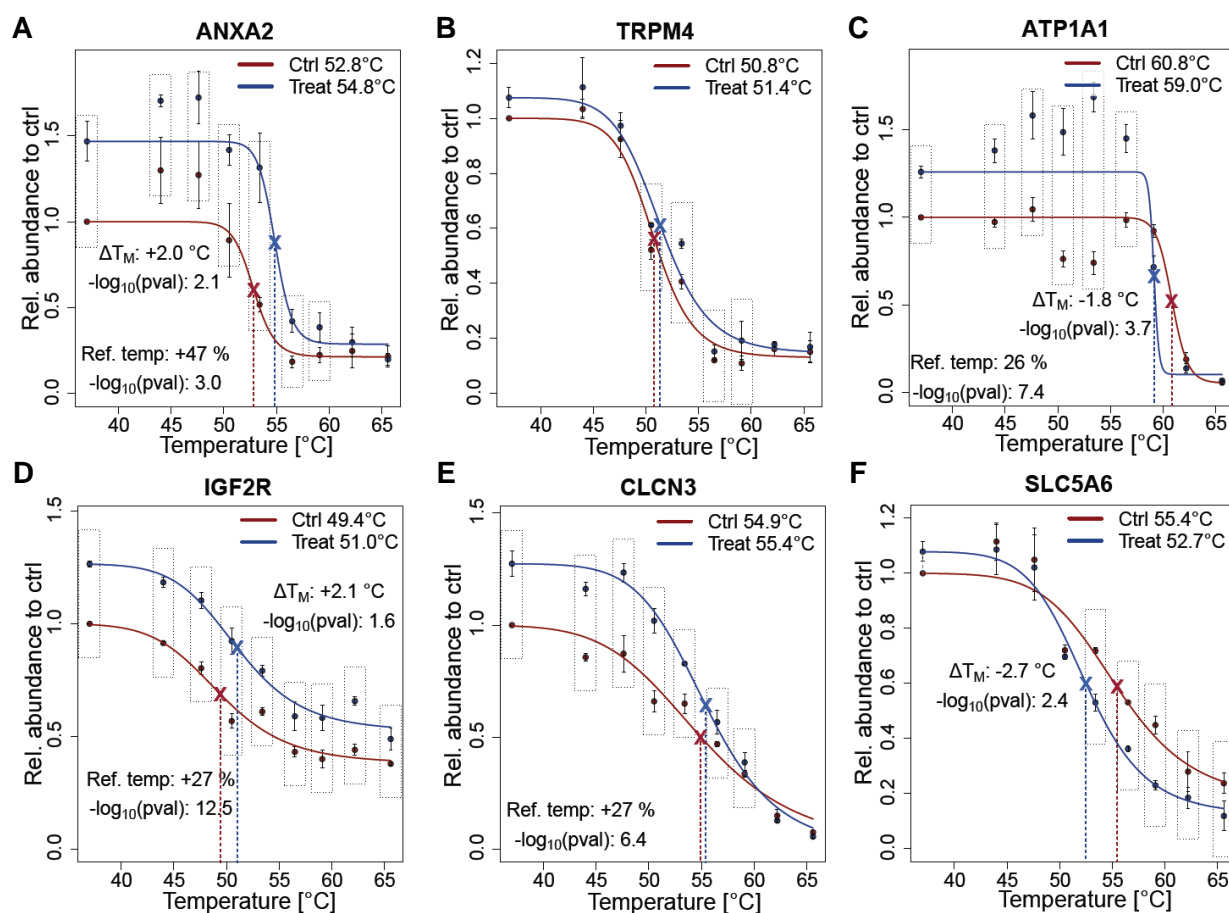
Supplemental Fig. 44 Monitoring cellular stimulation by hypercupremia. K562 cells were treated in three biological replicates with 20 µM CuSO4 or vehicle as control. (**A-F**) Mean melting curves in controls and treatments of selected significantly affected proteins. Error bars indicate standard deviations. Selected data points for cumulation are highlighted with dashed boxes. Treatment-induced thermal shifts and abundance changes are indicated with statistical significances.
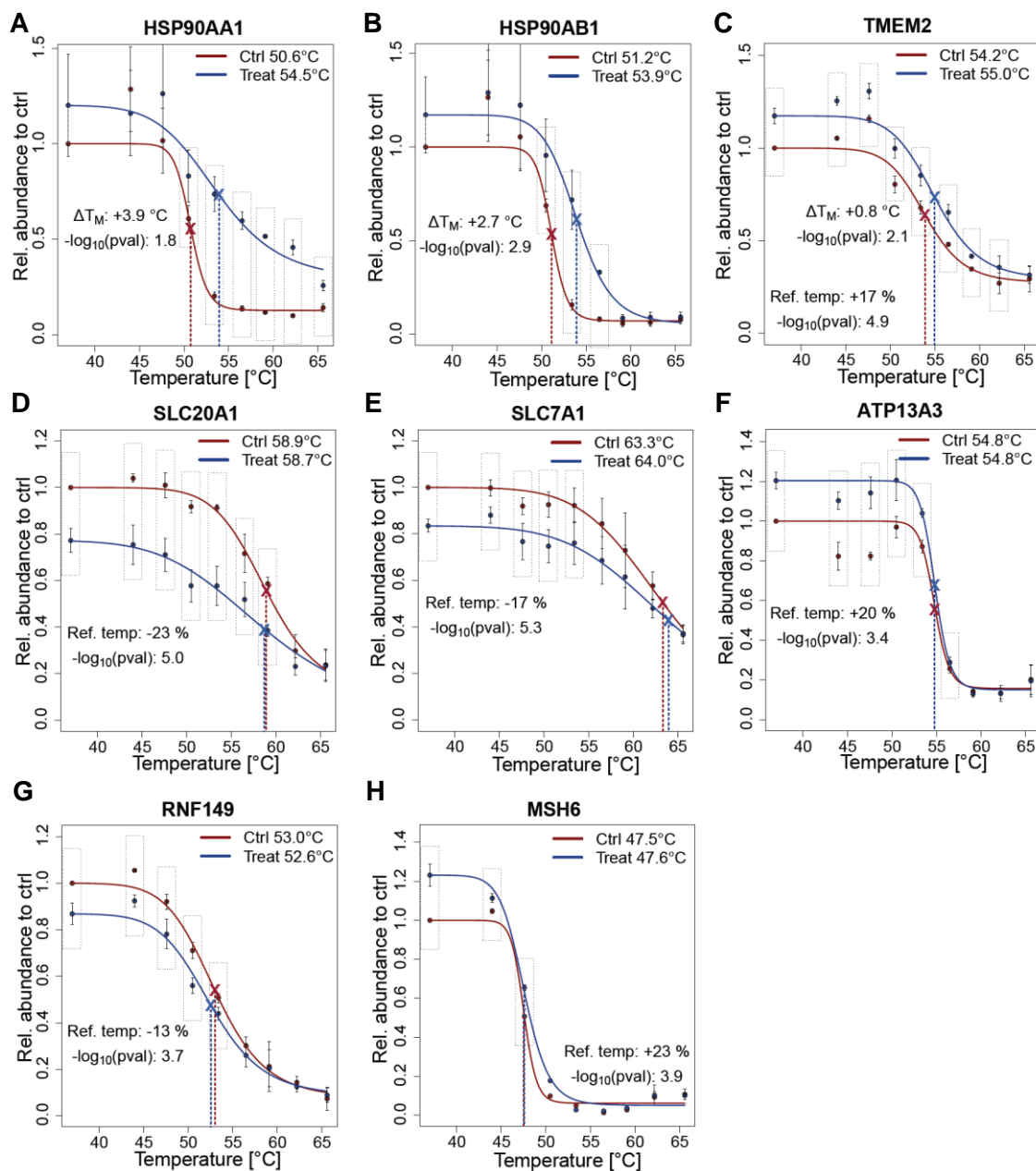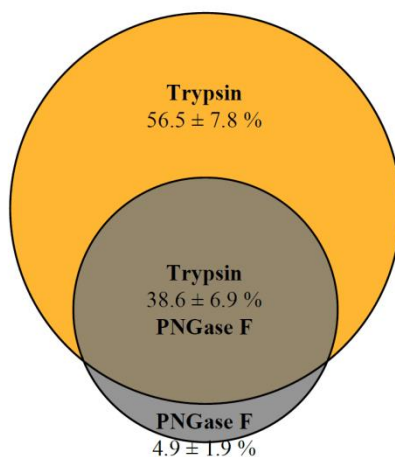
Supplemental Fig. 45 Cell surface thermal proteome profiling for identification of HSP90-targeted proteins. U937 cells were treated in three biological replicates for 30 min with 1 µM luminespib or vehicle as control. Subsequently, cells were exposed to hyperthermia at 42 °C for 30 min followed by additional 60 min at 37 °C for recovery. (**A-H**) Mean melting curves in controls and treatments of significantly affected proteins. Error bars indicate standard deviations. Selected data points for cumulation are highlighted with dashed boxes. Treatment-induced thermal shifts and abundance changes are indicated with statistical significances.

Supplemental Fig. 46 Comparison of tryptic on-bead digestion and PNGase F elution. Comparison of tryptic on-bead digestion and PNGase F elution based on eleven cell surface proteome mappings of cell lines and primary cells each in two biological replicates. Samples were analyzed by LC-MS/MS on a Q Exactive Hybrid-Quadrupole-Orbitrap mass spectrometer using a 270 min gradient. Identified proteins in trypsin samples were filtered for PSM ≥ 2. In PNGase F samples identified proteins were filtered for Mascot score ≥ 20. Venn diagram represents the average overlap of identified plasma membrane proteins in both elution fractions. Standard deviations are indicated.
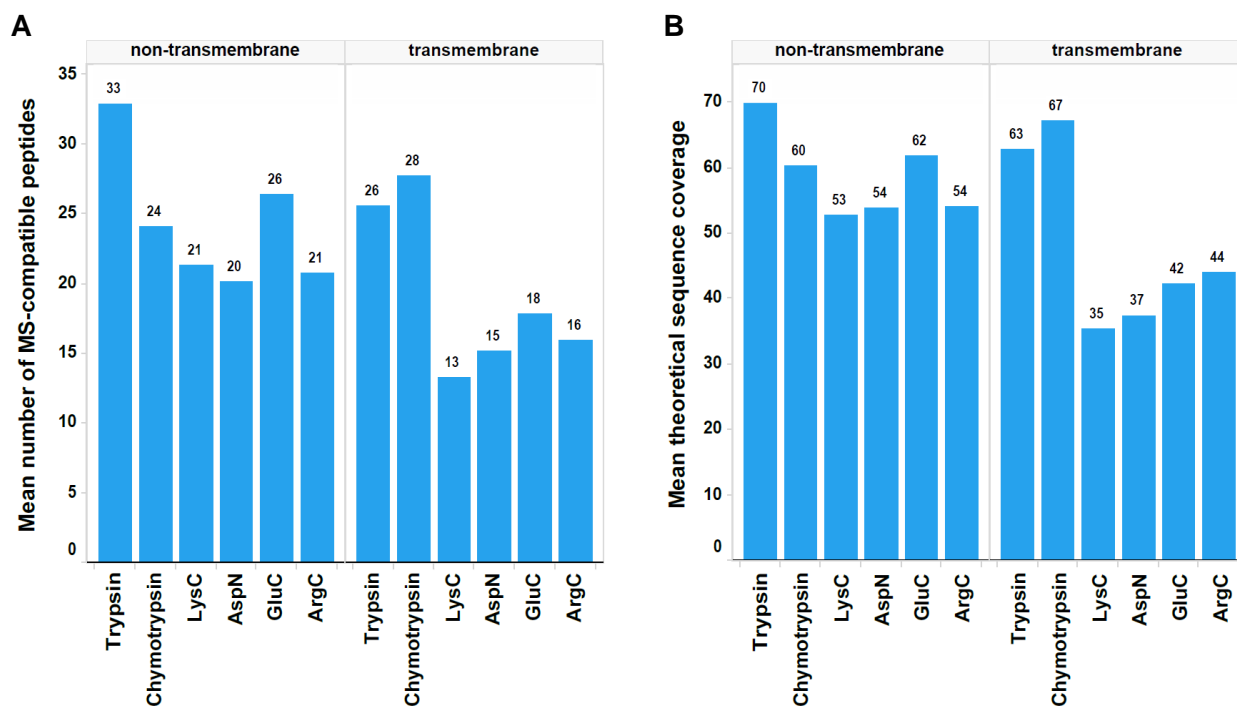
Supplemental Fig. 47 Comparison of proteases for plasma membrane proteomics. *In-silico* digestion of UniProt-annotated plasma membrane proteins with trypsin, chymotrypsin, LysC, AspN, GluC and ArgC without missed cleavages. MS-compatible peptides were defined as peptides with a length between 7 and 35 amino acids. (**A**) Average number of MS-compatible peptides generated by the proteases. (**B**) Average theoretical protein sequence coverage with MS-compatible peptides generated by the proteases.
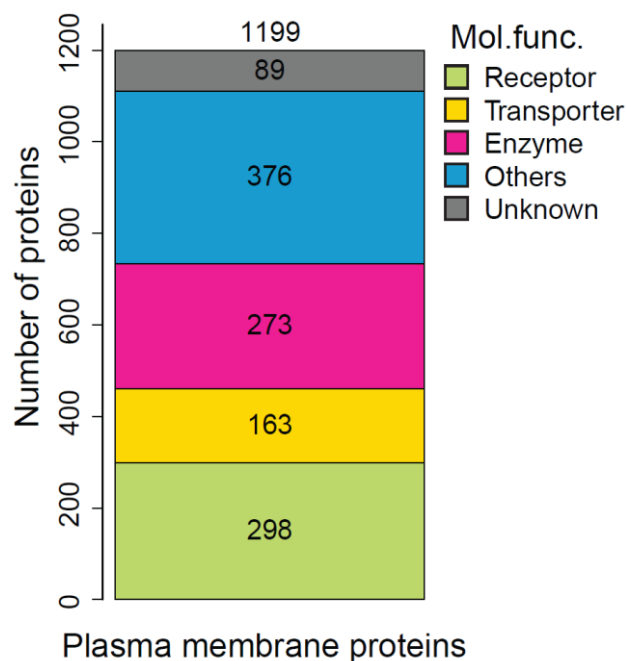
Supplemental Fig. 48 Overall identified plasma membrane proteins in CSTPP experiments. Number of all identified plasma membrane proteins with good quantification (qusm ≥ 3, qupm ≥ 2) in 34 individual CSTPP experiments grouped according to their annotated molecular function (UniProt).
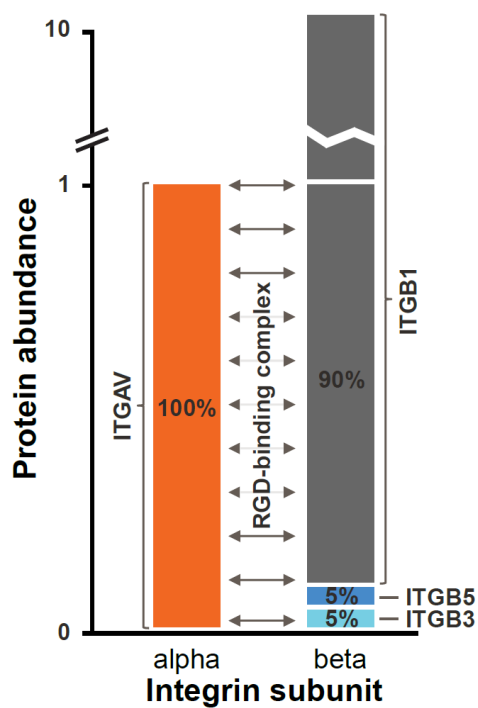
Supplemental Fig. 49 Comparison of absolute integrin abundances in K562 cells. Comparison of ms1intensity-based total abundances for ITGB1, ITGB3 and ITGB5 relative to ITGAV. Hypothesized contribution of respective beta subunits to the formation of functional RGD-binding integrin complexes relative to the alpha subunit are indicated.

9. Acknowledgement

I would like to express my genuine gratitude to Prof. Dr. Andrea Sinz for being my doctoral advisor and for her continuous support.

My sincere thanks also goes to Dr. Gitte Neubauer and Dr. Marcus Bantscheff who gave me the unique opportunity to work on my PhD thesis at Cellzome in Heidelberg.

I would like to thank Dr. Marcus Bantscheff and especially Dr. H. Christian Eberl for supervision, guidance, suggestions and all the constructive discussions and ideas. Without their precious support it would not have been possible to conduct this thesis.

I also want to thank my colleagues from the department for Mass Spectrometry: Markus Bösche, Kerstin Kammerer, Manuela Klös-Hudak and Tatjana Rudi who introduced me to the work with mass spectrometers and kept the instruments running.

Furthermore, I want to thank Stephanie Lehmann, Katrin Strohmer and especially Ina Günthner for sharing their expertise on biochemical methods and for helpful discussions about experimental setups. Special thanks goes to Ina Günthner for supporting me in establishing the protocols for the cell surface thermal proteome profiling.

I thank Jürgen Stuhlfauth, Nilma Garcia-Altrieth, Kerstin Beß and Annette Ruppert for their help and support in cell culture. It would not have been possible to work with this number of diverse cell lines and primary cells without their help.

I also want to thank the Experimental Bioinformatics and the Scientific IT group for help with data processing especially Toby Mathieson for help with our database, Holger Franken for help with TPP analysis and Stephan Gade for advice on statistics.

I thank all the Cellzomers for the pleasant working atmosphere, their open-mindedness and the wonderful time working with them. Special thanks goes to my office mates Johanna Vappiani, Cécile Echalier and Lars Dittus as well as Michael Steidel enabling me to also get through the tough days of a PhD student.

Mein besonderer Dank gilt meiner Familie und insbesondere meinen Eltern für ihre stetige Unterstützung und Hilfe. Ohne sie wäre mein Studium und die Doktorarbeit niemals möglich gewesen.

In liebevoller Erinnerung an meinen Vater.

10. List of publications

Published

Kalxdorf, M., Gade, S., Eberl, H.C., and Bantscheff, M. (2017): Monitoring cell surface N-glycoproteome dynamics by quantitative proteomics reveals mechanistic insights into macrophage differentiation. Mol. Cell. Proteomics mcp.M116.063859.

Accepted book chapter, estimated publication date: 2017

Kalxdorf, M., Eberl, H.C., and Bantscheff, M.: Monitoring dynamic changes of the cell surface glycoproteome by quantitative proteomics. Methods Molecular Biology, Vol. 1647, edited by Iuliana M. Lazar, 2017

Manuscript in preparation, estimated publication date: 2017

Kalxdorf, M., Tögel, I., Eberl, H.C., and Bantscheff, M.: Monitoring target engagement to the plasma membrane proteome by cell surface selective thermal proteome profiling.

Presentations

Kalxdorf, M., Gade, S., Eberl, H.C., and Bantscheff, M.: Monitoring the dynamic N-linked cell surface glycoproteome by quantitative proteomics. *EMBL–Wellcome Genome Campus Conference - Proteomics in Cell Biology and Disease Mechanisms, Heidelberg, September 14 - 17, 2016*

Kalxdorf, M., Tögel, I. and Eberl, H.C.: Towards cracking the plasma membrane proteome: analysis of protein cell surface presentation, its dynamics and direct and indirect effects of drug binding. *GSK's Annual Beautiful Biology Award, Upper Merion, USA, November 15, 2016*

Poster

Kalxdorf, M., Eberl, H.C., and Bantscheff, M.: Monitoring the dynamic N-linked cell surface glycoproteome by quantitative proteomics. *9th European Summer School for Proteomics, Brixen, Italy, August 2 - 8. August, 2015,* **Poster-award winner**

Kalxdorf, M., Tögel, I., Gade, S., Eberl, H.C., and Bantscheff, M.: Towards cracking the plasma membrane proteome: analysis of protein cell surface presentation, its dynamics and direct and indirect effects of drug binding. *GSK's First Annual Postdoctoral Symposium: Join Us in Advancing Science, Upper Merion, USA, November 30 – December 2, 2016*

Kalxdorf, M., Tögel, I., Eberl, H.C., and Bantscheff, M.: Cell surface thermal proteome profiling enables monitoring the interactions of small molecules and endogenous ligands with the plasma membrane proteome. *65th ASMS Conference on Mass Spectrometry and Allied Topics, Indianapolis, USA, June 4 - 8, 2017*

11. Curriculum vitae

Personalien

Name: Mathias Kalxdorf

Geburtsdatum: 18.09.1988

Geburtsort: Rostock

Nationalität: deutsch

Schulischer Werdegang

1995-1999   Grundschule Emmertsgrund, Heidelberg

1999-2008   Helmholtz-Gymnasium, Heidelberg

Hochschulausbildung

10/2008-03/2012   Bachelor-Studiengang Biologische Chemie, Hochschule Mannheim

Studienarbeit: Aufreinigung und Rückfaltung von rekombinant hergestelltem humanem Interferon gamma, Hochschule Mannheim

Bachelorarbeit: Stabilitätsmodell einer NAD-abhängigen Glukosedehydro-genase für Blutzuckerteststreifen, Roche Diagnostics GmbH, Penzberg

03/2012-10/2013   Master-Studiengang Biotechnology: Biomedical Science and Technology, Hochschule Mannheim

Masterarbeit: Development of a new, efficient and economic purification method for proteins and enzymes, Roche Diagnostics GmbH, Penzberg

12. Declaration of authorship

I hereby declare that I am the sole author of this thesis and that I have not used any sources other than those listed in the bibliography and identified as references. I further declare that I have not submitted this thesis at any other institution in order to obtain a degee of Doctor of Science (Dr. rer. nat.)

(City, Date)   (Mathias Kalxdorf)